

BULLETIN OF RUSSIAN STATE MEDICAL UNIVERSITY

BIOMEDICAL JOURNAL OF PIROGOV RUSSIAN NATIONAL RESEARCH MEDICAL UNIVERSITY

EDITOR-IN-CHIEF Denis Rebrikov, DSc, professor

DEPUTY EDITOR-IN-CHIEF Alexander Oettinger, DSc, professor

EDITORS Valentina Geidebrekht, PhD; Nadezda Tikhomirova

TECHNICAL EDITOR Evgeny Lukyanov

TRANSLATORS Nadezda Tikhomirova, Vyacheslav Vityuk

DESIGN AND LAYOUT Marina Doronina

EDITORIAL BOARD

Averin VI, DSc, professor (Minsk, Belarus)
Alipov NN, DSc, professor (Moscow, Russia)
Belousov VV, DSc, professor (Moscow, Russia)
Bogomilskiy MR, corr. member of RAS, DSc, professor (Moscow, Russia)
Bozhenko VK, DSc, CSc, professor (Moscow, Russia)
Bylova NA, CSc, docent (Moscow, Russia)
Gainetdinov RR, CSc (Saint-Petersburg, Russia)
Gendlin GYe, DSc, professor (Moscow, Russia)
Ginter EK, member of RAS, DSc (Moscow, Russia)
Gorbacheva LR, DSc, professor (Moscow, Russia)
Gordeev IG, DSc, professor (Moscow, Russia)
Gudkov AV, PhD, DSc (Buffalo, USA)
Gulyaeva NV, DSc, professor (Moscow, Russia)
Gusev EI, member of RAS, DSc, professor (Moscow, Russia)
Danilenko VN, DSc, professor (Moscow, Russia)
Zarubina TV, DSc, professor (Moscow, Russia)
Zatevakhin II, member of RAS, DSc, professor (Moscow, Russia)
Kagan VE, professor (Pittsburgh, USA)
Kzyzhkowska YuG, DSc, professor (Heidelberg, Germany)
Kobriniskii BA, DSc, professor (Moscow, Russia)
Kozlov AV, MD PhD (Vienna, Austria)
Kotelevtsev YuV, CSc (Moscow, Russia)
Lebedev MA, PhD (Darem, USA)
Manturova NE, DSc (Moscow, Russia)
Milushkina OYu, DSc, professor (Moscow, Russia)
Mitupov ZB, DSc, professor (Moscow, Russia)
Moshkovskii SA, DSc, professor (Moscow, Russia)
Munblit DB, MSc, PhD (London, Great Britain)

Negrebetsky VV, DSc, professor (Moscow, Russia)
Novikov AA, DSc (Moscow, Russia)
Pivovarov YuP, member of RAS, DSc, professor (Moscow, Russia)
Polunina NV, corr. member of RAS, DSc, professor (Moscow, Russia)
Poryadin GV, corr. member of RAS, DSc, professor (Moscow, Russia)
Razumovskii AYU, corr. member of RAS, DSc, professor (Moscow, Russia)
Rebrova OYu, DSc (Moscow, Russia)
Rudoy AS, DSc, professor (Minsk, Belarus)
Rylova AK, DSc, professor (Moscow, Russia)
Savelieva GM, member of RAS, DSc, professor (Moscow, Russia)
Semiglazov VF, corr. member of RAS, DSc, professor (Saint-Petersburg, Russia)
Skoblina NA, DSc, professor (Moscow, Russia)
Slavyanskaya TA, DSc, professor (Moscow, Russia)
Smirnov VM, DSc, professor (Moscow, Russia)
Spallone A, DSc, professor (Rome, Italy)
Starodubov VI, member of RAS, DSc, professor (Moscow, Russia)
Stepanov VA, corr. member of RAS, DSc, professor (Tomsk, Russia)
Suchkov SV, DSc, professor (Moscow, Russia)
Takhchidi KhP, member of RAS, DSc, professor (Moscow, Russia)
Trufanov GE, DSc, professor (Saint-Petersburg, Russia)
Favorova OO, DSc, professor (Moscow, Russia)
Filipenko ML, CSc, leading researcher (Novosibirsk, Russia)
Khazipov RN, DSc (Marsel, France)
Chundukova MA, DSc, professor (Moscow, Russia)
Shimanovskii NL, corr. member of RAS, DSc, professor (Moscow, Russia)
Shishkina LN, DSc, senior researcher (Novosibirsk, Russia)
Yakubovskaya RI, DSc, professor (Moscow, Russia)

SUBMISSION <http://vestnikrgmu.ru/login?lang=en>

CORRESPONDENCE editor@vestnikrgmu.ru

COLLABORATION manager@vestnikrgmu.ru

ADDRESS ul. Ostrovityanova, d. 1, Moscow, Russia, 117997

Indexed in Scopus. CiteScore 2022: 0.6

Scopus[®]

SCImago Journal & Country Rank 2020: 0.14

SJR
Scimago Journal & Country Rank

Indexed in WoS. JCR 2021: 0.5

WEB OF SCIENCE[™]

Listed in HAC 31.01.2020 (№ 507)

 **ВЫСШАЯ
АТТЕСТАЦИОННАЯ
КОМИССИЯ (ВАК)**

Five-year h-index is 8

Google
scholar

Open access to archive

CYBERLENINKA

Issue DOI: 10.24075/brsmu.2023-06

The mass media registration certificate № 012769 issued on July 29, 1994

Founder and publisher is Pirogov Russian National Research Medical University (Moscow, Russia)

The journal is distributed under the terms of Creative Commons Attribution 4.0 International License www.creativecommons.org



Approved for print 31.12.2023
Circulation: 100 copies. Printed by Print.Formula
www.print-formula.ru

ВЕСТНИК РОССИЙСКОГО ГОСУДАРСТВЕННОГО МЕДИЦИНСКОГО УНИВЕРСИТЕТА

НАУЧНЫЙ МЕДИЦИНСКИЙ ЖУРНАЛ РНИМУ ИМ. Н. И. ПИРОГОВА

ГЛАВНЫЙ РЕДАКТОР Денис Ребриков, д. б. н., профессор

ЗАМЕСТИТЕЛЬ ГЛАВНОГО РЕДАКТОРА Александр Эттингер, д. м. н., профессор

РЕДАКТОРЫ Валентина Гейдебрехт, к. б. н.; Надежда Тихомирова

ТЕХНИЧЕСКИЙ РЕДАКТОР Евгений Лукьянов

ПЕРЕВОДЧИКИ Надежда Тихомирова, Вячеслав Витюк

ДИЗАЙН И ВЕРСТКА Марины Дорониной

РЕДАКЦИОННАЯ КОЛЛЕГИЯ

В. И. Аверин, д. м. н., профессор (Минск, Белоруссия)
Н. Н. Алипов, д. м. н., профессор (Москва, Россия)
В. В. Белоусов, д. б. н., профессор (Москва, Россия)
М. Р. Богомилский, член-корр. РАН, д. м. н., профессор (Москва, Россия)
В. К. Боженко, д. м. н., к. б. н., профессор (Москва, Россия)
Н. А. Былова, к. м. н., доцент (Москва, Россия)
Р. Р. Гайнетдинов, к. м. н. (Санкт-Петербург, Россия)
Г. Е. Гендлин, д. м. н., профессор (Москва, Россия)
Е. К. Гинтер, академик РАН, д. б. н. (Москва, Россия)
Л. Р. Горбачева, д. б. н., профессор (Москва, Россия)
И. Г. Гордеев, д. м. н., профессор (Москва, Россия)
А. В. Гудков, PhD, DSc (Буффало, США)
Н. В. Гуляева, д. б. н., профессор (Москва, Россия)
Е. И. Гусев, академик РАН, д. м. н., профессор (Москва, Россия)
В. Н. Даниленко, д. б. н., профессор (Москва, Россия)
Т. В. Зарубина, д. м. н., профессор (Москва, Россия)
И. И. Затевахин, академик РАН, д. м. н., профессор (Москва, Россия)
В. Е. Каган, профессор (Питтсбург, США)
Ю. Г. Кжышковска, д. б. н., профессор (Гейдельберг, Германия)
Б. А. Кобринский, д. м. н., профессор (Москва, Россия)
А. В. Козлов, MD PhD (Вена, Австрия)
Ю. В. Котелевцев, к. х. н. (Москва, Россия)
М. А. Лебедев, PhD (Дарем, США)
Н. Е. Мантурова, д. м. н. (Москва, Россия)
О. Ю. Милушкина, д. м. н., доцент (Москва, Россия)
З. Б. Митупов, д. м. н., профессор (Москва, Россия)
С. А. Мошковский, д. б. н., профессор (Москва, Россия)
Д. Б. Мунблит, MSc, PhD (Лондон, Великобритания)

В. В. Негребцкий, д. х. н., профессор (Москва, Россия)
А. А. Новиков, д. б. н. (Москва, Россия)
Ю. П. Пивоваров, д. м. н., академик РАН, профессор (Москва, Россия)
Н. В. Полунина, член-корр. РАН, д. м. н., профессор (Москва, Россия)
Г. В. Порядин, член-корр. РАН, д. м. н., профессор (Москва, Россия)
А. Ю. Разумовский, член-корр., профессор (Москва, Россия)
О. Ю. Реброва, д. м. н. (Москва, Россия)
А. С. Рудой, д. м. н., профессор (Минск, Белоруссия)
А. К. Рылова, д. м. н., профессор (Москва, Россия)
Г. М. Савельева, академик РАН, д. м. н., профессор (Москва, Россия)
В. Ф. Семглазов, член-корр. РАН, д. м. н., профессор (Санкт-Петербург, Россия)
Н. А. Скоблина, д. м. н., профессор (Москва, Россия)
Т. А. Славянская, д. м. н., профессор (Москва, Россия)
В. М. Смирнов, д. б. н., профессор (Москва, Россия)
А. Спаллоне, д. м. н., профессор (Рим, Италия)
В. И. Стародубов, академик РАН, д. м. н., профессор (Москва, Россия)
В. А. Степанов, член-корр. РАН, д. б. н., профессор (Томск, Россия)
С. В. Сучков, д. м. н., профессор (Москва, Россия)
Х. П. Тахчиди, академик РАН, д. м. н., профессор (Москва, Россия)
Г. Е. Труфанов, д. м. н., профессор (Санкт-Петербург, Россия)
О. О. Фаворова, д. б. н., профессор (Москва, Россия)
М. Л. Филипенко, к. б. н. (Новосибирск, Россия)
Р. Н. Хазипов, д. м. н. (Марсель, Франция)
М. А. Чундокова, д. м. н., профессор (Москва, Россия)
Н. Л. Шимановский, член-корр. РАН, д. м. н., профессор (Москва, Россия)
Л. Н. Шишкина, д. б. н. (Новосибирск, Россия)
Р. И. Якубовская, д. б. н., профессор (Москва, Россия)

ПОДАЧА РУКОПИСЕЙ <http://vestnikrgmu.ru/login>

ПЕРЕПИСКА С РЕДАКЦИЕЙ editor@vestnikrgmu.ru

СОТРУДНИЧЕСТВО manager@vestnikrgmu.ru

АДРЕС РЕДАКЦИИ ул. Островитянова, д. 1, г. Москва, 117997

Журнал включен в Scopus. CiteScore 2022: 0,6

Журнал включен в WoS. JCR 2021: 0,5

Индекс Хирша (h²) журнала по оценке Google Scholar: 8

Scopus[®]

SCImago Journal & Country Rank 2020: 0,14

SJR
Scimago Journal & Country Rank

WEB OF SCIENCE[™]

Журнал включен в Перечень 31.01.2020 (№ 507)



**ВЫСШАЯ
АТТЕСТАЦИОННАЯ
КОМИССИЯ (ВАК)**

Google
scholar

Здесь находится открытый архив журнала

CYBERLENINKA

DOI выпуска: 10.24075/vrgmu.2023-06

Свидетельство о регистрации средства массовой информации № 012769 от 29 июля 1994 г.

Учредитель и издатель — Российский национальный исследовательский медицинский университет имени Н. И. Пирогова (Москва, Россия)

Журнал распространяется по лицензии Creative Commons Attribution 4.0 International www.creativecommons.org



Подписано в печать 31.12.2023
Тираж 100 экз. Отпечатано в типографии Print.Formula
www.print-formula.ru

ORIGINAL RESEARCH

5

Relationship between pro-inflammatory cytokine levels and blood bacterial DNA composition in obese children

Roumiantsev SA, Kirilina IV, Gaponov AM, Khusnutdinova DR, Grigoryeva TV, Teplyakova ED, Makarov VV, Yudin SM, Shestopalov AV

Взаимосвязь уровней провоспалительных цитокинов с составом бактериальной ДНК крови у детей с ожирением

С. А. Румянцев, И. В. Кирилина, А. М. Гапонов, Д. Р. Хуснутдинова, Т. В. Григорьева, Е. Д. Теплякова, В. В. Макаров, С. М. Юдин, А. В. Шестопалов

ORIGINAL RESEARCH

14

Altered circadian expression of cytokines in blood of patients with essential hypertension following COVID-19

Radaeva OA, Simbirtsev AS, Kostina YuA, Iskandryarova MS, Negodnova EV, Mashnina SV, Ereemeev VV, Krasnoglazova KA, Babushkin IO

Изменения циркадианных ритмов уровней цитокинов в крови пациентов с эссенциальной гипертензией в постковидном периоде

О. А. Радаева, А. С. Симбирцев, Ю. А. Костина, М. С. Искандрыарова, Е. В. Негоднова, С. В. Машнина, В. В. Еремеев, К. А. Красноглазова, И. О. Бабушкин

ORIGINAL RESEARCH

21

Comparative bioinformatics analysis of antimicrobial resistance gene pool in the genomes of representatives of genus *Corynebacterium*

Kulshan TA, Bugaeva IO, Soboleva EF, Allyanova MS, Popov DA, Shvidenko IG

Сравнительный биоинформатический анализ состава генов антимикробной устойчивости в геномах представителей рода *Corynebacterium*

Т. А. Кульшань, И. О. Бугаева, Е. Ф. Соболева, М. С. Аллянова, Д. А. Попов, И. Г. Швиденко

ORIGINAL RESEARCH

27

Impact of untranslated mRNA sequences on immunogenicity of mRNA vaccines against *M. tuberculosis* in mice

Shepelkova GS, Reshetnikov VV, Avdienko VG, Sheverev DV, Yermeev VV, Ivanov RA

Влияние нетранслируемых последовательностей мРНК на иммуногенность мРНК-вакцин против *M. tuberculosis* у мышей

Г. С. Шепелькова, В. В. Решетников, В. Г. Авдиенко, Д. В. Шевырев, В. В. Еремеев, Р. А. Иванов

ORIGINAL RESEARCH

34

Preparation of a recombinant ribonuclease inhibitor in *E. coli* for use in mRNA synthesis *in vitro*

Zakharova MV, Zagoskin AA, Ivanov RA, Nagornykh MO

Получение рекомбинантного ингибитора рибонуклеаз в *E. coli* для использования в синтезе мРНК *in vitro*

М. В. Захарова, А. А. Загоскин, Р. А. Иванов, М. О. Нагорных

ORIGINAL RESEARCH

42

Genetically encoded light-inducible sensor for nucleolar visualization

Zhurlova PA, Besedovskaia ZV, Sokolinskaya EL, Putlyayeva LV

Создание генетически кодируемого светоиндуцируемого сенсора для визуализации ядрышка

П. А. Журлова, З. В. Беседовская, Е. Л. Соколинская, Л. В. Путляева

ORIGINAL RESEARCH

47

NEAT1_1 long non-coding RNA reduces the survival of primary neuronal cells under ER-stress

Pukaeva NE, Zalevskaya VN, Deykin AV, Taubinskaya MI, Kukharskaya OA, Ovchinnikov RK, Antohin AI, Kukharsky MS

Длинная некодирующая РНК NEAT1_1 снижает выживаемость первичных нейронных клеток при ЭПР-стрессе

Н. Е. Пукаева, В. Н. Залевская, А. В. Дейкин, М. И. Таубинская, О. А. Кухарская, Р. К. Овчинников, А. И. Антохин, М. С. Кухарский

ORIGINAL RESEARCH

56

Prefrontal cortex transcranial theta-burst stimulation frequency-dependent effects on cognitive functions

Suponeva NA, Bakulin IS, Poydasheva AG, Sinityn DO, Zabirowa AH, Lagoda DYU, Piradov MA

Частотно-зависимый эффект транскраниальной стимуляции тета-вспышками префронтальной коры на когнитивные функции

Н. А. Супонева, И. С. Бакулин, А. Г. Пойдашева, Д. О. Ситицын, А. Х. Забиrowa, Д. Ю. Лагода, М. А. Пирадов

ORIGINAL RESEARCH

64

Predicting the outcomes of *in vitro* fertilization programs using a random forest machine learning model

Vladimirsky GM, Zhuravleva MA, Dashieva AE, Korneeva IE, Nazarenko TA

Прогнозирование исходов программ экстракорпорального оплодотворения с использованием модели машинного обучения «Случайный лес»

Г. М. Владимирский, М. А. Журавлева, А. Э. Дашиева, И. Е. Корнеева, Т. А. Назаренко

ORIGINAL RESEARCH

71

Exploration of the femtosecond laser pulse thermal effects on the mouse embryos during the assisted hatching procedure

Kubekina MV, Filatov MA, Silaeva YuYu, Sitnikov DS

Исследование теплового воздействия фемтосекундных лазерных импульсов на эмбрионы мыши в рамках процедуры вспомогательного хетчинга

М. В. Кубекина, М. А. Филатов, Ю. Ю. Силаева, Д. С. Ситников

ORIGINAL RESEARCH

79

The possibility of evaluation mRNA expression profiling to predict progression of local stage colorectal cancer

Goncharov SV, Bozhenko VK, Zakharenko MV, Chaptikov AA, Kulinich TM, Solodkiy VA

Возможности использования профилирования экспрессии мРНК для прогноза прогрессирования локальных стадий колоректального рака

С. В. Гончаров, В. К. Боженко, М. В. Захаренко, А. А. Чаптыков, Т. М. Кулинич, В. А. Солодкий

CLINICAL CASE

86

Methods for combination treatment of metastatic uveal melanoma

Kolomiets KV, Ponomareva ES, Posypina YaR, Mihailov II, Mandzhiev CB, Povetkina EV, Tuguz RR, Bulgakov SM, Repunova VI

Комбинированные методы лечения метастатической увеальной меланомы

К. В. Коломиец, Э. С. Пономарева, Я. Р. Посыпина, И. И. Михайлов, Ч. Б. Манджиев, Е. В. Поветкина, Р. Р. Тургуз, С. М. Булгаков, В. И. Репунова

ORIGINAL RESEARCH

90

Efficacy of the jawbone defect elimination

Poryadin GV, Eremin DA, Khelminskaya NM, Kravets VI, Zhitareva IV, Posadskaya AV, Krasnov NM, Shen PA, Gureshidze MA

Эффективность устранения костных дефектов челюстей

Г. В. Порядин, Д. А. Еремин, Н. М. Хелминская, В. И. Кравец, И. В. Житарева, А. В. Посадская, Н. М. Краснов, П. А. Шень, М. А. Гурешидзе

ORIGINAL RESEARCH

95

Preoperative planning of hip arthroplasty

Minasov BSh, Yakupov RR, Bilyalov AR, Minasov TB, Valeev MM, Mavlyutov TR, Nigamedzanov IE, Akbashev VN, Karimov KK

Предоперационное планирование артропластики тазобедренного сустава

Б. Ш. Минасов, Р. Р. Якупов, А. Р. Билялов, Т. Б. Минасов, М. М. Валеев, Т. Р. Мавлютов, И. Э. Нигамедзянов, В. Н. Акбашев, К. К. Каримов

METHOD

101

Foveal microsurgical reconstruction technique for macular hole

Takhchidi KP

Технология микрохирургической реконструкции фовеа при макулярных разрывах

Х. П. Тахчиди

RELATIONSHIP BETWEEN PRO-INFLAMMATORY CYTOKINE LEVELS AND BLOOD BACTERIAL DNA COMPOSITION IN OBESE CHILDREN

Roumiantsev SA^{1,2,3}, Kirilina IV^{1,2,3}✉, Gaponov AM², Khusnutdinova DR⁴, Grigoryeva TV⁴, Teplyakova ED⁵, Makarov VV⁶, Yudin SM⁶, Shestopalov AV^{1,2,3}

¹ Pirogov Russian National Research Medical University, Moscow, Russia

² Center for Digital and Translational Biomedicine, Center for Molecular Health, Moscow, Russia

³ The National Medical Research Center for Endocrinology, Moscow, Russia

⁴ Kazan (Volga Region) Federal University, Kazan, Russia

⁵ Rostov State Medical University, Rostov-on-Don, Russia

⁶ Center for Strategic Planning and Management of Biomedical Health Risks, Moscow, Russia

Adipose tissue, being a source of chronic low-grade inflammation, activates cells of the immune system by producing cytokines and chemokines. The balance between pro- and anti-inflammatory molecules and their relationship with blood bacterial DNA in obese children and adolescents has not been studied sufficiently. This study aimed to find patterns of interaction between fractions of bacterial families in healthy and obese children, analyze cytokine levels and their relationship with blood bacterial DNA content, evaluate alpha diversity of blood microbiome and similarities of blood and fecal microbiomes. We examined 163 individuals (children and adolescents), who were divided into 2 groups, obese ($n = 80$, obesity classes I through III) and healthy ($n = 83$). The material sampled and studied was venous blood. Only individuals that have not been taking antibiotics, pro- and prebiotics for at least 3 months before the study were included. The methods employed were multiplex ELISA (enzyme immunoassay) and 16S rRNA gene sequencing (region V3–V4). From the angle of bacterial families, we found differences in their content (fractions) in blood microbiome and the frequency of isolation of their DNA therein. Nineteen families accounted for over three quarters of all bacterial DNA identified in the blood. In obese children, one of the dominating roles was played by *Ruminococcaceae*, with their DNA a key part of the microbiome's alpha diversity, while in healthy participants this could be said about *Bacteroidaceae*. Analyzing beta diversity, we found that in obese children, fecal and blood microbiomes differed significantly, which indicates, mainly, extra-intestinal translocation of bacterial DNA. Obese children exhibited increased content of IL17A ($p = 0.017$) and PD-L1 ($p = 0.021$); there were differences in blood microbiome between groups. We identified the patterns of interaction between bacterial DNA fractions, and assessed cytokine levels.

Keywords: obesity, cytokines, bacterial DNA, blood microbiome, children, inflammation, PD-L1

Funding: the work was done in the context of agreement #0373100122119000041 under the Project "Compilation of a bank of blood serum and faecal samples from healthy donors and patients with obesity, metabolic syndrome, type II diabetes mellitus, disrupted intestinal mucosal barrier, with the aim of identifying candidate species-specific mediators of the human microbiota quorum sensing systems modulating endocrine and metabolic functions of adipose tissue."

Author contribution: Shestopalov AV, Roumiantsev SA — idea of the study, experiment planning, manuscript writing, editing; Yudin SM, Makarov VV — idea of the study, editing; Gaponov AM — idea, experiment planning, manuscript editing; Kirilina IV — idea, experiment planning, data processing, manuscript writing, editing; Grigoryeva TV — planning, data collection, data processing, editing; Teplyakova ED — experiment planning, manuscript editing; Khusnutdinova DR — data collection.

Compliance with ethical standards: the study was approved by the Local Ethics Committee of N.I. Pirogov Russian National Research Medical University (Minutes #186 of June 26, 2019) and Local Ethics Committee of Rostov State Medical University (Minutes #20/19 of December 12, 2019). To be included in the study, all patients and their parents mandatorily signed voluntary informed consent forms.

✉ **Correspondence should be addressed:** Irina V. Kirilina
Ostrovityanova, 1, Moscow, 117997, Russia; kirilina-irina@bk.ru

Received: 13.10.2023 **Accepted:** 25.11.2023 **Published online:** 23.12.2023

DOI: 10.24075/brsmu.2023.049

ВЗАИМОСВЯЗЬ УРОВНЕЙ ПРОВОСПАЛИТЕЛЬНЫХ ЦИТОКИНОВ С СОСТАВОМ БАКТЕРИАЛЬНОЙ ДНК КРОВИ У ДЕТЕЙ С ОЖИРЕНИЕМ

С. А. Румянцев^{1,2,3}, И. В. Кирилина^{1,2,3}✉, А. М. Гапонов², Д. Р. Хуснутдинова⁴, Т. В. Григорьева⁴, Е. Д. Теплякова⁵, В. В. Макаров⁶, С. М. Юдин⁶, А. В. Шестопалов^{1,2,3}

¹ Российский национальный исследовательский медицинский университет имени Н. И. Пирогова, Москва, Россия

² Центр молекулярного здоровья, Москва, Россия

³ Национальный исследовательский центр эндокринологии, Москва, Россия

⁴ Казанский (Приволжский) федеральный университет, Казань, Россия

⁵ Ростовский государственный медицинский университет, Ростов-на-Дону, Россия

⁶ Центр стратегического планирования и управления медико-биологическими рисками здоровью Федерального медико-биологического агентства, Москва, Россия

Жировая ткань как источник развития хронического низкоинтенсивного воспаления активизирует клетки иммунной системы путем выработки цитокинов и хемокинов. Баланс между про- и противовоспалительными молекулами и их связь с бактериальной ДНК крови при ожирении у детей и подростков недостаточно исследованы. Цель исследования — нахождение паттернов взаимодействия между долями семейств бактериальной ДНК у здоровых детей и с ожирением, анализ уровней цитокинов и их связь с бактериальной ДНК крови, оценка альфа-разнообразия микробиома крови и сходства микробиомов крови и кала. Обследовано 163 человека (дети и подростки), которых разделили на 2 группы: 80 человек с ожирением I–III степени и 83 здоровых. Материал исследования — венозная кровь. Критерии включения в группы — отсутствие приема антибиотиков, про- и пребиотиков в течение трех месяцев. Методы — мультиплексный ИФА (иммуноферментный анализ); секвенирование участка v3–v4 гена 16S рРНК. Выявлены различия в микробиоме крови на уровне семейств как по доле, так и по частоте выделения бактериальной ДНК. Более 3/4 ДНК крови в обеих группах приходилось на 19 семейств. Значимо больший вклад в альфа-разнообразие у детей с ожирением принадлежал бактериальной ДНК *Ruminococcaceae*, однако в группе здоровых детей эта роль принадлежала *Bacteroidaceae*. Анализ бета-разнообразия крови позволил выявить у детей с ожирением значимую отдаленность микробиома крови и кала, что свидетельствует о преимущественно внекишечной транслокации бактериальной ДНК. Выявлено увеличение содержания ИЛ-17А ($p = 0,017$) и PD-L1 ($p = 0,021$) у детей с ожирением, а также различия в микробиоме крови в группах. Определены паттерны взаимодействия между долями бактериальной ДНК, оценены уровни цитокинов.

Ключевые слова: ожирение, цитокины, бактериальная ДНК, микробиом крови, дети, воспаление, PD-L1

Финансирование: работа выполняется в рамках договора № 0373100122119000041 по проекту «Создание банка биообразцов сыворотки крови и фекалий от здоровых доноров и пациентов с ожирением, метаболическим синдромом, сахарным диабетом II типа, нарушением мукозального барьера желудочно-кишечного тракта с целью выявления кандидатных видоспецифических медиаторов систем quorum sensing микробиоты человека, модулирующих эндокринную и метаболическую функцию жировой ткани».

Вклад авторов: А. В. Шестопалов, С. А. Румянцев — идея, планирование эксперимента, написание и редактирование статьи; С. М. Юдин, В. В. Макаров — идея, редактирование; А. М. Гапонов — идея, планирование, редактирование; И. В. Кирилина — идея, планирование, сбор и обработка данных, написание и редактирование статьи; Т. В. Григорьева — планирование, сбор и обработка данных, редактирование; Е. Д. Теплякова — планирование эксперимента, редактирование статьи; Д. Р. Хуснутдинова — сбор данных.

Соблюдение этических стандартов: исследование одобрено ЛНЭК ФГБОУ ВО РНИМУ имени Н. И. Пирогова (протокол № 186 от 26 июня 2019 г.) и ЛНЭК ФГБОУ ВО РостГМУ (протокол № 20/19 от 12 декабря 2019 г.). Обязательным условием включения в исследование было добровольное подписание информированных согласий пациентами и их родителями.

✉ **Для корреспонденции:** Ирина Валерьевна Кирилина
ул. Островитянова, д. 1, г. Москва, 117997, Россия; kirilina-irina@bk.ru

Статья получена: 13.10.2023 **Статья принята к печати:** 25.11.2023 **Опубликована онлайн:** 23.12.2023

DOI: 10.24075/vrgmu.2023.049

Abnormal changes in human microbiota alter metabolism and promote growth of adipose tissue, gradually contributing to the development of obesity. This diagnosis is growing more and more common among both adults and children and adolescents, which substantiates the urgency of search for the yet unknown mechanisms behind this pathology. It is important to timely detect predisposition to obesity in children and adolescents, since it is possible to delay, or, at best, prevent progression of this disease, which leads to type II diabetes mellitus, dyslipidemia, disorders of cardiovascular, reproductive systems, liver, microvascular pathologies, etc. Obesity triggers morphological and functional changes in white adipose tissue, attracting immune cells such as macrophages, T cells, B cells, which infiltrate the tissue and start the inflammatory process. Such inflammation is smoldering and progressive, unlike acute inflammation aimed at eliminating the pathogen and restoring homeostasis. The inflammatory response can be conditioned by both endogenous (DAMP, Damage Associated Molecular Patterns) and exogenous (PAMP, Pathogen Associated Molecular Patterns) ligands (including bacterial DNA) recognized by PRR, pattern-recognizing receptors [1, 2]. Such receptors are expressed, inter alia, by adipocytes. Various pattern-recognizing receptors, such as Toll-like receptors (TLRs), ply an active part in antiviral and antibacterial protection of the body. PAMP boost expression of adipocyte receptors and secretion of proinflammatory cytokines and adipokines. Activation of TLR-3 triggers a cascade of intracellular events accompanied by activation of immune cells and production of chemokines and proinflammatory cytokines like TNF α , IL1 β , IL6, IL8, which are associated with expansion of inflammation in adipose tissue that supports development of insulin resistance [3].

At the same time, TLRs are involved in adipogenic differentiation: they are expressed together with PPARs (Peroxisome proliferator-activated receptors) at different stages of adipocyte differentiation [4, 5].

Currently, however, there are no descriptions of changes of blood microbiome composition and taxonomic diversity, nor its connections with the inflammatory factors.

Thus, the purpose of this work was to compare the levels of pro- and anti-inflammatory cytokines in blood of obese and healthy children, to reveal their relationship with blood microbiome's taxonomic diversity, and to identify the contribution of bacterial DNA (various families) to the formation of blood microbiome alpha diversity and its connections to the gut microbiome.

METHODS

The study was conducted in 2019–2020. We examined 163 people (children and adolescents) who applied to the children's city polyclinic № 1 in Rostov-on-Don seeking regular checkups. Of these, 80 individuals (aged 10–18 years, mean age 13.25 ± 2.00 years) comprised the study group: with alimentary constitutional obesity of varying degree, they have been diagnosed accordingly earlier and, therefore, followed-up (Table 1). The control group included 83 healthy children and

adolescents (aged 10–18 years, mean age 12.92 ± 2.21 years) who did not have obesity nor other metabolic disorders (Table 1).

The inclusion criteria for both groups were abstaining from antibiotics, probiotic and prebiotic drugs for at least 3 months before the study, and availability of a signed informed consent to participate in the study. The exclusion criteria for both groups were severe somatic diseases (chronic renal failure, chronic liver failure, chronic heart failure), intestinal diseases (ulcerative colitis, Crohn's disease), acute stage of any disease. To be included in the study group, the participants also had to have been diagnosed with alimentary constitutional obesity of class I through III and have the body mass index of SDS $> +2.0$. The study was single-center, single-stage, with a random sample.

Blood of microbiome taxonomic composition was studied at the Center for Digital and Translational Biomedicine of Center for Molecular Health; Rostov Region Children's City Hospital № 1; Pirogov Russian National Research Medical University; Kazan (Volga Region) Federal University. All participants donated blood and feces for laboratory studies, and had their anthropometric parameters registered.

We isolated microbial DNA in blood samples using a QIAamp BiOstic Bacteremia DNA Kit (Qiagen; Germany) in accordance with the manufacturer's protocol. DNA quality control, its quantitative and qualitative composition were evaluated by spectrophotometry (Qubit, Thermo Fisher Scientific; USA) and gel electrophoresis (1% agarose).

MiSeq benchtop sequencer (Illumina; USA) enabled library preparation and sequencing of the V3–V4 variable region of 16S rRNA gene. We analyzed the resulting 16S rRNA gene sequences (reads) with the help of QIIME software (version 1.9.1) [6] and Greengenes v.13.8 reference database [7], the sequence similarity threshold was put at 97%.

Concentrations of cytokines IL6, 8, 10, 17, TNF α were determined with commercially available kits: Milliplex (Merck; Germany) — Human Cytokine/Chemokine Magnetic Bead Panel; fractalkine — Human Myokine Magnetic Bead Panel; PD-L1 (programmed cell death-ligand 1) — Human Immunology Checkpoint Protein Panel Magnetic Bead Panel (ELISA), on a Magpix analyzer (Bio-Rad Laboratories; USA).

For statistical processing of the data, we used MedCalc® Statistical Software version 20.110 (MedCalc Software Ltd; Belgium). The normality of distribution in all datasets was checked with the Shapiro–Wilk test. Since no distribution was normal, we used the median and its [25–75] percentiles the measure of central tendency. Mann–Whitney U test enabled comparison of the values of beta diversity indices (Euclidean distance, Manhattan distance, Bray–Curtis dissimilarity), cytokine levels, and analysis of differences in blood bacterial DNA. Chi-squared test was used to establish the frequency of detection of DNA of different bacterial families in blood samples donated by the participants (both groups). Regardless of the test, the differences were considered significant at $p \leq 0.05$. To identify the relationship between the content of individual families (provided they were isolated in the blood samples) and the characteristics of diversity of blood microbiome, we calculated Spearman's rank correlation coefficient. Correlation

Table 1. Anthropometric indicators of groups

Group	Control group	Study group	<i>p</i> -value
BMI, kg/m ² , Me [Q ₁ ; Q ₃]	20.1 [19.4; 21.2]	27.0 [25.9; 28.8]	< 0.001
Weight, kg, Me [Q ₁ ; Q ₃]	49.0 [45.0; 55.5]	71.0 [61.0; 78.0]	< 0.001
Height, cm, Me [Q ₁ ; Q ₃]	157.0 [150.0; 165.0]	159.0 [154.0; 164.0]	0.619
Age, years, Me [Q ₁ ; Q ₃]	13.0 [11.0; 15.0]	13.0 [11.8; 15.0]	0.237
Gender (m/f)	57.8%/42.2%	52.5%/47.5%	0.187

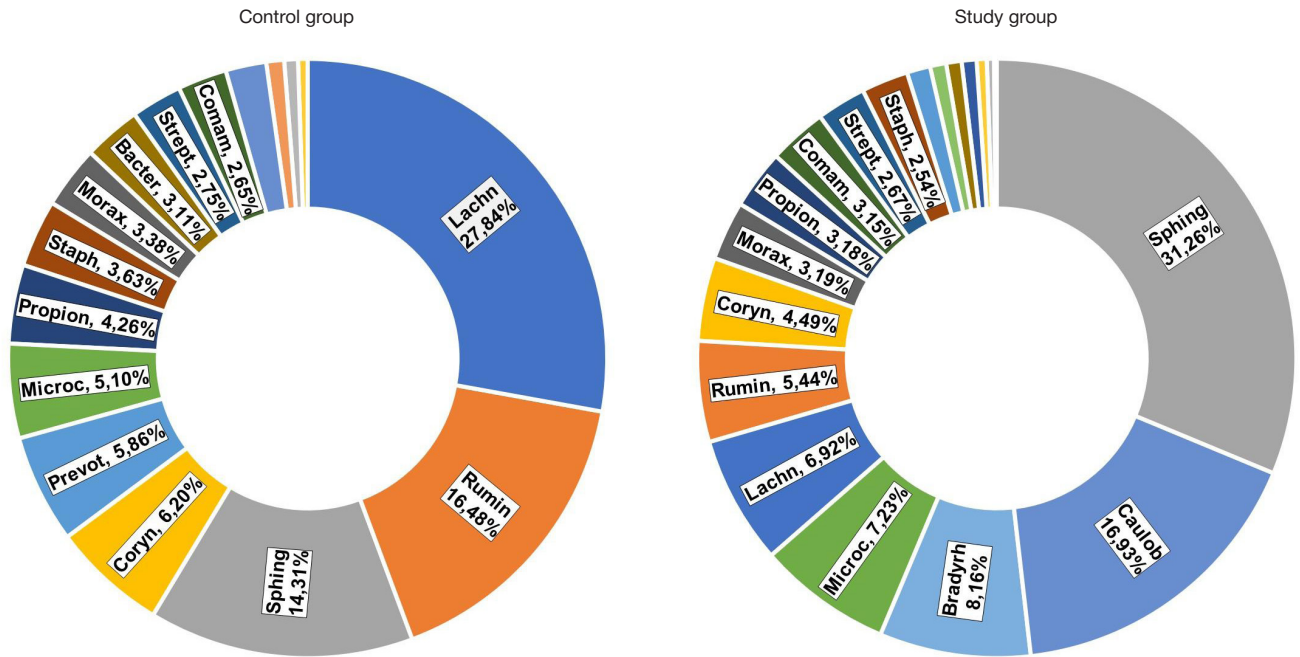


Fig. 1. Distribution of DNA of bacterial families identified the blood samples, both groups, %. *SpHING* — *Sphingomonadaceae*, *Caulob* — *Caulobacteraceae*, *Bradyrh* — *Bradyrhizobiaceae*, *Microc* — *Micrococcaceae*, *Lachn* — *Lachnospiraceae*, *Rumin* — *Ruminococcaceae*, *Coryn* — *Corynebacteriaceae*, *Morax* — *Moraxellaceae*, *Propion* — *Propionibacteriaceae*, *Comam* — *Comamonadaceae*, *Strept* — *Streptococcaceae*, *Staph* — *Staphylococcaceae*, *Prevot* — *Prevotellaceae*, *Bacter* — *Bacteroidaceae*

factors (ρ) were considered provided that $|\rho| \geq 0.3$, the constraint force was moderate on Chaddock scale (with $p \leq 0.05$).

RESULTS

In the blood of healthy children, we identified bacterial DNA from 29.0 [24.5–37.0] families, while samples donated by obese participants presented DNA belonging to 34.0 [28.0–42.0] bacterial families. In both groups, 19 families contributed over 75% of all the bacterial DNA registered: *Sphingomonadaceae*, *Caulobacteraceae*, *Bradyrhizobiaceae*, *Micrococcaceae*, *Lachnospiraceae*, *Ruminococcaceae*, *Corynebacteriaceae*, *Moraxellaceae*, *Propionibacteriaceae*, *Comamonadaceae*, *Streptococcaceae*, *Staphylococcaceae*, *Prevotellaceae*, *Chitinophagaceae*, *Bacteroidaceae*, *Porphyromonadaceae*, *Veillonellaceae*, *Enterobacteriaceae*, *Methylobacteriaceae* (Fig. 1).

Compared to the control group, blood donated by obese participants significantly more often contained DNA of the following bacteria: *Chitinophagaceae* ($p < 0.001$),

Caulobacteraceae ($p < 0.001$), *Bradyrhizobiaceae* ($p = 0.004$), *Porphyromonadaceae* ($p = 0.091$), and *Sphingomonadaceae* ($p < 0.001$); the situation was quite the contrary for *Prevotellaceae* ($p < 0.001$) and *Lachnospiraceae* ($p < 0.001$) (Table 2).

Statistically more common in obese children were bacterial DNA of: *Sphingomonadaceae* ($p = 0.026$), *Ruminococcaceae* ($p = 0.085$), *Caulobacteraceae* ($p = 0.020$), *Bradyrhizobiaceae* ($p < 0.001$), *Porphyromonadaceae* ($p = 0.033$), *Chitinophagaceae* ($p < 0.001$), *Pasteurellaceae* ($p = 0.061$); less frequently, we registered *Prevotellaceae* ($p = 0.044$), and *Thermaceae* ($p = 0.084$) (Table 2).

The analysis of taxonomic affiliation of blood bacterial DNA in the study group revealed a greater diversity thereof in obese children [8]. On the level of families, we analyzed relationships between indicators of alpha diversity and taxonomic composition of bacterial DNA, and, in both groups, found negative correlations between alpha diversity and DNA of the following families: *Corynebacteriaceae*, *Micrococcaceae*,

Table 2. Comparison of the frequency of occurrence of DNA from individual bacterial families and their shares in the total pool of blood bacterial DNA

Family	Frequency of occurrence in participants, %		Share of the family in the total bacterial DNA pool	
	Control group	Obese children	Control group	Obese children
<i>Lachnospiraceae</i>	85.5	86.3	0.1043 [0.0116–0.1954]	0.0314 [0.0074–0.0737]***
<i>Prevotellaceae</i>	84.3	71.3**	0.0220 [0.0053–0.0379]	0.0057 [0–0.0167]***
<i>Sphingomonadaceae</i>	84.3	95.0**	0.0536 [0.0115–0.1444]	0.1418 [0.0675–0.1946]***
<i>Comamonadaceae</i>	84.3	92.5	0.0100 [0.0029–0.0252]	0.0143 [0.0051–0.0371]*
<i>Ruminococcaceae</i>	71.1	82.5*	0.0618 [0–0.1281]	0.0247 [0.0035–0.0753]
<i>Caulobacteraceae</i>	65.1	81.3**	0.0082 [0–0.0750]	0.0768 [0.0148–0.1052]***
<i>Bradyrhizobiaceae</i>	49.4	78.8***	0 [0–0.3148]	0.0370 [0.0031–0.3191]**
<i>Porphyromonadaceae</i>	44.6	61.3**	0 [0–0.0097]	0.0036 [0; 0.0113]*
<i>Chitinophagaceae</i>	32.5	65.0***	0 [0–0.0039]	0.0039 [0–0.0118]***
<i>Pasteurellaceae</i>	22.9	36.3*	0 [0–0]	0 [0–0.0025]
<i>Thermaceae</i>	36.1	23.8*	0 [0–0.0053]	0 [0–0]*

Note: the differences are significant compared to the control group: * — $p < 0.1$; ** — $p < 0.05$; *** — $p < 0.001$.

Table 3. The relationship between blood microbiome's alpha diversity and blood bacterial DNA at the taxonomic level

	Control group	Obese children
	<i>Bacteroidaceae</i> family	
Shannon Index	$\rho = 0.669. p < 0.001. n = 57$	$\rho = 0.358^*. p = 0.015. n = 46$
Simpson Index	$\rho = 0.666. p < 0.001. n = 57$	$\rho = 0.356^*. p = 0.015. n = 46$
Chao1 Index	$\rho = 0.533. p < 0.001. n = 57$	
PD Index	$\rho = 0.586. p < 0.001. n = 57$	
OTUs	$\rho = 0.575. p < 0.001. n = 57$	
<i>Prevotellaceae</i> family		
Shannon Index	$\rho = 0.680. p < 0.001. n = 70$	$\rho = 0.540. p < 0.001. n = 56$
Simpson Index	$\rho = 0.678. p < 0.001. n = 70$	$\rho = 0.537. p < 0.001. n = 56$
Chao1 Index	$\rho = 0.320. p < 0.001. n = 70$	$\rho = 0.358. p = 0.007. n = 56$
PD Index	$\rho = 0.535. p < 0.001. n = 70$	$\rho = 0.329. p = 0.013. n = 56$
OTUs	$\rho = 0.445. p < 0.001. n = 70$	$\rho = 0.333. p = 0.012. n = 56$
<i>Lachnospiraceae</i> family		
Shannon Index	$\rho = 0.593. p < 0.001. n = 71$	$\rho = 0.638. p < 0.001. n = 68$
Simpson Index	$\rho = 0.614. p < 0.001. n = 71$	$\rho = 0.627. p < 0.001. n = 68$
Chao1 Index	$\rho = 0.348. p = 0.003. n = 71$	$\rho = 0.368. p = 0.002. n = 68$
PD Index	$\rho = 0.369. p = 0.002. n = 71$	$\rho = 0.365. p = 0.002. n = 68$
OTUs	$\rho = 0.345. p = 0.003. n = 71$	$\rho = 0.321. p = 0.008. n = 68$
<i>Ruminococcaceae</i> family		
Shannon Index	$\rho = 0.308. p = 0.018. n = 59$	$\rho = 0.714^*. p < 0.001. n = 65$
Simpson Index	$\rho = 0.357. p = 0.006. n = 59$	$\rho = 0.706^*. p < 0.001. n = 65$
Chao1 Index		$\rho = 0.394. p = 0.001. n = 65$
PD Index		$\rho = 0.461. p < 0.001. n = 65$
OTUs		$\rho = 0.390. p = 0.001. n = 65$

Note: * — reliability of differences in correlation coefficients between the groups.

Propionibacteriaceae, *Streptococcaceae*, *Staphylococcaceae*, *Caulobacteraceae*, *Bradyrhizobiaceae*, *Sphingomonadaceae*, *Comamonadaceae*, *Moraxellaceae*.

Only for families exhibited positive correlations with blood microbiome's diversity indicators, and, predominantly, their biotopes are large intestine (*Bacteroidaceae*, *Lachnospiraceae*, *Ruminococcaceae*) and oral cavity (*Prevotellaceae*) (Table 3).

To identify the biotopes that shape blood's microbiome, we analyzed correlations between the characteristics of the alpha diversity and shares of the various bacterial families that contributed the detected DNA. Positive correlations were established for *Bacteroidaceae*, *Prevotellaceae*, *Lachnospiraceae*, and *Ruminococcaceae*. Also, the correlations were positive for DNA of the microorganisms inhabiting mainly 2 biotopes, the large intestine and the oral cavity, as well as the upper respiratory tract, and the genitourinary system; as for negative correlations, such were registered for DNA of bacteria found in the large intestine, on the skin, oropharynx, nasopharynx, esophagus, stomach, water, soil.

A noteworthy fact: in obese children, we registered a multidirectional change in the degree of positive correlations of alpha diversity indicators and bacterial families inhabiting the same biotope, as in the case of *Bacteroidaceae* and *Ruminococcaceae* families, with the said degree becoming milder for the former and stronger for the latter.

Obese participants exhibited fewer extreme negative correlations between alpha diversity indicators and DNA of the *Caulobacteraceae* and *Bradyrhizobiaceae* families, while also showing negative correlations between the said indicators and DNA of the *Porphyromonadaceae* family; both of these observations are noteworthy in light of the fact that these families

grow significantly more common in the total pool of blood bacterial DNA. Bacteria of the *Caulobacteraceae* family inhabit soil and water, and those belonging to the *Bradyrhizobiaceae* family are part of the core of the breast milk's microbiome.

The analysis of correlations in the groups revealed differences in the structure of relationships between DNA of different taxonomies: there were identified patterns common to both groups of participants and those unique to either study or control group.

It should be noted that correlations revolve around DNA of the *Propionibacteriaceae* family, which establishes links through two correlation patterns, one involving *Lachnospiraceae*, *Prevotellaceae*, *Ruminococcaceae*, *Bacteroidaceae*, the other — *Enterobacteriaceae*, *Corynebacteriaceae*, *Streptococcaceae*, *Staphylococcaceae*, *Comamonadaceae*, *Moraxellaceae*, *Micrococcaceae*, *Caulobacteraceae*, *Sphingomonadaceae* (Fig. 2, 3).

A noteworthy fact: in the study group, there are more unique correlations, and they mainly revolve around DNA of microbiome inhabiting extracellular biotopes (skin, oral cavity, soil, water).

In the context of analysis of beta diversity, we compared blood and fecal microbiomes. This comparison revealed a significantly more advanced beta diversity in the study group (Euclidean distance $p = 0.03$, Manhattan distance $p = 0.07$, Bray-Curtis dissimilarity $p = 0.07$), which indicates a greater difference between the microbiomes of blood and feces in obese children, and, in turn, reflects the contributions of intestinal and extra-intestinal microbiomes in the formation of blood microbiome, with the part played by the former smaller than that of the latter (Fig. 4).

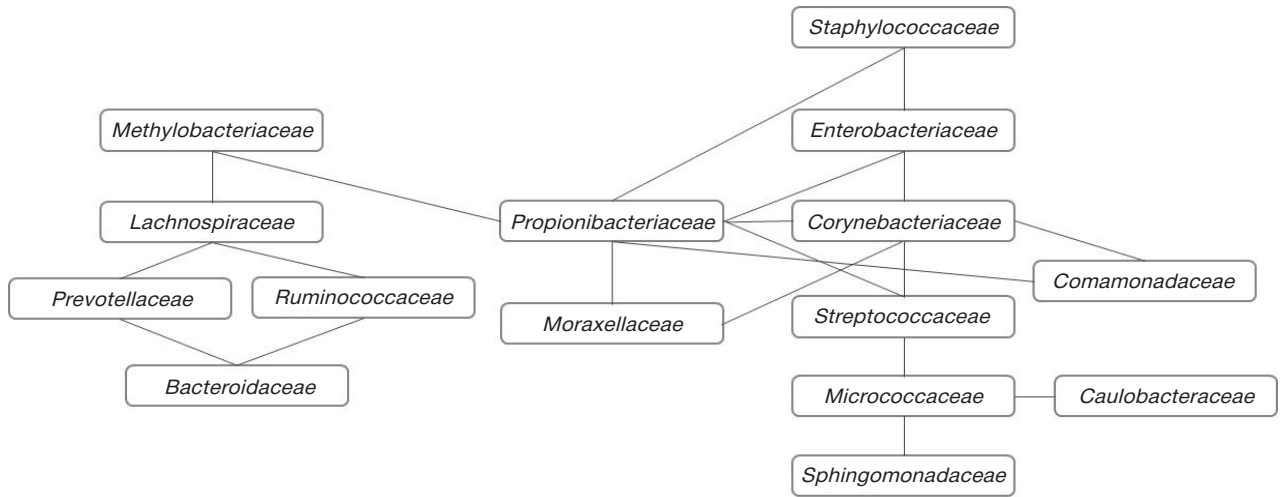


Fig. 2. Positive correlations between bacterial DNA, control group (healthy children)

Previously, we have shown that in the study group, blood microbiome's alpha diversity is insignificantly increased, which translates into a statistically significant growth of the number of operational taxonomic units (OTUs) and phylogenetic diversity (PD) index acquiring an upward trend. Given the above, these findings are complemented by the data on beta diversity and correlations between DNA of different families, with alpha diversity of obese children's blood microbiome enriched with DNA from extra-intestinal microbiomes and not intestinal microbiomes [8].

The study of cytokine levels revealed that obese children have the content of IL17A and PD-L1 significantly greater than their healthy peers (Table 4).

Based on the correlation analysis, we established statistically significant positive relationships in the study group (Table 5).

In the control group, correlation analysis allowed establishing the following relationships between cytokines and bacterial DNA (at the family level):

IL10 had moderate positive correlation with bacterial DNA of *Erysipelotrichaceae* ($\rho = 0.438, p = 0.005, n = 40$); IL8 — with *Bacteroidaceae* ($\rho = 0.370, p = 0.005, n = 57$); IL6 — with *Pseudomonadaceae* ($\rho = 0.528, p = 0.012, n = 22$); IL17A — with *Microbacteriaceae* ($\rho = 0.544, p = 0.006, n = 23$), *Bacillaceae* ($\rho = 0.796, p < 0.001, n = 18$), *Fusobacteriaceae* ($\rho = 0.506, p = 0.032, n = 18$); PD-L1 — with [*Tissierellaceae*] ($\rho = 0.353, p = 0.044, n = 33$), *Pseudomonadaceae* ($\rho = 0.528, p = 0.012, n = 22$).

In the study group, we identified that IL10 had a moderate positive correlation with *Lactobacillaceae* ($\rho = 0.395, p = 0.034, n = 29$); IL8 — with *Veillonellaceae* ($\rho = 0.354, p = 0.017, n = 45$); IL6 — with *Nocardiaceae* ($\rho = 0.605, p = 0.010, n = 17$), *Lactobacillaceae* ($\rho = 0.380, p = 0.042, n = 29$), *Veillonellaceae* ($\rho = 0.459, p = 0.002, n = 45$); IL17A — with *Nocardiaceae* ($\rho = 0.521, p = 0.032, n = 17$), TNF α — with *Nocardiaceae* ($\rho = 0.495, p = 0.043, n = 17$), fractalkine — with *Bacillaceae* ($\rho = 0.705, p = 0.010, n = 12$).

The correlations between bacterial DNA and cytokine content revealed in the groups were associated with different families. In the group of healthy children, the systemic pro-inflammatory cytokine IL8 correlated with bacterial DNA of *Bacteroidaceae*, which act as protectors in the intestine; in the group of obese children, we registered no such correlation. It should also be noted that in the control group, we found relationships with families belonging to five phyla: *Firmicutes*, *Bacteroidetes*, *Actinobacteria*, *Proteobacteria*, *Fusobacteria*; in the study group, there were only two phyla involved, *Firmicutes* and *Actinobacteria*.

DISCUSSION

Our study has shown that obese children and adolescents have significantly elevated levels of IL17A and PD-L1. Normally, IL17A participates in maintaining the integrity of the epithelial barrier of mucous membranes through regulation of occludin,

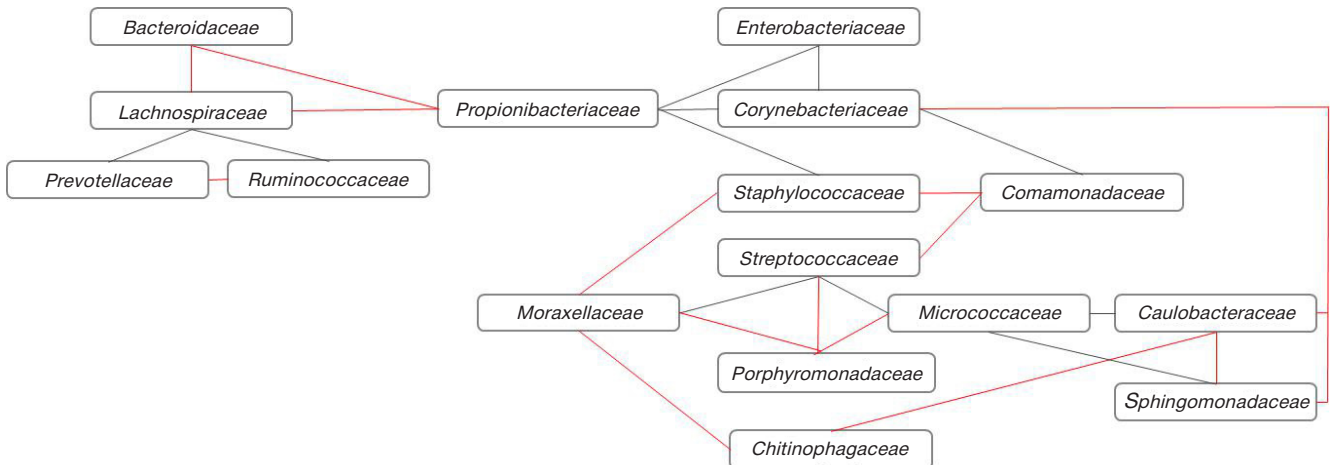


Fig. 3. Positive correlations between bacterial DNA, study group (obese children) Red lines show unique correlations in the group of obese children, black lines — correlations common with the control group

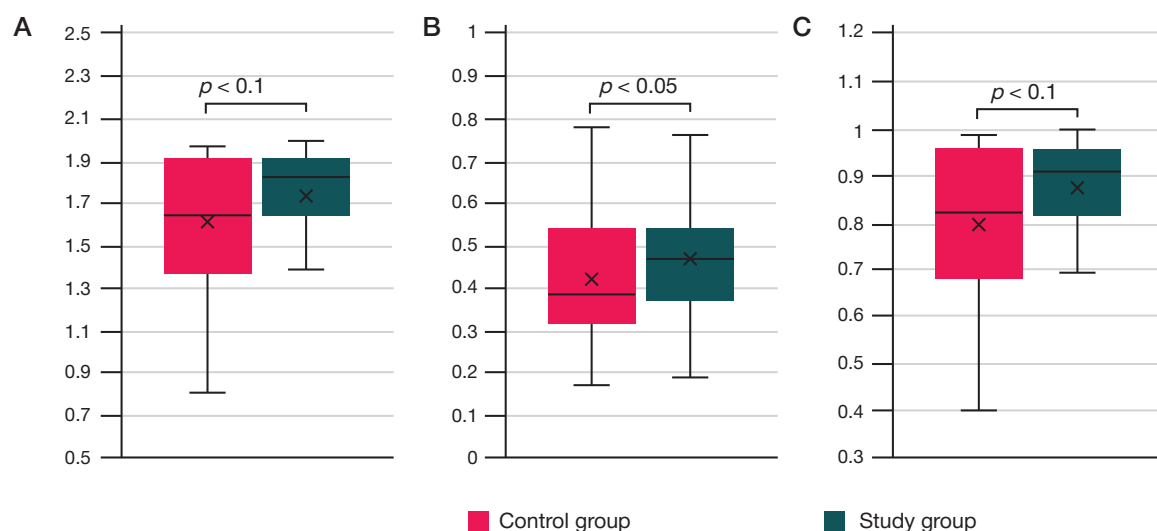


Fig. 4. Beta diversity in the groups. A. Manhattan distance. B. Euclidean distance. C. Bray-Curtis dissimilarity

but its main function is to recruit neutrophils into the intestine when there is a threat of excessive permeability and with the aim of maintaining homeostasis. In one study, it was shown that inhibition of IL17A or IL17RA translated into a serious deterioration of the epithelial barrier [9]. Moreover, IL17A is the main regulator of the host-microbiota interaction at the physiological level and in the context of immuno-mediated inflammatory diseases [10]. In mice experiments, knockout of the IL17 gene induced intestinal inflammation [11]. However, experiments on the transgenic mice model of multiple sclerosis (HLA-DR3. IL17A^{-/-} mice) promotes breeding of Treg-inducing intestinal bacteria, such as *Prevotella*, *Parabacteroides* and *Bacteroides*, which translates into a lighter course of the disease. It has also been shown that IL17A can regulate Treg activity and influence the course of the disease by modulating gut microbiota and establishing a new mechanism that allows immunomodulators to affect that microbiota. Interestingly, DR3 mice with sufficient content of IL17A have the disease in a lighter form when kept together with the mice deficient in IL17A, which further emphasizes the dominant role of the microbiota in inducing Treg and alleviating the disease [12]. IL17A is involved in the pathogenesis of autoimmune diseases, such as rheumatoid arthritis, psoriasis, systemic lupus erythematosus, bronchial asthma, etc. [13]. The protocols of treatment of spondyloarthritis and psoriatic arthritis that relied on inhibition of IL17 caused the

numbers of *Clostridiales* to shrink and those of *Bacteroidales* to grow. Thus, it can be assumed that, having elevated levels of IL17A, obese children are at risk of developing autoimmune diseases.

PD-L1 is a ligand that plays an important role in inhibiting the T cell-mediated immune response [14]. Binding of PD-L1 to PD-1 causes apoptosis of effector T cells and allows tumor cells to remain unaffected by the immune system, which makes the prognosis in the respective cases unfavorable. Several studies have shown that inhibition of interaction between PD-L1 and PD-1 enhances the adaptive immune response and increases antitumor activity [15–17]; it was also revealed that PD-L1 is expressed on white and brown adipocytes in mice [18]. PD-L1 is a rather complicated molecule: its low expression or knockout on adipocytes increases antitumor immunity in mice with a neoplasm, and in the absence of a tumor, ablation of PD-L1 adipocytes exacerbates diet-induced weight gain, infiltration of pro-inflammatory macrophages into adipose tissue and insulin resistance [19]. PD-L1 has a twofold effect: on the one hand, when it is expressed at a slower rate, the antitumor immunity becomes stronger and suppresses tumor growth, and on the other hand, its boosted expression in adipocytes allows maintaining adipose tissue homeostasis and mitigating smoldering inflammation associated with proliferation of the adipose tissue and its infiltration by macrophages [20]. The gut microbiome may modulate the response of melanoma patients

Table 4. Content of pro- and anti-inflammatory cytokines in children's blood serum

Analyzed indicator	Healthy children (n = 83)	Obese children (n = 80)	p-value
IL6, pg/ml, Me [Q ₁ ;Q ₃]	1.09 [0.28; 6.58]	1.19 [0.52; 8.24]	0.561
IL8, pg/ml, Me [Q ₁ ;Q ₃]	8.65 [4.05; 16.3]	11.5 [6.08; 21.4]	0.103
IL10, pg/ml, Me [Q ₁ ;Q ₃]	1.93 [0.67; 4.08]	2.30 [0.94; 6.02]	0.357
IL17A, pg/ml, Me [Q ₁ ;Q ₃]	0.69 [0.13; 4.88]	4.22 [0.39; 9.56]**	0.017
TNFα, pg/ml, Me [Q ₁ ;Q ₃]	12.8 [7.74; 21.8]	13.2 [9.00; 20.7]	0.856
Fractalkine, pg/ml, Me [Q ₁ ;Q ₃]	63.1 [47.1; 228]	90.8 [34.5; 209]	0.188
PD-L1, pg/ml, Me [Q ₁ ;Q ₃]	25.8 [9.10; 53.1]	35.7 [19.5; 55.0]**	0.021

Note: различия достоверны по сравнению с контрольной группой: * $p < 0,1$; ** $p < 0,05$; *** $p < 0,001$.

Table 5. Statistical parameters of the cytokines correlation analysis

	Obese children				Healthy children		
	IL6	IL8	IL10	IL17A	IL6	IL8	IL17A
IL8	$\rho = 0.583$ $p < 0.001$ $n = 80$				$\rho = 0.439$ $p < 0.001$ $n = 83$		
IL17A	$\rho = 0.505$ $p < 0.001$ $n = 80$	$\rho = 0.391$ $p < 0.001$ $n = 80$	$\rho = 0.349$ $p = 0.001$ $n = 80$		$\rho = 0.344$ $p = 0.001$ $n = 83$	$\rho = 0.446$ $p < 0.001$ $n = 83$	
IL10	$\rho = 0.383$ $p < 0.001$ $n = 80$						
TNF α		$\rho = 0.441$ $p < 0.001$ $n = 80$	$\rho = 0.400$ $p < 0.001$ $n = 80$	$\rho = 0.427$ $p < 0.001$ $n = 80$			$\rho = 0.316$ $p = 0.004$ $n = 83$

to PD-1 immunotherapy. A group of researchers suggested that patients with a "favorable" intestinal microbiome (e.g., with a high diversity and abundance of *Ruminococcaceae* and *Faecalibacterium*) have an enhanced systemic and antitumor immune response mediated by an improved antigen presentation and effector T cell function at the periphery of and inside tumor's microenvironment. Patients with "unfavorable" intestinal microbiome (e.g., with poor diversity and high relative content of *Bacteroidales*), on the contrary, have impaired systemic and antitumor immune responses mediated by limited intracellular lymphoid and myeloid infiltration and impaired ability to present antigens. The results of the respective study underscores therapeutic potential of modulation of the gut microbiome in patients receiving immunotherapy with checkpoint blockade [21].

The composition of dominant families of blood microbiome was similar in both group. Despite this we have registered significant differences in the frequency. This allows an assumption that children suffer significant negative changes in the permeability of intestine and other biotopes, mainly the skin. Alteration of the microbiota affects the quality and quantity of the wall microbiota, the processes of production of mucus by goblet cells that prevents penetration of pathogens. In the group of obese children, we have shown that DNA of the *Bacteroidaceae* family makes a significantly smaller contribution to the alpha diversity of the blood microbiome, which is consistent with the data from other researchers that investigated stool microbiome [8]. Other researchers have proven that a growing share of Proteobacteria against the background of obesity, non-alcoholic fatty liver disease and non-alcoholic steatohepatitis [22–24] indicates predisposition to impairments of functions of liver and the entire gastrointestinal tract. A statistically significant decrease of the share of *Lachnospiraceae* in the study group entails deceleration of butyrate synthesis, which means poorer supply of energy to the intestinal epithelial cells and thinning of the intestinal barrier due to a slower activation of the claudine-1 protein [25]. Studies show that *Ruminococcaceae* are associated with the development of

inflammatory bowel diseases, such as ulcerative colitis and Crohn's disease.

The main biotope for *Ruminococcaceae* is the large intestine, for *Bacteroidaceae* — large intestine, oral cavity, upper respiratory tract, and genitourinary system, and for *Prevotellaceae* — oral cavity, which suggests that translocation of bacterial DNA therefrom slows down.

According to the published papers, obese children exhibit positive correlations between the content of trefoil factors, namely, TFF3, and the intestinal microbiota, which indicates a violation of tolerance of the mucosal barrier to the microbial community [26].

Thus, it is likely that in obese children, due to the impaired peripheral tolerance and permeability of mucosal barriers, bacterial DNA translocates not only from the intestine, but also from the oral cavity and skin. As a result, blood microbiome grows more diverse. Bacterial DNA activates TLR9 receptors and triggers the secretion of pro-inflammatory cytokines, IL17A in particular, thus forcing the body to maintain balance and deploy anti-inflammatory mechanisms by activating PD-L1 synthesis.

CONCLUSIONS

In the group of obese children, alpha diversity is enriched with bacterial DNA of the *Lachnospiraceae*, *Prevotellaceae*, and *Ruminococcaceae* families. In that group, beta diversity becomes more advanced, too, which indicates a more intensive translocation of bacterial DNA from extra-intestinal microbiomes. Compared to the control group, there appear new patterns of correlations. In obese children, increased levels of IL17A and PD-L1 point to activation of pro- and anti-inflammatory mechanisms and the development of smoldering inflammation. Obesity is characterized by the appearance of significant correlations of DNA of the *Nocardiaceae* family with pro-inflammatory cytokines, which highlights the role of translocation of DNA of this taxon in the development of smoldering inflammation and the possibility of developing approaches to reduce this translocation as part of an obesity treatment protocol.

References

- Shin JJ, Lee EK, Park TJ, Kim W. Damage associated molecular patterns and their pathological relevance in diabetes mellitus. *Ageing Research Reviews*. 2015; 24 (Pt A): 66–76. Epub 2015 Jul 18.
- Land WG. The role of damage-associated molecular patterns in human diseases: part I — promoting inflammation and immunity. *Sultan Qaboos University Medical Journal*. 2015; 15: 9–21.
- Ballak D, van Asseldonk E, van Diepen J, et al. TLR-3 is present in human adipocytes, but its signalling is not required for obesity-induced inflammation in adipose tissue in vivo. *PLoS ONE*. 2015; 10 (4): e0123152.
- Yu L, Li Y, Du C, Zhao W, Zhang H, Yang Y, et al. Pattern recognition receptor-mediated chronic inflammation in the development and progression of obesity-related metabolic diseases. *Hindawi Mediators of Inflamm*. 2019 Sep; 2019: 5271295. PubMed PMID: 31582899. PubMed Central PMCID: PMC6754942.

5. Christodoulides C, Vidal-Puig A. PPARs and adipocytes function. *Mol Cell Endocrinol*. 2010 Apr; 318 (1–2): 61–8. Epub 2009 Sep 20.
6. Caporaso JG, Kuczynski J, Stombaugh J, et al. QIIME allows analysis of high-throughput community sequencing data. *Nature Methods*. 2010 May; 7 (5): 335–6. Epub 2010 Apr 11.
7. DeSantis T, Hugenholtz P, Larsen N, et al. Greengenes, a Chimera-Checked 16S rRNA Gene Database and Workbench Compatible with ARB. *Appl Environ Microbiol*. 2006; 72 (7): 5069–72.
8. Kirilina IV, Shestopalov AV, Gaponov AM, Kamaldinova DR, Khusnutdinova DR, Grigorieva TV, et al. Features of the blood microbiome in obese children. *Pediatrics n.a. G. N. Speransky*. 2022; 101 (5): 15–22. Russian.
9. Maxwell JR, Zhang Y, Brown WA, Smith CL, Byrne FR, Fiorino M et al. Differential roles for Interleukin-23 and Interleukin-17 in intestinal immunoregulation. *Immunity*. 2015; 43: 739–50.
10. Brevi A, Cogrossi LL, Grazi G, Masciovecchio D, Impellizzieri D, Lacanfora L, et al. Much more than IL-17A: cytokines of the IL-17 family between microbiota and cancer. Mini review article *Front. Immunol. Sec. Cancer Immunity and Immunotherapy*. 2020 Nov; 11: 565470.
11. Bi Y, Li C, Liu L, Zhou J, Li Z, Deng H, et al. IL-17A-dependent gut microbiota is essential for regulating diet-induced disorders in mice. *Science Bulletin*. 2017; 62 (15): 1052–63.
12. Shahi SK, Ghimire S, Jensen SN, Lehman P, Borchering N, Gibson-Corley KN, et al. IL-17A controls CNS autoimmunity by regulating gut microbiota and inducing regulatory T cells bioRxiv. 2022 Apr; 04.22.489206.
13. Chen K, Kolls JK. Interleukin-17A (IL17A). *Gene*. 2017; 30 (614): 8–14. Epub 2017 Jan 22.
14. Wang X, Teng F, Kong Li, Jinming Yu. PD-L1 expression in human cancers and its association with clinical outcomes. *Onco Targets Ther*. 2016; 9: 5023–39.
15. Wu Y, Chen W, Xu ZP, Gu W. PD-L1 distribution and perspective for cancer immunotherapy-blockade, knockdown, or inhibition. *Front Immunol*. 2019; 10: 2022.
16. Jiang X, Wang J, Deng X, Xiong F, Ge J, Xiang B, et al. Role of the tumor microenvironment in PD-L1/PD-1-mediated tumor immune escape. *Mol Cancer*. 2019; 18 (1): 10.
17. Dermani FK, Samadi P, Rahmani G, Kohlan AK, Najafi R. PD1/PD-L1 immune checkpoint: Potential target for cancer therapy. *J Cell Physiol*. 2019; 234 (2): 1313–25.
18. Ingram JR, Dougan M, Rashidian M, Knoll M, Keliher EJ, Garrett S, et al. PD-L1 is an activation-independent marker of brown adipocytes. *Nature Communication*. 2017 Sep 21; 8 (1): 647.
19. Wu B, Chiang H-C, Sun X, Yuan B, Mitra P, Hu Y, et al. Genetic ablation of adipocyte PD-L1 reduces tumor growth but accentuates obesity-associated inflammation. *J Immunother Cancer*. 2020 Aug; 8 (2): e000964. PubMed PMID: 32817394. PubMed Central PMCID: PMC7437875.
20. Fujii T, Nishiki E, Endo M, Yajima R, Katayama A, Oyama T. Implication of atypical supraclavicular F18-fluorodeoxyglucose uptake in patients with breast cancer: Relationship between brown adipose tissue and TILs, PD-L1. *Posters A: Risk factors*. 2020 Oct; (Suppl 1): S94.
21. Gopalakrishnan V, Spencer CN, Nezi L, Reuben A, Andrews MC, Karpinets TV, et al. Gut microbiome modulates response to anti-PD-1 immunotherapy in melanoma patients. *Science*. 2018 Jan 5; 359 (6371): 97–103. Epub 2017 Nov 2.
22. Plotnikova EY, Krasnov OA. Metabolic syndrome and intestinal microflora: what overall? *Experimental and Clinical Gastroenterology*. 2015; 112 (12): 64–73. Russian.
23. Mouzaki M, Comelli EM, Arendt BM, Bonengel J, Fung SK, et al. Intestinal microbiota in patients with nonalcoholic fatty liver disease. *Hepatology*. 2013; 58: 120–7.
24. Zhu L, Baker SS, Gill C, Liu W, Alkhoury R, et al. Characterization of gut microbiomes in nonalcoholic steatohepatitis (NASH) patients: A connection between endogenous alcohol and NASH. *Hepatology*. 2012; 57: 601–9.
25. Loranskaya ID, Khalif IL, Boldyreva MN, Kupaeva VA. Characteristic of microbiome in inflammatory bowel disease. *Experimental and Clinical Gastroenterology*. 2018; 153 (5): 104–11. Russian.
26. Shestopalov AV, Kolesnikova IM, Savchuk DV, Teplyakova ED, Shin VA, Grigoryeva TV, et al. Effect of the infant feeding type on gut microbiome taxonomy and levels of trefoil factors in children and adolescents. *Russian Journal of Physiology*. 2023; 109 (5): 656–72. Russian.

Литература

1. Shin JJ, Lee EK, Park TJ, Kim W. Damage associated molecular patterns and their pathological relevance in diabetes mellitus. *Ageing Research Reviews*. 2015; 24 (Pt A): 66–76. Epub 2015 Jul 18.
2. Land WG. The role of damage-associated molecular patterns in human diseases: part I — promoting inflammation and immunity. *Sultan Qaboos University Medical Journal*. 2015; 15: 9–21.
3. Ballak D, van Asseldonk E, van Diepen J, et al. TLR-3 is present in human adipocytes, but its signalling is not required for obesity-induced inflammation in adipose tissue in vivo. *PLoS ONE*. 2015; 10 (4): e0123152.
4. Yu L, Li Y, Du C, Zhao W, Zhang H, Yang Y, et al. Pattern recognition receptor-mediated chronic inflammation in the development and progression of obesity-related metabolic diseases. *Hindawi Mediators of Inflamm*. 2019 Sep; 2019: 5271295. PubMed PMID: 31582899. PubMed Central PMCID: PMC6754942.
5. Christodoulides C, Vidal-Puig A. PPARs and adipocytes function. *Mol Cell Endocrinol*. 2010 Apr; 318 (1–2): 61–8. Epub 2009 Sep 20.
6. Caporaso JG, Kuczynski J, Stombaugh J, et al. QIIME allows analysis of high-throughput community sequencing data. *Nature Methods*. 2010 May; 7 (5): 335–6. Epub 2010 Apr 11.
7. DeSantis T, Hugenholtz P, Larsen N, et al. Greengenes, a Chimera-Checked 16S rRNA Gene Database and Workbench Compatible with ARB. *Appl Environ Microbiol*. 2006; 72 (7): 5069–72.
8. Кирилина ИВ, Шестопалов АВ, Гапонов АМ, Камальдинова ДР, Хуснутдинова ДР, Григорьева ТВ и др. Особенности микробиома крови у детей с ожирением. *Педиатрия*. 2022; 101 (5): 15–22.
9. Maxwell JR, Zhang Y, Brown WA, Smith CL, Byrne FR, Fiorino M et al. Differential roles for Interleukin-23 and Interleukin-17 in intestinal immunoregulation. *Immunity*. 2015; 43: 739–50.
10. Brevi A, Cogrossi LL, Grazi G, Masciovecchio D, Impellizzieri D, Lacanfora L, et al. Much more than IL-17A: cytokines of the IL-17 family between microbiota and cancer. Mini review article *Front. Immunol. Sec. Cancer Immunity and Immunotherapy*. 2020 Nov; 11: 565470.
11. Bi Y, Li C, Liu L, Zhou J, Li Z, Deng H, et al. IL-17A-dependent gut microbiota is essential for regulating diet-induced disorders in mice. *Science Bulletin*. 2017; 62 (15): 1052–63.
12. Shahi SK, Ghimire S, Jensen SN, Lehman P, Borchering N, Gibson-Corley KN, et al. IL-17A controls CNS autoimmunity by regulating gut microbiota and inducing regulatory T cells bioRxiv. 2022 Apr; 04.22.489206.
13. Chen K, Kolls JK. Interleukin-17A (IL17A). *Gene*. 2017; 30 (614): 8–14. Epub 2017 Jan 22.
14. Wang X, Teng F, Kong Li, Jinming Yu. PD-L1 expression in human cancers and its association with clinical outcomes. *Onco Targets Ther*. 2016; 9: 5023–39.
15. Wu Y, Chen W, Xu ZP, Gu W. PD-L1 distribution and perspective for cancer immunotherapy-blockade, knockdown, or inhibition. *Front Immunol*. 2019; 10: 2022.
16. Jiang X, Wang J, Deng X, Xiong F, Ge J, Xiang B, et al. Role of the tumor microenvironment in PD-L1/PD-1-mediated tumor immune escape. *Mol Cancer*. 2019; 18 (1): 10.
17. Dermani FK, Samadi P, Rahmani G, Kohlan AK, Najafi R. PD1/PD-L1 immune checkpoint: Potential target for cancer therapy. *J Cell Physiol*. 2019; 234 (2): 1313–25.
18. Ingram JR, Dougan M, Rashidian M, Knoll M, Keliher EJ, Garrett S, et al. PD-L1 is an activation-independent marker of brown adipocytes. *Nature Communication*. 2017 Sep 21; 8 (1): 647.
19. Wu B, Chiang H-C, Sun X, Yuan B, Mitra P, Hu Y, et al. Genetic ablation of adipocyte PD-L1 reduces tumor growth but

- accentuates obesity-associated inflammation. *J Immunother Cancer*. 2020 Aug; 8 (2): e000964. PubMed PMID: 32817394. PubMed Central PMCID: PMC7437875.
20. Fujii T, Nishiki E, Endo M, Yajima R, Katayama A, Oyama T. Implication of atypical supraclavicular F18-fluorodeoxyglucose uptake in patients with breast cancer: Relationship between brown adipose tissue and TILs, PD-L1. *Posters A: Risk factors*. 2020 Oct; (Suppl 1): S94.
 21. Gopalakrishnan V, Spencer CN, Nezi L, Reuben A, Andrews MC, Karpinets TV, et al. Gut microbiome modulates response to anti-PD-1 immunotherapy in melanoma patients. *Science*. 2018 Jan 5; 359 (6371): 97–103. Epub 2017 Nov 2.
 22. Плотникова Е. Ю., Краснов О. А. Метаболический синдром и кишечная микрофлора; что общего? *Экспериментальная и клиническая гастроэнтерология*. 2015; 112 (12): 64–73.
 23. Mouzaki M, Comelli EM, Arendt BM, Bonengel J, Fung SK, et al. Intestinal microbiota in patients with nonalcoholic fatty liver disease. *Hepatology*. 2013; 58: 120–7.
 24. Zhu L, Baker SS, Gill C, Liu W, Alkhoury R, et al. Characterization of gut microbiomes in nonalcoholic steatohepatitis (NASH) patients: A connection between endogenous alcohol and NASH. *Hepatology*. 2012; 57: 601–9.
 25. Лоранская И. Д., Халиф И. Л., Болдырева М. Н., Купаева В. А. Характеристика микробиома при воспалительных заболеваниях кишечника. *Экспериментальная и клиническая гастроэнтерология*. 2018; 153 (5): 104–11.
 26. Шестопалов А. В., Колесникова И. М., Савчук Д. В., Теплякова Е. Д., Шин В. А., Григорьева Т. В. и др. Влияние вида вскармливания на таксономический состав кишечного микробиома и уровни трефоиловых факторов у детей и подростков. *Российский физиологический журнал им. И.М. Сеченова*. 2023; 109 (5): 656–72.

ALTERED CIRCADIAN EXPRESSION OF CYTOKINES IN BLOOD OF PATIENTS WITH ESSENTIAL HYPERTENSION FOLLOWING COVID-19

Radaeva OA¹✉, Simbirtsev AS², Kostina YuA¹, Iskandryarova MS¹, Negodnova EV¹, Mashnina SV¹, Ereemeev VV¹, Krasnoglazova KA¹, Babushkin IO¹

¹ National Research Mordovia State University, Saransk, Russia

² State Research and Development Institute of High Purity Biologicals of the Federal Medical and Biological Agency, Saint-Petersburg, Russia

In spite of a vast number of trials devoted to quantitative characteristics of the cytokine profile in patients with various diseases, no exact reference intervals are presented. It is just as important that there is a limited number of trials analyzing circadian rhythms of cytokine synthesis in patients with arterial hypertension. The purpose of the work was to analyze the characteristics of circadian rhythms of cytokines (IL18, IL18 BP, LIF, sLIFr, M-CSF, MCSFR) in patients with Grade II essential arterial hypertension, and to detect pathogenetically significant characteristics developed following Covid-19. Blood samples were taken at 7.00–8.00, 12.00–13.00, 19.00–20.00.00, 00.00–1.00 to determine the levels of IL18, IL18 BP, LIF, sLIFr, M-CSF, MCSFR in 18 patients (56 (95% CI (54–69) years) with essential arterial hypertension (EAH) within three days prior to and following Covid-19. For this, the immunoenzyme method was used. The obtained data demonstrated altered circadian expression of cytokines in the peripheral blood of patients with essential hypertension depending on whether they have EAH or not, and their additional distortion following Covid-19, which is stable in the majority of cases. It is preserved for six months as low IL18 BP ($p < 0.001$), and twofold increase of sLIFr and MCSF ($p < 0.001$) at 18.00. A significant association is determined between the circadian rhythms of sLIFr and altered systolic BP resulting in the abnormal rhythm with BP rise at night (night peaker) in patients with EAH following COVID-19. The obtained fundamental data offer prospects for new research of immunopathogenesis following COVID-19 in patients with hypertension taking into account circadian rhythms of cytokines in the blood.

Keywords: essential hypertension, LIF, sLIFr, M-CSF, circadian rhythms

Funding: supported by the grant of the Russian Science Foundation 'Analysis of altered circadian expression of cytokines in blood of patients with essential hypertension as predictor of cardiovascular complications', № 23-25-00147.

Author contribution: Radaeva OA — trial design, analysis of results, preparation of a manuscript; Simbirtsev AS — stating the purpose of the trial, editing; Kostina YuA — lab research, preparation of a manuscript; Iskandryarova MS — working with literature, editing; Negodnova EV — working with literature, surveillance over patients; Mashnina SV, Krasnoglazova KA, Babushkin IO — statistical treatment of data; Ereemeev VV — editing.

Compliance with ethical standards: The trial was approved by the Ethics Committee of the National Research Mordovia State University (protocol № 12 as of December 14, 2008, protocol № 85 as of May 27, 2020). All patients signed a voluntary informed consent form. Biological sample (blood) was obtained in accordance with the provisions of Declaration of Helsinki of BMA (2013), protocol of Council of Europe Convention for the Protection of Human Rights and Biomedicine (1999) and additional protocol to Convention for the Protection of Human Rights and Biomedicine in the area of biomedical research (2005).

✉ **Correspondence should be addressed:** Olga A. Radaeva
Ulyanova, d. 26a, Saransk, 430032, Russia; radaevamed@mail.ru

Received: 29.11.2023 **Accepted:** 14.12.2023 **Published online:** 31.12.2023

DOI: 10.24075/brsmu.2023.056

ИЗМЕНЕНИЯ ЦИРКАДИАНЫХ РИТМОВ УРОВНЕЙ ЦИТОКИНОВ В КРОВИ ПАЦИЕНТОВ С ЭССЕНЦИАЛЬНОЙ ГИПЕРТЕНЗИЕЙ В ПОСТКОВИДНОМ ПЕРИОДЕ

О. А. Радаева¹✉, А. С. Симбирцев², Ю. А. Костина¹, М. С. Искандрярова¹, Е. В. Негоднова¹, С. В. Машнина¹, В. В. Еремеев¹, К. А. Красноглазова¹, И. О. Бабушкин¹

¹ Национальный исследовательский Мордовский государственный университет имени Н. П. Огарёва, Саранск, Россия

² Государственный научно-исследовательский институт особо чистых биопрепаратов Федерального медико-биологического агентства, Санкт-Петербург, Россия

Несмотря на большое число исследований, посвященных количественным характеристикам цитокинового профиля пациентов с различными заболеваниями, нет точных референсных интервалов, и что не менее важно, ограничено число исследований, анализирующих циркадианные ритмы синтеза цитокинов у лиц с артериальной гипертензией. Целью работы было проанализировать особенности циркадианных ритмов содержания цитокинов (IL18, IL18 BP, LIF, sLIFr, M-CSF, MCSFR) в крови пациентов с эссенциальной артериальной гипертензией II стадии и выделить патогенетически значимые особенности, сформированные после перенесенной новой коронавирусной инфекции. Проводили забор крови в 7.00–8.00, 12.00–13.00, 19.00–20.00.00, 00.00–1.00 для определения иммуноферментным методом уровней IL18, IL18 BP, LIF, sLIFr, M-CSF, MCSFR в течение трех суток у 18 пациентов (56 (95% ДИ (54–69) лет) с эссенциальной артериальной гипертензией (ЭАГ) до и после перенесенной новой коронавирусной инфекции. Полученные данные демонстрируют изменения циркадианных ритмов содержания цитокинов в периферической крови у пациентов в зависимости от наличия ЭАГ, а также их дополнительное искажение в постковидном периоде, что в значимом проценте случаев имеет стойкий характер с сохранением более шести месяцев в виде снижения содержания IL18 BP ($p < 0,001$), двукратного увеличения sLIFr и MCSF ($p < 0,001$) в 18.00. Определена достоверная связь между циркадианными ритмами содержания sLIFr в крови и изменения уровня систолического АД с формированием патологического ритма с ростом АД в ночное время (Найт-пикер) у лиц с ЭАГ в постковидном периоде. Полученные фундаментальные данные открывают перспективы для новых исследований иммунопатогенеза постковидного периода у лиц с гипертензией с учетом циркадианных ритмов содержания цитокинов в крови.

Ключевые слова: эссенциальная гипертензия, LIF, sLIFr, M-CSF, циркадианные ритмы

Финансирование: поддержано грантом РНФ «Анализ изменения циркадианных ритмов синтеза цитокинов в крови пациентов с эссенциальной артериальной гипертензией как предиктор развития сердечно-сосудистых осложнений», № 23-25-00147.

Вклад авторов: О. А. Радаева — дизайн исследования, анализ результатов, оформление рукописи; А. С. Симбирцев — формулирование цели исследования, редактирование; Ю. А. Костина — лабораторные исследования, оформление рукописи; М. С. Искандрярова — работа с литературой, редактирование; Е. В. Негоднова — работа с литературой, наблюдение за пациентами; С. В. Машнина, К. А. Красноглазова, И. О. Бабушкин — статистическая обработка данных; В. В. Еремеев — редактирование.

Соблюдение этических стандартов: исследование одобрено этическим комитетом Мордовского государственного университета имени Н. П. Огарева (протокол № 12 от 14 декабря 2008 г., протокол № 85 от 27 мая 2020 г.). Все пациенты подписали добровольное информированное согласие. Получение биологического материала (кровь) произведено с учетом положений Хельсинской декларации ВМА (2013 г.), протокола Конвенции Совета Европы о правах человека и биомедицине (1999) и дополнительного протокола к Конвенции по правам человека и биомедицине в области биомедицинских исследований (2005).

✉ **Для корреспонденции:** Ольга Александровна Радаева
ул. Ульянова, д. 26а, г. Саранск, 430032, Россия; radaevamed@mail.ru

Статья получена: 29.11.2023 **Статья принята к печати:** 14.12.2023 **Опубликована онлайн:** 31.12.2023

DOI: 10.24075/vrgmu.2023.056

The trials devoted to the role of cytokines from post-COVID perspective are pressing as a large amount of knowledge related to the altered link of immune regulation during COVID-19 is obtained. The restoration is a long-term process, including both early, and late periods of reconvalescence. Meanwhile, in the post-COVID era, virus-mediated changes of the cytokine profile can determine modification of non-infectious disease pathogenesis due to multiple organ action, including patients with essential arterial hypertension (EAH). It should be noted that in spite of a vast number of trials devoted to quantitative characteristics of the cytokine profile in patients with various diseases, no exact reference intervals are presented. It is just as important that there is a limited number of trials analyzing circadian rhythms of cytokine synthesis in patients with certain diseases. The things mentioned above are most significant for patients with EAH as daily curves of BP are essential and have been taken into account in practice for long. An increased rate of cardiovascular complications and development of the metabolic syndrome are detected in the post-COVID era. This can be associated with methods of therapy (wide use of corticosteroids) and role of coronavirus depending on pre-existing immunopathogenetic and clinical characteristics of patients. Cytokine synthesis concentrations are not only factors, which are subject to daily patterns. In case of clinical or subclinical imbalance, they can influence the main center of the circadian clock such as the suprachiasmatic nucleus in the brain. It can also promote the loss of synchronization between the main center and peripheral 'clocks' [1, 2]. The chronobiology is perspective. It has a vast scope of significant scientific data [3, 4] and needs to expand a number of trials in the post-covid era. It should be noted that the individual analysis of daily curves of cytokines in the peripheral blood allows to be declarative of more complex patterns as compared to two-phase day and

night changes. According to some data, the amount of IL2 in the serum forms a single peak approximately at noon, whereas IL10, TNF and GM-CSF display a two-phase pattern [5]. In the subjects, the first peak and second peak of TNF occur at 07:30 and 13:30, respectively. So, it can't be considered as a cytokine of rest. The levels of IL10 are also displayed a biphasic pattern with one peak at 07:30 and the other one at 19:30 in 12 hours. According to these results, the temporal patterns are unique for every cytokine with daylight peaks and night minima [2]. Thus, fundamental data about altered circadian rhythms of cytokine synthesis following the previous novel coronavirus can be both of a scientific and practical interest in the future.

The purpose of the work was to analyze the characteristics of circadian rhythms of cytokines (IL18, IL18 BP, LIF, sLIFr, M-CSF, MCSFR) in patients with Grade II EAH, and to detect pathogenetically significant characteristics developed following Covid-19.

METHODS

The trial was conducted in 2019-2023 at the departments of immunology, microbiology, virus ology of the National Research Mordovia State University (microbiological and immunological laboratory — license № 13.01.04. 0001. Л.000005.06.11, permanent), Katkov SV National Clinical Hospital, North Caucasus Sanatorium Resort of the Ministry of Defense of Russia.

27 patients (10 females and 17 males) with Grade 2 EAH (group 1) and 16 healthy people (7 females and 9 males) with normal BP (group 2) have undergone through a dynamic complex (clinical, laboratory ad instrumental) observation. In 2019 (prior to pandemic), they had their blood cytokine levels analyzed (7.00–8.00, 12.00–13.00, 19.00–20.00, 00.00–1.00) within three days. In 2020 (Wuhan-Hu-1 circulation), 18 patients

Table 1. Analysis of cytokines in the blood of patients with EAH prior to COVID-19

Time interval		7.00–8.00	12.00–13.00	19.00–20.00	0.00–1.00
		1	2	3	4
IL18, pg/ml	Day 1	356 [271–460]	402 [258–437]	523 [391–639]*1.2	610 [489–720]*1.2.3
	Day 2	317 [286–451]	398 [310–469]	551 [406–668]*1.2	689 [464–783]*1.2.3
	Day 3	368 [239–490]	417 [267–452]	584 [390–627]*1.2	621 [429–718]*1.2.3
IL18 BP, pg/ml	Day 1	6100 [3800–6900]	6300 [4100–7200]	5900 [3700–6800]	5500 [3500–6400]
	Day 2	5790 [3240–6450]	6100 [4320–7400]	6400 [4300–7100]	5800 [3200–6700]
	Day 3	5900 [3400–6600]	5800 [4200–6700]	6200 [4500–6900]	5700 [3500–6900]
LIF, pg/ml	Day 1	7.48 [4.21–101.3]	7.64 [4.37–11.5]	12.3 [8.25–14.1]*1.2	10.1 [9.88–11.9]^1.2'3
	Day 2	7.33 [4.18–12.1]	7.42 [3.91–11.9]	12.6 [8.12–14.3]*1.2	9.97 [10.2–12.2]^1.2.3
	Day 3	7.54 [4.12–11.8]	7.48 [4.11–12.5]	12.7 [7.96–14.4]*1.2	10.2 [9.97–12.5]^1.2'3
sLIFr, pg/ml	Day 1	3850 [2600–5100]	4100 [3600–4900]	5400 [4500–7300]*1.2	2900 [2300–3800]*1.2.3
	Day 2	3910 [2770–5300]	3870 [3540–5200]	5640 [4800–7200]*1.2	3100 [2500–4200]*1.2.3
	Day 3	3960 [2650–5250]	3840 [3590–5300]	5700 [4900–7400]*1.2	3720 [2400–4100]*1.2.3
M-CSF, pg/ml	Day 1	371 [308–493]	410 [290–482]	419 [327–494]*1^2	395 [315–526]
	Day 2	350 [292–471]	421 [287–475]	415 [347–484]*1^2	405 [321–519]
	Day 3	363 [315–488]	442 [293–490]	426 [351–492]*1^2	398 [309–524]
IL34, pg/ml	Day 1	127 [96.7–152]	144 [102–168]	93.6 [81.2–105]*2	80.2 [68.1–85.5]*1.2.3
	Day 2	118 [90.8–141]	136 [96–153]	98.5 [85.6–117]*2	81.9 [66.2–87.7]*1.2.3
	Day 3	131 [101.1–159]	148 [108–172]	101.7 [90.1–120]*2	92.7 [69.3–90.5]*1.2.3
MCSFR, µg/ml	Day 1	22.8 [17.4–28.3]	18.7 [12.2–31.1]	20.6 [12.5–35.7]	19.9 [17.9–31.2]
	Day 2	24.4 [18.1–29.8]	19.3 [13.7–32.6]	23.2 [13.9–38.5]	26.2 [19.7–33.3]
	Day 3	23.6 [17.8–27.7]	17.5 [12.8–31.9]	22.5 [13.1–37.2]	21.7 [18.5–32.7]

Note: * — significant level $p < 0.001$, ^ — $p < 0.01$, ' — $p < 0.05$ (dependent and independent samples were compared with the Wilcoxon and Mann–Whitney tests respectively) indicating time intervals (1–7:00; 2–12:00; 3–19:00; 4–00:00.)

Table 2. Analysis of cytokines in the blood of healthy people prior to COVID-19

Time interval		7.00–8.00	12.00–13.00	19.00–20.00	0.00–1.00
		1	2	3	4
IL18, pg/ml	Day 1	185 [143–201]	164 [138–194]	214 [144–229]	301 [246–385]*1.2.3
	Day 2	178 [135–194]	157 [127–183]	196 [124–205]	289 [235–369]*1.2.3
	Day 3	190 [148–210]	171 [145–201]	220 [151–235]	314 [253–390]*1.2.3
IL18 BP, pg/ml	Day 1	4720 [4210–5110]	4830 [4160–5200]	4660 [4320–5170]	6100 [5720–6930]*1.2.3
	Day 2	4810 [4320–5230]	4920 [4210–5350]	4730 [4460–5250]	6450 [5840–7010]*1.2.3
	Day 3	4780 [4270–5160]	4870 [4190–5280]	4690 [4410–5190]	6320 [5800–7000]*1.2.3
LIF, pg/ml	Day 1	1.38 [1.15–1.68]	1.47 [1.31–1.73]	1.33 [1.26–1.75]	1.35 [1.24–1.63]
	Day 2	1.40 [1.17–1.71]	1.51 [1.35–1.77]	1.35 [1.29–1.78]	1.37 [1.27–1.66]
	Day 3	1.41 [1.19–1.75]	1.54 [1.40–1.81]	1.37 [1.31–1.82]	1.41 [1.30–1.69]
sLIFr, pg/ml	Day 1	3920 [3130–4870]	4260 [3450–4610]	4440 [3610–4830]	4160 [3780–4520]
	Day 2	3870 [3070–4790]	4990 [3390–4650]	4380 [3580–4770]	4130 [3690–4430]
	Day 3	4010 [3210–4980]	5180 [3520–4700]	4530 [3720–4950]	4240 [3870–4610]
M-CSF, pg/ml	Day 1	220 [143–283]	187 [137–240]	235 [138–281]	357 [315–394]*1.2.3
	Day 2	237 [160–299]	198 [149–243]	253 [155–310]	369 [328–404]*1.2.3
	Day 3	228 [151–295]	191 [142–239]	244 [147–293]	361 [321–398]*1.2.3
IL34, pg/ml	Day 1	162 [112–203]	170 [126–212]	169 [147–235]*2	158 [127–216]
	Day 2	158 [107–196]	167 [122–208]	165 [141–233]*2	155 [121–210]
	Day 3	165 [116–210]	174 [131–218]	172 [150–239]*2	163 [133–215]
MCSFR, µg/ml	Day 1	31.6 [25.7–39.2]	27.9 [19.3–37.1]	44.7 [32.1–49.8]*2.3	67.7 [42.1–93.6]*1.2.3
	Day 2	28.9 [23.5–38.7]	26.5 [18.2–35.3]	41.9 [29.9–48.3]*2.3	63.6 [38.8–89.7]*1.2.3
	Day 3	32.1 [26.3–40.1]	28.6 [20.4–39.2]	45.3 [33.7–50.6]*2.3	69.5 [44.6–96.3]*1.2.3

Note: * — significant level $p < 0.001$, ^ — $p < 0.01$, † — $p < 0.05$ (dependent and independent samples were compared with the Wilcoxon and Mann–Whitney tests respectively) indicating time intervals (1–7:00; 2–12:00; 3–19:00; 4–00:00).

from group 1 (8 females and 10 males) and 9 patients (4 females and 5 males) from group 2 were diagnosed with COVID-19 as per relevant temporary methodical recommendations related to prevention, diagnostics and treatment of moderately to severely novel coronavirus infection, pneumonia (grade I–II CT). Comparable treatment regimens were used (16 mg of dexamethasone per day, 500 mg of Sumamed TID, heparin (a group of researchers failed to influence the therapy).

Inclusion criteria in 2019: Grade II EAH for 10 years (first stage of the trial), comparable hypotensive therapy (ACE inhibitors ± diuretic), 55–60 years, total cholesterol less than 5.0 mmol/L, LDL less than 3.0 mmol/L, HDL more than 1.0 mmol/L, TG less than 1.7 mmol/L, IMT less than 0.9 mm, glucose less than 5.5 mg/dl, BMI less than 30 kg/m², comparable characteristics of day regimen (sleeping from 23.00 to 6.00, last food intake at 20.00, no disturbed sleep, intake of hypnotic agents and/or melatonin-containing preparations (as assessed by a neurologist), signing of an informed consent from by the patient.

Additional inclusion criteria in 2020: participation in the trial of circadian rhythm in cytokines administration in patients with EAH in 2019, a history of COVID-19 (day 10 following clinical and laboratory convalescence in comparable hospitalization duration of 14–16 days), whereas group 2 included people without a history of EAH + COVID-19 (day 10 following clinical and laboratory convalescence in comparable hospital stay of 14–16 days), COVID-19 was confirmed with the PCR method and results of a serologic examination, moderate to severe, with involvement of the lungs (grade I–II CT), comparable therapy of COVID-19, and a written consent form.

In 2019 and 2020, there were general exclusion criteria such as type 1 or 2 diabetes mellitus, allergic/autoimmune diseases, mental diseases, symptomatic AH, smoking, lack

of readiness for a long-term examination, use of antiviral and immunomodulating medicinal agents during COVID-19 and six months prior to the trial. Patients who had to take antihypertensive medicinal agents apart from ACE inhibitors and/or thiazide/thiazide-like diuretics (only for patients with Grade II EAH) were excluded from the trial.

Blood sampling times (7.00–8.00, 12.00–13.00, 19.00–20.00, 00.00–1.00) and specter of cytokines (IL18, IL18 BP, LIF, sLIFr, M-CSF, MCSFR) were determined based on scientific trials of circadian rhythms of human cytokines biology [6, 7] and previous own trials of cytokines in EAH pathogenesis [8]. Based on our 10-year trial, the levels of IL18, IL18 BP, LIF, sLIFr, M-CSF, MCSFR are associated with the rate of cardiovascular complications in patients with EAH in a statistically independent mode. It explains the data about the specter of cells having the cytokines receptors [9] and their relation with metabolism of vasopressors and vasodilators.

Blood sampling was done at 7.00–8.00, 12.00–13.00, 18.00–19.00, 00.00–1.00 (three days) using BD Vacutainer (Becton Dickinson; USA (for blood serum release), blood was centrifuged (1,500–2,000 rounds per minutes, 15 min) to get serum, which will be subsequently stored in labeled test tubes at –30° C for no longer than 30 days. Time from blood sampling to freezing was 60 min. Cytokines (IL18, IL18 BP, LIF, sLIFr, M-CSF, MCSFR) were determined by a certified professional with an enzyme-linked immunosorbent assay and Personal Lab TM immunoassay analyzer (Adaltis; Italy). Test systems produced by eBioscience (Bender MedSystems; Austria) and R&D Systems (USA).

Daily characteristics of patients were determined as per the following classification: dippers (BP decline from 10 to 20%), nondippers (BP declines less than 10%) and night-peakers (rise at night). Daily monitoring was done to all patients. It was

Table 3. Analysis of blood cytokines levels in patients with EAH 10 days following the novel coronavirus infection

Time interval		7.00–8.00	12.00–13.00	19.00–20.00	0.00–1.00
		1	2	3	4
IL18, pg/ml	Day 1	460 [396–510]	445 [368–474]	590 [453–670]	792 [373–821]*1.2.3
	Day 2	446 [370–482]	435 [352–459]	582 [442–649]	759 [338–803]*1.2.3
	Day 3	454 [387–503]	440 [361–467]	588 [447–658]	781 [352–811]*1.2.3
IL18 BP, pg/ml	Day 1	6300 [4110–7500]	6110 [3730–7460]	5100 [3700–6400]*1.2	5310 [3230–6370]*3
	Day 2	6150 [4030–7350]	5980 [3610–7320]	4820 [3550–6240]	4830 [3050–6180]
	Day 3	6220 [4090–7460]	6050 [3690–7380]	4950 [3630–6330]	4910 [3170–6250]
LIF, pg/ml	Day 1	7.69 [4.35–10.8]	7.92 [4.51–10.5]	13.1 [8.74–15.6]*1.2	9.83 [9.12–11.7]*3
	Day 2	7.33 [4.25–9.9]	7.63 [4.00–10.2]	12.6 [8.11–14.9]	9.10 [8.92–10.8]*3
	Day 3	7.51 [4.31–10.4]	7.88 [4.32–10.4]	12.9 [8.55–15.4]	9.58 [9.05–11.3]*3
sLIFr, pg/ml	Day 1	4100 [2720–5000]	3820 [2910–4500]	7900 [6200–8400]*1.2	3870 [3100–4200]*3
	Day 2	3850 [2680–4930]	3530 [2850–4320]	7590 [6030–7990]	3480 [2860–4080]
	Day 3	3980 [2700–4980]	3660 [2890–4470]	7770 [6120–8250]	3750 [2970–4110]
IL34, pg/ml	Day 1	630 [570–810]	593 [492–685]	830 [540–973]*1.2	601 [518–710]*3
	Day 2	605 [561–792]	561 [477–661]	812 [521–953]	582 [501–695]
	Day 3	616 [569–802]	582 [485–672]	826 [530–964]	593 [512–693]
MCSFR, µg/ml	Day 1	9.18 [8.3–31.5]	10.23 [7.16–12.4]	10.5 [8.53–13.2]	9.51 [6.42–12.3]
	Day 2	9.05 [8.1–29.6]	9.81 [6.91–11.5]	9.93 [8.41–12.8]	9.11 [6.30–11.8]
	Day 3	9.10 [8.2–30.2]	10.12 [7.02–12.0]	10.4 [8.49–13.1]	9.26 [6.39–12.1]

Note: * — significant level $p < 0.001$, ^ — $p < 0.01$, ' — $p < 0.05$ (dependent and independent samples were compared with the Wilcoxon and Mann–Whitney tests respectively) indicating time intervals (1–7:00; 2–12:00; 3–19:00; 4–00:00).

accompanied by blood sampling to determine the levels of cytokines.

The obtained results were statistically processed using StatTech v. 2.8.8 (StatTech, Russia) and Stat Soft Statistica 10.0 (USA). The results were presented as a median (Me) and percentiles ($Q_{0.25}$ – $Q_{0.75}$). It was assessed whether qualitative characteristics corresponded to normal distribution with the Shapiro–Wilk test. Dependent and independent samples were compared with the Wilcoxon and Mann–Whitney tests respectively. Regression Cox model was used, and the regression coefficient was assessed. Differences at $p < 0.05$ were taken as statistically significant.

RESULTS

Analysis of altered concentration of investigated blood cytokines in patients with EAH allowed to determine the differences from regular patterns found among healthy persons (Table 1) within two days of the prepandemic period (Table 2).

Within the system of IL18–IL18BP, an increase of IL18 in the peripheral blood was observed at 19.00 and 0.00 when compared with the results obtained at 7.00 and 12.00 ($p < 0.001$) with no growth of IL18 during the observation period. No increase of IL18 was found among healthy people. However, an increase of IL18 BP ($p < 0.05$) was detected at 00.00. Meanwhile, qualitative levels of IL18 are significantly increased in patients with hypertension ($p < 0.001$). During the early convalescence following novel coronavirus, patients with EAH had an additional decrease of 18 BP at 19.00, which was preserved at 00.00 ($p < 0.001$) when compared with data obtained at 7.00, 13.00, 19.00 (Table 3). This is how the group was extinguished from healthy people with an increased level of IL18 at 00.00 but with a compensatory increase of IL18 BP at 20.00 (Table 4).

It was found out during analysis of LIF–sLIFR prior to SARS-CoV-2 that patients with EAH had experienced a growth of two components at 19.00, which was decreased at 00.00

(Table 1). These changes were not observed among healthy people (table 2). During convalescence following the previous novel coronavirus, patients with EAH had a more pronounced (200%) increase of sLIFr at 19.00 with preserved changes and qualitative characteristics of LIF.

Levels of M-CSF and its receptors in patients with EAH went through no changes during a day of the pre-COVID period (Table 1). Meanwhile, healthy people had seen a growth of M-CSF at 00.00 against the background of increased M-CSF at 19.00 and 00.00 with restoration at 7.00. Qualitative characteristics of M-CSF were significantly higher in patients with hypertension during all time points ($p < 0.001$) as compared with healthy people. During convalescence following COVID-19, a peak increase of M-CSF was seen at 19.00 with a decrease at 00.00 among patients with EAH (not previously detected) with no changes of M-CSFR. Healthy people had no changes of circadian rhythms as compared to data obtained prior to SARS-CoV-2.

It should be noted that during monitoring of similar cytokines performed six months following COVID-19 85% of patients with EAH had circadian patterns developed after COVID-19 as a decrease of IL18 BP at 19.00, two-fold increase of sLIFr and MCSF (Table 5) with restored patterns of post-COVID era among healthy people (Table 6).

Compared characteristics of circadian rhythms of analyzed cytokines during the post-COVID era and altered course of EAH allowed to find out (during the intraquartile analysis) that an increase of sLIFr by 200% and more (quartiles III and IV of altered sLIFr in 8 people) was accompanied with a rise in systolic BP above 150 mm Hg at 19.00 in spite of antihypertensive therapy, which provided a therapeutic effect prior to the previous novel coronavirus therapy and in the morning/in the afternoon following the infection. It was required to change therapy (time of intake of a medicinal product) and increase the dose of basic preparations. Moreover, 8 of 18 patients with EAH included into the trial during the post-COVID era had a daily rhythm of BP as per the results of Holter monitoring. It was night peaker

Table 4. Analysis of blood cytokines levels in patients with EAH 10 days following the novel coronavirus infection

Time interval		7.00–8.00	12.00–13.00	19.00–20.00	0.00–1.00
		1	2	3	4
IL18, pg/ml	Day 1	151 [144–203]	158 [129–214]	169 [136–223]	291 [247–383]*1.2.3
	Day 2	138 [133–196]	141 [120–203]	161 [128–215]	273 [233–375]*1.2.3
	Day 3	145 [139–201]	149 [125–211]	165 [131–220]	282 [242–379]*1.2.3
IL18 BP, pg/ml	Day 1	4670 [4170–5120]	4590 [4210–5310]	6400 [5370–7510]*1.2	6100 [5330–7820]*1.2.3
	Day 2	4320 [3890–5010]	4250 [4030–5100]	6050 [5150–7270]*1.2	5880 [5140–6510]*1.2.3
	Day 3	4590 [3960–5090]	4420 [4110–5230]	6230 [5230–7440]*1.2	6010 [5220–6680]*1.2.3
LIF, pg/ml	Day 1	1.39 [1.12–1.64]	1.47 [1.24–1.72]	1.36 [1.05–1.55]	1.36 [1.21–1.7]
	Day 2	1.25 [1.09–1.54]	1.38 [1.21–1.68]	1.33 [0.98–1.43]	1.34 [1.15–1.63]
	Day 3	1.32 [1.11–1.61]	1.41 [1.22–1.70]	1.28 [0.91–1.20]	1.31 [1.08–1.56]
sLIFr, pg/ml	Day 1	4120 [3620–4510]	3960 [3310–4580]	4210 [3640–4660]	4170 [3580–4790]
	Day 2	4030 [3430–4360]	3650 [3050–4270]	4090 [3400–4530]	3960 [3410–4530]
	Day 3	4090 [3580–4420]	3820 [3220–4390]	4130 [3550–4610]	4080 [3490–4670]
M-CSF, pg/ml	Day 1	190 [138–236]	171 [139–247]	182 [121–268]	333 [287–412]*1.2.3
	Day 2	175 [129–227]	160 [121–236]	171 [115–253]	292 [263–393]*1.2.3
	Day 3	183 [131–230]	169 [128–241]	179 [119–261]	314 [275–403]*1.2.3
IL34, pg/ml	Day 1	146 [121–198]	152 [127–231]	221 [169–262]*1.2	155 [127–193]*3
	Day 2	131 [115–179]	135 [113–219]	203 [153–248]*1.2	138 [115–174]*3
	Day 3	142 [119–183]	148 [121–227]	217 [161–254]*1.2	144 [123–188]*3
MCSFR, µg/ml	Day 1	31.6 [24.3–39.7]	29.6 [21.2–36.5]	51.9 [34.2–58.8]*2.3	66.2 [38.5–101.3]*1.2.3
	Day 2	27.6 [21.7–35.3]	26.8 [19.8–33.7]	48.3 [31.8–52.3]*2.3	59.1 [33.2–97.5]*1.2.3
	Day 3	29.4 [23.8–38.2]	28.3 [20.9–35.9]	50.2 [33.4–55.7]*2.3	63.5 [35.9–99.7]*1.2.3

Note: * — significant level $p < 0.001$, ^ — $p < 0.01$, ' — $p < 0.05$ (dependent and independent samples were compared with the Wilcoxon and Mann–Whitney tests respectively) indicating time intervals (1 — 7:00; 2 — 12:00; 3 — 19:00; 4 — 00:00.).

(increase of BP at night). Prior to SARS-CoV-2, all patients were classified as dippers. The patients had alternated circadian rhythms mentioned above such as a drop of IL18 BP for more than 58% and two-fold increase of sLIFr and MCSF. Meanwhile, a multiple correlation analysis of the relations between cytokine levels (IL18, IL18 BP, LIF, sLIFr, M-CSF, MCSFR) during all analyzed time points and level of systolic arterial pressure (as per results of daily monitoring of BP) has seen a statistically independent relation between the level of sLIFr and systolic BP: regression coefficient of 2.48, standard error of 0.22, t-criterion of 9.83, relative risk of increased systolic BP after 18.00 equal to 4.2 and Wald criterion of 16.3.

DISCUSSION

The obtained data show that circadian rhythms of cytokines in the peripheral blood are alternated depending on the presence of EAH and their additional distortion during the post-COVID era. In the majority of cases, it is stable and can be preserved

for over six months. Taking into account previously published data about the correlation between increased sLIFr over 5,000 pg/ml and increased NT-proBNP ($r = 0.87$; $p = 0.0007$), and the correlation between MCSF and SDMA ($r = 0.83$; $p = 0.0008$) [7] it is shown that there is a pathogenetic significance of discovered circadian changes as EAH progresses. Thus, in spite of ability for vasodilation, which produces a positive effect in case of EAH, the secondary growth of NT-proBNP will result in progression of chronic cardiac failure and an increased risk of cardiovascular complications [10]. The positive relation between MCSF and IL18 and growth of SDMA [8] is more frequently of a renal origin [11]. It can determine the vector of hypertension progression by canceling the essential nature. It is known about its production by endothelial cells under the influence of proinflammatory cytokines [12], which can be induced by viruses in this case.

Fundamental trials devoted to circadian rhythms of synthesis of certain regulatory peptides require high comparability of included patients (this was achieved during the

Table 5. Analysis of blood cytokines levels in patients with EAH 6 months following the novel coronavirus infection

Time interval		7.00–8.00	12.00–13.00	19.00–20.00	0.00–1.00	7.00–8.00
		1	2	3	4	5
IL18, pg/ml	Day 1	457 [388–514]	449 [374–493]	589 [431–661]	791 [370–818]*1.2.3	461 [369–505]
IL18 BP, pg/ml	Day 1	6280 [4100–7490]	6070 [3670–7350]	5210 [3280–6500]*1.2	5380 [3510–6400]*3	6220 [4010–7090]
LIF, pg/ml	Day 1	7.26 [4.03–9.9]	7.88 [4.19–10.7]	12.9 [7.81–16.1]*1.2	10.1 [8.12–12.3]*3	7.31 [4.15–10.1]
sLIFr, pg/ml	Day 1	4020 [2510–5100]	3790 [2880–4430]	7870 [6150–8390]*1.2	3690 [3110–4180]*3	3990 [2490–5020]
M-CSF, pg/ml	Day 1	621 [554–816]	588 [461–625]	815 [593–954]*1.2	650 [521–733]*3	618 [560–831]
MCSFR, µg/ml	Day 1	9.04 [7.3–13.5]	11.12 [6.76–13.1]	11.3 [8.41–13.9]	9.42 [7.12–13.1]	8.95 [6.81–12.8]

Note: * — significant level $p < 0.001$, ^ — $p < 0.01$, ' — $p < 0.05$ (dependent and independent samples were compared with the Wilcoxon and Mann–Whitney tests respectively) indicating time intervals (1 — 7:00; 2 — 12:00; 3 — 19:00; 4 — 00:00.).

Table 6. Analysis of blood cytokines levels in patients with EAH 6 months following the novel coronavirus infection

Time interval		7.00–8.00	12.00–13.00	19.00–20.00	0.00–1.00	7.00–8.00
		1	2	3	4	5
IL18, pg/ml	Day 1	143 [138–193]	151 [126–210]	163 [128–264]	273 [232–357]*1.2.3	154 [129–201]
IL18 BP, pg/ml	Day 1	4530 [4030–4990]	4490[4010–5170]	6340 [4970–6960]*1.2	5990 [5330–7340]*1.2.3	4710 [3980–4920]
LIF, pg/ml	Day 1	1.31[1.05–1.44]	1.39 [1.13–1.55]	1.29 [0.98–1.45]	1.32 [1.19–1.68]	1.33 [1.01–1.38]
sLIFr, pg/ml	Day 1	4060 [3490–4330]	3830 [3110–4270]	4100 [3340–4220]	4160 [3390–4580]	4020 [3530–4290]
M-CSF, pg/ml	Day 1	179 [128–216]	168[123–221]	181 [118–246]	311 [269–403]*1.2.3	184 [131–226]
IL34, pg/ml	Day 1	139 [110–173]	154 [129–242]	218[159–258]*1.2	144 [107–173]*3	140 [114–185]
MCSFR, µg/ml	Day 1	28.7 [23.8–37.7]	29.1 [20.3–36.4]	52.2 [35.7–60.1]*2.3	64.9 [36.5–110.1]*1.2.3	30.1 [21.4–32.9]

Note: * — significant level $p < 0.001$, ^ — $p < 0.01$, ' — $p < 0.05$ (dependent and independent samples were compared with the Wilcoxon and Mann–Whitney tests respectively) indicating time intervals (1 — 7:00; 2 — 12:00; 3 — 19:00; 4 — 00:00).

trial and allowed to reduce the sample scope) and stable daily rhythms of life, alternated day and night phases; they are rather of a theoretical significance. However, in the analyzed clinical situations, there exist essential connections that determine clinical characteristics of hypertension with altered treatment regimens due to loss of control over BP when the daily rhythm developed prior to infection with SARS-CoV-2 is altered.

The lack of a compensatory increase of cytokines with protected properties in relation to progressive endothelial dysfunction (IL18 BP, M-CSFR) was seen in patients with EAH during the post-COVID era. IL18-BP reduces the risk of renal damage on ischemia and reperfusion animal models due to anti-inflammatory and antioxidant activity [13]. It is essential in AH. A new prospect of IL18 BP as a therapeutic target in cardiovascular diseases was recorded in a number of publications [13, 14].

A detailed analysis confirms the necessity of assessing four time points; the largest prognostic significance of the analyzed cytokines was determined at 19.00. It is essential for further related trials, which examine the role of cytokines in

the pathogenesis of cardiovascular diseases and post-COVID syndrome. However, they are oriented towards a morning blood sample. It is probably less significant than blood sample taken at 19.00.

CONCLUSIONS

Analysis of the role of infection with SARS-CoV-2 in the altered circadian rhythms of cytokines (IL18, IL18 BP, LIF, sLIFr, M-CSF, MCSFR) in the blood of patients with EAH opens up prospects for the analysis of the role and other infectious agents in the change of the cytokine component of progressing endothelial dysfunction. Altered cytokines levels were assessed within a day at several time points. During surveillance of a patient over several days it was verified whether the observed regular patterns were repeated. Chronobiology requires diversified examination to expand the scope of fundamental data, which can explain clinical features of socially significant diseases and can be the basis of new principles of therapy in the future.

References

- Richards J, Gumz ML. Mechanism of the circadian clock in physiology. *Am J Physiol Regul Integr Comp Physiol.* 2013; 304 (12): 1053–64. DOI: 10.1152/ajpregu.00066.2013.
- Jin RR, Cheung CN, Wong CHY, Lo CCW, Lee CPI, Tsang HW, et al. Sleep quality mediates the relationship between systemic inflammation and neurocognitive performance. *Brain Behav Immun Health.* 2023; 30: 365–74. DOI: 10.1016/j.bbih.2023.100634.
- Katinas GS, Chibisov SM, Halabi GM, Dementev MV. *Analiticheskaja hronobiologija.* M.: Bejrut, 2017; 224 s. Russian.
- Chibisova SM, Rapoport SI, Blagonravova ML. *Hronobiologija i hronomedicina.* M.: Izd-vo RUDN, 2018; 828 s. Russian.
- Young MR, Matthews JP, Kanabrocki EL, Sothorn RB, Roitman-Johnson B, Scheving LE. Circadian rhythmometry of serum interleukin-2, interleukin-10, tumor necrosis factor-alpha, and granulocyte-macrophage colony-stimulating factor in men. *Chronobiol Int.* 1995; 12 (1): 19–27. DOI: 10.3109/07420529509064496.
- Scheiermann C, Gibbs J, Ince L, Loudon A. Clocking in to immunity. *Nat Rev Immunol.* 2018; 18 (7): 423–37. DOI: 10.1038/s41577-018-0008-4.
- Geiger SS, Fagundes CT, Siegel RM. Chrono-immunology: progress and challenges in understanding links between the circadian and immune systems. *Immunology.* 2015; 146 (3): 349–58. DOI: 10.1111/imm.12525.
- Radaeva OA, Simbircev AS. Citokiny v immunopatogeneze arterial'noj gipertenzii. M.: Nauka, 2021; 350 s. Russian.
- The Human Protein Atlas project is funded by the Knut & Alice Wallenberg foundation. 2023 [25.11.2023]. Available from: <https://www.proteinatlas.org/>.
- Daya NR, McEvoy JW, Christenson RH, Tang O, Foti K, Juraschek SP, et al. Prevalence of Elevated NT-proBNP and its Prognostic Value by Blood Pressure Treatment and Control. *Am J Hypertens.* 2023; 36 (11): 602–11. DOI: 10.1093/ajh/hpad065.
- Dahlem DP, Neiger R, Schweighauser A, Francey T, Yerramilli M, Obare E, et al. Plasma Symmetric Dimethylarginine Concentration in Dogs with Acute Kidney Injury and Chronic Kidney Disease. *J Vet Intern Med.* 2017; 31 (3): 799–804. DOI: 10.1111/jvim.14694.
- Chen S, Martens-Lobenhoffer J, Weissenborn K, Kielstein JT, Lichtinghagen R, Deb-Chatterji M, et al. Correction: Association of dimethylarginines and mediators of inflammation after acute ischemic stroke. *J Neuroinflammation.* 2023; 20 (1): 103. DOI: 10.1186/s12974-023-02775-0.
- Nakanishi Y, Horimasu Y, Yamaguchi K, Sakamoto S, Masuda T, Nakashima T, et al. IL18 binding protein can be a prognostic biomarker for idiopathic pulmonary fibrosis. *PLoS One.* 2021; 16 (6): 252–64. DOI: 10.1371/journal.pone.0252594.
- Ain QU, Dewi TI, Kurniati NF. Plasma Levels of Interleukin-6 and -18 Significantly Increase in Patients with Acute Coronary Syndrome. *Oman Med J.* 2023; 38 (4): 529–32. DOI: 10.5001/omj.2023.94.

Литература

- Richards J, Gumz ML. Mechanism of the circadian clock in physiology. *Am J Physiol Regul Integr Comp Physiol*. 2013; 304 (12): 1053–64. DOI: 10.1152/ajpregu.00066.2013.
- Jin RR, Cheung CN, Wong CHY, Lo CCW, Lee CPI, Tsang HW, et al. Sleep quality mediates the relationship between systemic inflammation and neurocognitive performance. *Brain Behav Immun Health*. 2023; 30: 365–74. DOI: 10.1016/j.bbih.2023.100634.
- Катинас Г. С., Чибисов С. М., Халаби Г. М., Дементьев М. В. Аналитическая хронобиология. М.: Бейрут, 2017; 224 с.
- Чибисова С. М., Рапопорт С. И., Благодирова М. Л. Хронобиология и хрономедицина. М.: Изд-во РУДН, 2018; 828 с.
- Young MR, Matthews JP, Kanabrocki EL, Sothorn RB, Roitman-Johnson B, Scheving LE. Circadian rhythmometry of serum interleukin-2, interleukin-10, tumor necrosis factor-alpha, and granulocyte-macrophage colony-stimulating factor in men. *Chronobiol Int*. 1995; 12 (1): 19–27. DOI: 10.3109/07420529509064496.
- Scheiermann C, Gibbs J, Ince L, Loudon A. Clocking in to immunity. *Nat Rev Immunol*. 2018; 18 (7): 423–37. DOI: 10.1038/s41577-018-0008-4.
- Geiger SS, Fagundes CT, Siegel RM. Chrono-immunology: progress and challenges in understanding links between the circadian and immune systems. *Immunology*. 2015; 146 (3): 349–58. DOI: 10.1111/imm.12525.
- Радаева О. А., Симбирцев А. С. Цитокины в иммунопатогенезе артериальной гипертензии. М.: Наука, 2021; 350 с.
- The Human Protein Atlas project is funded by the Knut & Alice Wallenberg foundation. 2023 [25.11.2023]. Available from: <https://www.proteinatlas.org/>.
- Daya NR, McEvoy JW, Christenson RH, Tang O, Foti K, Juraschek SP, et al. Prevalence of Elevated NT-proBNP and its Prognostic Value by Blood Pressure Treatment and Control. *Am J Hypertens*. 2023; 36 (11): 602–11. DOI: 10.1093/ajh/hpad065.
- Dahlem DP, Neiger R, Schweighauser A, Francey T, Yerramilli M, Obare E, et al. Plasma Symmetric Dimethylarginine Concentration in Dogs with Acute Kidney Injury and Chronic Kidney Disease. *J Vet Intern Med*. 2017; 31 (3): 799–804. DOI: 10.1111/jvim.14694.
- Chen S, Martens-Lobenhoffer J, Weissenborn K, Kielstein JT, Lichtinghagen R, Deb-Chatterji M, et al. Correction: Association of dimethylarginines and mediators of inflammation after acute ischemic stroke. *J Neuroinflammation*. 2023; 20 (1): 103. DOI: 10.1186/s12974-023-02775-0.
- Nakanishi Y, Horimasu Y, Yamaguchi K, Sakamoto S, Masuda T, Nakashima T, et al. IL18 binding protein can be a prognostic biomarker for idiopathic pulmonary fibrosis. *PLoS One*. 2021; 16 (6): 252–64. DOI: 10.1371/journal.pone.0252594.
- Ain QU, Dewi TI, Kurniati NF. Plasma Levels of Interleukin-6 and -18 Significantly Increase in Patients with Acute Coronary Syndrome. *Oman Med J*. 2023; 38 (4): 529–32. DOI: 10.5001/omj.2023.94.

COMPARATIVE BIOINFORMATICS ANALYSIS OF ANTIMICROBIAL RESISTANCE GENE POOL IN THE GENOMES OF REPRESENTATIVES OF GENUS *CORYNEBACTERIUM*

Kulshan TA [✉], Bugaeva IO, Soboleva EF, Allyanova MS, Popov DA, Shvidenko IG

Razumovsky Saratov State Medical University, Saratov, Russia

Currently, multidrug resistance of bacterial infectious agents poses a serious threat to the global public health. The following *Corynebacterium* strains are of special importance for infections, including hospital-acquired ones: *C. amycolatum*, *C. urealyticum*, *C. striatum*, *C. jeikeium*, *C. aurimucosum*, *C. genitalium* that are resistant to the broad spectrum of antimicrobial drugs. The study was aimed to conduct bioinformatics analysis of the pool of antimicrobial resistance genes in the published genomes of some members of the genus *Corynebacterium*. The data on the whole genome nucleotide sequences of 22 *Corynebacterium* isolates readily available from NCBI GenBank were assessed. Bioinformatics analysis of the whole genome sequences conducted in order to search for antimicrobial resistance genes in the specified genomes was performed using the PATRIC online resource. It was found that the genomes provided comprised various combinations of 25 antimicrobial drug resistance genes. Amino acid substitutions in *GyrA* (positions 87, 88 and 91) were revealed in some *Corynebacterium* strains, through which quinolone/fluoroquinolone resistance could be realized.

Keywords: *C. amycolatum*, *C. jeikeium*, *C. striatum*, *C. urealyticum*, *C. aurimucosum*, genomes, antimicrobial resistance genes, *gyrA*, antimicrobial drugs

Author contribution: Kulshan TA — study planning, literature review, dealing with molecular genetic data (selection of genomes, genome annotation, comparative analysis of *gyrA* amino acid sequences), data analysis, manuscript writing; Bugaeva IO — study planning, data analysis, interpretation of findings, manuscript writing; Soboleva EF — literature review, data analysis, manuscript writing; Allyanova MS — literature review, analysis of the antimicrobial resistance gene pool in the genomes of corynebacterial strains, dealing with the PATRIC online service; Popov DA — literature review, search for *gyrA* amino acid sequences in the genomes of corynebacterial strains, comparative analysis of amino acid sequences; Shvidenko IG — advising during manuscript writing, data analysis.

✉ **Correspondence should be addressed:** Tatiana A. Kulshan
B. Kazachiya, 112, Saratov, 410012, Russia; tatjana.kulshan@yandex.ru

Received: 20.10.2023 **Accepted:** 03.12.2023 **Published online:** 19.12.2023

DOI: 10.24075/brsmu.2023.047

СРАВНИТЕЛЬНЫЙ БИОИНФОРМАТИЧЕСКИЙ АНАЛИЗ СОСТАВА ГЕНОВ АНТИМИКРОБНОЙ УСТОЙЧИВОСТИ В ГЕНОМАХ ПРЕДСТАВИТЕЛЕЙ РОДА *CORYNEBACTERIUM*

T. A. Кульшань [✉], И. О. Бугаева, Е. Ф. Соболева, М. С. Аллянова, Д. А. Попов, И. Г. Швиденко

Саратовский государственный медицинский университет имени В. И. Разумовского Министерства здравоохранения Российской Федерации, Саратов, Россия

В настоящее время множественная антимикробная резистентность бактериальных инфекционных агентов представляет серьезную угрозу для мирового здравоохранения. Особое значение в развитии инфекций, в том числе госпитальных, играют следующие виды коринебактерий: *C. amycolatum*, *C. urealyticum*, *C. striatum*, *C. jeikeium*, *C. aurimucosum*, *C. genitalium*, которые устойчивы к большому арсеналу антимикробных препаратов. Целью исследования было проведение биоинформатического анализа спектра генов устойчивости к антимикробным препаратам в опубликованных геномах некоторых представителей рода *Corynebacterium*. Исследованы данные о нуклеотидных последовательностях полных геномов 22 штаммов коринебактерий, представленных в свободном доступе в NCBI GenBank. Биоинформатический анализ полногеномных последовательностей с целью поиска генов антимикробной устойчивости в указанных геномах осуществляли с помощью онлайн-ресурса PATRIC. Установлено, что представленные геномы в различных комбинациях содержали 25 генов устойчивости к антимикробным препаратам. У некоторых штаммов коринебактерий выявлены аминокислотные замены в *GyrA* (позиции 87, 88 и 91), с которыми может быть связана реализация устойчивости к хинолонам/фторхинолонам.

Ключевые слова: *C. amycolatum*, *C. jeikeium*, *C. striatum*, *C. urealyticum*, *C. aurimucosum*, геномы, гены антимикробной устойчивости, *gyrA*, антимикробные (противомикробные) препараты

Вклад авторов: Т. А. Кульшань — планирование исследования, анализ литературы, работа с молекулярно-генетическими данными (подбор геномов, аннотация генома, сравнительный анализ аминокислотной последовательности гена *gyrA*), аналитическая работа с полученными данными, написание публикации; И. О. Бугаева — планирование исследования, аналитическая работа с полученными данными, интерпретирование результатов, участие в написании публикации; Е. Ф. Соболева — анализ литературы, аналитическая работа с полученными данными, написание публикации; М. С. Аллянова — анализ литературы, анализ состава генов антимикробной устойчивости в геномах штаммов коринебактерий, работа с онлайн-сервисом PATRIC; Д. А. Попов — анализ литературы, поиск аминокислотных последовательностей гена *gyrA* в геномах коринебактерий, сравнительный анализ аминокислотных последовательностей; И. Г. Швиденко — консультирование в ходе написания статьи, аналитическая работа с полученными данными.

✉ **Для корреспонденции:** Татьяна Алексеевна Кульшань
ул. Б. Казачья, д. 112, г. Саратов, 410012, Россия; tatjana.kulshan@yandex.ru

Статья получена: 20.10.2023 **Статья принята к печати:** 03.12.2023 **Опубликована онлайн:** 19.12.2023

DOI: 10.24075/vrgmu.2023.047

Today, antimicrobial multidrug resistance of bacterial infectious agents poses a serious threat to global public health. Irrational use of antimicrobials for treatment of humans, in the livestock sector and agriculture is a determinant of widespread resistance to drugs among bacteria [1–3].

Selective pressure of antimicrobials on the bacterial population contributes to realization of various resistance mechanisms emerging due to acquisition of genetic determinants of resistance or spontaneous mutations

[1, 4–6]. Assessment of evolutionary transformation of bacterial genomes associated with antibiotic resistance contributes to optimization of treatment strategies and preventive measures.

Currently, the greater role played by normal flora members, specifically by members of the genus *Corynebacterium*, in infectious diseases can be associated with the spread of genes responsible for antimicrobial resistance across bacterial genomes. The increasingly frequent isolation of *Corynebacterium*

Table 1. *Corynebacterium non diphtheriae* strains, the whole genome nucleotide sequences of which are used in the study

№	Strain	Year, place, isolation source	GenBank ID:
1	<i>Corynebacterium amycolatum</i> BER245	2011, Brazil, human (biomaterial collected from the ear)	CP102778.1
2	<i>Corynebacterium amycolatum</i> ICIS 53	2016, Russia, human (vaginal discharge)	MIFV00000000
3	<i>Corynebacterium amycolatum</i> VH6958	2016, Spain, human	JAFJMB000000000.1
4	<i>Corynebacterium amycolatum</i> ICIS 9	2017, Russia, human (vaginal discharge)	MTPT000000000.1
5	<i>Corynebacterium amycolatum</i> SB-1	2019, South Korea, human (skin)	CP120206.1
6	<i>Corynebacterium amycolatum</i> ICIS 99	2020, Russia, human (vaginal discharge)	JAIUSU000000000
7	<i>Corynebacterium amycolatum</i> 1189	n/a, Germany, n/a	CP069513.1
8	<i>Corynebacterium urealyticum</i> DSM 7109	1985, Germany, human (urine)	AM942444
9	<i>Corynebacterium urealyticum</i> VH3073	2017, Spain, human (urine)	VTFJ000000000
10	<i>Corynebacterium urealyticum</i> 996	n/a, Germany, n/a	CP065982.1
11	<i>Corynebacterium urealyticum</i> 994	n/a, Germany, n/a	CP066064.1
12	<i>Corynebacterium striatum</i> 2308	2011, Brazil, human (blood)	NRIO000000000.1
13	<i>Corynebacterium striatum</i> 708C	2021, UK (synovial fluid)	JASNMG000000000
14	<i>Corynebacterium striatum</i> 824M	2022, UK, blood	JASNMH000000000
15	<i>Corynebacterium striatum</i> 1197	n/a, Germany, n/a	CP069514.1
16	<i>Corynebacterium striatum</i> 1115	n/a, Germany, n/a	CP068158.1
17	<i>Corynebacterium striatum</i> ATCC 6940	n/a, human (urogenital tract)	ACGE000000000
18	<i>Corynebacterium jeikeium</i> K411	2004, Germany, human (axilla region)	CR931997.1
19	<i>Corynebacterium jeikeium</i> 574	2016, USA, human	CP033784.1
20	<i>Corynebacterium jeikeium</i> ATCC 43734	n/a, human (urogenital tract)	ACYW000000000
21	<i>Corynebacterium aurimucosum</i> UMB7769	2013, USA, human (urine)	JASOLN000000000
22	<i>Corynebacterium genitalium</i> ATCC 33030	n/a, USA, human (urogenital tract)	ACLJ000000000

as pathogens, especially in immunocompromised individuals, is indicative of the greater role in the development of infectious complications in patients played by *Corynebacterium* [2].

The following *Corynebacterium* species are of special importance for development of infections: *C. amycolatum* (skin and soft tissue infections, bacteremia, endocarditis, genital infections), *C. urealyticum* (acute and chronic urinary tract infections, urolithiasis), *C. striatum* (true bacteremia, bacterial colonization of prostheses, catheters, breathing tubes, etc.), *C. jeikeium* (bacteremia, endocarditis, pneumonia, skin and soft tissue infections), *C. aurimucosum* (acute and chronic joint infections, diabetic foot ulcer infection), *C. genitalium* (urinary tract infections) [2, 3, 5, 7–14]. Multidrug resistance of some *Corynebacterium* species to β -lactams, macrolides, aminoglycosides, quinolones, tetracyclines and rifampicins, lincosamides, etc., should be noted [1, 4, 12–14].

However, the data on the *Corynebacterium* drug resistance are contradictory, that is why our study was aimed to conduct bioinformatics analysis of the pool of antimicrobial resistance genes in the published genomes of some representatives of the genus *Corynebacterium*.

METHODS

The study involved data on the whole genome nucleotide sequences of 22 strains of six *Corynebacterium* species (*C. amycolatum*, *C. urealyticum*, *C. striatum*, *C. jeikeium*, *C. aurimucosum*, *C. genitalium*) readily available from NCBI GenBank, isolated in different countries over the years (Table 1).

Bioinformatics analysis of whole genome sequences aimed at the search for antibiotic resistance genes in the specified genomes was performed using PATRIC (Pathosystems Resource Integration Center), Comprehensive Antibiotic Resistance Database (CARD), and Database of Antibiotic-Resistant Organisms (NDARO) [15].

Amino acid sequences of *gyrA* gene were acquired from Genbank. The UGENE (Unipro UGENE) 48.1 software package was used for analysis of *gyrA* amino acid sequences [16]. Amino acid sequence alignment was performed using the MUSCLE tool integrated into UGENE.

RESULTS

Bioinformatics analysis showed that the genomes provided comprised various combinations of antimicrobial resistance genes. A total of 25 different genes encoding resistance to drugs exhibiting antimicrobial activity were determined (Table 2).

It should be noted that the following genes were significantly less often found in the genomes of studied isolates (Table 3):

1) *tetO* (*tetW*) (encodes resistance to tetracyclines) — was not found in genomes of 19 strains (86.4%);

2) *aph* (*3'*)-*I*, *aph* (*6*)-*Ic* (encode resistance to aminoglycosides) — were not found in genomes of 14 strains (63.6%);

3) *ermX* (encodes resistance to macrolides, lincosamides, streptogramins) — was not found in genomes of 13 strains (59%);

4) *Isu* (*rplF*) (encodes resistance to fusidic acid) — was not found in genomes of 12 strains (54.5%);

5) *cmx* (encodes resistance to chloramphenicol) — was not found in genomes of eight strains (36.4,3%);

6) *ispC* (*dxr*) (encodes resistance to fosfomycin) — was not found in genomes of seven strains (32%);

7) *gibB* (encodes resistance to aminoglycosides), *oxyR* (encodes resistance to изониазид), *fabG* (encodes resistance to triclosan) — were not found in genome of one strain (4,5%) (*Corynebacterium striatum* 824M, *Corynebacterium striatum* 1197, *Corynebacterium striatum* 708C, respectively).

However, resistance to aminoglycosides, fusidic acid, fosfomycins was encoded by several genes. In this regard, the

Table 2. List of antimicrobial resistance genes found in the genomes of the studied *Corynebacterium non diphtheriae* strains using the PATRIC online resource

Antimicrobial drugs	Genes encoding antimicrobial resistance
Lipopeptides	<i>pgsA</i> , <i>gdpD</i> (<i>ugpQ</i> , <i>glpQ</i>)
Macrolides, penicillins	<i>mtrA</i> , <i>mtrB</i>
Macrolides, lincosamides, streptogramins	<i>ermX</i>
Diaminopyrimidines	<i>folA</i> (<i>dfp</i>)
Tetracyclines, glycolcyclines	<i>s10p</i> (<i>rpsJ</i>)
Tetracyclines	<i>tetO</i> (<i>tetW</i>)
Sulfonamides	<i>folP</i>
Aminoglycosides	<i>s12p</i> (<i>rpsL</i> , <i>rpsJ</i>), <i>gibB</i> , <i>aph(3')-I</i> , <i>aph(6)-Ic</i>
Fusidic acid	<i>ef-G</i> (<i>fusA</i>), <i>lsu</i> (<i>rplF</i>)
Cycloserine	<i>alc</i> , <i>dlr</i>
Isoniazid	<i>oxyR</i>
Fosfomycins	<i>murA</i> , <i>ispC</i> (<i>dxx</i>)
Chloramphenicol	<i>cmx</i>
Mupirocin	<i>ileS</i>
Triclosan	<i>fabG</i>
Bicyclomycin	<i>rho</i>
Elfamycins	<i>ef-Tu</i> (<i>tufA</i>)

lack of one gene in the genome can not indicate the isolate sensitivity to these antimicrobial substances.

All other genes provided in Table 2 were found in 100% of genomes of 22 *Corynebacterium* strains.

C. striatum 2308 was the strain containing 24 identified antimicrobial resistance genes out of 25. Only the *tetO* (*tetW*) gene was not found in its genome. According to the literature, this strain was isolated in 2011 from the blood culture of a man, who was treated at the hospital in Rio de Janeiro. Based on phenotypic characteristics, it showed sensitivity to tetracycline (MIC 1 mg/L), linezolid (MIC 0.25 mg/L) and vancomycin (MIC 0.5 mg/L) only [12]. The data of bioinformatics analysis we have obtained confirm the phenotypic study results [12]: no *tetO* (*tetW*) gene (tetracycline resistance), no genes encoding resistance to oxazolidones (linezolid) and glycopeptides (vancomycin). It is worth noting that no linezolid and vancomycin resistance genes were found in any of the studied strains. However, the authors point out that this strain showed phenotypic resistance to erythromycin (MIC > 256 mg/L) and clindamycin (MIC > 256 mg/L), as well as to gentamicin (aminoglycoside) (MIC 256 mg/L) [12]. Such phenotypic effects may result from the presence of genes *ermX* and *aph(3')-I*, *aph(6)-Ic*.

Corynebacterium amycolatum ICIS 9 extracted from vagina of a healthy woman in 2017 in Russia turned out to be one more strain with the genome showing the lack of gene *ispC* (*dxx*) (fosfomycin resistance) only. However, fosfomycin resistance is also encoded by the *murA* gene, which was found in the genome. The authors of the paper considered *Corynebacterium amycolatum* ICIS 9 as a potential probiotic agent for treatment of vaginal dysbiosis [9–11]. The *Corynebacterium amycolatum* ICIS 9 phenotypic resistance to antimicrobials (amikacin, gentamicin (aminoglycosides), amoxicillin (β -lactams), clarithromycin (macrolide), chloramphenicol, ciprofloxacin (fluoroquinolone) and tetracycline) was determined [9–11]. Indeed, our bioinformatics study showed that the genome of this isolate comprised genes encoding resistance to penicillins, aminoglycosides, macrolides, chloramphenicol, fluoroquinolones, and tetracyclines (Table 2).

As for strains, the genomes of which lack a significant number of antimicrobial resistance genes (6–10 genes), these included the following: *C. amycolatum* ICIS 99, *C. amycolatum*

ICIS 53, *C. amycolatum* SB-1, *C. amycolatum* 1189, *C. striatum* 824M, *C. striatum* 708 (Table 3).

The *C. striatum* 708 strain extracted from synovial fluid of a patient in the UK (BioSample: SAMN34403526) comprised the lowest number of antimicrobial resistance genes (19 genes).

Currently, many causes of antimicrobial resistance of microorganisms are distinguished. This phenomenon results not only from the presence of genetic determinants associated with antimicrobial resistance, but also with various mutations in these genes. It has been found that mutations in the short regions of genes *gyrA* and *gyrB* (quinolone resistance-determining regions (QRDR)) encoding A and B subunits of DNA gyrase result in quinolone/fluoroquinolone resistance [9].

In *Corynebacterium*, quinolone/fluoroquinolone resistance results from spontaneous mutations in the gene encoding gyrase A subunit [12, 13]. It has been found that mutations associated with amino acid changes in positions 87, 88 and 91 increase the minimum inhibitory concentrations (MICs) of quinolones/fluoroquinolones. Thus, amino acid substitutions in position 87, Ser (S) to Arg (R), Phe (F), Val (V), in position 88, Ala (A) to Pro (P), in position 91, Asp (D) to Tyr (Y), Gly (G), Ala (A), increased the ciprofloxacin, levofloxacin and moxifloxacin MICs [12, 13]. In this regard we considered it necessary to conduct a molecular genetic analysis of the gene amino acid sequence in 22 studied strains. *GyrA* of *Corynebacterium glutamicum* ATCC 13032 (GenBank ID: NP599264) was used as a reference when performing comparative analysis and determining the amino acid position number [13].

According to the literature data, the *C. striatum* ATCC 6940, *C. jeikeium* ATCC 43734 and *C. urealyticum* DSM 7109 isolates showed quinolone/fluoroquinolone resistance [13]. The *gyrA* amino acid sequences of these strains were used as controls.

The analysis showed that in the *C. striatum* ATCC 6940, *C. jeikeium* ATCC 43734, *C. amycolatum* 1189, *C. aurimucosum* UMB7769, *C. striatum* 1115, *C. urealyticum* 994, *C. urealyticum* 996, *C. urealyticum* DSM 7109, *C. jeikeium* K411, *C. amycolatum* SB-1, *C. genitalium* ATCC 33030 strains, position 87 was occupied by Ser (S), while position 91 was occupied by Asp (D). According to the literature, such gene structure ensured the strains' sensitivity to quinolones/fluoroquinolones, despite the presence of resistance genes [12, 13].

Table 3. List of antimicrobial resistance genes not found in the genomes of the studied *Corynebacterium non diphtheriae* strains

№	Strain	Antimicrobial resistance genes not found in the genome
1	<i>Corynebacterium amycolatum</i> BER245	<i>ermX, tetO (tetW), ispC (dxr)</i>
2	<i>Corynebacterium amycolatum</i> ICIS 53	<i>ermX, tetO (tetW), aph(3')-I, aph(6)-I, lsu (rplF), ispC (dxr), cmx</i>
3	<i>Corynebacterium amycolatum</i> VH6958	<i>tetO (tetW), lsu (rplF), ispC (dxr)</i>
4	<i>Corynebacterium amycolatum</i> ICIS 9	<i>ispC (dxr)</i>
5	<i>Corynebacterium amycolatum</i> SB-1	<i>ermX, tetO (tetW), aph(3')-I, aph(6)-I, lsu (rplF), ispC (dxr), cmx</i>
6	<i>Corynebacterium amycolatum</i> ICIS 99	<i>ermX, tetO (tetW), aph(3')-I, aph(6)-I, lsu (rplF), ispC (dxr)</i>
7	<i>Corynebacterium amycolatum</i> 1189	<i>ermX, tetO (tetW), aph(3')-I, aph(6)-I, lsu (rplF), ispC (dxr), cmx</i>
8	<i>Corynebacterium urealyticum</i> DSM 7109	<i>ermX, tetO (tetW), aph(3')-I, aph(6)-I</i>
9	<i>Corynebacterium urealyticum</i> VH3073	<i>tetO (tetW), lsu (rplF)</i>
10	<i>Corynebacterium urealyticum</i> 996	<i>ermX, tetO (tetW), lsu (rplF)</i>
11	<i>Corynebacterium urealyticum</i> 994	<i>tetO (tetW), lsu (rplF)</i>
12	<i>Corynebacterium striatum</i> 2308	<i>tetO (tetW)</i>
13	<i>Corynebacterium striatum</i> 708C	<i>mtrA, mtrB, ermX, tetO (tetW), gibB, aph(3')-I, aph(6)-I, lsu (rplF), fabG, cmx</i>
14	<i>Corynebacterium striatum</i> 824M	<i>ermX, tetO (tetW), aph(3')-I, aph(6)-I, lsu (rplF), gibB</i>
15	<i>Corynebacterium striatum</i> 1197	<i>oxyR</i>
16	<i>Corynebacterium striatum</i> 1115	<i>tetO (tetW), aph(3')-I, aph(6)-I, lsu (rplF), cmx</i>
17	<i>Corynebacterium striatum</i> ATCC 6940	<i>ermX, tetO (tetW), aph(3')-I, aph(6)-I</i>
18	<i>Corynebacterium jeikeium</i> K411	<i>ermX, tetO (tetW), aph(3')-I, aph(6)-I</i>
19	<i>Corynebacterium jeikeium</i> 574	<i>tetO (tetW), aph(3')-I, aph(6)-I, lsu (rplF), cmx</i>
20	<i>Corynebacterium jeikeium</i> ATCC 43734	<i>ermX, tetO (tetW), aph(3')-I, aph(6)-I</i>
21	<i>Corynebacterium aurimucosum</i> UMB776	<i>aph(3')-I, aph(6)-I, lsu (rplF), cmx</i>
22	<i>Corynebacterium genitalium</i> ATCC 33030	<i>ermX, tetO (tetW), aph(3')-I, aph(6)-I, cmx</i>

Ser (S) replaced with Arg (R) in position 87 was reported in *C. amycolatum* ICIS 53, *C. amycolatum* ICIS 99. As for *C. amycolatum* VH6958 strain, Ala (A) replaced with Pro (P) in position 88 was reported in addition to Ser (S) replaced with Arg (R) in position 87. It is worth paying attention to the *C. amycolatum* BER245 strain, for which Asp (D) replaced with Tyr (Y) in position 91 was reported along with Ser (S) replaced with Arg (R) in position 87. Such mutations dramatically increased the MICs of quinolones/fluoroquinolones [12, 13].

C. urealyticum VH3073 had two unique substitutions: 87 — Ser (S)/ Val (V) and 91 — Asp (D)/ Tyr (Y). *C. striatum* 2308, *C. striatum* 708C, *C. striatum* 824M had only one amino acid substitution: 87 — Ser (S)/ Val (V). Moreover, strains carrying unique substitutions were identified: 87 — Ser (S)/ Ile (I), 91 — Asp (D)/ Ala (A) — *C. amycolatum* ICIS 9; 87 — Ser (S)/ Ile (I), 91 — Asp (D)/ Gly (G) — *C. jeikeium* 574; 87 — Ser (S)/ Phe (F), 91 — Asp (D)/ Gly (G) — *C. striatum* 1197 (Fig.). The evolutionary significance of these substitutions is to be determined in further studies.

Thus, 11 isolates have position 87 occupied by Ser (S), in 4 strains it is occupied by Val (V), in 4 strains by Arg (R), in 2 strains by Ile (I), in one strain by Phe (F). A total of 21 strains have position 88 occupied by Ala (A), while in one isolate it is occupied by Pro (P). A total of 17 isolates have position 91 occupied by Asp (D), in 2 strains it is occupied by Tyr (Y), in 2 strains by Gly (G), in 1 strain by Ala (A).

To summarize, it is worth noting that double mutations in *gyrA* described in the literature as mutations causing a dramatic increase in MICs of quinolones/fluoroquinolones were found in: *C. amycolatum* VH6958 isolated in 2016 in Spain (BioSample: SAMN18038700) — Ser (S) replaced with (R) in position 87, Ala (A) replaced with Pro (P) in position 88; *C. amycolatum* BER245 isolated in 2011 in Brazil from the patient with otitis — Ser (S) replaced with Arg (R) in position 87, Asp (D) replaced with Tyr (Y) in position 91; *C. urealyticum* VH3073 isolated in 2017 in

Spain from the patient's urine (BioSample: SAMN12621417) — Ser (S)/ Val (V) substitution in position 87, Asp (D)/ Tyr (Y) in position 91.

One mutation was found in two strains (*C. amycolatum* ICIS 53, *C. amycolatum* ICIS 99): Ser (S) replaced with Arg (R).

DISCUSSION

The spread of antimicrobial drug resistance genes by horizontal transfer causes the increase in the number of resistant microorganisms, including opportunistic pathogens. It is worth noting that *Corynebacterium* strains, such as *C. amycolatum* ICIS 53, *C. amycolatum* ICIS 9, *C. amycolatum* ICIS 99 isolates extracted from vaginal discharge of healthy women we have studied, had a large enough pool of antimicrobial resistance genes [9, 11]. In this regard, it is necessary to continuously monitor antimicrobial resistance of bacteria in order to develop effective measures against their growing resistance to antimicrobial drugs. The databases containing information about antibiotic resistance of bacteria will make it possible to compare the results obtained using different methods and estimate the abundance of antimicrobial resistance genes.

Our findings allowed us to single out a core set of antimicrobial resistance genes comprised in the *Corynebacterium* genomes. These data can be used as potential estimates of the use of antimicrobials for treatment of patients. However, molecular genetic testing should be combined with other methods based on phenotypic assessment of sensitivity to drugs, since the data on phenotypic and genotypic resistance are not always correlated.

Antimicrobial resistance can be associated with various mutations. In particular, quinolone/fluoroquinolone resistance is realized mainly through acquisition of point mutations in the sequence of *gyrA* gene encoding DNA gyrase A subunit, while overexpressed efflux pump can also contribute to acquisition

Consensus sequence:

C.glutamicum_ATCC_13032
C.striatum_ATCC_6940
C.jeikeyum_ATCC_43734
C.amycolatum_FDAARGOS_1189
C.aurimucosum_UMB7769
C.striatum_FDAARGOS_1115
C.urealyticum_FDAARGOS_994
C.urealyticum_FDAARGOS_996
C.jeikeyum_K411
C.urealyticum_DSM_7109
C.amycolatum_SB-1
C.genitalium_ATCC_33030
C.amycolatum_ICIS_53
C.amycolatum_ICIS_99
C.amycolatum_VH6958
C.amycolatum_BER245
C.urealyticum_VH3073
C.striatum_2308
C.striatum_708C
C.striatum_824M
C.amycolatum_ICIS_9
C.jeikeyum_FDAARGOS_574
C.striatum_FDAARGOS_1197

	87	88	90	91	92	94	96	98	100					
86	T	A	I	Y	D	T	L	V	R	M	A	Q	P	W
86	S	A	I	Y	D	T	L	V	R	L	A	Q	S	W
86	S	A	I	Y	D	T	L	V	R	L	A	Q	P	W
86	S	A	I	Y	D	T	M	V	R	M	A	Q	P	W
86	S	A	I	Y	D	T	L	V	R	L	A	Q	P	W
86	S	A	I	Y	D	T	L	V	R	L	A	Q	S	W
86	S	A	I	Y	D	T	L	V	R	M	A	Q	P	W
86	S	A	I	Y	D	T	L	V	R	M	A	Q	P	W
86	S	A	I	Y	D	T	L	V	R	L	A	Q	P	W
86	S	A	I	Y	D	T	M	V	R	M	A	Q	P	W
86	S	A	I	Y	D	T	L	V	R	L	A	Q	P	W
86	R	A	I	Y	D	T	M	V	R	M	A	Q	P	W
86	R	A	I	Y	D	T	M	V	R	M	A	Q	P	W
86	R	P	V	Y	D	T	M	V	R	M	A	Q	P	W
86	R	A	I	Y	Y	T	M	V	R	M	A	Q	P	W
86	V	A	I	Y	Y	T	L	V	R	M	A	Q	P	W
86	V	A	I	Y	D	T	L	V	R	L	A	Q	S	W
86	V	A	I	Y	D	T	L	V	R	L	A	Q	S	W
86	V	A	I	Y	D	T	L	V	R	L	A	Q	S	W
86	I	A	I	Y	A	T	M	V	R	M	A	Q	P	W
86	I	A	I	Y	G	T	M	V	R	M	A	Q	P	W
86	F	A	I	Y	G	T	L	V	R	L	A	Q	S	W

Fig. The *gyrA* amino acid sequence of *Corynebacterium non diphtheriae* isolates taken as examples. Positions of point mutations found in the *gyrA* amino acid sequence, which, according to the literature, affect the increase in the quinolone/fluoroquinolone minimum inhibitory concentrations (MICs), are marked with frames

of quinolone resistance [12, 13]. In *C. amycolatum*, alteration in the *GyrA* position 87 ensured resistance to all the tested quinolones/fluoroquinolones [12, 13]. Such substitutions were also observed in the genomes of *C. amycolatum* strains we had assessed. Furthermore, some *Corynebacterium* strains carried several mutations in the *gyrA* amino acid sequence, which increased the MICs of quinolones/fluoroquinolones [12, 13]. Investigation of genetic variability through mutation is important for the study of evolutionary transformation of bacterial genomes and can be used to develop rapid molecular diagnostic tests.

CONCLUSIONS

A growing etiological significance of *Corynebacterium* for infectious diseases, especially as hospital-acquired pathogens among immunocompromised patients having a history of the long-term hospital stay, several courses of antibiotic therapy and treatment with the use of invasive medical devices, determines the need to constantly monitor pathogens. Antimicrobial resistance of bacteria is a major concern: 1) it was found

that there was a large pool of antimicrobial resistance genes (25 genes) forming various combinations in the *Corynebacterium* genomes. The presence of gene was correlated to the isolate capability of being resistant to antimicrobial drugs. This represented an important evolutionary effect of the impact of antibiotics on the population structure of microorganisms. It should be noted that antimicrobial resistance is most often encoded by several genes. Variability of antimicrobial resistance determinants emphasizes the need for continuous monitoring of the *Corynebacterium* resistance profiles; 2) mutations were detected in the *gyrA* amino acid sequences of the studied strains (positions 87, 88, 91), which were considered to be associated with quinolone/fluoroquinolone resistance.

The goal of the study was achieved. The limited data on *Corynebacterium*, including molecular genetic data, hamper comparative analysis. Expansion of the range of strains, including ones represented in various databases, will contribute to better understanding of the genome structure, phenotypic characteristics, while identification of the range of antimicrobial resistance genes will expand the knowledge about the directions of antibiotic therapy.

References

1. Kharseeva GG, Voronina NA, Gasretova TD, Tyukavkina SYu, Sylka OI, Mironov AYu. The sensitivity to antibiotics of *Corynebacterium non diphtheriae* isolated in hospitals of Rostov-on-don and the Rostovskaya oblast. *Russian Clinical Laboratory Diagnostics*. 2017; 62 (8): 502–6. Russian.
2. Fernandez LV, Fortuny AS, Rodriguez EF. *Corynebacterium pyruviciproducens* and *Corynebacterium amycolatum* mastitis in immunocompetent no breastfeeding women. *Revista Argentina de Microbiologia*. 2021; 53 (11): 39–42.
3. Jesus HNR, Rocha DJPG, Ramos RTJ, Silva A, Brenig B, Góes-Neto A, et al. Pan-genomic analysis of *Corynebacterium amycolatum* gives insights into molecular mechanisms underpinning the transition to a pathogenic phenotype. *Front Microbiol*. 2022; 13: 1–11.
4. Kharseeva GG, Voronina NA, Mironov AYu, Kharysova AR. The antibiotics sensitivity of strains of *Corynebacterium non diphtheriae* circulating in Rostov-on-don and Rostov oblast. *Russian Clinical Laboratory Diagnostics*. 2012; 10: 62–4. Russian.
5. Alibi S, Fejani A, Boukadida J, Cano ME, Fernández-Martínez M, Martínez-Martínez L, et al. Occurrence of *Corynebacterium striatum* as an emerging antibiotic-resistant nosocomial pathogen in a Tunisian hospital. *Sci Rep*. 2017; 7: 1–8. PubMed PMID: 28848236.
6. Kharseeva GG, Mangutov EO, But OM, Chepusova AV, Alutina EL. Analysis of the frequency of allocation of *Corynebacteria non diphtheriae* from patients with inflammatory diseases of the respiratory tract. *Russian Clinical Laboratory Diagnostics*. 2019; 64 (7): 430–34. Russian.
7. Sahu V, Pathak MM, Das P, Ravi A. *Corynebacterium jeikeium* as an unusual cause of keratitis: a case report from a tertiary care hospital in Chhattisgarh, India. *Cureus*. 2021; 13 (12): 1–11.
8. Salem N, Salem L, Saber S, Ismail G, Bluth MH. *Corynebacterium urealyticum*: a comprehensive review of an understated organism. *Infection and Drug Resistance*. 2015; 8: 129–45.
9. Gladysheva IV, Chertkov KL, Cherkasov SV, Khlopko YA, Kataev VY, Valyshev AV. Probiotic potential, safety properties, and antifungal activities of *Corynebacterium amycolatum* ICIS 9 and *Corynebacterium amycolatum* ICIS 53 strains. *Probiotics Antimicrob Proteins*. 2023; 15 (3): 588–600. PubMed PMID: 34807410.
10. Gladysheva IV, Cherkasov SV, Khlopko YA, Plotnikov AO. Genome characterization and probiotic potential of *Corynebacterium amycolatum* human vaginal isolates. *Microorganisms*. 2022; 10 (2): 1–17. PubMed PMID: 35208706.
11. Gladysheva IV, Khlopko YA, Cherkasov SV. Draft genome sequence of the vaginal isolate *Corynebacterium amycolatum* ICIS 9. *Genome Announc*. 2017; 5 (37): 1–2. PubMed PMID: 28912325.
12. Ramos JN, Rodrigues IDS, Baio Pa VP, Veras JFC, Ramos RTJ, Pacheco LG, et al. Genome sequence of a multidrug-resistant *Corynebacterium striatum* isolated from bloodstream infection from a nosocomial outbreak in Rio de Janeiro, Brazil. *Mem. Inst. Oswaldo Cruz*. 2018; 113 (9): 1–5.
13. Sierra JM, Martínez-Martínez L, Vázquez F, Giralt E, Vila J. Relationship between mutations in the *gyrA* gene and quinolone resistance in clinical isolates of *Corynebacterium striatum* and *Corynebacterium amycolatum*. *Antimicrob Agents Chemother*. 2005; 49 (5): 1714–19. PubMed PMID: 15855486.
14. Silva-Santana G, Silva CMF, Olivella JGB, Silva IF, Fernandes LMO, Sued-Karam BR. Worldwide survey of *Corynebacterium striatum* increasingly associated with human invasive infections, nosocomial outbreak, and antimicrobial multidrug-resistance, 1976–2020. *Arch Microbiol*. 2021; 203 (5): 1863–80. PubMed PMID: 33625540.
15. PATRIC (Pathosystems Resource Integration Center). Available from: <https://www.patricbrc.org>.
16. UGENE (Unipro UGENE) 48.1. Available from: <https://ugene.net/ru/>.

Литература

1. Харсеева Г. Г., Воронина Н. А., Гасретова Т. Д., Тюкавкина С. Ю., Сылка О. И., Миронов А. Ю. Чувствительность к антибиотикам штаммов *Corynebacterium non diphtheriae*, выделенных в стационарах Ростова-на-Дону и Ростовской области. *Клиническая лабораторная диагностика*. 2017; 62 (8): 502–6.
2. Fernandez LV, Fortuny AS, Rodriguez EF. *Corynebacterium pyruviciproducens* and *Corynebacterium amycolatum* mastitis in immunocompetent no breastfeeding women. *Revista Argentina de Microbiologia*. 2021; 53 (11): 39–42.
3. Jesus HNR, Rocha DJPG, Ramos RTJ, Silva A, Brenig B, Góes-Neto A, et al. Pan-genomic analysis of *Corynebacterium amycolatum* gives insights into molecular mechanisms underpinning the transition to a pathogenic phenotype. *Front Microbiol*. 2022; 13: 1–11.
4. Харсеева Г. Г., Воронина Н. А., Миронов А. Ю., Харисова А. П. Антибиотикочувствительность штаммов *Corynebacterium non diphtheriae*, циркулирующих в Ростове-на-Дону и Ростовской области. *Клиническая лабораторная диагностика*. 2012; 10: 62–4.
5. Alibi S, Fejani A, Boukadida J, Cano ME, Fernández-Martínez M, Martínez-Martínez L, et al. Occurrence of *Corynebacterium striatum* as an emerging antibiotic-resistant nosocomial pathogen in a Tunisian hospital. *Sci Rep*. 2017; 7: 1–8. PubMed PMID: 28848236.
6. Харсеева Г. Г., Мангутков Э. О. Бут О. М., Чепусова А. В., Алутина Э. Л. Анализ частоты выделения недифтерийных коринебактерий от больных с воспалительными заболеваниями респираторного тракта. *Клиническая лабораторная диагностика*. 2019; 64 (7): 430–34.
7. Sahu V, Pathak MM, Das P, Ravi A. *Corynebacterium jeikeium* as an unusual cause of keratitis: a case report from a tertiary care hospital in Chhattisgarh, India. *Cureus*. 2021; 13 (12): 1–11.
8. Salem N, Salem L, Saber S, Ismail G, Bluth MH. *Corynebacterium urealyticum*: a comprehensive review of an understated organism. *Infection and Drug Resistance*. 2015; 8: 129–45.
9. Gladysheva IV, Chertkov KL, Cherkasov SV, Khlopko YA, Kataev VY, Valyshev AV. Probiotic potential, safety properties, and antifungal activities of *Corynebacterium amycolatum* ICIS 9 and *Corynebacterium amycolatum* ICIS 53 strains. *Probiotics Antimicrob Proteins*. 2023; 15 (3): 588–600. PubMed PMID: 34807410.
10. Gladysheva IV, Cherkasov SV, Khlopko YA, Plotnikov AO. Genome characterization and probiotic potential of *Corynebacterium amycolatum* human vaginal isolates. *Microorganisms*. 2022; 10 (2): 1–17. PubMed PMID: 35208706.
11. Gladysheva IV, Khlopko YA, Cherkasov SV. Draft genome sequence of the vaginal isolate *Corynebacterium amycolatum* ICIS 9. *Genome Announc*. 2017; 5 (37): 1–2. PubMed PMID: 28912325.
12. Ramos JN, Rodrigues IDS, Baio Pa VP, Veras JFC, Ramos RTJ, Pacheco LG, et al. Genome sequence of a multidrug-resistant *Corynebacterium striatum* isolated from bloodstream infection from a nosocomial outbreak in Rio de Janeiro, Brazil. *Mem. Inst. Oswaldo Cruz*. 2018; 113 (9): 1–5.
13. Sierra JM, Martínez-Martínez L, Vázquez F, Giralt E, Vila J. Relationship between mutations in the *gyrA* gene and quinolone resistance in clinical isolates of *Corynebacterium striatum* and *Corynebacterium amycolatum*. *Antimicrob Agents Chemother*. 2005; 49 (5): 1714–19. PubMed PMID: 15855486.
14. Silva-Santana G, Silva CMF, Olivella JGB, Silva IF, Fernandes LMO, Sued-Karam BR. Worldwide survey of *Corynebacterium striatum* increasingly associated with human invasive infections, nosocomial outbreak, and antimicrobial multidrug-resistance, 1976–2020. *Arch Microbiol*. 2021; 203 (5): 1863–80. PubMed PMID: 33625540.
15. PATRIC (Pathosystems Resource Integration Center). Available from: <https://www.patricbrc.org>.
16. UGENE (Unipro UGENE) 48.1. Available from: <https://ugene.net/ru/>.

IMPACT OF UNTRANSLATED mRNA SEQUENCES ON IMMUNOGENICITY OF mRNA VACCINES AGAINST *M. TUBERCULOSIS* IN MICE

Shepelkova GS¹✉, Reshetnikov VV^{2,3}, Avdienko VG¹, Sheverev DV², Yermeev VV¹, Ivanov RA²

¹ Central Tuberculosis Research Institute, Moscow, Russia

² Sirius University of Science and Technology, Sochi, Russia

³ Institute of Cytology and Genetics, Siberian Branch of Russian Academy of Sciences, Novosibirsk, Russia

Vaccination is among the most effective measures to reduce tuberculosis morbidity and mortality. In 1974, BCG vaccination was included in the Expanded Program on Immunization. Today, it covers 80% of all children around the globe. Unfortunately, BCG vaccine provides no protection against pulmonary tuberculosis, the most prevalent form of tuberculosis. It is necessary to urgently develop new vaccination strategies to stop large-scale dissemination of infection caused by the multidrug-resistant pathogen. The study was aimed to compare the capabilities of three variants of mRNA vaccines encoding ESAT6 epitopes of stimulating adaptive immune response formation in C57BL/6 mice (ELISpot, delayed hypersensitivity, IgG titers), as well as of protecting I/St mice against *M. tuberculosis* infection. Efficacy of mRNA vaccines comprising different untranslated regions packaged in lipid nanoparticles was compared with that of BCG vaccine. The 5'-TPL-Esat6-3'-Mod vaccine demonstrated the highest efficacy in our experimental model. Thus, the 5'-TPL-Esat6-3'-Mod mRNA vaccine can be considered as a candidate vaccine for further optimization, improving efficacy and subsequent use for prevention of tuberculosis.

Keywords: mRNA vaccine, BCG, adaptive immune response, tuberculosis

Funding: the study was supported by the Ministry of Science and Higher Education of the Russian Federation (agreement № 075-10-2021-113, project ID RF----193021X0001).

Acknowledgements: the authors express their gratitude to staff members of the Sirius University of Science and Technology I. M. Terenin for *in vitro* transcription, O. V. Zaborova for mRNA formulation into lipid nanoparticles.

Author contribution: Shepelkova GS — planning the experiments and experimental procedure (*in vivo* and *ex vivo*), data analysis, manuscript writing; Reshetnikov VV — cloning, mRNA vaccine preparation, manuscript writing; Avdienko VG — experimental procedure (*in vivo* and *ex vivo*), data analysis; Sheverev DV — mRNA vaccine preparation, data analysis; Yermeev VV — study design, data analysis, manuscript writing; Ivanov RA — study design, manuscript writing.

Compliance with ethical standards: the study was approved by the Ethics Committee of the Central Tuberculosis Research Institute (protocol № 3/2 dated 11 May 2023) and conducted in accordance with the Order of the Ministry of Health No. 755 and the Guidelines issued by the Office of Laboratory Animal Welfare (A5502-01).

✉ **Correspondence should be addressed:** Galina S. Shepelkova, Jauzskaja alleja, 2, 107564, Moscow, Russia; g.shepelkova@ctri.ru; Vasily V. Reshetnikov, Olimpiyskiy prospekt, 1, Sochi, 354340, Russia; reshetnikov.vv@talantiuspeh.ru

Received: 17.11.2023 **Accepted:** 19.12.2023 **Published online:** 31.12.2023

DOI: 10.24075/brsmu.2023.054

ВЛИЯНИЕ НЕТРАНСЛИРУЕМЫХ ПОСЛЕДОВАТЕЛЬНОСТЕЙ мРНК НА ИММУНОГЕННОСТЬ мРНК-ВАКЦИН ПРОТИВ *M. TUBERCULOSIS* У МЫШЕЙ

Г. С. Шепелькова¹✉, В. В. Решетников^{2,3}, В. Г. Авдиенко¹, Д. В. Шевырев², В. В. Еремеев¹, Р. А. Иванов²

¹ Центральный научно-исследовательский институт туберкулеза, Москва, Россия

² Автономная некоммерческая образовательная организация высшего образования «Научно-технологический университет «Сириус», Сириус, Россия

³ Институт цитологии и генетики Сибирского отделения Российской академии наук, Новосибирск, Россия

Вакцинация является одним из наиболее успешных медицинских мероприятий по снижению заболеваемости и смертности от туберкулеза. В 1974 г. вакцинация БЦЖ была включена в Расширенную программу вакцинации, и на сегодня охватывает 80% всех детей на земном шаре. К сожалению, вакцина БЦЖ не защищает от наиболее распространенной формы туберкулеза — туберкулеза легких. Требуется срочно разработать новые стратегии вакцинации, чтобы остановить широкомасштабное распространение инфекции с множественной лекарственной устойчивостью возбудителя. Целью исследования было сравнить способность трех вариантов мРНК-вакцин, кодирующих эпитопы ESAT6, стимулировать формирование адаптивного иммунитета у мышей C57BL/6 (ELISpot, ГЗТ, титры IgG), а также защищать мышей I/St от заражения *M. tuberculosis*. Эффективность упакованных в наноллипидные частицы мРНК-вакцин, различающихся последовательностями нетранслируемых регионов, сравнивали с эффективностью БЦЖ. В полученной нами экспериментальной модели максимальную эффективность по большинству показателей продемонстрировала вакцина 5'-TPL-Esat6-3'-Mod. Таким образом, мРНК-вакцина 5'-TPL-Esat6-3'-Mod может быть рассмотрена в качестве кандидатной для дальнейшей оптимизации, повышения ее эффективности и последующего применения для профилактики туберкулеза.

Ключевые слова: мРНК-вакцины, БЦЖ, адаптивный иммунный ответ, туберкулез

Финансирование: исследование выполнено при поддержке Министерства науки и высшего образования Российской Федерации (соглашение № 075-10-2021-113, уникальный идентификатор проекта РФ----193021X0001).

Благодарности: авторы выражают благодарность сотрудникам АНО ВО «Университет «Сириус» И. М. Теренину за постановку транскрипции *in vitro*, О. В. Заборовой за формулировку мРНК в липидные наночастицы.

Вклад авторов: Г. С. Шепелькова — планирование и постановка экспериментов (*in vivo* и *ex vivo*), анализ результатов, написание рукописи; В. В. Решетников — клонирование, подготовка мРНК вакцины, написание рукописи; В. Г. Авдиенко — постановка экспериментов (*in vivo* и *ex vivo*), анализ результатов; Д. В. Шевырев — подготовка мРНК вакцины, анализ результатов; В. В. Еремеев — дизайн исследования, анализ результатов, написание рукописи; Р. А. Иванов — дизайн исследования, написание рукописи.

Соблюдение этических стандартов: исследование одобрено этическим комитетом ФГБНУ «ЦНИИТ» (протокол № 3/2 от 11 мая 2023 г.), проведено в соответствии с Приказом Минздрава № 755 и Руководством Управления по охране лабораторных животных А5502-01.

✉ **Для корреспонденции:** Галина Сергеевна Шепелькова, Яузская аллея, д. 2, 107564, г. Москва, Россия; g.shepelkova@ctri.ru; Василий Владимирович Решетников, Олимпийский пр-т, д. 1, г. Сочи, 354340; Россия; reshetnikov.vv@talantiuspeh.ru

Статья получена: 17.11.2023 **Статья принята к печати:** 19.12.2023 **Опубликована онлайн:** 31.12.2023

DOI: 10.24075/vrgmu.2023.054

About 10 million cases of active tuberculosis (TB) and about 1.5 million TB deaths are revealed annually all over the world [1]. The search for new TB vaccine frustrated many generations of enthusiastic researchers. Numerous painstaking attempts to understand the fundamental mechanisms underlying protective immunity in mycobacterial infection resulting only in understanding its complexity and not allowing to determine reliable immunological correlates of protection and form the basis for rational selection of promising vaccines. It is clear that unique features of effective immune response to the appropriate pathogen should be considered when developing the new generation vaccines [2]. The requirements for such vaccines should include: 1) induction of the “correct” ratio of T cell subpopulations and cytokine spectrum associated with the response to infection in combination with induction of protective and long-term (immunological memory) immunity; 2) activation of the “correct” effector mechanisms aimed at prevention of infection or elimination of the infectious agent; 3) high specificity for the infectious agent allowing to avoid the risk of autoaggression on account of cross-reacting antigens; 4) the use of bacterial antigens expressed in the host by all isolates and strains; 5) immunogenicity for all major histocompatibility complex (MHC) haplotypes in the human population.

The aspects most important for development of new effective TB vaccine are as follows: a) selection and combination of antigens, selection of the antigen physical and chemical properties (intracellular, surface-associated or secreted proteins, glycolipids, phospholipids); b) vaccine type (whole proteins or peptides, whole live attenuated or heat-killed bacteria, recombinant bacteria, DNA vaccines); c) vaccine form and administration route (high/low doses, adjuvants, immunomodulatory cytokines, immunostimulant DNA sequences).

The use of mRNA-based vaccines is a relatively new direction of vaccinology [3, 4]. The first experimental mRNA vaccines were developed in early 1990s. It has been shown that these induce both humoral and cell-based immunity *in vivo* [5, 6]. However, the first carriers used for transfer of mRNA molecules had poor safety profiles, while the per se use of mRNA led to the nucleic acid recognition by the immune system and degradation by RNAses [6]. These problems were partially overcome by using modified nucleosides in the mRNA molecule (replacement of uridine with pseudouridine or other analogues) making it possible to avoid induction of interferon-mediated antiviral pathways resulting in disruption of mRNA molecules [7]. At the same time, the toll-like receptor mediated activation of the innate immunity mechanisms by mRNA molecules can improve vaccination efficacy [8]. The development of carriers in the form of lipid nanoparticles (containing PEGylated lipids, cholesterol, ionizable lipids, and phospholipids) with improved safety profile increased the effectiveness of mRNA delivery. In general, these advances resulted in the growth and a constant interest in the use of mRNA vaccines for prevention of various infectious diseases, mostly viral. However, the experience of using mRNA vaccines for infectious diseases caused by bacteria is extremely limited.

Nevertheless, not all mRNA-based agents show high efficacy. Low RNA stability in the cell results in premature RNA degradation, low translation efficacy, decreased levels and expression duration of the target protein [9]. One of the key roles in ensuring stability of mRNA molecules and effectiveness of their translation is played by regulatory sequences of untranslated regions (5'-UTR and 3'-UTR). It should be noted that, despite extensive studies of the UTR properties, the number of studies focused on assessing the contribution of distinct UTRs to

translation of heterologous RNA is limited [10, 11]. The study was aimed to assess immunogenicity and protective effects of the TB mRNA vaccines comprising various combinations of 5'-UTR and 3'-UTR sequences in the experimental murine model.

METHODS

Experimental design

The experiment involved 65 female C57BL/6Cit (B6) mice and 65 female I/StSnEgYCit (I/St) mice (body weight 20–25 g, age 2–4 months) taken from the Central Tuberculosis Research Institute breeding nursery. The animals were kept in a conventional vivarium with the fixed 12.00 : 12.00 h light/dark cycle and *ad libitum* access to water and food. B6 mice were intramuscularly immunized twice at a 3-week interval using three different mRNA vaccine variants: mRNA 5'-TPL-Esat6-3'Mod, 5'-Rabb-Esat6-3'EMCV and 5'-Mod-Esat6-3'Mod, 50 µg of RNA per injection (Fig. 1). Control animals were administered phosphate-buffered saline (PBS). BCG vaccination (BCG Pasteur) was performed once by subcutaneous injection with 100,000 CFU/mouse five weeks before tissue harvesting (B6)/infection (I/St).

Eight animals from each group of B6 mice were used to assess delayed hypersensitivity. The remaining mice (five per group) were used to estimate T cell response (ELISpot) and titers of IgG and IgM against *M. tuberculosis* antigens. In I/St mice (five per group), mycobacterial load in the spleen and lung was determined 50 days after infection, along with the dynamic changes in mouse death rate after infection.

Cloning

To obtain constructs for further *in vitro* RNA transcription, a cassette comprising 5'-UTR, 3'-UTR and the earlier reported sequence encoding various ESAT6 protein epitopes [12] was inserted in the pSmart commercially available vector (Lucigen; USA). The 5'-UTR sequence of vaccine against SARS-CoV2 (Moderna; USA), sequence of the late adenoviral tripartite leader (TPL) or Rabb rabbit β-globin (Appendix 1) were used as 5'-UTR. The 3'-UTR sequence of vaccine against SARS-CoV2 (Moderna; USA) or 3'-UTR sequence of the encephalomyocarditis virus (EMCV) was used as 3'-UTR. Fragments were linked together by PCR involving overlapping primers. The EcoRI and BglII restriction sites were introduced into the 5'-UTR-Esat6-3'-UTR construct that were used for cloning into the pSmart vector. The NEB-stable strain was used for culturing (New England Biolabs; UK).

In vitro mRNA transcription

In vitro transcription was performed as described earlier [12]. RNA was precipitated by adding LiCl to the concentration of 0.32 M and EDTA (pH 8.0) to the concentration of 20 mM with subsequent incubation on ice for an hour. Then the solution was centrifuged for 15 min (25,000 g, 4 °C). The RNA precipitate was washed with 70% ethanol, dissolved in ultrapure water and then precipitated again with alcohol in accordance with the standard procedure. RNA concentration was determined by spectrophotometry based on absorption at 260 nm.

Formulation of mRNA into lipid nanoparticles

Formulation of mRNA into lipid nanoparticles was performed in the NanoAssemblr™ Benchtop system (Precision Nanosystems;

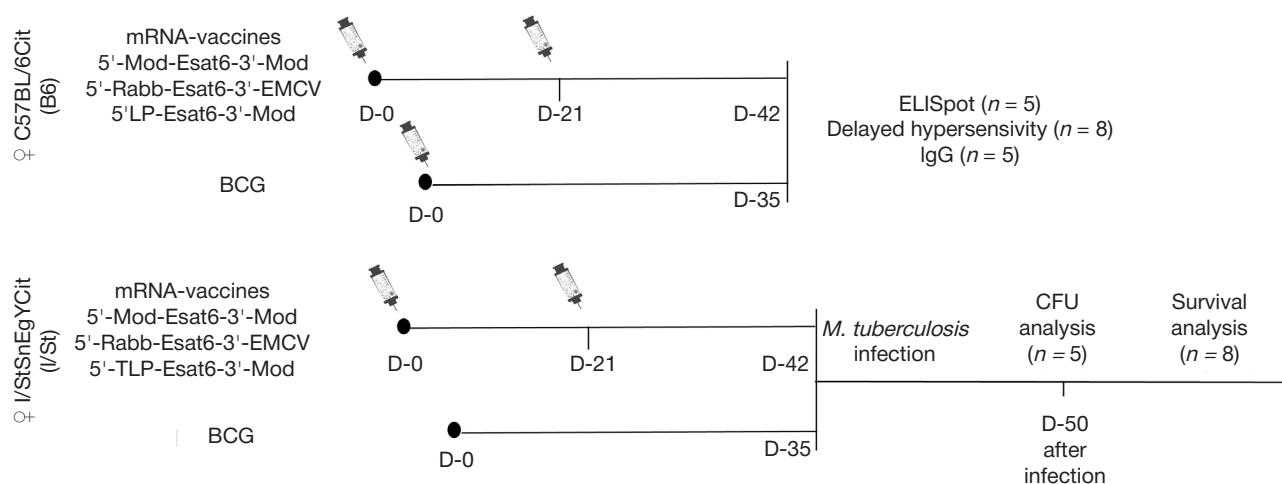


Fig. 1. Experimental design

USA) as described earlier [13]. The lipid mixture components were as follows: ionizable lipidoid ALC-0315 (BroadPharm; USA), distearoylphosphatidylcholine (DSPC) (Avanti Polar Lipids; USA), cholesterol (Sigma-Aldrich; USA), DMG-PEG-2000 (BroadPharm; USA); the molar ratio (%) was 46.3 : 9.4 : 42.7 : 1.6.

The concentration of mRNA loaded onto lipid nanoparticles was determined based on the difference in the fluorescent signal levels upon RiboGreen (Thermo Fischer Scientific; USA) staining of suspended particles before and after their destruction. The Triton X-100 detergent (Sigma-Aldrich; USA) was used to destroy the particles. The amount of encapsulated RNA in the particles in all samples constituted more than 95% of the total amount of RNA (encapsulated + free). Particle size was 80–90 nm, and polydispersity index was below 0.15.

Delayed hypersensitivity reaction measurement

Delayed hypersensitivity reaction in mice of each group (eight mice per group) was assessed four weeks after vaccination based on the left hind paw swelling in response to administration of 40 μ L of PBS containing 50 IU of tuberculin purified protein derivative (SCEEMP; Russia) 48 h after injection. The data were presented as Δ (difference in thickness of the left and right paws in mm).

Antigens

The H37Rv *M. tuberculosis* sonicate, the soluble fraction of *M. tuberculosis* H37Rv disrupted by ultrasound, was used as antigen in *ex vivo* experiments [14].

Determination of titers of IgG and IgM against *M. tuberculosis* antigens

Murine blood serum was used to determine titers of specific antibodies (IgG and IgM) against mycobacterial antigens by enzyme immunoassay routinely used in laboratory settings [15, 16]. Serum dilutions between 1 : 50 and 1 : 400 were used for antibody determination.

Quantification of IFN γ -producing cells

Protective T cell immune response was estimated based on the counts of splenocytes secreting IFN γ in response to stimulation with mycobacterial antigens using the Mouse IFN γ ELISpot Set (BD NJ; USA) and AEC Substrate Set (BD NJ; USA) in accordance with the manufacturer's instructions.

Evaluation of protective response

The I/St mice were immunized twice (42 and 21 days before infection) with mRNA-based vaccines. BCG immunization was performed 35 days before infection. Mice were infected with the *M. tuberculosis* virulent strain in a dose of 500,000 CFU/mouse. Mycobacteria were quantified in the internal organs of infected mice on day 50 after infection. For that lungs and spleens of infected animals were isolated in the sterile environment and homogenized in 2 mL of saline. Then 10-fold serial dilutions of organ homogenates were prepared and sown on Petri dishes with Middlebrook 7H10 agar, 50 μ L per dish. The Petri dishes with applied suspensions were incubated at 37 $^{\circ}$ C. Then, 21 days later the *M. tuberculosis* H37Rv macrocolonies were enumerated in the dish and their number was recalculated with reference to the organ.

Statistical analysis

Statistical processing of the results was performed using the Student's t-test; Bonferroni correction was applied when comparing more than two groups. The differences were considered significant at $p < 0.05$. The data provided in figures are presented as means \pm SEM. The Gehan–Breslow–Wilcoxon method was used for survival curves.

RESULTS

Immunogenicity of the tested vaccines was assessed based on their ability to induce specific cellular immune response *ex vivo* (ELISpot) and *in vivo* (delayed hypersensitivity), as well as on the specific antibody response in blood of vaccinated mice (Fig. 2). Fig. 2A presents the results of IFN γ -producing cell quantification in the spleens of experimental animals. Significant differences from controls were obtained for the 5'-Mod-Esat6-3'-Mod and 5'-TLP-Esat6-3'-Mod mRNA vaccines ($p < 0.004$ and $p < 0.0008$, respectively). Among groups of animals immunized with mRNA vaccines, the group that received 5'-TLP-Esat6-3'-Mod was the leader based on the IFN γ -producing cell counts ($p < 0.004$ and $p < 0.0004$ vs. 5'-Mod-Esat6-3'-Mod, 5'-Rabb-Esat6-3'-EMCV mRNA vaccines, respectively). At the same time, the highest IFN γ -producing cell counts were found in the group of BCG-vaccinated mice ($p < 0.006$, $p < 0.006$ and $p < 0.03$ vs. 5'-Mod-Esat6-3'-Mod, 5'-Rabb-Esat6-3'-EMCV and 5'-TLP-Esat6-3'-Mod mRNA vaccines, respectively).

The delayed hypersensitivity reaction of mice immunized with the 5'-Rabb-Esat6-3'-EMCV and 5'-TLP-Esat6-3'-Mod

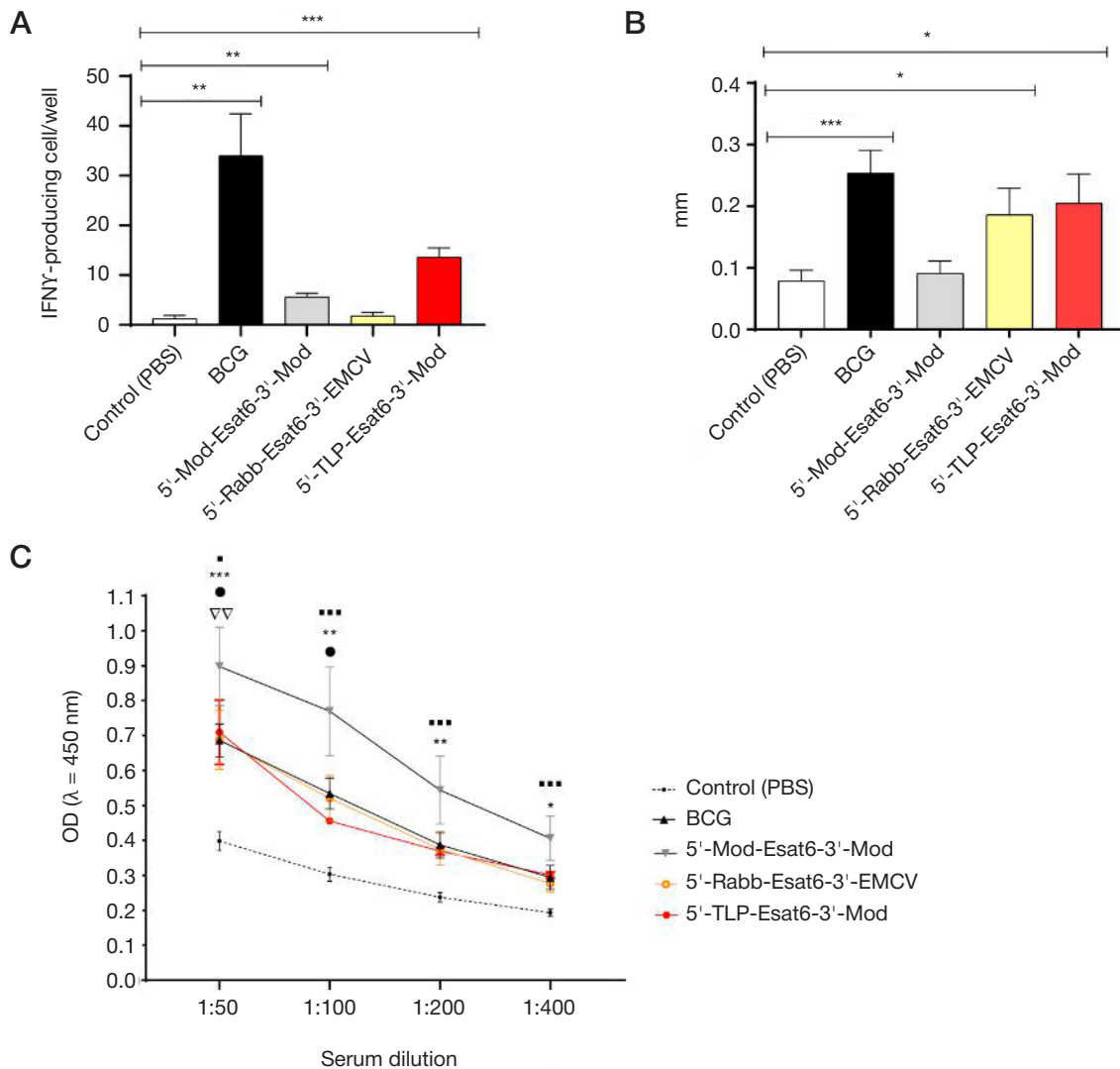


Fig. 2. Adaptive immune response induction by mRNA vaccines. B6 mice were immunized twice (42 and 21 days before the experiment) with mRNA vaccines. BCG immunization was performed 35 days before the experiment. On the day of experiment, IFN γ -producing cell counts were determined in responders to mycobacterial antigens (A), as well as the delayed hypersensitivity reaction (B) and production of specific antibodies against mycobacterial antigens (C). Means \pm SEM are presented, where n — five mice per group for A and C, eight mice per group for B. A, B. * — $p < 0.05$; ** — $p < 0.01$; *** — $p < 0.001$ compared to control. C. * — significant difference from control for BCG, Δ — significant difference from control for 5'-Mod-Esat6-3'-Mod vaccine, \bullet — significant difference from control for 5'-Rabb-Esat6-3'-EMCV vaccine, \blacksquare — significant difference from control for 5'-TLP-Esat6-3'-Mod vaccine

mRNA vaccines was significantly different from that of controls ($p < 0.04$ for these groups) and similar to the delayed hypersensitivity reaction of BCG-vaccinated mice (Fig. 2B). There were no significant differences between the 5'-Rabb-Esat6-3'-EMCV, 5'-TLP-Esat6-3'-Mod and BCG groups.

The studies focused on assessing the development of humoral immune response to the TB mRNA vaccines also showed differences from controls. The results of determining (titration curves) the antigen-specific antibodies (IgG) are presented in Fig. 2C. All the tested vaccines, including BCG, stimulated production of anti-mycobacterial IgG in immunized mice. Furthermore, among mRNA vaccines, the maximum production of antigen-specific IgG was reported in response to immunization with 5'-Rabb-Esat6-3'-EMCV and 5'-TLP-Esat6-3'-Mod (compared to controls). There were no significant differences between the 5'-Rabb-Esat6-3'-EMCV, 5'-TLP-Esat6-3'-Mod and BCG groups. The levels of antigen-specific IgM production in vaccinated mice were similar to that of controls (Appendix 2). Thus, our findings have shown that the Esat6 epitope-based mRNA vaccines cause the adaptive immune response induction. Despite the fact that all mRNA vaccine variants were less effective than BCG, we observed

significant differences in their efficacy depending on the UTR sequences. The best results of testing the vaccine for both cellular and humoral immune response were obtained for the 5'-TLP-Esat6-3'-Mod mRNA vaccine.

The development of protective immune response was studied in the I/St mice susceptible to TB infection. Fig. 3 presents the results of determining mycobacterial load in infected animals, as well as the dynamic changes in death rate of immunized animals after infection. A significant decrease in the lung tissue mycobacterial counts compared to unvaccinated controls was revealed in mice immunized with the 5'-Rabb-Esat6-3'-EMCV, 5'-TLP-Esat6-3'-Mod mRNA vaccines and BCG (Fig. 3B). Furthermore mycobacterial load in the lung tissue of the groups of mice vaccinated with the 5'-TLP-Esat6-3'-Mod mRNA vaccine and BCG showed no significant differences. As for the spleen, significant differences from non-immunized controls were reported for BCG-vaccinated mice only (Fig. 3A).

The animals' extended lifespan after infection is among major criteria of the vaccine protective effect. That is why we compared the dynamic changes in death rate in the control and experimental groups of mice after infection. Significant

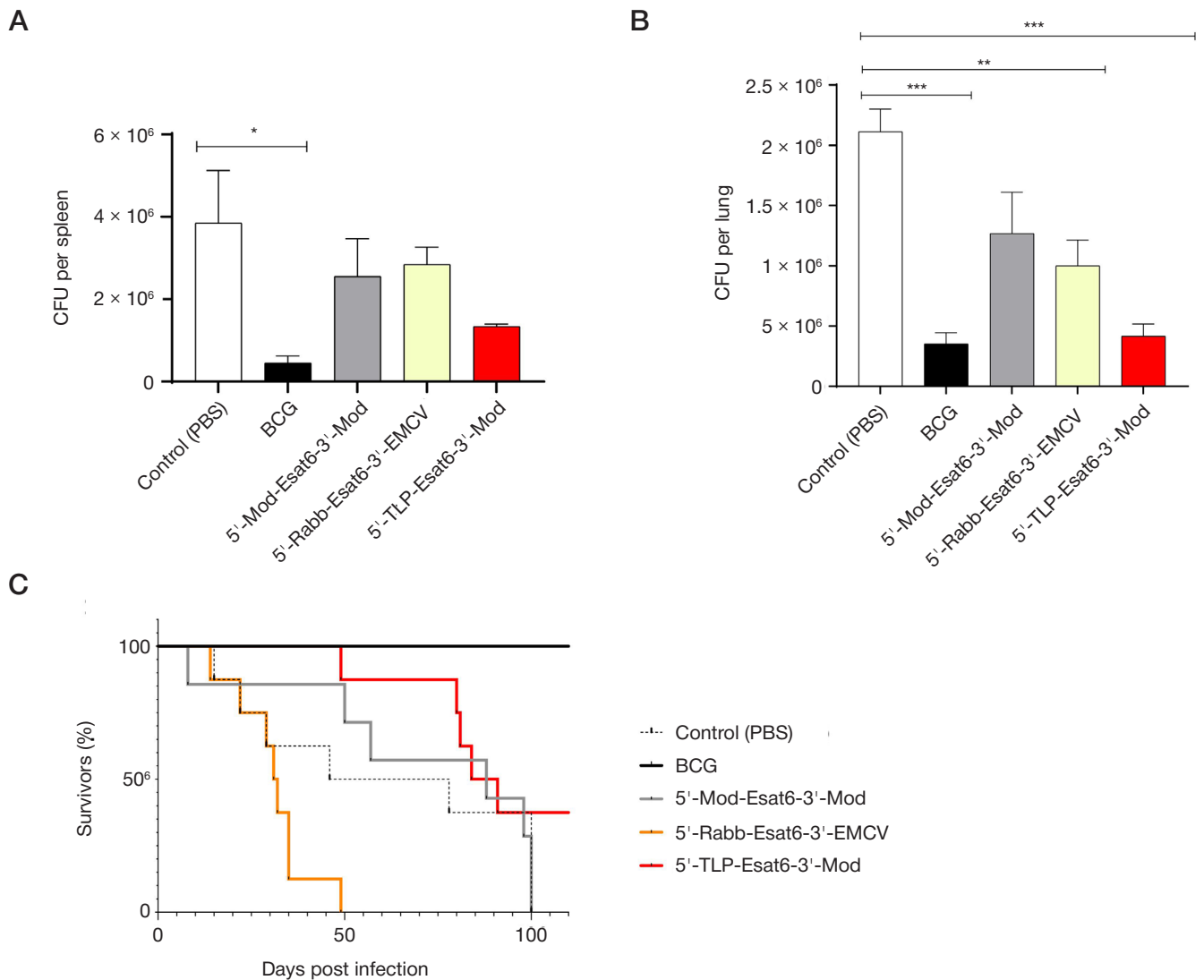


Fig. 3. Protective immune response associated with immunization with mRNA vaccines. I/St mice were immunized twice (42 and 21 days before the experiment) with mRNA vaccines. BCG immunization was performed 35 days before the experiment. Mice were infected with the *M. tuberculosis* virulent strain in a dose of 500,000 CFU/mouse. Mycobacterial load in the spleen (A) and the lungs (B) of infected animals was assessed 50 days later, along with the dynamic changes in the mouse death rate after infection (C). Means \pm SEM are presented, where $n =$ five (A, B) and eight (C) mice per group; * — $p < 0.05$; ** — $p < 0.01$; *** — $p < 0.001$

differences from unvaccinated controls (Gehan–Breslow–Wilcoxon method for survival curves) were reported for BCG-immunized mice and mice immunized with the 5'-TLP-Esat6-3'-Mod mRNA vaccine ($p = 0.0005$ and $p = 0.04$, respectively). Significant differences in the death rate of I/St mice vaccinated with BCG and 5'-TLP-Esat6-3'-Mod mRNA vaccine were also revealed ($p = 0.01$) (Fig. 3C). Similar to the adaptive immune response induction results, the 5'-TLP-Esat6-3'-Mod mRNA vaccine showed the highest efficacy among mRNA vaccines; it was the only vaccine that ensured reduced mortality relative to unvaccinated animals.

DISCUSSION

In this study involving the murine model of TB infection we have shown that administration of two doses of mRNA vaccines consisting of mRNA encoding some ESAT6 mycobacterial protein epitopes encapsulated in lipid particles yields protective immune response, the efficacy of which depends, inter alia, on the mRNA untranslated sequences comprised in the vaccine. Furthermore, stimulation of humoral immune response by various vaccine variants determined based on production of specific antibodies after vaccination is significantly different

from activation of cell-based immunity assessed based on the delayed hypersensitivity reaction intensity and IFN γ production (based on ELISpot).

Historically, the studies of immune response to infection caused by *M. tuberculosis* were focused mainly on T cells and macrophages, since their role in granuloma formation was rather well understood. In contrast, the role of B cells in the TB infection pathogenesis was relatively understudied. Therefore, the majority of newly developed TB vaccines were focused on the cellular immune response induction [2]. However, a number of recent studies of TB vaccine efficacy in mice, nonhuman primates and humans revealed minor induction of antibodies against *M. tuberculosis*, which could be associated with the observed vaccine efficacy [17]. In our study, among all mRNA vaccines, maximum protection (based on the lung-derived mycobacterial culture and survival of infected mice) was achieved by using the 5'-TLP-Esat6-3'-Mod mRNA vaccine. Immunization with the 5'-TLP-Esat6-3'-Mod mRNA vaccine results in formation of pronounced cellular immune response and moderate production of specific anti-mycobacterial IgG. At the same time, immunization of mice with the 5'-Mod-Esat6-3'-Mod mRNA vaccine stimulates active production of specific antibodies, but it is not associated with generation of protection

and does not activate the adaptive immune response cellular component.

We assume that the differences between three mRNA vaccines differing only by untranslated sequences can be associated with the mRNA translation duration and intensity and, therefore, with different antigen presentation effectiveness. The adenovirus tripartite leader (TPL) sequence acts as an enhancer of the viral late gene mRNA translation and is believed to be capable of initiating cap-independent translation of the adenovirus late mRNA [18, 19]. The 5'-UTR TPL consists of 245 nucleotides and has a complex secondary structure. It has been shown that TPL comprises IRES, through which it can recruit the ribosome regardless of interactions with cap [18, 19]. However, since cap-independent translation initiation is activated only under conditions of cellular stress, we assume that our data on TRL are not related to the cap-independent translation initiation. In addition to longer length, the TPL sequence has a higher GC content and a very negative minimum Gibbs free energy (ΔG), which is due to translation inhibition [20]. In contrast, 5'-UTR of rabbit β -globin (Rabb) and 5'-UTR of the mRNA-1273 vaccine (Moderna) have the length of about 50 nucleotides and comprise no strong secondary structures [21]. Apparently, the secondary structures emerging in the 5'-UTR without any RNA-binding protein involvement

have no pronounced inhibitory effect on translation, since these structures can be uncoiled by the eIF4A factor immediately before the translation initiation [22]. At the same time, the TPL strong secondary structure can contribute to engaging RNA-binding proteins positively affecting translation.

Thus, the 5'-TPL-Esat6-3'-Mod mRNA vaccine seems to be the most promising for further research. Despite the fact that it is inferior to BCG, further optimization, including increasing the dose of vaccine, cap or using the uridine analogues, can improve its efficacy. Assessment of prospects of using the 5'-TPL-Esat6-3'-Mod mRNA vaccine for revaccination after primary BCG vaccination can constitute the next phase of vaccine testing.

CONCLUSIONS

The mRNA-based multi-epitope vaccines can be considered as independent preventive vaccines or booster vaccines against *M. tuberculosis*. Despite the fact that the studied vaccine variants have lower efficacy compared to BCG, the relationship between the efficacy and the sequence of regulatory regions has been revealed. Our findings have made it possible to determine the optimal combination of the expression cassette regulatory elements. Further development of mRNA vaccine against *M. tuberculosis* will be focused on improving its efficacy.

References

1. Global tuberculosis report, 2023.
2. Lai R, Ogunsola AF, Rakib T, Behar SM. Key advances in vaccine development for tuberculosis-success and challenges. NPJ vaccines. 2023; 8: 158. DOI: 10.1038/s41541-023-00750-7.
3. Self WH, Tenforde MW, Rhoads JP, Gaglani M, Ginde AA, Douin DJ, et al. Comparative Effectiveness of Moderna, Pfizer-BioNTech, and Janssen (Johnson & Johnson) Vaccines in Preventing COVID-19 Hospitalizations Among Adults Without Immunocompromising Conditions — United States, March–August 2021. MMWR. Morbidity and mortality weekly report. 2021; 70: 1337–43. DOI: 10.15585/mmwr.mm7038e1.
4. Melo A, de Macedo LS, Invencao M, de Moura IA, da Gama M, de Melo CML, et al. Third-generation vaccines: features of nucleic acid vaccines and strategies to improve their efficiency. Genes. 2022; 13. DOI:10.3390/genes13122287.
5. Martinon F, Krishnan S, Lenzen G, Magne R, Gomard E, Guillet JG, et al. Induction of virus-specific cytotoxic T lymphocytes in vivo by liposome-entrapped mRNA. European journal of immunology. 1993; 23: 1719–22. DOI: 10.1002/eji.1830230749.
6. Conry RM, LoBuglio AF, Wright M, Sumerel L, Pike MJ, Johanning F, et al. Characterization of a messenger RNA polynucleotide vaccine vector. Cancer research. 1995; 55: 1397–400.
7. Anderson BR, Muramatsu H, Jha BK, Silverman RH, Weissman D, Kariko K. Nucleoside modifications in RNA limit activation of 2'-5'-oligoadenylate synthetase and increase resistance to cleavage by RNase L. Nucleic acids research. 2011; 39: 9329–38. DOI: 10.1093/nar/gkr586.
8. Muslimov A, Tereshchenko V, Shevryev D, Rogova A, Lepik K, Reshetnikov V, et al. The dual role of the innate immune system in the effectiveness of mRNA therapeutics. International journal of molecular sciences. 2023; 24. DOI: 10.3390/ijms241914820.
9. Weng Y, Li C, Yang T, Hu B, Zhang M, Guo S, et al. The challenge and prospect of mRNA therapeutics landscape. Biotechnology advances. 2020; 40: 107534. DOI: 10.1016/j.biotechadv.2020.107534.
10. Orlandini von Niessen AG, Poleganov MA, Rechner C, Plaschke A, Kranz LM, Fesser S, et al. Improving mRNA-based therapeutic gene delivery by expression-augmenting 3' UTRs identified by cellular library screening. Molecular therapy: the journal of the American Society of Gene Therapy. 2019; 27: 824–36. DOI: 10.1016/j.ymthe.2018.12.011.
11. Cao J, Novoa EM, Zhang Z, Chen WCW, Liu D, Choi GCG, et al. High-throughput 5' UTR engineering for enhanced protein production in non-viral gene therapies. Nature communications. 2021; 12: 4138. DOI: 10.1038/s41467-021-24436-7.
12. Vasileva O, Tereshchenko TV, Krapivin B, Muslimov A, Kukushkin I, Pateev I, et al. Immunogenicity of full-length and multi-epitope mRNA vaccines for *M. Tuberculosis* as demonstrated by the intensity of T-cell response: a comparative study in mice. Bulletin of RSMU. 2023; 03: 42–48. DOI: 10.24075/brsmu.2023.021.
13. Kirshina AS, Kazakova AA, Kolosova ES, Imasheva EA, Vasileva OO, Zaborova OV, et al. Effects of various mRNA-LNP vaccine doses on neuroinflammation in BALB/c mice. Bulletin of RSMU. 2022; 6. DOI: 10.24075/brsmu.2022.068.
14. Avdienko VG, Babaian SS, Guseva AN, Kondratiuk NA, Rusakova LI, Averbakh MM, et al. Quantitative, spectral, and serodiagnostic characteristics of antimycobacterial IgG, IgM, and IgA antibodies in patients with pulmonary tuberculosis. Problemy tuberkuleza i boleznei legkikh. 2006; 47–55.
15. Nikonenko BV, Apt AS, Mezhlumova MB, Avdienko VG, Yermeev VV, Moroz AM. Influence of the mouse Bcg, Tbc-1 and xid genes on resistance and immune responses to tuberculosis infection and efficacy of bacille Calmette-Guerin (BCG) vaccination. Clinical and experimental immunology. 1996; 104: 37–43. DOI: 10.1046/j.1365-2249.1996.d01-643.x.
16. Kozlova IV, Avdienko VG, Babayan SS, Andrievskaya IYu, Gergert VY. Diagnosis of Bactec samples by immunoglobulins of mouse hyperimmune sera obtained against modified antigens of the cell wall of *Mycobacterium tuberculosis*. Tuberculosis and Lung Diseases. 2019; 97: 25–30.
17. Rijnik WF, Ottenhoff THM, Joosten SA. B-Cells and Antibodies as Contributors to Effector Immune Responses in Tuberculosis. Frontiers in immunology. 2021; 12: 640168. DOI: 10.3389/fimmu.2021.640168.
18. Logan J, Shenk T. Adenovirus tripartite leader sequence enhances translation of mRNAs late after infection. Proceedings of the National Academy of Sciences of the United States of America. 1984; 81: 3655–9. DOI: 10.1073/pnas.81.12.3655.
19. Kaufman RJ. Identification of the components necessary for adenovirus translational control and their utilization in cDNA expression vectors.

- Proceedings of the National Academy of Sciences of the United States of America. 1985; 82: 689–93. DOI: 10.1073/pnas.82.3.689.
20. Sample PJ, Wang B, Reid DW, Presnyak V, McFadyen IJ, Morris DR, et al. Human 5' UTR design and variant effect prediction from a massively parallel translation assay. *Nature biotechnology*. 2019; 37: 803–9. DOI: 10.1038/s41587-019-0164-5.
 21. Kozak M. Features in the 5' non-coding sequences of rabbit alpha and beta-globin mRNAs that affect translational efficiency. *Journal of molecular biology*. 1994; 235: 95–110. DOI: 10.1016/s0022-2836(05)80019-1.
 22. Kumari S, Bugaut A, Huppert JL, Balasubramanian S. An RNA G-quadruplex in the 5' UTR of the NRAS proto-oncogene modulates translation. *Nature chemical biology*. 2007; 3: 218–21. DOI: 10.1038/nchembio864.

Литература

1. Global tuberculosis report, 2023.
2. Lai R, Ogunisola AF, Rakib T, Behar SM. Key advances in vaccine development for tuberculosis-success and challenges. *NPJ vaccines*. 2023; 8: 158. DOI: 10.1038/s41541-023-00750-7.
3. Self WH, Tenforde MW, Rhoads JP, Gaglani M, Ginde AA, Douin DJ, et al. Comparative Effectiveness of Moderna, Pfizer-BioNTech, and Janssen (Johnson & Johnson) Vaccines in Preventing COVID-19 Hospitalizations Among Adults Without Immunocompromising Conditions — United States, March–August 2021. *MMWR. Morbidity and mortality weekly report*. 2021; 70: 1337–43. DOI: 10.15585/mmwr.mm7038e1.
4. Melo A, de Macedo LS, Invencao M, de Moura IA, da Gama M, de Melo CML, et al. Third-generation vaccines: features of nucleic acid vaccines and strategies to improve their efficiency. *Genes*. 2022; 13. DOI:10.3390/genes13122287.
5. Martinon F, Krishnan S, Lenzen G, Magne R, Gomard E, Guillet JG, et al. Induction of virus-specific cytotoxic T lymphocytes in vivo by liposome-entrapped mRNA. *European journal of immunology*. 1993; 23: 1719–22. DOI: 10.1002/eji.1830230749.
6. Conry RM, LoBuglio AF, Wright M, Sumerel L, Pike MJ, Johanning F, et al. Characterization of a messenger RNA polynucleotide vaccine vector. *Cancer research*. 1995; 55: 1397–400.
7. Anderson BR, Muramatsu H, Jha BK, Silverman RH, Weissman D, Kariko K. Nucleoside modifications in RNA limit activation of 2'–5'-oligoadenylate synthetase and increase resistance to cleavage by RNase L. *Nucleic acids research*. 2011; 39: 9329–38. DOI: 10.1093/nar/gkr586.
8. Muslimov A, Tereshchenko V, Shevryev D, Rogova A, Lepik K, Reshetnikov V, et al. The dual role of the innate immune system in the effectiveness of mRNA therapeutics. *International journal of molecular sciences*. 2023; 24. DOI: 10.3390/ijms241914820.
9. Weng Y, Li C, Yang T, Hu B, Zhang M, Guo S, et al. The challenge and prospect of mRNA therapeutics landscape. *Biotechnology advances*. 2020; 40: 107534. DOI: 10.1016/j.biotechadv.2020.107534.
10. Orlandini von Niessen AG, Poleganov MA, Rechner C, Plaschke A, Kranz LM, Fesser S, et al. Improving mRNA-based therapeutic gene delivery by expression-augmenting 3' UTRs identified by cellular library screening. *Molecular therapy: the journal of the American Society of Gene Therapy*. 2019; 27: 824–36. DOI: 10.1016/j.ymthe.2018.12.011.
11. Cao J, Novoa EM, Zhang Z, Chen WCW, Liu D, Choi GCG, et al. High-throughput 5' UTR engineering for enhanced protein production in non-viral gene therapies. *Nature communications*. 2021; 12: 4138. DOI: 10.1038/s41467-021-24436-7.
12. Vasileva O, Tereschenko TV, Krapivin B, Muslimov A, Kukushkin I, Pateev I, et al. Immunogenicity of full-length and multi-epitope mRNA vaccines for M. Tuberculosis as demonstrated by the intensity of T-cell response: a comparative study in mice. *Bulletin of RSMU*. 2023; 03: 42–48. DOI: 10.24075/brsmu.2023.021.
13. Kirshina AS, Kazakova AA, Kolosova ES, Imasheva EA, Vasileva OO, Zaborova OV, et al. Effects of various mRNA-LNP vaccine doses on neuroinflammation in BALB/c mice. *Bulletin of RSMU*. 2022; 6. DOI: 10.24075/brsmu.2022.068.
14. Avdienko VG, Babaian SS, Guseva AN, Kondratiuk NA, Rusakova LI, Averbakh MM, et al. Quantitative, spectral, and serodiagnostic characteristics of antimycobacterial IgG, IgM, and IgA antibodies in patients with pulmonary tuberculosis. *Problemy tuberkuleza i boleznei legkikh*. 2006; 47–55.
15. Nikonenko BV, Apt AS, Mezhlumova MB, Avdienko VG, Yeremeev VV, Moroz AM. Influence of the mouse Bcg, Tbc-1 and xid genes on resistance and immune responses to tuberculosis infection and efficacy of bacille Calmette-Guerin (BCG) vaccination. *Clinical and experimental immunology*. 1996; 104: 37–43. DOI: 10.1046/j.1365-2249.1996.d01-643.x.
16. Kozlova IV, Avdienko VG, Babayan SS, Andrievskaya IYu, Gergert VY. Diagnosis of Bactec samples by immunoglobulins of mouse hyperimmune sera obtained against modified antigens of the cell wall of Mycobacterium tuberculosis. *Tuberculosis and Lung Diseases*. 2019; 97: 25–30.
17. Rijnik WF, Ottenhoff THM, Joosten SA. B-Cells and Antibodies as Contributors to Effector Immune Responses in Tuberculosis. *Frontiers in immunology*. 2021; 12: 640168. DOI: 10.3389/fimmu.2021.640168.
18. Logan J, Shenk T. Adenovirus tripartite leader sequence enhances translation of mRNAs late after infection. *Proceedings of the National Academy of Sciences of the United States of America*. 1984; 81: 3655–9. DOI: 10.1073/pnas.81.12.3655.
19. Kaufman RJ. Identification of the components necessary for adenovirus translational control and their utilization in cDNA expression vectors. *Proceedings of the National Academy of Sciences of the United States of America*. 1985; 82: 689–93. DOI: 10.1073/pnas.82.3.689.
20. Sample PJ, Wang B, Reid DW, Presnyak V, McFadyen IJ, Morris DR, et al. Human 5' UTR design and variant effect prediction from a massively parallel translation assay. *Nature biotechnology*. 2019; 37: 803–9. DOI: 10.1038/s41587-019-0164-5.
21. Kozak M. Features in the 5' non-coding sequences of rabbit alpha and beta-globin mRNAs that affect translational efficiency. *Journal of molecular biology*. 1994; 235: 95–110. DOI: 10.1016/s0022-2836(05)80019-1.
22. Kumari S, Bugaut A, Huppert JL, Balasubramanian S. An RNA G-quadruplex in the 5' UTR of the NRAS proto-oncogene modulates translation. *Nature chemical biology*. 2007; 3: 218–21. DOI: 10.1038/nchembio864.

PREPARATION OF A RECOMBINANT RIBONUCLEASE INHIBITOR IN *E. COLI* FOR USE IN mRNA SYNTHESIS *IN VITRO*

Zakharova MV¹, Zagoskin AA^{1,2}, Ivanov RA², Nagornykh MO^{1,2}✉

¹ Institute of Biochemistry and Physiology of Microorganisms, Russian Academy of Sciences, Pushchino, Russia

² Sirius University of Science and Technology, Sirius, Sochi, Russia

Technologies underlying the production of synthetic mRNAs *in vitro* have significantly expanded the possibilities for research and therapeutic use of this class of molecules. The flagship application area has been the niche of mRNA vaccines, but this class of therapeutic molecules has the potential to be applied in a much broader range of situations. The process of *in vitro* production of artificial RNA molecules is based on an enzymatic synthesis reaction, one of the components of which is a ribonuclease inhibitor. This protein protects synthesized RNA from attacks by ribonucleases and prevents degradation of the molecules, which is critically important for RNA. Eukaryotic ribonuclease inhibitor synthesized as a recombinant protein in the cells of *E. coli* bacteria is the most common choice. However, the structure of this protein makes it a difficult product to make in bacteria. This study aimed to test the production of a recombinant ribonuclease inhibitor in various strains of *E. coli*, and to show the effect that helper polypeptides and cellular chaperones have on this process. Using genetic engineering approaches, we constructed plasmids, from which chimeric ribonuclease inhibitor molecules and helper polypeptides were produced. The influence of various components on solubility of the target recombinant protein was assessed with the help of densitometry, to which we have subjected products of the PAGE electrophoresis. It was determined that combinations of a vector with a strong promoter for the expression of the *RNH1* ribonuclease inhibitor gene and helper polypeptides MBP and TIG against the background of increased expression of cellular chaperones dnaK, dnaJ, grpE give the target product yield of 45 mg/l and 60 mg/l, respectively. The selected conditions allow large-scale production of this protein for further use in *in vitro* RNA synthesis in the context of production of medicines.

Keywords: ribonuclease inhibitor, production of recombinant proteins, chaperones, fusion polypeptides

Funding: the study was financially supported in the context of the program of Ministry of higher education and science of the Russian Federation (agreement #075-10-2021-113, unique project number RF----193021X0001).

Author contribution: Zakharov MV — selection of conditions of production of recombinant proteins, production experiments in different *E. coli* strains; Zagoskin AA — chromatographic clearing of recombinant proteins; Nagornykh MO — conceptualization, design of genetic constructs, article authoring; Ivanov RA — general management.

✉ **Correspondence should be addressed:** Maxim O. Nagornykh
Prospekt Nauki, 5, Pushchino, 142290, Russia; derbanner@gmail.com

Received: 16.11.2023 **Accepted:** 17.12.2023 **Published online:** 31.12.2023

DOI: 10.24075/brsmu.2023.058

ПОЛУЧЕНИЕ РЕКОМБИНАНТНОГО ИНГИБИТОРА РИБОНУКЛЕАЗ В *E. COLI* ДЛЯ ИСПОЛЬЗОВАНИЯ В СИНТЕЗЕ мРНК *IN VITRO*

М. В. Захарова¹, А. А. Загоскин^{1,2}, Р. А. Иванов², М. О. Нагорных^{1,2}✉

¹ Институт биохимии и физиологии микроорганизмов Российской академии наук, Пущино, Россия

² Научно-технологический университет «Сириус», Сочи, Россия

Технологии, лежащие в основе получения синтетических мРНК *in vitro*, значительно расширили возможности их исследовательского и терапевтического применения. Флагманской областью применения стала ниша мРНК-вакцин, однако этот класс терапевтических молекул может быть применим к гораздо более широкому кругу задач. В основе процесса получения искусственных молекул РНК лежит реакция ферментативного синтеза *in vitro*, одним из компонентов которой является ингибитор рибонуклеаз. Этот белок необходим для защиты синтезированных РНК от атак рибонуклеаз с целью предотвращения деградации молекул, что критично для РНК. Чаще всего используют ингибитор рибонуклеаз эукариотического происхождения, полученный в виде рекомбинантного белка в клетках бактерий *E. coli*. Однако он является сложной мишенью для наработки в бактериях, что обусловлено его структурой. Целью работы было проверить наработку рекомбинантного ингибитора рибонуклеаз в различных штаммах *E. coli*, а также показать влияние хелперных полипептидов и клеточных шаперонов на этот процесс. При помощи подходов геной инженерии были сконструированы плазмиды, с которых проводили наработку химерных молекул ингибитора рибонуклеаз и вспомогательных полипептидов. Оценку вклада различных компонентов, влияющих на растворимость целевого рекомбинантного белка, проводили в ходе денситометрического анализа результатов электрофореза в ПААГ. Определили, что комбинации вектора с сильным промотором для экспрессии гена ингибитора рибонуклеазы *RNH1* и вспомогательных полипептидов MBP и TIG на фоне повышенной экспрессии клеточных шаперонов dnaK, dnaJ, grpE дают выход целевого продукта 45 мг/л и 60 мг/л соответственно. Подобранные условия дают возможность крупномасштабных наработок этого белка для дальнейшего использования в синтезе РНК *in vitro* при производстве терапевтических препаратов.

Ключевые слова: ингибитор рибонуклеаз, продукция рекомбинантных белков, шапероны, вспомогательные полипептиды

Финансирование: работа выполнена при поддержке программы Министерства высшего образования и науки РФ (соглашение №. 075-10-2021-113, уникальный номер проекта RF----193021X0001).

Вклад авторов: М. В. Захарова — подбор условий наработки рекомбинантных белков, эксперименты по наработке в разных штаммах *E. coli*; А. А. Загоскин — хроматографическая очистка рекомбинантных белков; М. О. Нагорных — концепция работы, создание генетических конструкций, написание статьи; Р. А. Иванов — общее руководство.

✉ **Для корреспонденции:** Максим Олегович Нагорных
Проспект Науки, д. 5, г. Пущино, 142290, Россия; derbanner@gmail.com

Статья получена: 16.11.2023 **Статья принята к печати:** 17.12.2023 **Опубликована онлайн:** 31.12.2023

DOI: 10.24075/vrgmu.2023.058

Encoded by the *RNH1* gene, ribonuclease inhibitor is a protein expressed in the cytosol; it inhibits pancreatic ribonucleases, merging with them into complexes and protecting cellular RNA from premature degradation [1, 2]. The inhibiting effect stems from non-covalent binding of protein ribonuclease molecules, which leads to blocking of both RNA-binding and catalytic ribonuclease domains [3]. Ribonuclease inhibitor is a fairly conservative protein, with homology over 70% in mammals - humans, mice, horses, and pigs. It consists of 15–16 leucine-rich repeats (the exact number of repeats depends on the type of mammal), and each repeat includes 28–29 amino acids, has one alpha helix and one beta sheet. The repeats make up a U-shaped structure weighing approximately 50 kDa [4, 5]. Physico-chemical properties of ribonuclease inhibitor put it among acidic proteins, with isoelectric point in the region of 4.5. Thirty-two cysteine residues, which enable the enzyme, are another important characteristic of ribonuclease inhibitor. In native protein, cysteines are in a reduced state; they participate in the formation of a hydrophobic protein core. Oxidation of cysteine residues is accompanied by appearance of disulfide bridges between them, and conformational changes weaken the activity of ribonuclease inhibitor [6, 7].

Protein preparations of the ribonuclease inhibitor are of biotechnological value for the purposes of both research (*in vitro* RNA synthesis, *in vitro* translation, cDNA production) and mass production of medicines based on artificial RNA molecules. Therefore, since its discovery, there have been attempts to synthesize this enzyme in large quantities. Historically, the first of the said attempts sought to make the ribonuclease inhibitor from mammalian tissues [8]. As the recombinant DNA technologies matured, the focus of attention shifted to the most widely used *E. coli* bacterial system. However, recombinant ribonuclease inhibitor tends to aggregate in *E. coli*, like other proteins containing a large number of hydrophobic amino acids, and with cysteine residues in particular. Several other factors, including the high rate of translation associated with transcription in bacteria, bring accumulation of such recombinant proteins as inclusion bodies formed from aggregates of improperly folded protein molecules [9]. Therefore, early experiments designed to produce a functionally active soluble ribonuclease inhibitor in *E. coli* often ended with the entire protein accumulating as inactive aggregates, and when these were refolded *in vitro*, the resulting protein most often lost its potency, and the yield thereof was very low [10].

Various approaches have been developed to solve this problem. One of them suggests employing a vector with a weak promoter (for example, *P_{trp}*) and a minimal medium for expression of the ribonuclease inhibitor gene. Such conditions weakened the expression of the target protein gene significantly, which allowed yielding considerable amounts of the recombinant inhibitor in a soluble form, but the overall level of the final product turned out to be significantly lower compared to expression systems where the target gene is controlled by the T7 promoter [2]. Another approach involves enriching the culture medium with DTT (dithiothreitol), thus keeping cysteines in a reduced state, which has a positive effect on the folding of many proteins prone to aggregation, including ribonuclease inhibitor [11]. This technique was further developed with cultivation under anaerobic conditions at a reduced temperature and with co-expression of the GroEL cellular chaperone, which brings the production of ribonuclease inhibitor to a fairly high level [12]. The downsides of this method are its complexity and the large number of additional components required, both complicating the technological process when the goal is to synthesize the protein at scale. Finally, another approach aims

at producing the target product as a chimeric molecule with an fusion polypeptide that improves solubility of the target protein. In an earlier study, MBP fusion polypeptide was shown to positively affect production of the ribonuclease inhibitor in soluble form in *E. coli* [4].

The purpose of this work was to identify the conditions of production of the recombinant human ribonuclease inhibitor in *E. coli* that would simplify the process in the laboratories and facilities synthesizing the product at semi-industrial scale.

METHODS

Plasmid design

The genetic constructs used in this work were produced by the restriction ligase DNA cloning method. The DNA sequence of the *RNH1* gene encoding human ribonuclease inhibitor was synthesized *de novo* with codon optimization for *E. coli* (IDT, <https://www.idtdna.com/>). Amplification of all DNA sequences followed the manufacturer's protocol (NEB) and employed Q5 high-fidelity polymerase. Cloning of the ribonuclease inhibitor gene into the set of vectors with fusion polypeptides based on pET28a (Novagen; USA) and pSol (Lucigen; USA) was done by restriction sites NdeI and NotI, in an enzymatic reaction, with two corresponding restriction endonucleases (Sibenzyme; Russia); the procedure lasted for 1 hour at the temperature of 37 °C. Next, we did electrophoresis in agarose gel and purified DNA fragments therefrom with the help of a GeneJET Gel Extraction Kit (Thermo; USA). These fragments, corresponding to the vector part and the ribonuclease inhibitor gene, were then used in the ligation reaction with T4-DNA ligase (NEB), which lasted for 30 minutes at room temperature. Competent *E. coli* 10G cells (Lucigen; USA) were transformed with the help of electroporation (Bio-Rad; USA) as prescribed by the manufacturer. Plasmid DNA was isolated from clones containing correct inserts, with confirmed correctness by the Sanger sequencing reaction.

Production of recombinant proteins in *E. coli*

We used the following strains intended for production of recombinant proteins in *E. coli*: BL21 (DE3) (Invitrogen; USA); KRX (Promega; USA); Rosetta (DE3) pLysS (Novagen; USA); BL21 Star (DE3) (Invitrogen; USA), Origami 2 (DE3) (Novagen; USA). Using plasmids containing genes of fusion polypeptides and the ribonuclease inhibitor, we electroporated each strain and seeded the LB liquid medium in test tubes (35 ml, including selective antibiotics) with a transformation mixture (100 µl). The incubation lasted for 12–14 hours at 37 °C, with the stirring speed of 180 rpm. Next, we transplanted the grown culture in a ratio of 1:200 into test tubes or flasks containing the required amount of the LB culture medium (10–500 ml) with selective antibiotics. The cell culture was built up to the optical density (OD) of = 0.5–0.6 in a shaker at 180 rpm at 37 °C. Once the needed OD was reached, we cooled the culture on ice for 10 minutes, added the 1 mM IPTG inductor for pET28a-based vectors or 0.2% L-rhamnose for pSol-based vectors, and incubated at different temperatures while stirring (120 rpm) for 10 hours (16 °C) or 2 hours (37 °C). Co-expressed cellular chaperone genes were induced by the introduced L-arabinose (0.5%) or tetracycline (5 ng/ml), with pre-incubation before adding the target gene expression inducers. Then, bacterial cells were deposited by centrifugation for 20 minutes at 6000 g and 4 °C.

To measure solubility of the resulting protein, we transferred the deposited cells into buffer A (50 mM Tris-HCl pH 7.5; 0.3

M NaCl; 0.005 M imidazole) and destroyed them using a Qsonica Q700 ultrasound disintegrator until the cell suspension on ice was clarified (ultrasonic pulses for 10 s, cooling — 60 s). The destroyed cells were deposited by centrifugation (15000 g), which lasted 30 minutes at 4 °C. Next, we collected samples of the supernatant containing the target protein in the soluble form, and the precipitate with aggregates was dissolved in urea (2 M) for further electrophoretic analysis. PAAG electrophoresis (10%) was used to separate protein under denaturing conditions, as prescribed by the standard methods. After staining with Coomassie blue dye and washing it off, we photographed the gels and quantified the soluble and insoluble forms of protein. Image Lab application (Bio-Rad; USA) enabled densitometric analysis of the gels.

Protein purification using affinity chromatography

After ultrasonic destruction of the biomass and centrifugation of cellular debris, we filtered the remaining supernatant through a membrane with 0.22 µm pores. The resulting preparation for chromatographic purification contained the soluble fraction of proteins in buffer A (50 mM Tris-HCl pH 7.5; 0.3 M NaCl; 0.005 M imidazole); it was applied on Nuvia IMAC Resin (Bio-Rad), a chromatographic sorbent. The proteins were eluted by chromatographic buffer B (50 mM Tris-HCl pH 7.5; 0.5 M imidazole). In a Spin-X centrifuge concentrator (pore size 10 kDa), purified preparation was concentrated from 5 to 1 ml. If necessary, we further treated it with TEV protease (following manufacturer's recommendations) overnight at 4 °C, and then repeated chromatographic purification, but after that only one fraction, that which did not bind to the sorbent and contained purified ribonuclease inhibitor, was collected. The target fraction was dialyzed against the storage buffer (40 mM HEPES-KOH pH 7.6, 100 mM KCl) at 4 °C. Glycerin (50%) and DTT (8 mM) were added for long-term storage at -20 °C.

RESULTS

Our first step in identification of the optimal conditions for production of soluble recombinant ribonuclease inhibitor was extension of the list of screened fusion polypeptides that

increase solubility of this protein, since this approach has already been tested earlier [4]. For this purpose, we have constructed a set of twenty vectors based on two expression plasmids, pET28a (Novagen; USA) and pSol (Lucigen; USA). Two vectors contained the human ribonuclease inhibitor (*RNH1*) gene codon optimized for expression in *E. coli*, with its sequence encoding polyhistidine tag at the protein's N-terminus, which ultimately encoded the target protein molecule with a histidine tail for affine purification. The remaining plasmids encoded chimeric proteins consisting of fusion polypeptides (MBP, TIG, TSF, FH8, PpiB, YrhB, SUMO, TRX, GST) and a recombinant ribonuclease inhibitor. The induction of expression from T7 (pET28a) or rhamnose (in the case of pSol) promoter in these plasmids enables production of chimeric proteins comprised of combinations of a ribonuclease inhibitor with different fusion polypeptides carrying the polyhistidine tag on the N-terminus for affinity purification (Fig. 1). It should be noted that a sequence encoding the proteolysis site for TEV protease was inserted between the ribonuclease inhibitor gene and genes of the fusion polypeptides. Thus, after primary affinity purification, it is possible to split off the fusion polypeptide and use affinity chromatography to produce a pure ribonuclease inhibitor preparation.

All the resulting genetic constructs were tested under the typical conditions of production of recombinant proteins in *E. coli*; for the purpose, they transformed cells of BL21 (DE3) strain, and enabled the said production at 37 °C. As expected, incubation of bacterial cultures at 37 °C yielded no soluble form of the ribonuclease inhibitor but only insoluble aggregates, regardless of the fusion peptide and from what promoter the target gene's expression was initiated (data not provided). When the incubation temperature was lowered to 16 °C, variants without fusion peptides also formed inclusion bodies, but in the end, there were several chimeric proteins in the soluble form (Fig. 2). Therefore, all our further attempts at production of the recombinant ribonuclease inhibitor were conducted at lower temperature (16 °C). In particular, we registered good results when using the following fusion polypeptides: MBP (70–75% of the target product in soluble form), TIG (about 90% of the target product in soluble form) and, to a lesser extent, PpiB (about 60% of the target product in soluble form).

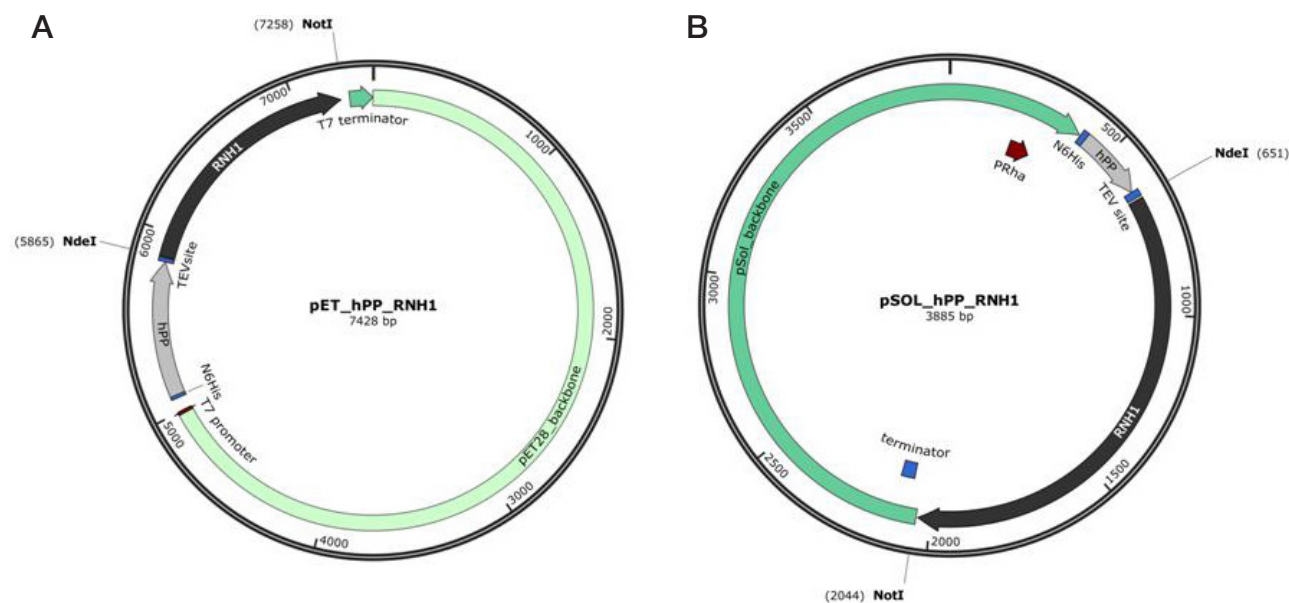


Fig. 1. Maps of vectors for production of ribonuclease inhibitor with the fusion polypeptides that increase solubility of recombinant proteins in *E. coli*. **A.** Variants based on the pET28a vector, T7 promoter. **B.** Variants based on the pSol vector, PRha promoter. *RNH1* — gene encoding the human ribonuclease inhibitor; *hPP* — gene encoding one of the fusion polypeptides (MBP, TIG, TSF, FH8, PpiB, YrhB, SUMO, TRX, GST). pET28a vector backbone contains the kanamycin resistance gene, pBR322 replication origin, and the sequence encoding the lacI repressor. pSol vector backbone contains the kanamycin resistance gene, pUC replication origin, the rhamnose-induced PRha promoter, and the transcription terminator

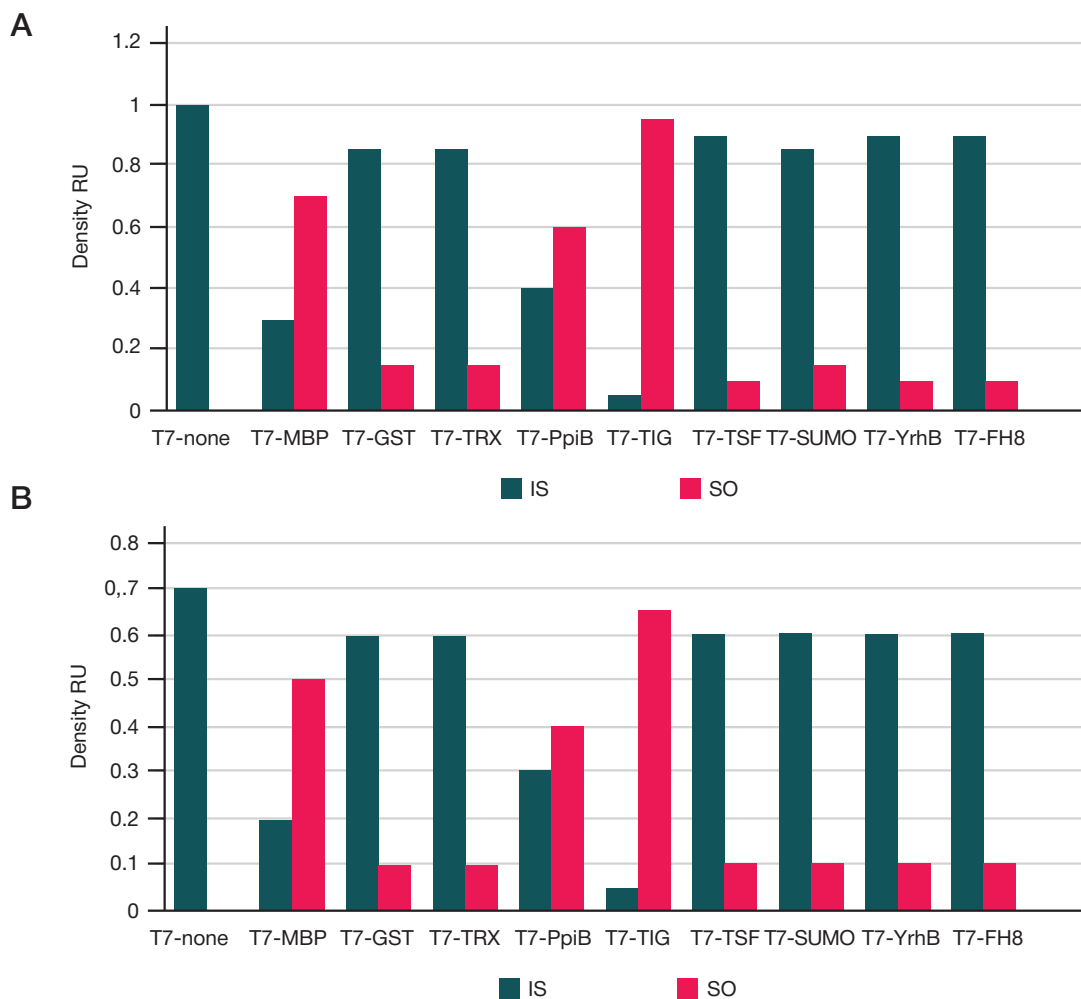


Fig. 2. Effect of fusion polypeptides on solubility of ribonuclease inhibitor, production in *E. coli* BL21 (DE3) strain at 16 °C. **A.** Variants based on the pET28a vector, T7 promoter. **B.** Variants based on the pSol vector, PRha promoter. IS is the relative level of insoluble fraction, shown in red. SO is the the level produced soluble ribonuclease inhibitor, shown in blue. Density RU are densitometry of PAAG results shown in relative units

Stronger promoter T7 ensured considerably bigger yield of the protein in pET28a vector systems compared to the pSol vector, which relies on a weaker rhamnose promoter (Fig. 2). Nevertheless, part of the target protein still transitioned into a functionally inactive state in the inclusion bodies, a problem that could be remedied by further optimization of the operating conditions.

The next step was to compare the yield of soluble ribonuclease inhibitor in different *E. coli* strains designed specifically for the production of recombinant proteins. As a rule, previous attempts on the task incorporated the experience of working with recombinant producers based on the *E. coli* BL21 (DE3) strain, but, in most cases, it is not the optimal choice in case of proteins prone to aggregation: a significant proportion of the product are insoluble aggregates. Therefore, seeking to refine the conditions of production of ribonuclease inhibitor, we compared the amounts of protein yielded by four more *E. coli* purpose-designed strains. Thus, in addition to the BL21 (DE3) strain, the following commercially available strains were experimented with (all with various design specifics conditioned by their intended use in the context of production of recombinant proteins). Origami strain 2 (DE3), with mutations in the genes of thioredoxin reductase (*trxB*) and glutathione reductase (*gor*), which promote formation of disulfide bonds and correct folding of some recombinant proteins in the cytoplasm of bacterial cells. BL21 Star (DE3) strain, with a mutation in the gene encoding ribonuclease

E (rne131), which improves stability of the target gene's mRNA and may boost production of recombinant proteins. It was also interesting to try the Rosetta (DE3) pLysS strain, which can produce proteins without codon optimization to *E. coli* and also allows reducing background expression from the T7 promoter by additional expression of the T7 lysozyme gene, a natural inhibitor of DNA-dependent RNA polymerase of the T7 phage, which is of particular importance in the context of production of proteins potentially toxic to bacteria. Finally, the *E. coli* KRX strain, with a chromosomal copy of the T7 DNA-dependent RNA polymerase gene controlled by the rhamnose promoter, which governs basal expression better, and is also well titrated by rhamnose while producing high amounts of recombinant proteins, as ensured by the T7 promoter [13].

To see how selection of the strain affects production of the soluble form of the inhibitor, we continued working with the variants that showed best results at the previous stage, i.e., pET28a-based vectors encoding chimeric proteins, with fusion polypeptides MBP and TIG. As mentioned above, all comparative experiments with these strains implied bacterial culture incubation at 16 °C. Ultimately, it was the KRX strain that delivered the best yield (Fig. 3). The possible reason behind this result is a more suitable mode of expression by the T7 DNA-dependent RNA polymerase gene controlled by the rhamnose promoter, which refines the dose of T7 DNA-dependent RNA polymerase accumulated in cells; accordingly, the recombinant ribonuclease inhibitor gene expression is

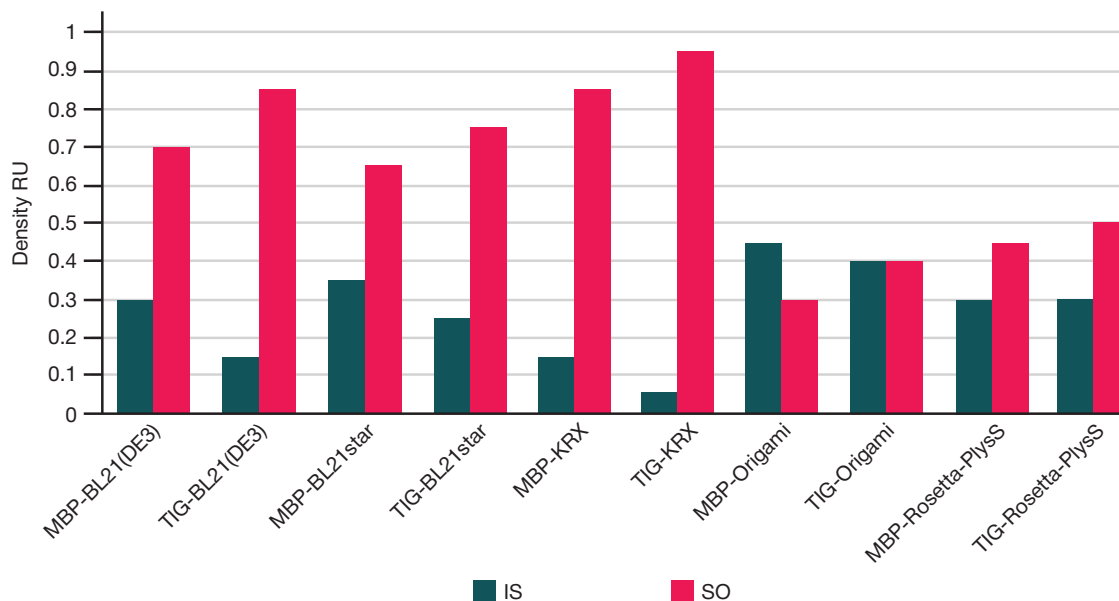


Fig. 3. Selection of the *E. coli* strain optimal for production of the recombinant ribonuclease inhibitor in soluble form, using vectors encoding a chimeric protein consisting of combinations of a ribonuclease inhibitor and two fusion polypeptides (MBP, TIG). IS is the relative level of insoluble fraction, shown in red. SO is the level produced soluble ribonuclease inhibitor, shown in blue. Density RU are densitometry of PAAG results shown in relative units

not "overloaded," as in the case of direct induction of the T7 promoter with IPTG of lacUV5 promoter, when it is virtually impossible to weaken expression by titration. The BL21 (DE3) and BL21 Star (DE3) strains are also good options for the recombinant ribonuclease inhibitor production when combined with the selected fusion polypeptides and cultivated at low temperatures, but their yield of the soluble product is 10–15% (depending on the polypeptide) lower than that of the KRX strain. The remaining two strains performed considerably worse, with Origami 2 (DE3) being the outsider, probably due to its specific mutations designed to create intracellular conditions for the formation of disulfide bridges. Another possible reason for the poor results is the lower amount of biomass produced by these strains compared to KRX, BL21 (DE3) and BL21 Star (DE3), which may apparently be attributed to the introduced mutations affecting viability and metabolic processes in the cells. Thus, the second stage of the work revealed that in the context of production of the soluble form of ribonuclease inhibitor, the best "strain — fusion polypeptide" combinations are *E. coli* KRX-MBP and *E. coli* KRX-TIG.

There is one more tool used against formation of insoluble aggregates in production of recombinant proteins in *E. coli*: cellular chaperone genes co-expression, which helps proteins to adopt a native conformation. We tested the efficacy of this tool on chaperones *dnaK*, *dnaJ*, *grpE*, *groES* and *groEL*. Earlier, researchers reported a positive effect of some chaperones on the production of functional ribonuclease inhibitor [14, 15]. We decided to test them in the best combinations of the KRX *E. coli* strain and fusion polypeptide MBP, TIG, PpiB. This experiment revealed that the maximum effect — about 10% uptick of the target protein yield — was achieved against co-expression of genes *dnaK*, *dnaJ*, *grpE* (Figure 4). An earlier study mentioned that GroELS chaperone positively influenced production of the soluble form of ribonuclease inhibitor [12]; in this regard, the likely reason behind the differences with our findings is the use of different strains.

Thus, the highest yielding ribonuclease inhibitor production combination identified in this work includes the KRX *E. coli* strain, TIG and MBP fusion polypeptides, co-expressing *dnaK*, *dnaJ*, *grpE* chaperone genes, and cultivation temperature of 16 °C. To accurately assess the yield of the target protein given

by the tested combinations, we used affinity chromatography on a metal chelate carrier and subsequent proteolysis reaction with TEV protease. The total amount of soluble ribonuclease inhibitor was 60 mg/l in case of *E. coli* KRX-TIG-*dnaK*, *dnaJ*, *grpE*, and 45 mg/l for *E. coli* KRX-MBP-*dnaK*, *dnaJ*, *grpE*.

DISCUSSION

The rapid development of therapeutic applications of synthetic mRNAs underpins the need for preparative amounts of proteins required to produce large amounts of RNA *in vitro* [16, 17]. Apart from the enzymes that synthesize and modify RNA *in vitro*, another important component of the reaction mixture is ribonuclease inhibitor, a protein that prevents degradation of the RNA molecules caused by ribonucleases, which is crucial for medicines. Ribonuclease inhibitor is also widely used in research tasks related to the synthesis of RNA, cDNA, and *in vitro* translation. The production of this protein in recombinant *E. coli* strains is complicated by the specificity of its structure with abundant cysteine residues, and the tendency to aggregate in bacterial cells. Previous attempts at production of the soluble form of ribonuclease inhibitor in *E. coli* require special conditions that significantly complicate the technological process and make it costly to scale [11, 12]. This work aimed to find the ribonuclease inhibitor production conditions and method that would deliver large yields and be cost-effective from the technological point of view.

As the first stage, we screened a number of fusion peptides that could increase the proportion of soluble ribonuclease inhibitor produced in *E. coli*. Previous studies have shown that polypeptides can significantly increase the yield of soluble form of recombinant proteins, including ribonuclease inhibitors [4, 18]. The ability to improve solubility of various recombinant proteins stems from the formation of chimeric molecules, the fusion part of which (polypeptide) can later be removed by proteolysis [9, 19]. We tested nine different fusion polypeptides: MBP, TIG, TSF, FH8, PpiB, YrhB, SUMO, TRX, GST; they differ significantly in their physico-chemical properties. Additionally, we tested them in two expression systems, one based on the commercially available plasmid pET28a (target gene expression controlled by a strong T7 promoter), and another on the pSOL

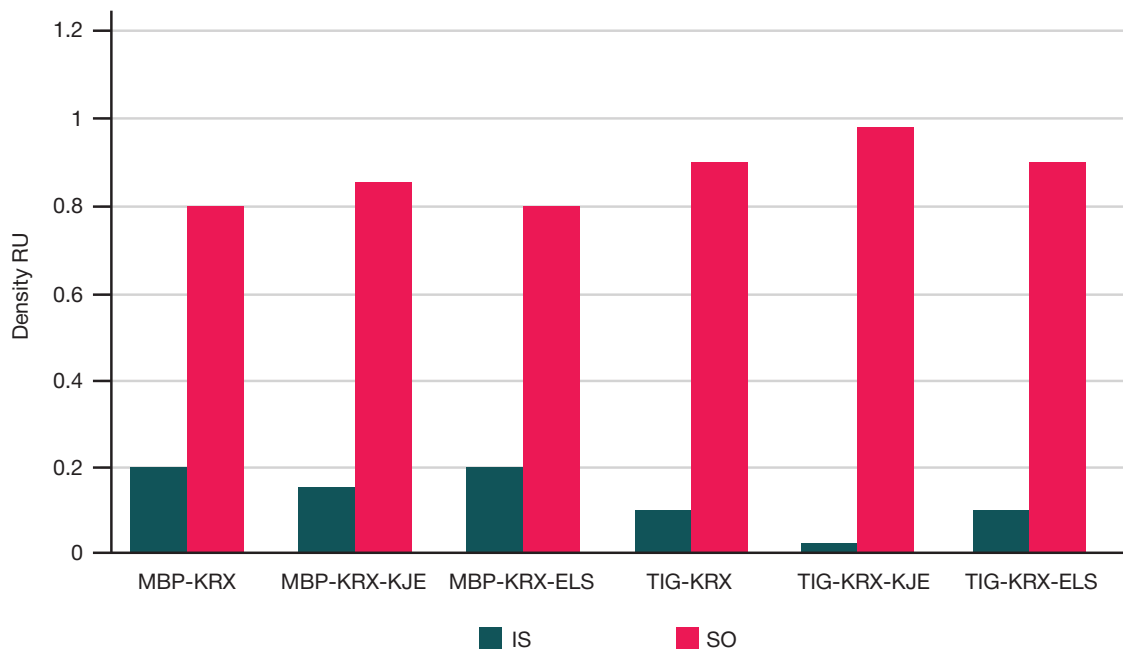


Fig. 4. Effect of additional gene co-expression, cellular chaperones *dnaK*, *dnaJ*, *grpE* (shown as KJE), *groES* and *groEL* (shown as ELS), on production of the recombinant ribonuclease inhibitor in the KRX *E. coli* strain at 16 °C. IS is the relative level of insoluble fraction, shown in red. SO is the the level produced soluble ribonuclease inhibitor, shown in blue. Density RU are densitometry of PAAG results shown in relative units

vector (expression controlled by a rhamnose promoter). The best results were ensured by MBP, TIG, and PpiB, with the yield highest in the systems utilizing MBP and TIG, and that with PpiB performing considerably worse (Fig. 2). Overall, all the experiments of this work have shown that larger polypeptides, such as MBP (42 kDa) and TIG (49 kDa), provide more of the final target product than fusions with smaller molecular weight, like PpiB (19 kDa). Comparing the yield of target products at the level of vector lines (pET28a and pSol, in this study), the unambiguous system of choice for production of ribonuclease inhibitor is that where a strong T7 promoter controls target gene expression (Fig. 2).

Having established that the most productive vector is that based on pET28a, encoding chimeric ribonuclease inhibitor variants with MBP and TIG fusion polypeptides, we moved to the next stage of optimization: selection of the suitable strain of *E. coli* from several commercially available options. For this purpose, we compared the ribonuclease inhibitor production capacity of BL21 (DE3), Origami 2 (DE3), BL21 Star (DE3), Rosetta (DE3) pLysS, and KRX *E. coli* strains, all of which are designed for production of recombinant proteins, but have certain specifics, which enables the comparison and allows selecting that which maximizes production of the soluble form ribonuclease inhibitor [20]. Under the conditions of this study, the highest ribonuclease inhibitor yield was delivered by the KRX *E. coli* strain (Fig. 3), likely because of the rhamnose promoter control over the T7 gene of DNA-dependent RNA polymerase, since this promoter has a low basal activity level and is better titrated by L-rhamnose. Apparently, this design feature allows finding the optimal balance of conditions for bacterial production of toxic or aggregation-prone recombinant proteins, while also ensuring a high yield of the target protein by reducing the amount of protein loss in inclusion bodies, which is common for production in strains with the chromosomal copy of T7 DNA-dependent RNA polymerase controlled by the lacUV5 promoter and induced by IPTG [21].

Finally, having established that the best "strain — fusion polypeptide" combinations are *E. coli* KRX-MBP and *E. coli* KRX-TIG, we decided to investigate the effect of the additional

cellular chaperone genes co-expression on the yield of the target protein. For this purpose, we used a commercial kit (Takara; USA) that includes vectors carrying the genes of chaperones *dnaK*, *dnaJ*, *grpE*, *groES* and *groEL*, which, when produced additionally in the *E. coli* cells, often help "problematic" recombinant proteins to adopt the correct conformation, thus reducing the formation of insoluble aggregates [14, 15]. For recombinant ribonuclease inhibitor, the positive effect of *groES* and *groEL* on the protein production under anaerobic conditions has already been shown [12], but this approach is not always convenient when scaling technological processes to produce larger amounts of recombinant proteins. Interestingly, in our experimental conditions, aerobic cultivation of *E. coli* at a reduced temperature (16 °C), the best ribonuclease inhibitor yields were given by two combinations: a) MBP fusion polypeptide, *dnaK*, *dnaJ*, *grpE*, chaperone genes co-expression, KRX *E. coli* strain, and b) TIG fusion polypeptide, *dnaK*, *dnaJ*, *grpE* chaperone genes co-expression, KRX *E. coli* strain (Fig. 4). To accurately quantify recombinant ribonuclease inhibitor in such combinations, we performed affinity purification and then compared the the yield of the target product. The first combination produced 45 mg/l. However, the maximum yield of the final product, that is, the soluble form of ribonuclease inhibitor, was achieved in aerobic cultivation of the KRX *E. coli* strain at a reduced temperature (16 °C), transformed by the expression vector based on pET28a with a codon optimized ribonuclease inhibitor gene, in combination with the TIG fusion polypeptide gene, against the background of *dnaK*, *dnaJ*, *grpE* chaperone genes co-expression. This combination gives a yield of 60 mg/l when culturing bacteria in flasks on a standard LB medium, which is significantly higher than the results achieved earlier, and also easier from the bacteria cultivation perspective [4, 11, 12, 22].

The results of our study confirm the need for an integrated approach to the search for optimal conditions of production of aggregation-prone recombinant proteins in *E. coli*, especially when the goal is to scale up the process of synthesis of enzymes, therapeutic proteins, cytokine preparations or antigens for vaccines [23].

CONCLUSIONS

This work shows that a systemic approach to identification of conditions and components for production of enzymes and therapeutic recombinant proteins in *E. coli*, given that they are prone to aggregation and form inclusion bodies under normal bacterial cultivation conditions, allows finding combinations delivering significantly higher yields of the target protein in soluble form. Moreover, it is possible to find the balance of conditions and components needed to establish production at semi-industrial and

industrial scales, and to minimize protein loss to aggregation. It should be noted that the final ribonuclease inhibitor production protocol compiled in this study can be optimized further by incorporating the experience of earlier works and opting for a nutrient media other than the standard LB, as well as introduction of cultivation in a fermenter, which will further increase the final product yield. However, even in its present form, the protocol can support semi-industrial production of this protein in preparative quantities for further use in enzymatic RNA synthesis *in vitro*.

References

- Moenner M, Vosoghi M, Ryazantsev S, Glitz DG. Ribonuclease inhibitor protein of human erythrocytes: characterization, loss of activity in response to oxidative stress, and association with Heinz bodies. *Blood Cells, Molecules, and Diseases*. 1998; 24 (2): 149–64. DOI: 10.1006/bcmd.1998.0182.
- Klink TA, Vicentini AM, Hofsteenge J, Raines RT High-level soluble production and characterization of porcine ribonuclease inhibitor. *Protein expression and purification*. 2001; 22 (2): 174–79. DOI: 10.1006/prep.2001.1422.
- Kobe B, Deisenhofer J. Mechanism of ribonuclease inhibition by ribonuclease inhibitor protein based on the crystal structure of its complex with ribonuclease A. *Journal of molecular biology*. 1996; 264 (5): 1028–43. DOI: 10.1006/jmbi.1996.0694.
- Guo W, Cao L, Jia Z, Wu G, Li T, Lu F, et al. High level soluble production of functional ribonuclease inhibitor in *Escherichia coli* by fusing it to soluble partners. *Protein expression and purification*. 2011; 77 (2): 185–92. DOI: 10.1016/j.pep.2011.01.015.
- Dickson KA, Haigis MC, Raines RT. Ribonuclease inhibitor: structure and function. *Progress in nucleic acid research and molecular biology*. 2005; 80: 349–74. DOI: 10.1016/S0079-6603(05)80009-1.
- Fominaya JM, Hofsteenge J. Inactivation of ribonuclease inhibitor by thiol-disulfide exchange. *Journal of Biological Chemistry*. 1992; 267 (34): 24655–60.
- Kobe B, Kajava AV. The leucine-rich repeat as a protein recognition motif. *Current opinion in structural biology*. 2001; 11 (6): 725–32. DOI: 10.1016/s0959-440x(01)00266-4.
- Blackburn P. Ribonuclease inhibitor from human placenta: rapid purification and assay. *Journal of Biological Chemistry*. 1979; 254 (24): 12484–7.
- Rosano GL, Ceccarelli EA. Recombinant protein expression in *Escherichia coli*: advances and challenges. *Frontiers in microbiology*. 2014; 5: 172. DOI: 10.3389/fmicb.2014.00172.
- Lee FS, Vallee BL. Expression of human placental ribonuclease inhibitor in *Escherichia coli*. *Biochemical and biophysical research communications*. 1989; 160 (1): 115–20. DOI: 10.1016/0006-291x(89)91628-8.
- Šiurkus J, Neubauer P. Reducing conditions are the key for efficient production of active ribonuclease inhibitor in *Escherichia coli*. *Microbial Cell Factories*. 2011; 10 (1): 1–15. DOI: 10.1186/1475-2859-10-31.
- Šiurkus J, Neubauer P. Heterologous production of active ribonuclease inhibitor in *Escherichia coli* by redox state control and chaperonin coexpression. *Microbial cell factories*. 2011; 10: 1–11. DOI: 10.1186/1475-2859-10-65.
- Ohana RF, Encell LP, Zhao K, Simpson D, Slater MR, Urh M, et al. HaloTag7: A genetically engineered tag that enhances bacterial expression of soluble proteins and improves protein purification. *Protein Expression and Purification*. 2009; 68 (1): 110–20. DOI: 10.1016/j.pep.2009.05.010.
- Nishihara K, Kanemori M, Kitagawa M, Yanagi H, Yura, T. Chaperone coexpression plasmids: differential and synergistic roles of DnaK-DnaJ-GrpE and GroEL-GroES in assisting folding of an allergen of Japanese cedar pollen, Cryj2, in *Escherichia coli*. *Appl. Environ Microbiol*. 1998; 64: 1694–99. DOI: 10.1128/AEM.64.5.1694-1699.
- Nishihara K, Kanemori M, Yanagi H, Yura T. Overexpression of trigger factor prevents aggregation of recombinant proteins in *Escherichia coli*. *Appl. Environ Microbiol*. 2000; 66: 884–89. DOI: 10.1128/AEM.66.3.884-889.2000.
- Zaharova MV, Nagornyh MO. Poluchenie bakterial'nogo producenta DNK-zavisimoy RNK-polimerazy bakteriofaga T7 dlja sinteza RNK in vitro. *Mezhdunarodnyj zhurnal prikladnyh i fundamental'nyh issledovanij*. 2022; 12: 9–14. DOI: 10.17513/mjpf.13476. Russian.
- Fuchs AL, Neu A, Sprangers R. A general method for rapid and cost-efficient large-scale production of 5' capped RNA. *RNA*. 2016; 22 (9): 1454–66. DOI: 10.1261/rna.056614.116.
- Ortega C, Oppezzo P, Correa A. Overcoming the Solubility Problem in *E. coli*: Available Approaches for Recombinant Protein Production. *Methods Mol Biol*. 2022; 2406: 35–64. DOI: 10.1007/978-1-0716-1859-2_2.
- Jia B, Jeon CO. High-throughput recombinant protein expression in *Escherichia coli*: current status and future perspectives. *Open biology*. 2016; 6 (8): 160196. DOI: 10.1098/rsob.160196.
- Morão LG, Manzi LR, Clementino LOD, Wrenger C, Nascimento AS. A scalable screening of *E. coli* strains for recombinant protein expression. *PLOS ONE* 2022; 17 (7): e0271403. DOI: 10.1371/journal.pone.0271403.
- Zhang ZX, Nong FT, Wang YZ, Yan CX, Gu Y, Song P, et al. Strategies for efficient production of recombinant proteins in *Escherichia coli*: alleviating the host burden and enhancing protein activity. *Microb Cell Fact*. 2022; 21 (191). DOI: 10.1186/s12934-022-01917-y.
- Flachner B, Dobi K, Benedek A, Cseh S, Lőrincz Z, Hajdú I. Robust Recombinant Expression of Human Placental Ribonuclease Inhibitor in Insect Cells. *Biomolecules*. 2022; 12 (2): 273. DOI: 10.3390/biom12020273.
- Mital S, Christie G, Dikicioglu D. Recombinant expression of insoluble enzymes in *Escherichia coli*: a systematic review of experimental design and its manufacturing implications. *Microb Cell Fact*. 2021; 20 (1): 208. DOI: 10.1186/s12934-021-01698-w.

Литература

- Moenner M, Vosoghi M, Ryazantsev S, Glitz DG. Ribonuclease inhibitor protein of human erythrocytes: characterization, loss of activity in response to oxidative stress, and association with Heinz bodies. *Blood Cells, Molecules, and Diseases*. 1998; 24 (2): 149–64. DOI: 10.1006/bcmd.1998.0182.
- Klink TA, Vicentini AM, Hofsteenge J, Raines RT High-level soluble production and characterization of porcine ribonuclease inhibitor. *Protein expression and purification*. 2001; 22 (2): 174–79. DOI: 10.1006/prep.2001.1422.
- Kobe B, Deisenhofer J. Mechanism of ribonuclease inhibition by

- ribonuclease inhibitor protein based on the crystal structure of its complex with ribonuclease A. *Journal of molecular biology*. 1996; 264 (5): 1028–43. DOI: 10.1006/jmbi.1996.0694.
4. Guo W, Cao L, Jia Z, Wu G, Li T, Lu F, et al. High level soluble production of functional ribonuclease inhibitor in *Escherichia coli* by fusing it to soluble partners. *Protein expression and purification*. 2011; 77 (2): 185–92. DOI: 10.1016/j.pep.2011.01.015.
 5. Dickson KA, Haigis MC, Raines RT. Ribonuclease inhibitor: structure and function. *Progress in nucleic acid research and molecular biology*. 2005; 80: 349–74. DOI: 10.1016/S0079-6603(05)80009-1.
 6. Fominaya JM, Hofsteenge J. Inactivation of ribonuclease inhibitor by thiol-disulfide exchange. *Journal of Biological Chemistry*. 1992; 267 (34): 24655–60.
 7. Kobe B, Kajava AV. The leucine-rich repeat as a protein recognition motif. *Current opinion in structural biology*. 2001; 11 (6): 725–32. DOI: 10.1016/S0959-440X(01)00266-4.
 8. Blackburn P. Ribonuclease inhibitor from human placenta: rapid purification and assay. *Journal of Biological Chemistry*. 1979; 254 (24): 12484–7.
 9. Rosano GL, Ceccarelli EA. Recombinant protein expression in *Escherichia coli*: advances and challenges. *Frontiers in microbiology*. 2014; 5: 172. DOI: 10.3389/fmicb.2014.00172.
 10. Lee FS, Vallee BL. Expression of human placental ribonuclease inhibitor in *Escherichia coli*. *Biochemical and biophysical research communications*. 1989; 160 (1): 115–20. DOI: 10.1016/0006-291X(89)91628-8.
 11. Šiurkus J, Neubauer P. Reducing conditions are the key for efficient production of active ribonuclease inhibitor in *Escherichia coli*. *Microbial Cell Factories*. 2011; 10 (1): 1–15. DOI: 10.1186/1475-2859-10-31.
 12. Šiurkus J, Neubauer P. Heterologous production of active ribonuclease inhibitor in *Escherichia coli* by redox state control and chaperonin coexpression. *Microbial cell factories*. 2011; 10: 1–11. DOI: 10.1186/1475-2859-10-65.
 13. Ohana RF, Encell LP, Zhao K, Simpson D, Slater MR, Urh M, et al. HaloTag7: A genetically engineered tag that enhances bacterial expression of soluble proteins and improves protein purification. *Protein Expression and Purification*. 2009; 68 (1): 110–20. DOI: 10.1016/j.pep.2009.05.010.
 14. Nishihara K, Kanemori M, Kitagawa M, Yanagi H, Yura, T. Chaperone coexpression plasmids: differential and synergistic roles of DnaK-DnaJ-GrpE and GroEL-GroES in assisting folding of an allergen of Japanese cedar pollen, Cryj2, in *Escherichia coli*. *Appl. Environ Microbiol*. 1998; 64: 1694–99. DOI: 10.1128/AEM.64.5.1694-1699.
 15. Nishihara K, Kanemori M, Yanagi H, Yura T. Overexpression of trigger factor prevents aggregation of recombinant proteins in *Escherichia coli*. *Appl. Environ Microbiol*. 2000; 66: 884–89. DOI: 10.1128/AEM.66.3.884-889.2000.
 16. Захарова М. В., Нагорных М. О. Получение бактериального продуцента ДНК-зависимой РНК-полимеразы бактериофага Т7 для синтеза РНК in vitro. *Международный журнал прикладных и фундаментальных исследований*. 2022; 12: 9–14. DOI: 10.17513/mjpf.13476.
 17. Fuchs AL, Neu A, Sprangers R. A general method for rapid and cost-efficient large-scale production of 5' capped RNA. *RNA*. 2016; 22 (9): 1454–66. DOI: 10.1261/rna.056614.116.
 18. Ortega C, Oppezzo P, Correa A. Overcoming the Solubility Problem in *E. coli*: Available Approaches for Recombinant Protein Production. *Methods Mol Biol*. 2022; 2406: 35–64. DOI: 10.1007/978-1-0716-1859-2_2.
 19. Jia B, Jeon CO. High-throughput recombinant protein expression in *Escherichia coli*: current status and future perspectives. *Open biology*. 2016; 6 (8): 160196. DOI: 10.1098/rsob.160196.
 20. Morão LG, Manzi LR, Clementino LOD, Wrenger C, Nascimento AS. A scalable screening of *E. coli* strains for recombinant protein expression. *PLOS ONE* 2022; 17 (7): e0271403. DOI: 10.1371/journal.pone.0271403.
 21. Zhang ZX, Nong FT, Wang YZ, Yan CX, Gu Y, Song P, et al. Strategies for efficient production of recombinant proteins in *Escherichia coli*: alleviating the host burden and enhancing protein activity. *Microb Cell Fact*. 2022; 21 (191). DOI: 10.1186/s12934-022-01917-y.
 22. Flachner B, Dobi K, Benedek A, Cseh S, Lőrincz Z, Hajdú I. Robust Recombinant Expression of Human Placental Ribonuclease Inhibitor in Insect Cells. *Biomolecules*. 2022; 12 (2): 273. DOI: 10.3390/biom12020273.
 23. Mital S, Christie G, Dikicioglu D. Recombinant expression of insoluble enzymes in *Escherichia coli*: a systematic review of experimental design and its manufacturing implications. *Microb Cell Fact*. 2021; 20 (1): 208. DOI: 10.1186/s12934-021-01698-w.

GENETICALLY ENCODED LIGHT-INDUCIBLE SENSOR FOR NUCLEOLAR VISUALIZATION

Zhurlova PA, Besedovskaia ZV, Sokolinskaya EL, Putlyaeva LV ✉

Skolkovo institute of science and technology, Center for Molecular and Cellular Biology, Moscow, Russia

Nucleolus plays a vital role in enhancing rRNA production and maintaining ribosome biogenesis in tumor cells, making the nucleolus a desirable target for genetic and oncological research. The most convenient method for nucleolus monitoring is fluorescent microscopy, combining high efficiency and accessibility. Nevertheless, currently available fluorescent visualization methods are unsuitable for live-cell monitoring of nucleolus because they require continuous labeling. To address this issue, we have developed a genetically encoded Light-Activated Nucleolus Sensing (LANS) system for real-time nucleolar visualization. The combination of eMags domains and reader domain of DPF3 protein, responsible respectively for the light-induced dimerization and targeting the nucleolus, allowed LANS system to efficiently target nucleolus in several cancer cell lines without affecting cell morphology. This system makes it possible to increase the representation of the LANS2 sample in the nucleolus by 1.5 times relative to the fluorescence intensity values obtained before irradiation of the nucleolus. LANS holds the potential to accelerate the search for new drugs and enhance the primary screening of drug compounds in *in vivo* models.

Keywords: epigenetics, fluorescent proteins, eMags, optogenetics, nucleolus

Funding: this work was supported by the Russian Science Foundation grant № 22-24-01109.

✉ **Correspondence should be addressed:** Lidia V. Putlyaeva
Bolshoy Boulevard, 30, Moscow, Russia, 121205; lidia.mikhailova@mail.ru

Received: 27.11.2023 **Accepted:** 11.12.2023 **Published online:** 17.12.2023

DOI: 10.24075/brsmu.2023.048

СОЗДАНИЕ ГЕНЕТИЧЕСКИ КОДИРУЕМОГО СВЕТОИНДУЦИРУЕМОГО СЕНСОРА ДЛЯ ВИЗУАЛИЗАЦИИ ЯДРЫШКА

П. А. Журлова, З. В. Беседовская, Е. Л. Соколинская, Л. В. Путляева ✉

Сколковский институт науки и технологий, Центр молекулярной и клеточной биологии, Москва, Россия

Ядрышки участвуют в усилении продукции рРНК и поддержании биогенеза рибосом в опухолевых клетках, что делает их желанной мишенью в генетических и онкологических исследованиях. Наиболее удобным методом визуализации ядрышка благодаря своей эффективности и доступности является флуоресцентная микроскопия. В настоящее время методы визуализации ядрышек либо неточны, либо непригодны для живых клеток, либо требуют постоянного окрашивания для живого мониторинга. Целью исследования было создать генетически кодируемую систему фотоиндуцируемых сенсоров (light-activated nucleolus sensor, LANS) для визуализации ядрышка в реальном времени. Комбинация домена eMag для фотоиндуцируемой димеризации и ридерного домена белка DPF3 позволяет системе LANS эффективно осуществлять направленное перемещение целевого белка в ядрышко посредством облучения клетки короткими импульсами синего света, не влияя на морфологию клеток. Данная система позволяет увеличить представленность пробы LANS2 в ядрышке в 1,5 раза относительно значений интенсивности флуоресценции, полученных до облучения ядрышка. Созданная система сенсоров LANS позволит ускорить поиск новых лекарств и улучшить первичный скрининг лекарственных соединений в моделях *in vivo*.

Ключевые слова: эпигенетика, флуоресцентные белки, eMags, оптогенетика, ядрышко

Финансирование: работа была поддержана грантом РФФ № 22-24-01109.

✉ **Для корреспонденции:** Лидия Викторовна Путляева
Большой бульвар, д. 30, стр. 1, г. Москва, Россия, 121205; lidia.mikhailova@mail.ru

Статья получена: 27.11.2023 **Статья принята к печати:** 11.12.2023 **Опубликована онлайн:** 17.12.2023

DOI: 10.24075/vrgmu.2023.048

The nucleolus is an intranuclear compartment that orchestrates cell cycle regulation, ribosome biogenesis, telomerase activity, p53 metabolism, and small RNA processing. Nevertheless, the primary role of nucleolus is the ribosome biogenesis, one of the most energy-intensive and tightly regulated processes in a cell [1]. Downregulation of rRNA gene transcription is related to the reduction in nucleolar size, while the amount of nucleolar rRNA has a positive correlation with the rate of protein synthesis and cell growth [2, 3]. Nucleolus undergoes changes during carcinogenesis, including increase in the size and abnormally stimulated functions, altering molecular pathways of such tumor suppressors as pRb, p53, c-Myc, cyclin D1, NF-κB, ErbB3, BCL-2, RAD51, and BCL-2 [4–8]. Numerous therapeutic strategies rely on targeting nucleolus, including using the selective inhibitors of RNA Pol I, mTOR, AKT, etc. [9] in therapy of haematological cancers [10, 11], non-small cell lung cancer [12], renal cell carcinoma, breast cancer, lymphoma [13], and others. Therefore, the development of new

chemotherapeutic agents as well as studying their potential side effects may benefit from nucleolar visualization methods.

The most common method to visualize nucleolus is immunofluorescent staining using antibodies specific to nucleolar proteins [14]. Immunofluorescence is only compatible with fixed cells, therefore it cannot be used to study dynamic cell processes, while fluorescent microscopy appears to be a possible solution allowing for research of spatio-temporal changes in the nucleolus. [15]. Recently, a fluorescent probe for simultaneous mitochondria and nucleoli visualization was developed. It contained two emission metal complexes based on pyrazole linked to triphenylphosphine and copper (C1 and C2) [16]. Another fluorescent probe using a 9-(dicyanovinyl)julolidine (DCVJ) rotor was shown to efficiently target both mitochondria and nucleoli with minimal cytotoxicity [17]. These methods are useful for both imaging of live cells and monitoring their responses to stimuli, yet they are limited by the fact that fluorescent dyes degrade over time and are not inherited by daughter cells.

Genetically encoded fluorescent sensors overcome the limitations of the fluorescent dyes, providing the same flexibility, specificity, and compatibility with biological systems. Additionally, these sensors are non-toxic, suitable for real-time monitoring, and more time-efficient compared to fixed-cell analyses [18]. Recently, researchers have introduced a novel optogenetic system known as enhanced Magnets (eMags) [19]. This system is based on photodimerizing protein domains derived from the photoreceptor Vivid (VVD) found in *Neurospora crassa*. When exposed to blue light, oppositely charged VVD monomers, named eMagA and eMagB, undergo conformational changes forming dimers. The dimers dissociate without the presence of blue light, therefore the system can be used for the reversible light-dependent dimerization of the target proteins.

In this study, we developed the Light-Activated Nucleolus Sensing (LANS), a novel genetically encoded fluorescent sensor system for real-time nucleolar monitoring. LANS take advantage of eMags light-dependent dimerization, suggesting possible application of the sensor in recruiting proteins of interest to the nucleolus using light stimuli. The LANS system can be beneficial for biomedical research, specifically for testing drugs affecting nucleolus functioning.

METHODS

Molecular Cloning

All plasmids were constructed using the Golden Gate cloning system [20] and the MoClo Toolkit vector set (AddGene Kit #1000000044). The sequences of eMagA and eMagB were obtained from [19] and synthesized by "Cloning Facility" (Moscow, Russia) in the pAGM1301 vector. The DPF3 sequence was amplified using the following primers (DPF3_CCAT_FOR gttGAAGACatCCATgggaacagtcattccaataactactgtgactctctctgggggctccaacatgaacaagaagagtgggcggcc, DPF3_AATG_REV gttGAAGACatCATTGTGGCGACCGG TCCGGATCCGCCCGCCGCTtttgagcagttcccag), which introduced a Bpil restriction site into the sequence, and then cloned into the pAGM1276 vector.

The MoClo technology and pICH47732 vector were used for the assembly of the final plasmids eMagB-mScarlet(LANS2) and DPF3-mNeonGreen-NLS-eMagA(LANS1), following the protocol described in [20]. Bpil (BbsI) and Eco31I (BsaI) restriction enzymes (Thermo Scientific, Waltham, MA; USA) and T4 phage ligase (Evrogen; Russia) were used for cloning.

Cell Culture and Transfection

HeLa Kyoto cells were cultured at 37 °C (5% CO₂) in DMEM medium (PanEco; Russia) supplemented with 10% fetal bovine serum (BioSera, France), 100 U/ml penicillin, and 100 µg/ml streptomycin (PanEco; Russia). For transfection, HeLa cells were cultured in DMEM-full medium in 35 mm Petri dishes with glass bottoms (SPL Life Sciences; Korea) and transfected using GenJect-39 reagent (Molox; Russia) following the manufacturer's instructions.

Live Cell Fluorescence Microscopy

For live-cell visualization, cells were cultured in confocal dishes with glass bottoms (SPL Life Sciences). Just before microscopy, the DMEM medium was replaced with MEM visualization medium (PanEco) supplemented with 10% fetal bovine serum (BioSera) and 20 mM HEPES (Corning, New York, NY, USA).

In vivo fluorescence microscopy was performed using the Keyence Biorevo BZ-9000 fluorescent microscope (Keyence; Japan). Cells were imaged at 60x magnification using the CFI Plan Apo λ60xH/NA1.40 objective. Images were acquired in two channels: green (GFP-B filter cube, excitation 480/30 nm) for blue light irradiation of cells for 200 ms and visualization of LANS1, red (Texas Red filter cube, excitation 560/40 nm, emission 630/75 nm) for detection of LANS2 fluorescence.

Image Analysis

To calculate relative nucleolus to cytoplasm distribution of the sensors over time, the "ROI manager" tool of the Fiji software was used. First ROI was manually set by tracing the nucleolus, second ROI was set as an area of the cytoplasm in the same cell. The values corresponding to nucleolus/cytoplasm ratio (Fluorescence intensity; Fig. 1) were obtained by first dividing intensity of the first ROI (normalized by the area) by the corresponding value of the second ROI, and second dividing the obtained value by the same value corresponding to the preinduction image. Graph was made with GraphPad Prism 8.

RESULTS

We engineered a genetically encoded fluorescent system LANS, which is based on a photodimerizing pair of probes, LANS1 and LANS2. LANS1 consists of the PHD domain sequence taken from the DPF3 protein, the green fluorescent protein mNeonGreen, a nuclear localization signal (NLS), and the eMagA (Fig. 1A, upper panel). eMagA is part of the light-dependent enhanced Magnets (eMags) system, based on the Vivid photoreceptor (VVD) from *Neurospora crassa* [19]. The complementary LANS2 contains the eMagB and the red fluorescent protein mScarlet (Fig. 1A, lower panel). Also, DPF3, is a domain with affinity for the histone modification H3K4me1 in its dimeric state, however, in our laboratory it has been experimentally demonstrated that the sensor based on the monomeric DPF3 accumulates in the nucleolus (Fig. 1C). Therefore, before blue light induction LANS1 was enriched in the nucleolar regions, while LANS2 was distributed uniformly across the cellular compartments. After the 200 ms induction LANS1 and LANS2 interacted by oppositely charged eMag domains, forming a heterodimer (Fig. 1B).

To demonstrate the reversibility of LANS2 binding to the nucleolus, we exposed cells expressing LANS to 200 ms of blue light, followed by incubation in darkness. We compared the relative changes in fluorescence levels before and after the exposure and revealed that the probe returned to its initial distribution within approximately 60 seconds (Fig. 1D).

Our findings demonstrate the potential of the developed LANS system for reversible light-dependent visualization of the nucleolus compartment in live cells. A combination of LANS1 enriching the nucleoli regions and LANS2 freely moving across the cell enabled recruitment of LANS2 to the nucleolar regions through brief exposure to blue light. Moreover, this sensor can be effectively used to investigate nucleolus dynamics and to directly transport proteins of interest to the nucleolus by fusing the proteins to LANS2.

DISCUSSION

The nucleolus is a dynamic subnuclear compartment, which plays a crucial role in ribonucleoprotein assembly for ribosome biogenesis as well as in rRNA synthesis and processing. Therefore, nucleolar alterations are associated with aging and

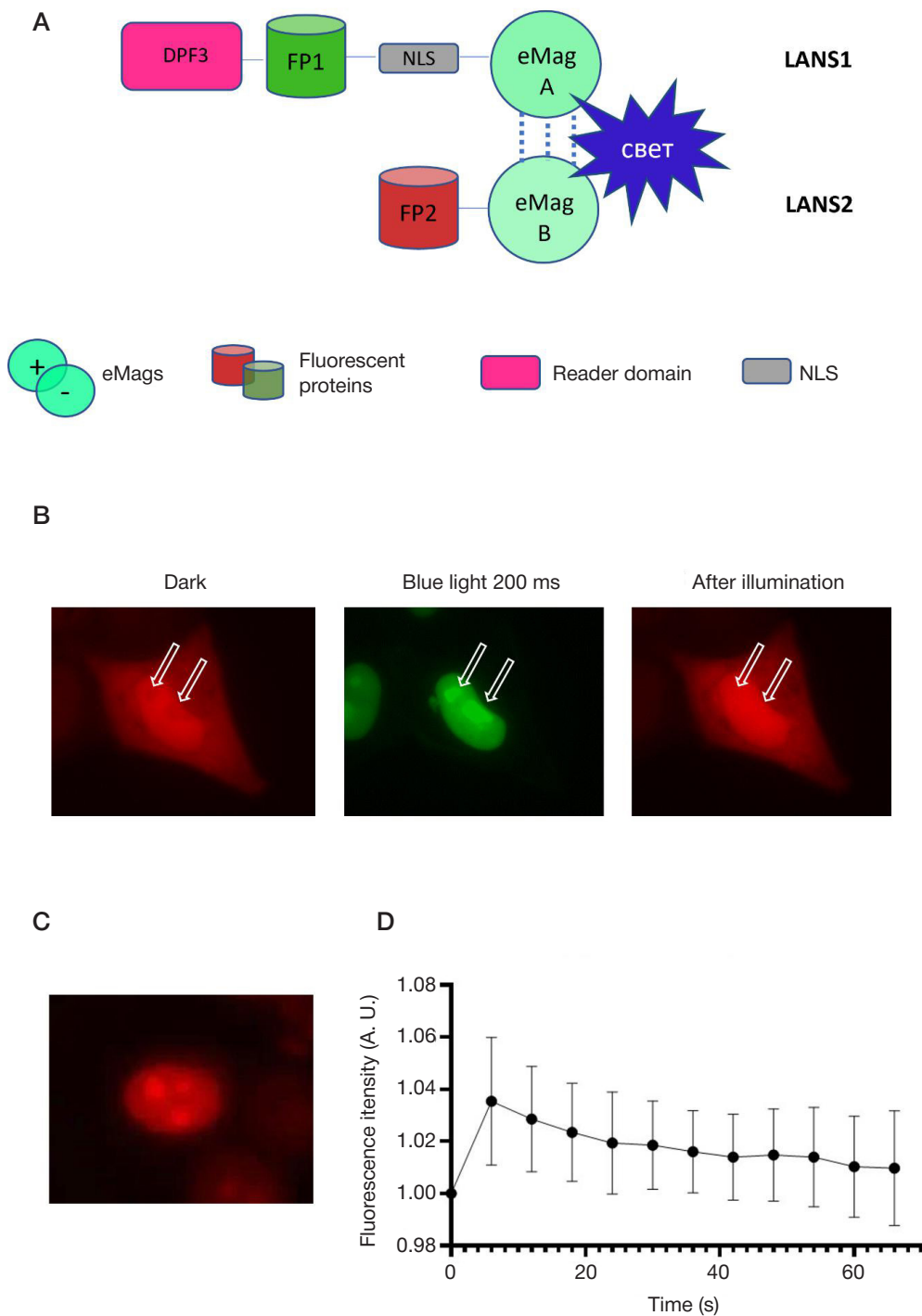


Fig. 1. Characterization of the genetically engineered LANS system enabling light-dependent recruitment of LANS2 to nucleoli. **A.** Schematic representation of the light-dependent dimerization probes LANS1 and LANS2. FP=fluorescent protein. **B.** Fluorescence microscopy images of HeLa cells transfected with LANS1 and LANS2 before (*left*), during (*middle*), and after (*right*) blue light irradiation. White arrows indicate the nucleoli. **C.** Fluorescence image of the nucleolus in HeLa cell expressing the DPF3-mScarlet sensor. **D.** Graph showing the nucleolus/cytoplasm relative fluorescence ratio for LANS2 during the experiment. Data represent mean \pm range ($n = 33$ nucleoli)

are critical in development of different human pathologies, including cancer and neurodegeneration [21]. Numerous research laboratories are actively developing optogenetic delivery systems to target proteins to the nucleolus [22]. These systems rely on photosensitive proteins that undergo structural changes and form dimers when exposed to specific wavelengths of light. As a result, such systems bring target proteins together. Researchers have effectively utilized photodimerizing domains to control diverse cellular processes, including signaling pathways [23, 24], organelle transport [25, 26], nucleocytoplasmic transport [27, 28], cytoskeleton dynamics [29], and phase separation [30, 31].

The results obtained in this work indicating the possibility of light-induced targeting into the nucleus, are quite consistent with data obtained in other laboratories. For example, the photoinduced nuclear localization signal LINuS allowed researchers to translocate the mCherry protein from the cytoplasm into the nucleus, increasing its representation in the nucleus by approximately 1.8 times [32], while the LANS system allowed us to increase the representation of the LANS2 probe in the nucleolus by 1.5 times regarding to the fluorescence intensity values obtained before irradiation of the nucleolus. Thus, this sensor system may be useful for light-induced recruitment of target proteins into the nucleolus.

CONCLUSIONS

In this study we introduced LANS, a novel genetically encoded light-dependent sensor system, which exhibits minimal cellular toxicity. By triggering the light-induced heterodimerization of the sensor system by eMagA and eMagB photodomains, we observed the translocation of the LANS2 probe to the nucleolus,

allowing us to visualize this compartment. It is important to mention that the nucleolus/cytoplasm fluorescence intensity ratio before and after irradiation is relatively modest (Fig. 1D), likely due to the high expression levels of the LANS1 and LANS2 in our experimental setup. This concern can be addressed in the future by optimizing the concentrations of sensor components or creating a stable cell line expressing LANS.

References

- Engbrecht M, Mangerich A. The Nucleolus and PARP1 in Cancer Biology. *Cancers*. 2020; 12.
- Bersaglieri C, Santoro R. Genome Organization in and around the Nucleolus. *Cells*. 2019; 8.
- Weeks SE, Metge BJ, Samant RS. The nucleolus: a central response hub for the stressors that drive cancer progression. *Cell Mol Life Sci*. 2019; 76: 4511–24.
- Tréré D, Ceccarelli C, Montanaro L, Tosti E, Derenzini M. Nucleolar size and activity are related to pRb and p53 status in human breast cancer. *J Histochem Cytochem*. 2004; 52: 1601–7.
- Russo A, Russo G. Ribosomal Proteins Control or Bypass p53 during Nucleolar Stress. *Int J Mol Sci*. 2017; 18.
- Peddibhotla S, Wei Z, Papineni R, Lam MH, Rosen JM, Zhang P. The DNA damage effector Chk1 kinase regulates Cdc14B nucleolar shuttling during cell cycle progression. *Cell Cycle*. 2011; 10: 671–9.
- Andrique L, Fauvin D, El Maassarani M, Colasson H, Vannier B, Séité P. ErbB3(80 kDa), a nuclear variant of the ErbB3 receptor, binds to the Cyclin D1 promoter to activate cell proliferation but is negatively controlled by p14ARF. *Cell Signal*. 2012; 24: 1074–85.
- Sasaki M, Kawahara K, Nishio M, Mimori K, Kogo R, Hamada K, et al. Regulation of the MDM2-P53 pathway and tumor growth by PICT1 via nucleolar RPL11. *Nat Med*. 2011; 17: 944–51.
- Carotenuto P, Pecoraro A, Palma G, Russo G, Russo A. Therapeutic Approaches Targeting Nucleolus in Cancer. *Cells*. 2019; 8.
- Bywater MJ, Poortinga G, Sanij E, Hein N, Peck A, Cullinane C, et al. Inhibition of RNA polymerase I as a therapeutic strategy to promote cancer-specific activation of p53. *Cancer Cell*. 2012; 22: 51–65.
- Quin JE, Devlin JR, Cameron D, Hannan KM, Pearson RB, Hannan RD. Targeting the nucleolus for cancer intervention. *Biochim Biophys Acta*. 2014; 1842: 802–16.
- Chan JC, Hannan KM, Riddell K, Ng PY, Peck A, Lee RS, et al. AKT promotes rRNA synthesis and cooperates with c-MYC to stimulate ribosome biogenesis in cancer. *Sci Signal*. 2011; 4: ra56.
- Wall M, Poortinga G, Stanley KL, Lindemann RK, Bots M, Chan CJ, et al. The mTORC1 inhibitor everolimus prevents and treats Eμ-Myc lymphoma by restoring oncogene-induced senescence. *Cancer Discov*. 2013; 3: 82–95.
- Stenström L, Mahdessian D, Gnann C, Cesnik AJ, Ouyang W, Leonetti MD, et al. Mapping the nucleolar proteome reveals a spatiotemporal organization related to intrinsic protein disorder. *Mol Syst Biol*. 2020; 16: e9469.
- Farhy C, Hariharan S, Ylanko J, Orozco L, Zeng F-Y, Pass I, et al. Improving drug discovery using image-based multiparametric analysis of the epigenetic landscape. *Elife*. 2019; 8.
- Mayank, Rani R, Singh A, Garg N, Kaur N, Singh N. Mitochondria- and nucleolus-targeted copper(II) complexes with pyrazole-linked triphenylphosphine moieties for live cell imaging. *Analyst*. 2019; 145: 83–90.
- Mukherjee T, Soppina V, Ludovic R, Mély Y, Klymchenko AS, Collot M, et al. Live-cell imaging of the nucleolus and mapping mitochondrial viscosity with a dual function fluorescent probe. *Org Biomol Chem*. 2021; 19: 3389–95.
- Martin RM, Herce HD, Ludwig AK, Cardoso MC. Visualization of the Nucleolus in Living Cells with Cell-Penetrating Fluorescent Peptides. *Methods Mol Biol*. 2016; 1455: 71–82.
- Benedetti L, Marvin JS, Falahati H, Guillén-Samander A, Looger LL, De Camilli P. Optimized Vivid-derived Magnets photodimerizers for subcellular optogenetics in mammalian cells. *Elife*. 2020; 9.
- Werner S, Engler C, Weber E, Gruetzner R, Marillonnet S. Fast track assembly of multigene constructs using Golden Gate cloning and the MoClo system. *Bioeng Bugs*. 2012; 3: 38–43.
- Corman A, Sirozh O, Lafarga V, Fernandez-Capetillo O. Targeting the nucleolus as a therapeutic strategy in human disease. *Trends Biochem Sci*. 2023; 48: 274–87.
- Tan P, Hong T, Cai X, Li W, Huang Y, He L, et al. Optical control of protein delivery and partitioning in the nucleolus. *Nucleic Acids Res*. 2022; 50: e69.
- Gray NW, Weimer RM, Bureau I, Svoboda K. Rapid redistribution of synaptic PSD-95 in the neocortex in vivo. *PLoS Biol*. 2006; 4: e370.
- Grusch M, Schelch K, Riedler R, Reichhart E, Differ C, Berger W, et al. Spatio-temporally precise activation of engineered receptor tyrosine kinases by light. *EMBO J*. 2014; 33: 1713–26.
- van Bergeijk P, Adrian M, Hoogenraad CC, Kapitein LC. Optogenetic control of organelle transport and positioning. *Nature*. 2015; 518: 111–4.
- Duan L, Che D, Zhang K, Ong Q, Guo S, Cui B. Optogenetic control of molecular motors and organelle distributions in cells. *Chem Biol*. 2015; 22: 671–82.
- Lerner AM, Yumerefendi H, Goudy OJ, Strahl BD, Kuhlman B. Engineering Improved Photoswitches for the Control of Nucleocytoplasmic Distribution. *ACS Synth Biol*. 2018; 7: 2898–907.
- Niopek D, Wehler P, Roensch J, Eils R, Di Ventura B. Optogenetic control of nuclear protein export. *Nat Commun*. 2016; 7: 10624.
- van Haren J, Charafeddine RA, Ettinger A, Wang H, Hahn KM, Wittmann T. Local control of intracellular microtubule dynamics by EB1 photodissociation. *Nat Cell Biol*. 2018; 20: 252–61.
- Shin Y, Berry J, Pannucci N, Haataja MP, Toettcher JE, Brangwynne CP. Spatiotemporal Control of Intracellular Phase Transitions Using Light-Activated optoDroplets. *Cell*. 2017; 168: 159–71.e14.
- Dine E, Gil AA, Uribe G, Brangwynne CP, Toettcher JE. Protein Phase Separation Provides Long-Term Memory of Transient Spatial Stimuli. *Cell Syst*. 2018; 6: 655–63.e5.
- Niopek D, Benzinger D, Roensch J, Draebing T, Wehler P, Eils R, et al. Engineering light-inducible nuclear localization signals for precise spatiotemporal control of protein dynamics in living cells. *Nat Commun*. 2014; 5: 4404.

Литература

- Engbrecht M, Mangerich A. The Nucleolus and PARP1 in Cancer Biology. *Cancers*. 2020; 12.
- Bersaglieri C, Santoro R. Genome Organization in and around the Nucleolus. *Cells*. 2019; 8.
- Weeks SE, Metge BJ, Samant RS. The nucleolus: a central response hub for the stressors that drive cancer progression. *Cell Mol Life Sci*. 2019; 76: 4511–24.
- Tréré D, Ceccarelli C, Montanaro L, Tosti E, Derenzini M. Nucleolar size and activity are related to pRb and p53 status in human breast cancer. *J Histochem Cytochem*. 2004; 52: 1601–7.

5. Russo A, Russo G. Ribosomal Proteins Control or Bypass p53 during Nucleolar Stress. *Int J Mol Sci.* 2017; 18.
6. Peddibhotla S, Wei Z, Papineni R, Lam MH, Rosen JM, Zhang P. The DNA damage effector Chk1 kinase regulates Cdc14B nucleolar shuttling during cell cycle progression. *Cell Cycle.* 2011; 10: 671–9.
7. Andrique L, Fauvin D, El Maassarani M, Colasson H, Vannier B, Séité P. ErbB3(80 kDa), a nuclear variant of the ErbB3 receptor, binds to the Cyclin D1 promoter to activate cell proliferation but is negatively controlled by p14ARF. *Cell Signal.* 2012; 24: 1074–85.
8. Sasaki M, Kawahara K, Nishio M, Mimori K, Kogo R, Hamada K, et al. Regulation of the MDM2-P53 pathway and tumor growth by PICT1 via nucleolar RPL11. *Nat Med.* 2011; 17: 944–51.
9. Carotenuto P, Pecoraro A, Palma G, Russo G, Russo A. Therapeutic Approaches Targeting Nucleolus in Cancer. *Cells.* 2019; 8.
10. Bywater MJ, Poortinga G, Sanij E, Hein N, Peck A, Cullinane C, et al. Inhibition of RNA polymerase I as a therapeutic strategy to promote cancer-specific activation of p53. *Cancer Cell.* 2012; 22: 51–65.
11. Quin JE, Devlin JR, Cameron D, Hannan KM, Pearson RB, Hannan RD. Targeting the nucleolus for cancer intervention. *Biochim Biophys Acta.* 2014; 1842: 802–16.
12. Chan JC, Hannan KM, Riddell K, Ng PY, Peck A, Lee RS, et al. AKT promotes rRNA synthesis and cooperates with c-MYC to stimulate ribosome biogenesis in cancer. *Sci Signal.* 2011; 4: ra56.
13. Wall M, Poortinga G, Stanley KL, Lindemann RK, Bots M, Chan CJ, et al. The mTORC1 inhibitor everolimus prevents and treats Eμ-Myc lymphoma by restoring oncogene-induced senescence. *Cancer Discov.* 2013; 3: 82–95.
14. Stenström L, Mahdessian D, Gnann C, Cesnik AJ, Ouyang W, Leonetti MD, et al. Mapping the nucleolar proteome reveals a spatiotemporal organization related to intrinsic protein disorder. *Mol Syst Biol.* 2020; 16: e9469.
15. Farhy C, Hariharan S, Ylanko J, Orozco L, Zeng F-Y, Pass I, et al. Improving drug discovery using image-based multiparametric analysis of the epigenetic landscape. *Elife.* 2019; 8.
16. Mayank, Rani R, Singh A, Garg N, Kaur N, Singh N. Mitochondria- and nucleolus-targeted copper(I) complexes with pyrazole-linked triphenylphosphine moieties for live cell imaging. *Analyst.* 2019; 145: 83–90.
17. Mukherjee T, Soppina V, Ludovic R, Mély Y, Klymchenko AS, Collot M, et al. Live-cell imaging of the nucleolus and mapping mitochondrial viscosity with a dual function fluorescent probe. *Org Biomol Chem.* 2021; 19: 3389–95.
18. Martin RM, Herce HD, Ludwig AK, Cardoso MC. Visualization of the Nucleolus in Living Cells with Cell-Penetrating Fluorescent Peptides. *Methods Mol Biol.* 2016; 1455: 71–82.
19. Benedetti L, Marvin JS, Falahati H, Guillén-Samander A, Looger LL, De Camilli P. Optimized Vivid-derived Magnets photodimerizers for subcellular optogenetics in mammalian cells. *Elife.* 2020; 9.
20. Werner S, Engler C, Weber E, Gruetzner R, Marillonnet S. Fast track assembly of multigene constructs using Golden Gate cloning and the MoClo system. *Bioeng Bugs.* 2012; 3: 38–43.
21. Corman A, Sirozh O, Lafarga V, Fernandez-Capetillo O. Targeting the nucleolus as a therapeutic strategy in human disease. *Trends Biochem Sci.* 2023; 48: 274–87.
22. Tan P, Hong T, Cai X, Li W, Huang Y, He L, et al. Optical control of protein delivery and partitioning in the nucleolus. *Nucleic Acids Res.* 2022; 50: e69.
23. Gray NW, Weimer RM, Bureau I, Svoboda K. Rapid redistribution of synaptic PSD-95 in the neocortex in vivo. *PLoS Biol.* 2006; 4: e370.
24. Grusch M, Schelch K, Riedler R, Reichhart E, Differ C, Berger W, et al. Spatio-temporally precise activation of engineered receptor tyrosine kinases by light. *EMBO J.* 2014; 33: 1713–26.
25. van Bergeijk P, Adrian M, Hoogenraad CC, Kapitein LC. Optogenetic control of organelle transport and positioning. *Nature.* 2015; 518: 111–4.
26. Duan L, Che D, Zhang K, Ong Q, Guo S, Cui B. Optogenetic control of molecular motors and organelle distributions in cells. *Chem Biol.* 2015; 22: 671–82.
27. Lerner AM, Yumerefendi H, Goudy OJ, Strahl BD, Kuhlman B. Engineering Improved Photoswitches for the Control of Nucleocytoplasmic Distribution. *ACS Synth Biol.* 2018; 7: 2898–907.
28. Niopek D, Wehler P, Roensch J, Eils R, Di Ventura B. Optogenetic control of nuclear protein export. *Nat Commun.* 2016; 7: 10624.
29. van Haren J, Charafeddine RA, Ettinger A, Wang H, Hahn KM, Wittmann T. Local control of intracellular microtubule dynamics by EB1 photodissociation. *Nat Cell Biol.* 2018; 20: 252–61.
30. Shin Y, Berry J, Pannucci N, Haataja MP, Toettcher JE, Brangwynne CP. Spatiotemporal Control of Intracellular Phase Transitions Using Light-Activated optoDroplets. *Cell.* 2017; 168: 159–71.e14.
31. Dine E, Gil AA, Uribe G, Brangwynne CP, Toettcher JE. Protein Phase Separation Provides Long-Term Memory of Transient Spatial Stimuli. *Cell Syst.* 2018; 6: 655–63.e5.
32. Niopek D, Benzinger D, Roensch J, Draebing T, Wehler P, Eils R, et al. Engineering light-inducible nuclear localization signals for precise spatiotemporal control of protein dynamics in living cells. *Nat Commun.* 2014; 5: 4404.

NEAT1_1 LONG NON-CODING RNA REDUCES THE SURVIVAL OF PRIMARY NEURONAL CELLS UNDER ER-STRESS

Pukaeva NE^{1,2}, Zalevskaya VN², Deykin AV³, Taubinskaya MI², Kukharskaya OA², Ovchinnikov RK^{1,2}, Antohin AI¹, Kukharsky MS^{1,2}✉

¹ Pirogov Russian National Research Medical University, Moscow, Russia

² Institute of Physiologically Active Compounds at Federal Research Center of Problems of Chemical Physics and Medicinal Chemistry, Russian Academy of Sciences, Chernogolovka, Russia

³ Belgorod State National Research University, Belgorod, Russia

NEAT1 long non-coding RNAs play an important role in the central nervous system (CNS) and are associated with a number of pathological conditions. Increased levels of NEAT1 in the brain have been observed in neurodegenerative and psychiatric diseases — the significance of such an increase is still poorly understood. Functionally, NEAT1 is associated with cellular stress pathways in the nervous system. The aim of the current study was to evaluate the effect of increased levels of the short isoform NEAT1_1 on survival of mice primary hippocampal cultures under ER-stress induced by MG132 proteasome inhibitor. Primary cultures were obtained from transgenic animals expressing human NEAT1_1. Cellular composition and apoptosis were assessed using immunocytochemical staining. The expression of apoptosis signaling pathway genes was analyzed by quantitative PCR with reverse transcription. No differences in cellular composition and morphological characteristics of neurons were observed in primary neuronal cultures obtained from transgenic animals as compared to wild type cultures. Induction of ER-stress resulted in a more significant increase in apoptotic death of cells including neurons in NEAT1_1 expressing cultures in comparison with the wild type cultures. ER-stress signaling pathway genes *Atf4* and *Ddit3* were less expressed in transgenic cultures under stress. Expression of *Bcl2l2* and *Mcl1* anti-apoptotic genes was reduced as well. Thus, high levels of NEAT1_1 in primary neuronal cultures increased apoptotic cell death under ER-stress.

Keywords: long non-coding RNAs, NEAT1_1, ER-stress, primary neuronal cultures, apoptosis

Funding: The study was supported by the Russian Science Foundation, Project No. 22-25-00645.

Acknowledgements: Authors would like to express their gratitude to FRC PCP MC RAS Collective Use Center (FFSN-2021-0005 (2021 – 2023) for providing the opportunity to conduct experiments using laboratory animals.

Author contribution: Pukaeva NE — cell culture experiments, apoptosis data analysis, Zalevskaya VN — cell culture experiments, Deykin AV — generating transgenic mice, Taubinskaya MI — cell culture experiments, neuron morphology analysis, Kukharskaya OA — cell culture experiments, cell death analysis, Ovchinnikov RK — data analysis, manuscript writing, Antohin AI — manuscript editing, Kukharsky MS — study design, data analysis, manuscript writing and editing.

Compliance with ethical standards: the study was approved by the Ethics Committee of the FRC PCP MC RAS (Protocol № 53 dated December 18, 2020); animal experimental work was carried out in accordance with the Rules of Good Laboratory Practice in the Russian Federation (2016).

✉ **Correspondence should be addressed:** Michail S. Kukharsky
Ostrovitianova, 1/9, Moscow, 117997, Russia; kukharskym@rsmu.ru

Received: 08.11.2023 **Accepted:** 16.12.2023 **Published online:** 31.12.2023

DOI: 10.24075/brsmu.2023.053

ДЛИННАЯ НЕКОДИРУЮЩАЯ РНК NEAT1_1 СНИЖАЕТ ВЫЖИВАЕМОСТЬ ПЕРВИЧНЫХ НЕЙРОННЫХ КЛЕТОК ПРИ ЭПР-СТРЕССЕ

Н. Е. Пукаева^{1,2}, В. Н. Залевская², А. В. Дейкин³, М. И. Таубинская², О. А. Кухарская², Р. К. Овчинников^{1,2}, А. И. Антохин¹, М. С. Кухарский^{1,2}✉

¹ Российский национальный исследовательский медицинский университет имени Н. И. Пирогова, Москва, Россия

² Институт физиологически активных веществ Федерального исследовательского центра проблем химической физики и медицинской химии Российской академии наук, Черноголовка, Россия

³ Белгородский государственный национальный исследовательский университет, Белгород, Россия

Длинная некодирующая РНК NEAT1 играет важную роль в работе центральной нервной системы (ЦНС) и участвует в развитии ряда патологических состояний. Повышение уровня NEAT1 в мозге происходит при нейродегенеративных и психических заболеваниях. Какую роль играет такое повышение остается неясным. Функционально NEAT1 связывают с реализацией ответа на клеточный стресс в нервной системе. Целью работы было оценить влияние повышенного уровня короткой изоформы NEAT1_1 на выживаемость первичных гиппокампальных культур мышей, при ЭПР-стрессе, индуцированном с помощью ингибитора протеасом MG132. Первичные культуры были получены от трансгенных животных, экспрессирующих NEAT1_1 человека. Характеристику клеточного состава и оценку апоптоза проводили с помощью иммуноцитохимического окрашивания. Анализ экспрессии генов сигнальных путей апоптоза осуществляли методом количественной ПЦР с обратной транскрипцией. Первичные нейронные культуры, полученные от трансгенных животных, не отличались от культур дикого типа по клеточному составу и морфологическим характеристикам нейронов. При индукции ЭПР-стресса происходило усиление апоптотической гибели клеток, в том числе нейронов, в культурах, экспрессирующих NEAT1_1 в сравнении с культурами дикого типа. Активация генов сигнальных путей ЭПР-стресса *Atf4* и *Ddit3* была менее выражена в трансгенных культурах при стрессе. Кроме того, был снижен уровень экспрессии антиапоптотических генов *Bcl2l2* и *Mcl1*. Таким образом, повышенный уровень NEAT1_1 в первичных нейронных культурах усиливает апоптотическую гибель клеток при ЭПР-стрессе.

Ключевые слова: длинные некодирующие РНК, NEAT1_1, ЭПР-стресс, первичные нейронные культуры, апоптоз

Финансирование: исследование выполнено при финансовой поддержке Российского Научного Фонда, проект № 22-25-00645.

Благодарности: авторы выражают благодарность Центру коллективного пользования ИФВ РАН (FFSN-2021-0005 (2021–2023) за предоставленную возможность проведения экспериментов с использованием лабораторных животных.

Вклад авторов: Н. Е. Пукаева — проведение экспериментов на клеточных культурах, анализ клеточной гибели; В. Н. Залевская — работа с клеточными культурами; А. В. Дейкин — получение трансгенной линии мышей; М. И. Таубинская — работа с клеточными культурами, анализ морфологии нейронов, О. А. Кухарская — работа с клеточными культурами, анализ клеточной гибели; Р. К. Овчинников — анализ и интерпретация результатов, подготовка текста рукописи; А. И. Антохин — редактирование рукописи; М. С. Кухарский — планирование исследования, анализ и интерпретация данных, подготовка и редактирование статьи.

Соблюдение этических стандартов: исследование одобрено этическим комитетом ИФВ ФГБУН ФИЦ ПХФ и МХ РАН (протокол № 53 от 18 декабря 2020 г.); работу с животными проводили в соответствии с «Правилами надлежащей лабораторной практики в Российской Федерации» от 2016 г.

✉ **Для корреспонденции:** Михаил Сергеевич Кухарский
ул. Островитянова, д. 1, стр. 9, г. Москва, 117997, Россия; kukharskym@rsmu.ru

Статья получена: 08.11.2023 **Статья принята к печати:** 16.12.2023 **Опубликована онлайн:** 31.12.2023

DOI: 10.24075/vrgmu.2023.053

Long noncoding RNAs (lncRNAs) are molecules longer than 200 nucleotides without open reading frames [1]. lncRNAs are involved in various physiological and pathological processes such as cell cycle regulation, cell differentiation, apoptosis, and inflammation [2]. The role of lncRNAs in evolution of mammalian and human brain seems to be of particular importance. This is supported by the fact that about 40% of all identified human lncRNAs are specifically expressed in the brain [3]. Many studies have demonstrated the involvement of lncRNAs in the development of the nervous system, neuronal plasticity as well as in the pathogenesis of neurological diseases [4]. NEAT1 (nuclear enriched abundant transcript 1) is one of the lncRNAs that has been convincingly shown to be associated with the development of pathological conditions of the nervous system. Changes in NEAT1 levels in the brain are observed in a number of neurodegenerative diseases and psychiatric disorders such as amyotrophic lateral sclerosis (ALS), frontotemporal dementia (FTD), Huntington's disease (HD), Alzheimer's disease (AD), and schizophrenia [5]. In most cases, increased NEAT1 levels in the brain of patients with these diseases are [6–8]. Whether the role of such increase is protective or pathogenetic is still unclear. Experimental data suggest that NEAT1 is a stress-activated gene and its expression is increased in response to pathological effects of stress at the cellular level [9, 10]. NEAT1 gene is transcribed into two RNA isoforms, NEAT1_1 (3.7 kb) and NEAT1_2 (23 kb) overlapping at their 5'-ends [5]. Accumulation of the long NEAT1_2 isoform in human nervous system cells has been confirmed for developing ALS conditions only [11, 12]. For other diseases, NEAT1 dysfunctions are apparently associated with changes in the short isoform levels (NEAT1_1) [13]. In mice, the long isoform was not normally detected in the nervous tissue while the short isoform is expressed in all parts of the CNS [14].

Under physiological conditions, endoplasmic reticulum (ER) is the main subcellular compartment involved in protein quality control, where proteins are properly folded, matured, and degraded [15]. When these processes are disrupted, unfolded and misfolded proteins are accumulated in cells resulting in ER stress, a specific type of cellular stress [16]. This most common pathologic event at the cellular level occurs in neurons located in the lesion zone during neurodegeneration [17]. In case of impossibility to restore protein homeostasis, cell adaptive programs shift towards induction of apoptotic signaling pathways leading to death of the irreversibly damaged neurons [18].

NEAT1 is involved in forming specific ribonucleoprotein (RNP) complexes in cells [6, 11, 13]. Pathological aggregation of RNP proteins TDP-43 and FUS leads to ER stress and neuronal death. TDP-43 and FUS aggregation in the nervous system was found in ALS, FTD, AD and other neurodegenerative diseases. The direct interaction of NEAT1 with such proteins raises the question about the possible influence of this RNA on the development of pathological aggregation and cell death [12, 13].

In the current study, we investigated the effect of the increased levels of NEAT1_1 lncRNA on cell survival in primary hippocampal cultures obtained from transgenic mice under ER stress induced by the proteasome inhibitor MG132.

METHODS

Primary hippocampal cultures

The study was performed on primary neuronal cultures obtained from NEAT1_1Tg transgenic mice expressing the

short isoform of human NEAT1_1 in the nervous system. The mice were obtained by transgenesis as described previously [19] and harbor a transgene encoding human NEAT1_1 in the genome under the control of the pan-neuronal Thy1 promoter on a C57BL6 genetic background (in press). The transgene presence was confirmed by PCR. Animals were maintained at a 12h light/12h dark cycle, with food and water supplied *ad libitum*.

Primary neuronal cultures were obtained from the hippocampus of NEAT1_1Tg transgenic mice and wild-type (WT) control mice on the third day after birth (P3) as described previously [20]. Hippocampi isolated from at least three animals of the same genotype were used for culture; each experiment was independently repeated at least twice. After hippocampal dissection, the samples were incubated in a solution of 0.1% trypsin in Hanks' balanced salt solution (HBSS) with 10 mM HEPES (4-(2-hydroxyethyl)-1-piperazineethanesulfonic acid) and 1 mM sodium pyruvate for 40 min. This was followed by mechanical dissociation in a solution of Neurobasal medium (PanEco; Russia) containing 50 units/mL penicillin/streptomycin, 0.2% beta-mercaptoethanol, 500 μ M L-glutamine, 0.36% glucose, and 10% horse serum. Samples were centrifuged for 5 min at 1500 rpm. The cell pellet was resuspended in freshly prepared medium, and cell counting was performed using a Goryaev chamber (hemocytometer) and trypan blue staining. B27 supplement (Thermo Fisher Scientific; USA) or NeuroMax supplement (PanEco; Russia) was added to the medium to increase the survival of primary neurons in culture. Cells were seeded on 12-mm-diameter coverslips coated with poly-L-lysine, with approximately 3×10^4 cells per glass. On the next day, medium was changed to fresh medium without serum. A subsequent medium change was performed every 3 days replacing only half of the medium. Cultures were incubated at 37 °C, 5% carbon dioxide, and 95% humidity. The cultures were analyzed after 7 days from seeding.

To induce endoplasmic reticulum stress (ER stress), cells were treated with a solution of MG132 proteasome inhibitor (Sigma-Aldrich; USA) in DMSO (PanEco; Russia) with a final concentration of 200 μ M or 10 μ M.

Immunocytochemical staining using microtubule-associated protein Tau antibody (SAB4300377; Sigma-Aldrich, USA) was performed to visualize neuronal bodies and outgrowth processes, for subsequent Sholl analysis; to confirm the neuronal phenotype, cells were stained with NeuN marker (antibody MAB377; Millipore, USA). Images were obtained using a Carl Zeiss Axio Observer 3 microscope (Germany) equipped with an AxioCam 712 mono camera (Carl Zeiss; Germany). Semi-automatic Sholl analysis was performed using the ImageJ plugin as described earlier [10]. For each genotype, 30 neurons were analyzed.

Immunocytochemical staining

To characterize the cellular composition of primary neuronal cultures, we performed the immunocytochemical staining using markers of the main types of neuronal tissue cells: NeuN, a marker of differentiated neurons (antibody MAB377; Millipore, USA), GFAP, a marker of astrocytes (antibody G9269; Sigma-Aldrich, USA), Olig2, a marker of oligodendrocytes (antibody ab109186; Abcam, UK), and Iba1, a marker of microglia (antibody ab178846; Abcam, UK). For each marker, six glass coverslips from two independent cultures for each genotype were analyzed. Apoptotic cell death was assessed by staining with antibodies to the activated form of caspase 3, CC3 (antibody AB3623; Sigma-Aldrich, USA). Cells were washed from the medium with 1× PBS (phosphate-buffered saline),

Table. Sequences of primers used for RT-qPCR

Name of primer	Sequence of forward primer	Sequence of reverse primer
<i>B2m</i>	CATGGCTCGCTCGGTGAC	CAGTTCAGTATGTTCCGGCTTCC
<i>Atf4</i>	GGGTTCTGTCTCCACTCCA	AAGCAGCAGAGTCAGGCTTTC
<i>Ddit3</i>	CCACCACACCTGAAAGCAGAA	AGGTGAAAGGCAGGGACTCA
<i>Hspa5</i>	TCGACTTGGGGACCACCTAT	AGTGAAGGCCACATACGACG
<i>Emc4</i>	ATACCAGCGTGCAAGAGACC	GGAATCTGCTTGAGGGGACC
<i>Bcl2l1</i>	CGGATTGCAAGTTGGATGGC	TGCTGCATTGTTCCCGTAGA
<i>Bcl2l2</i>	ATTGGATGGTGGCCTACCTG	CCCGTATAGAGCTGTGAACTCC
<i>Mcl1</i>	AACGGGACTGGCTTGTCAAA	CTGATGCCGCCTTCTAGGTC
<i>Casp3</i>	CGGGGAGCTTGAACGGTA	CCACTGACTTGCTCCCATGT

fixed with 4% paraformaldehyde for 15 min and permeabilized with ice-cold methanol for five minutes. Non-specific binding was blocked using 5% goat serum blocking solution in PBS with Tween 20 for 1 hour at room temperature. The coverslips were then incubated with primary antibodies at 1:1000 dilution in a blocking solution for 1 hour at room temperature, washed out with 1× PBS, and incubated with secondary fluorescently labeled antibodies Goat anti-Rabbit IgG Alexa Fluor™ 568 (A-11011; Thermo Fisher Scientific, USA) and Goat anti-Mouse IgG Alexa Fluor™ 488 (A-11029; Thermo Fisher Scientific, USA) at 1:1000 dilution in PBS-Tween 20 solution for 30 minutes at room temperature. Cell nuclei were stained with DAPI solution (Sigma-Aldrich; USA). The coverslips were mounted on slides, in a drop of Immu-Mount medium (Thermo Fisher Scientific; USA). For analyzing cell types and apoptosis, coverslips were imaged on a Cytation 3 Reader (BioTek; USA) with Gen5 3.08 Software (BioTek; USA). At least 3000 $\mu\text{m} \times 3000 \mu\text{m}$ area was scanned in a multichannel fluorescence mode. The scanned area was stitched into a single panoramic image, and a number of positively stained cells for each specific marker was analyzed. For each marker, the results were normalized to the total number of cells estimated by DAPI-stained nuclei counting.

Gene Expression Analysis

Expression of genes involved in ER stress major signaling pathways and apoptosis were assessed by quantitative real-time reverse transcription PCR (RT-PCR) on a CFX96 instrument (Bio-Rad; USA). Cells were grown on a six-well plate for 7 days. Total RNA was isolated using ExtractRNA reagent (Evrogen; Russia) according to the manufacturer's protocol. RNA samples were further treated with DNase (Sigma-Aldrich; USA) according to the manufacturer's protocol. The concentration of purified RNA was measured using Nanodrop 2000 spectrophotometer (Thermo Fisher Scientific; USA). Synthesis of complementary cDNA strand was performed using the Magnus Reverse Transcriptase kit (Evrogen; Russia) according to the manufacturer's protocol. Quantitative real-time PCR was performed on a CFX96 instrument (Bio-Rad; USA) using qPCRmix-HS SYBR kit (Evrogen; Russia) according to the manufacturer's protocol. Beta-2-microglobulin gene (*B2m*) was used as an endogenous control. The list of primers we used is presented in Table.

The program for qPCR included initial denaturation for 5 min at 95 °C, followed by 40 cycles: at 95 °C for 20 s, at 60 °C for 30 s, at 68 °C for 30 s. The results were analyzed using Bio-Rad CFX Manager software (Bio-Rad; USA).

Statistical Analysis of Data

Statistical analysis was performed using Statistica 12.0 (StatSoft, Inc.; USA) and GraphPad Prism 8 (GraphPad

Software; USA) software. In all cases, results are presented as arithmetic mean and standard error of the mean ($x \pm m$) with individual values where appropriate. Details of the statistical analysis for each group of data are presented in the figure description. Differences in the obtained results were considered statistically significant at a significance level of $p < 0.05$.

RESULTS

Cellular composition and morphology of neurons in primary neuronal cultures expressing NEAT1_1 do not differ from control ones

Primary hippocampal cell cultures obtained from NEAT1_1Tg transgenic mice and from wild-type (WT) animals on the third day of postnatal development (P3) were used in the experiment. The isolated cells were cultured in vitro for 7 days. Culturing conditions (use of serum, nutrient supplement B27, etc.) were selected to obtain a mixed culture containing all major cell types of nervous tissue. Staining for markers of cell types showed that the primary neuronal cultures contained approximately $9 \pm 1.3\%$ neurons, $61 \pm 5.6\%$ astrocytes, $28 \pm 2.5\%$ oligodendrocytes, and $2 \pm 0.5\%$ microgliaocytes (Fig. 1A, B). No differences were found between cultures of different genotypes — NEAT1_1Tg and WT - in terms of cellular composition.

To characterize neuron morphology and assess the effect of increased NEAT1_1 expression on morphofunctional characteristics related to cell activity and plasticity, we performed Sholl analysis evaluating the neurite outgrowth. No significant differences in the branching complexity in neurons of two different genotypes (NEAT1_1Tg and WT) were detected although a tendency of decreasing number of neurites in neuron proximal regions was observed for transgenic NEAT1_1Tg cultures (Fig. 2A, B). Thus, NEAT1_1 expression was shown to have no effect on neuronal plasticity.

In transgenic NEAT1_1Tg cultures, apoptotic cell death was more often observed under ER stress

Analysis of apoptotic cell death by immunocytochemical staining for activated caspase-3 (CC3) showed that under normal conditions, a small number (2–4%) of CC3-positive (CC3⁺) cells were detected in cell cultures while the signal was mostly not colocalized with NeuN marker indicating the glial nature of dying cells (Fig. 3 A–B).

Acute and moderate ER stress was induced by treatment with MG132 proteasome inhibitor (200 μM and 10 μM MG132 concentrations, respectively). On the seventh day of cultivation, MG132 proteasome inhibitor was added to the medium for 4 h, after that the medium was changed. Apoptosis levels were evaluated after 4 h, 12 h and 24 h. The total cell death

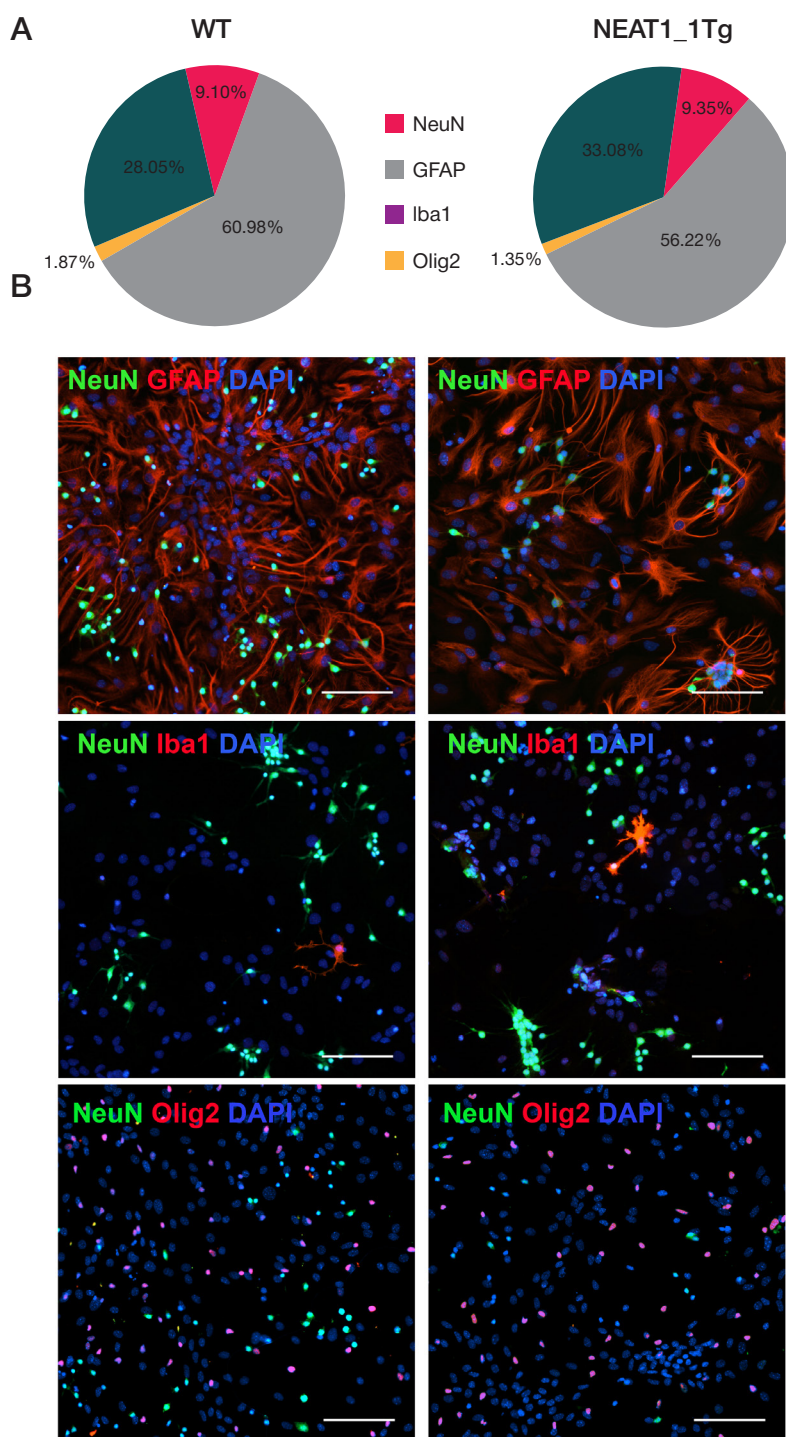


Fig. 1. Cellular composition of hippocampal primary cultures derived from transgenic (NEAT1_1Tg) and wild-type (WT) mice **A.** Percentages of neurons (NeuN), astrocytes (GFAP), microglia (Iba1), and oligodendrocytes (Olig2) in primary cultures. **B.** Representative photographs of primary cultures stained for markers of different cell types. Cell nuclei are stained with DAPI. The scale bar is 100 μ m

was analyzed, i.e. all CC3⁺ cells (both neurons and glia) were counted.

Under acute ER stress induced by high concentration of MG132 (200 μ M) in WT cultures, cell death was detected in 4 h after treatment. Number of cells dying as a result of apoptosis increased in 12 h and remained high in 24 h. At the same time, in cultures obtained from transgenic animals, a significantly higher number of apoptotic cells was detected 4 h after treatment, whereas at subsequent time points this index was comparable to WT cultures treated with MG132 (Fig. 3A).

A low concentration of MG132 (10 μ M) was used to model a moderate transient ER stress. In this case, total apoptotic death

also increased in 4 hours however, in 12 hours the number of CC3⁺ cells decreased, and in 24 hours it matched the values for control cultures without MG132 treatment indicating recovery of cell cultures after stress. Compared with WT after stress, in NEAT1_1Tg cultures the number of apoptotic cells was higher 4 hours after treatment, and the same trend persisted for 12 hours, whereas the difference leveled off at 24 hours (Fig. 3B).

To assess how ER stress affects neuronal survival, we performed co-staining for CC3 and the differentiated neuron marker NeuN, and then counted cells expressing both markers. In cultures with a high concentration of MG132, neuronal death peaked at 4 h (Fig. 4A), whereas at a low MG132 concentration

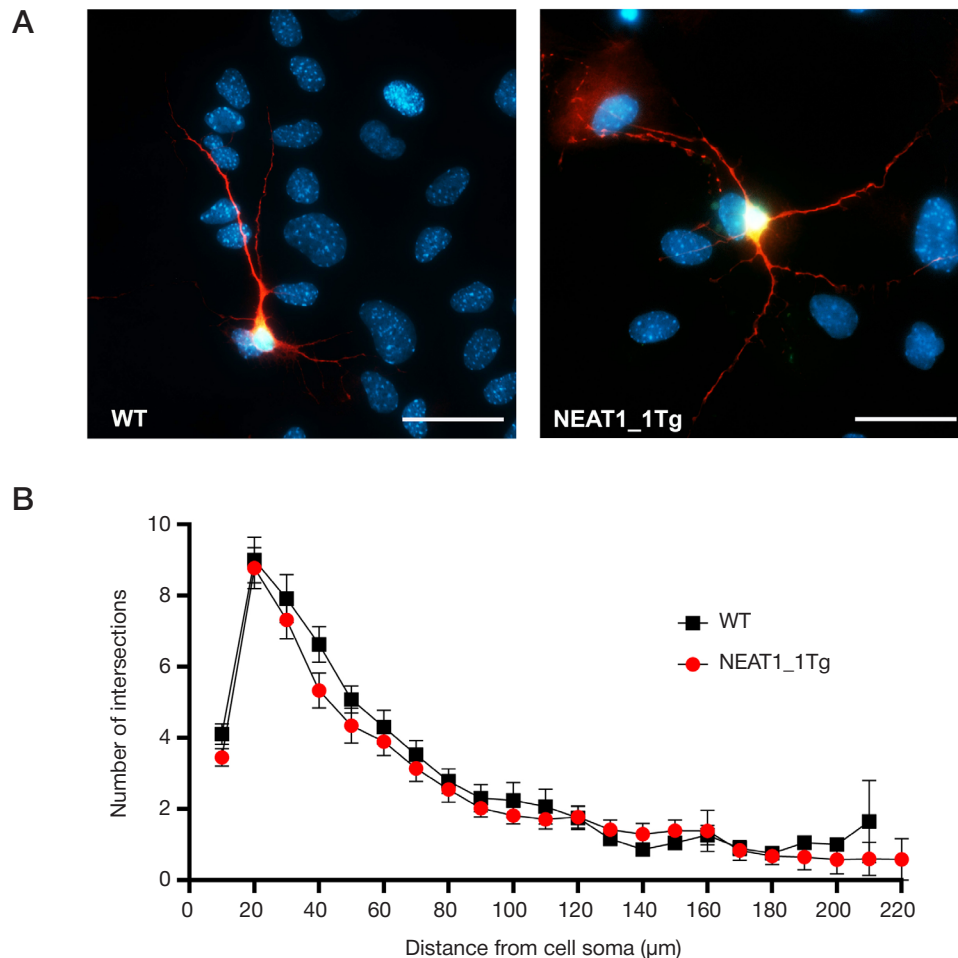


Fig. 2. Morphofunctional characterization of primary neurons. **A.** Representative photographs of wild-type (WT) and transgenic neurons (NEAT1_1Tg). Immunocytochemical staining for microtubule-associated protein Tau (shown in red), neuronal marker NeuN (shown in green), and cell nuclei stained with DAPI. The scale bar is 50 μm . **B.** Analysis of branching of primary neuron processes (Sholl-analysis). The graph shows the average number of intersections of circles of a given radius with processes. Multiple t-test with Holm-Sidak correction

it peaked at 12 h (Fig. 4B). In each case, neuronal death was significantly higher in cultures expressing the NEAT1_1Tg transgene.

Response to ER-stress is altered in transgenic NEAT1_1Tg cultures

To determine the possible mechanism of increased death of cells, particularly neurons, in transgenic neuronal cultures expressing human NEAT1_1, we analyzed the expression of genes involved in signaling pathways of cellular response to ER stress as well as apoptosis genes. It was shown that 4 h after treatment with 10 μM MG132, there was an increase in the expression of the following ER stress marker genes: transcription factor *Atf4*, proapoptotic gene *Chop* (*Ddit3*), chaperone *Hspa5* (*Grp78* or *BiP*) (Fig. 5A–B). Similar changes in the expression of these genes occurred in transgenic cultures after MG132 treatment. At the same time, the expression of *Atf4* and *Ddit3* did not reach the levels observed in WT cultures after ER stress induction. The expression level of the gene encoding ER protein *Emc4* having protective properties under stress [21] was significantly reduced in NEAT1_1Tg cultures both under normal conditions and under ER stress (Fig. 5G).

Caspase-3 (*Casp3*) mRNA levels did not differ between transgenic and control cultures and did not change in response to stress (Fig. 5D). Analysis of expression of apoptosis inhibitor genes (*Bcl2l1*, *Bcl2l2*, *Mcl1*) (Fig. 5E–Z) showed that induction of moderate ER stress in WT cultures resulted in increased

mRNA levels for *Bcl2l2* and *Mcl1* genes, whereas *Bcl2l1* expression remained unchanged. In contrast, in transgenic NEAT1_1Tg cultures, no significant activation of *Bcl2l2* and *Mcl1* was observed under stress, with some upward trend for *Mcl1* though.

DISCUSSION

NEAT1 has been convincingly shown to be involved in various pathological processes associated with neurodegeneration, including neuroinflammation and apoptosis [5]. *NEAT1* gene promoter has a binding site with p53 protein which is capable of increasing NEAT1 levels [22]. An extended experimental data indicates a protective role of NEAT1. In mouse experiments using an adenoviral vector for RNA delivery, *Neat1_1* was shown to have an anti-apoptotic effect in a brain injury model as well as in cell culture of hippocampal neurons from HT-22 mice under hypoxia and glucose deficiency [23]. NEAT1 knockdown in human neuroblastoma SH-SY5Y cells increased apoptotic death in the simulation of viral infection using double-stranded RNA treatment [12]. At the same time, NEAT1 overexpression can stimulate ferroptosis in HepG2 hepatocarcinoma cells [24], and inhibition of NEAT1 in toxic (MPP⁺) cell and animal models of Parkinson's disease led to a decrease in cell death and proapoptotic markers [25, 26]. Thus there are conflicting data on the effect of NEAT1 on cell death. Specific pro- or anti-apoptotic effect of NEAT1 may possibly depend on a type of damaging effect. Understanding the mechanism of NEAT1

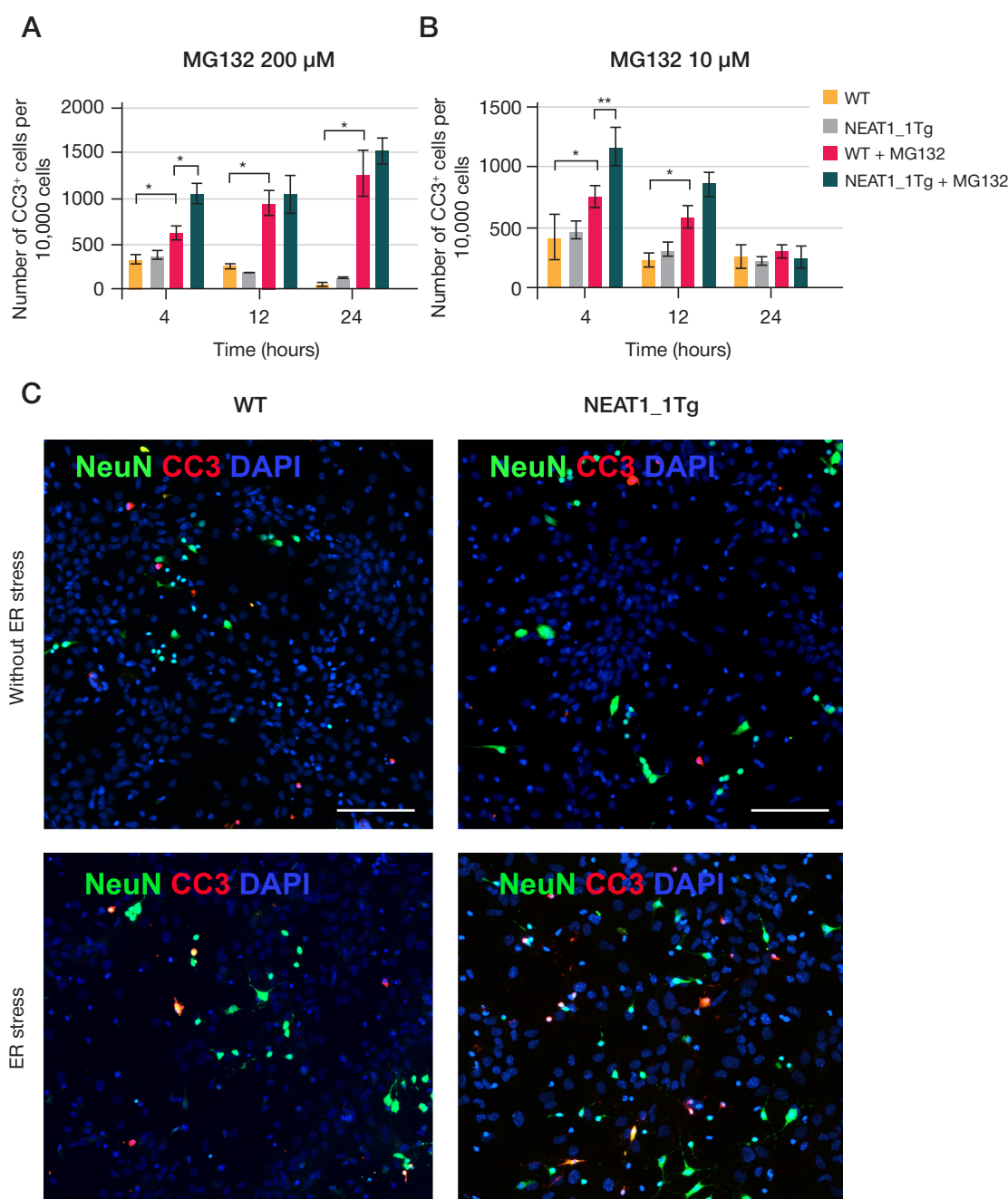


Fig. 3. Apoptotic death in transgenic (NEAT1_1Tg) primary cultures and wild-type (WT) cultures. **A.** Apoptosis in cultures when treated with 200 μM MG132. **B.** Apoptosis in cultures when treated with 10 μM MG132. Two-factor analysis of variance, Fisher's test. * — $p < 0.05$; ** — $p < 0.01$. **B.** Representative photographs of cell cultures upon treatment with 10 μM MG132 after 12 h. Neurons stained for the differentiated neuron marker NeuN (shown in green), the apoptotic cell death marker activated caspase 3, CC3 (shown in red), and nuclei stained with DAPI (shown in blue). Scale section is 100 μm

action is further complicated by the fact that unlike *in vivo* nervous tissue and primary neurons, in most cell cultures the long isoform (NEAT1_2), a basis for paraspecies assembly, is expressed as well [5, 12]. Formation of paraspecies, in turn, can be stimulated by cellular stress of various types including proteasome inhibition [27]. Therefore, it is difficult to identify independent roles of short and long NEAT1 isoforms in the cellular response to stress.

We have shown that ectopic expression of the transgene encoding the short isoform of human NEAT1_1 in the mouse nervous system had no effect on cellular composition (Fig. 1) and morphology of primary neuronal cultures (Fig. 2) derived from hippocampi. Induction of ER stress with the proteasome inhibitor MG132 resulted in apoptotic cell death of primary culture cells (Fig. 3), and apoptosis intensity depended on stress

level (MG132 concentration). At the same time, the number of apoptotic cells was higher in cultures expressing the NEAT1_1 transgene compared with WT cells in stress conditions. As it was shown earlier for mouse embryonic Neat1 knockout fibroblasts, the absence of Neat1 increases death of these cells in response to MG132 treatment [27]. Stable Neat1 levels might be important for cell survival under stress or its effect on cell death depends on type of cells. The primary culture used in this study was mixed and contained both neurons and glial cells. This made it possible to assess survival of neurons in the experiment under the mutual influence of different cell populations of neuronal origin. To determine the specific effect of increasing NEAT1_1 levels on neuronal survival, we estimated the number of cells expressing both the mature neuronal marker NeuN and activated caspase-3 (CC3). Stress resulted in a more

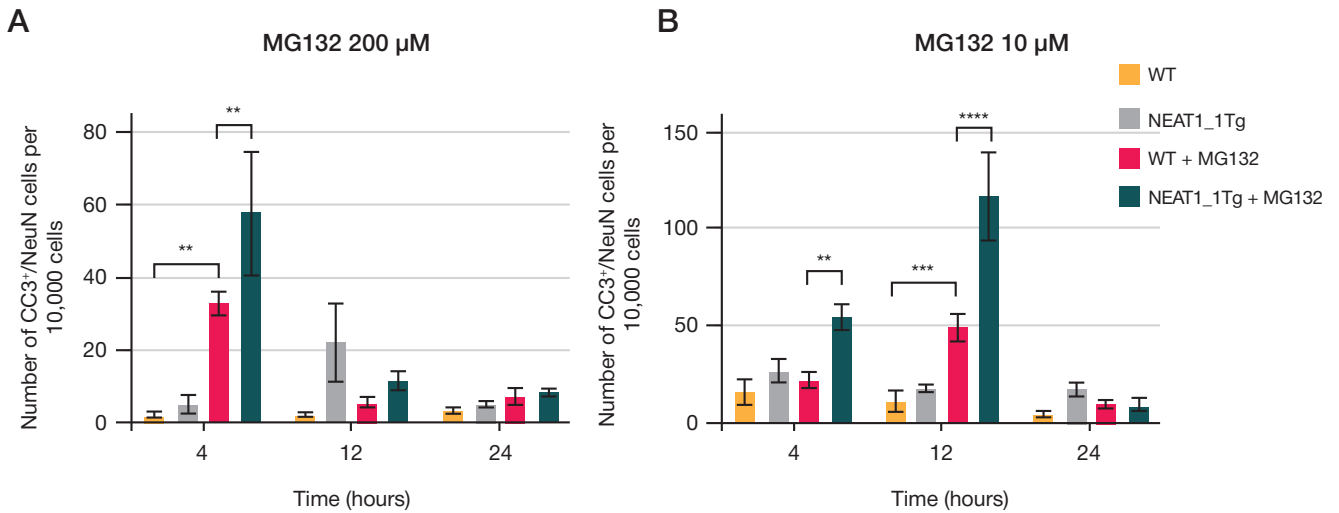


Fig. 4. Apoptotic neuronal death in transgenic (NEAT1_1Tg) primary and wild-type (WT) cultures. **A.** Apoptosis in cultures treated with 200 μM MG132. **B.** Apoptosis in cultures treated with 10 μM MG132. Two-way analysis of variance, Fisher's test. ** — $p < 0.01$; *** — $p < 0.001$; **** — $p < 0.0001$

intensive neuronal death in transgenic cultures (NEAT1_1Tg) compared with wild-type cultures (WT) (Fig. 4). Thus, NEAT1_1 expression enhanced apoptosis of primary neurons under ER stress. An increased number of apoptotic neurons in transgenic cultures without treatment compared with control cultures was observed for all time points. Although these differences are not statistically significant, it can be assumed that there is some predisposition of transgenic neurons to trigger apoptosis under normal conditions, and this should be investigated further.

Cellular ER stress response includes three different signaling pathways based on kinases acting as stress sensors: PERK, ATF6, and IRE1 [16]. When they are activated, an overall

protein synthesis is inhibited and protective mechanisms are triggered, primarily aimed at adapting to stress and restoring protein homeostasis. However, under severe stress or its prolonged persistence, the balance shifts towards activation of proapoptotic signaling pathways leading to cell death [28]. We have shown that ER stress causes activation of the PERK pathway evidenced by an increase in *Atf4* mRNA levels however, this activation was less in NEAT1_1Tg cultures (Fig. 5). Accordingly, activation of proapoptotic *Ddit3* (*Chop*) gene which belongs to the same PERK/ATF4/CHOP signaling pathway and acting as activator of cell transition to apoptosis under ER stress, was also reduced in NEAT1_1Tg cultures [29]. In both

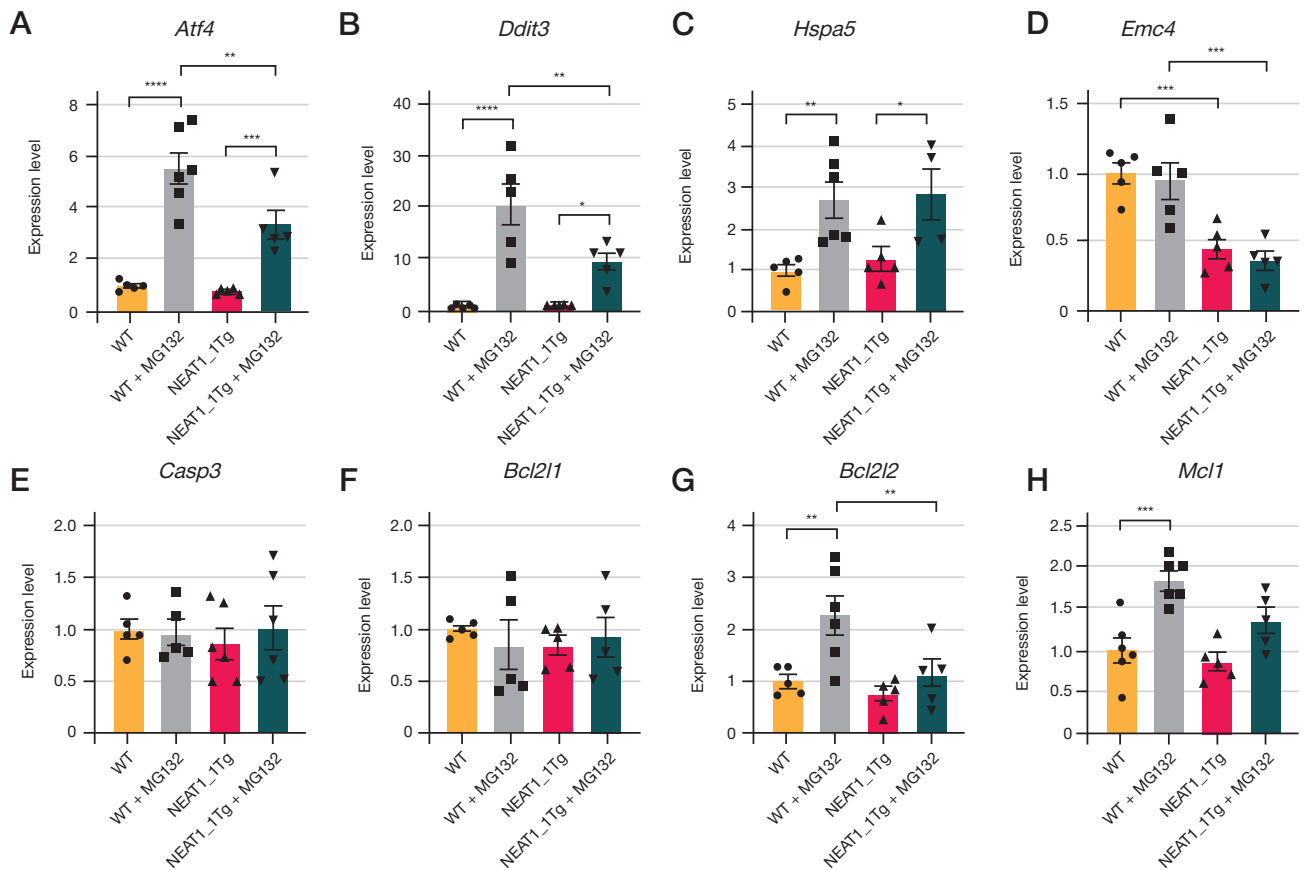


Fig. 5. Gene expression changes in transgenic (NEAT1_1Tg) primary and wild-type (WT) cultures treated with 10 μM MG132. **A–G.** Expression of genes associated with ER stress. **D–Z.** Expression of apoptosis-related genes. One-way analysis of variance, Fisher's test. * — $p < 0.05$; ** — $p < 0.01$, *** — $p < 0.001$; **** — $p < 0.0001$

cultures, expression of Hspa5 chaperone gene (BiP) increased under ER stress. Rapid response of NEAT1_1Tg cells to stress and triggering of apoptosis through caspase-3 activation could be explained by initial differences in the amounts of caspase-3 inactive form in cells. Analysis of caspase-3 (*Casp3*) expression showed that at least at the initial stage of stress development, 4 h after MG132 treatment of cells, its levels were similar in all four groups. Since the number of cells stained with antibodies against caspase-3 activated form was increased in 4 hours after the stress induction, the difference between NEAT1_1Tg- and WT-cell death levels is likely to be due to some other regulatory factors, in particular the cleavage of procaspase-3 with formation of its activated form. We analyzed the expression of the following apoptosis inhibitor genes: *Bcl2l1*, *Bcl2l2*, and *Mcl1* [30]. *Bcl2l1* expression did not change in response to ER stress. For *Bcl2l2* and *Mcl1* genes, an increase in their levels was observed in WT cultures while in NEAT1_1Tg cultures such

activation was practically absent for *Bcl2l2* and was significantly less for *Mcl1*. In NEAT1_1Tg cultures, there was a decrease in mRNA level of *Emc4* gene related to conserved transmembrane proteins required for protein stacking in ER. The lack of Emc proteins can lead to ER stress [31]. Thus, an increased level of NEAT1_1 in neuronal cultures during ER stress results in a decrease in regulatory anti-apoptotic signals which enhances cell death including neuronal death.

CONCLUSIONS

Additional expression of transgenic human NEAT1_1 long non-coding RNA under ER stress promotes apoptotic neuronal death in primary hippocampal cultures. Increasing levels of this RNA in the nervous system of patients suffering neurodegenerative diseases (ALS, FTD, HD) with protein aggregation and ER stress can be considered as a pathogenetic factor.

References

- Kopp F, Mendell JT. Functional Classification and Experimental Dissection of Long Noncoding RNAs. *Cell*. 2018; 172 (3): 393–407.
- Mercer TR, Dinger ME, Mattick JS. Long non-coding RNAs: insights into functions. *Nat Rev Genet*. 2009; 10 (3): 155–9.
- Zimmer-Bensch G. Emerging Roles of Long Non-Coding RNAs as Drivers of Brain Evolution. *Cells*. 2019; 8 (11).
- Wan P, Su W, Zhuo Y. The Role of Long Noncoding RNAs in Neurodegenerative Diseases. *Mol Neurobiol*. 2017; 54 (3): 2012–21.
- An H, Williams NG, Shelkovernikova TA. NEAT1 and paraspeckles in neurodegenerative diseases: A missing linc found? *Noncoding RNA Res*. 2018; 3 (4): 243–52.
- Tollervey JR, Curk T, Rogelj B, Briese M, Cereda M, Kaykici M, et al. Characterizing the RNA targets and position-dependent splicing regulation by TDP-43. *Nat Neurosci*. 2011; 14 (4): 452–8.
- Sunwoo JS, Lee S, Kim JH, Lim JA, Kim TJ, Byun JI, et al. Altered functional connectivity in idiopathic rapid eye movement sleep behavior disorder: a resting-state EEG study. *Sleep*. 2017; 40 (6).
- Cheng C, Spengler RM, Keiser MS, Monteyes AM, Rieders JM, Ramachandran S, et al. The long non-coding RNA NEAT1 is elevated in polyglutamine repeat expansion diseases and protects from disease gene-dependent toxicities. *Hum Mol Genet*. 2018; 27 (24): 4303–14.
- An H, Tan JT, Shelkovernikova TA. Stress granules regulate stress-induced paraspeckle assembly. *J Cell Biol*. 2019; 218 (12): 4127–40.
- Kukharsky MS, Ninkina NN, An H, Telezhkin V, Wei W, Meritens CR, et al. Long non-coding RNA Neat1 regulates adaptive behavioural response to stress in mice. *Transl Psychiatry*. 2020; 10 (1): 171.
- Nishimoto Y, Nakagawa S, Hirose T, Okano HJ, Takao M, Shibata S, et al. The long non-coding RNA nuclear-enriched abundant transcript 1_2 induces paraspeckle formation in the motor neuron during the early phase of amyotrophic lateral sclerosis. *Mol Brain*. 2013; 6: 31.
- Shelkovernikova TA, Kukharsky MS, An H, Dimasi P, Alexeeva S, Shabir O, et al. Protective paraspeckle hyper-assembly downstream of TDP-43 loss of function in amyotrophic lateral sclerosis. *Mol Neurodegener*. 2018; 13 (1): 30.
- Matsukawa K, Kukharsky MS, Park SK, Park S, Watanabe N, Iwatsubo T, et al. Long non-coding RNA NEAT1_1 ameliorates TDP-43 toxicity in in vivo models of TDP-43 proteinopathy. *RNA Biol*. 2021; 18 (11): 1546–54.
- Nakagawa S, Naganuma T, Shioi G, Hirose T. Paraspeckles are subpopulation-specific nuclear bodies that are not essential in mice. *J Cell Biol*. 2011; 193 (1): 31–9.
- Wiseman RL, Mesgarzadeh JS, Hendershot LM. Reshaping endoplasmic reticulum quality control through the unfolded protein response. *Mol Cell*. 2022; 82 (8): 1477–91.
- Kukharsky MS, Everett MW, Lytkina OA, Raspopova MA, Kovrazhkina EA, Ovchinnikov RK, et al. Protein homeostasis dysregulation in pathogenesis of neurodegenerative diseases. *Mol Biol (Mosk)*. 2022; 56 (6): 1044–56.
- Merighi A, Lossi L. Endoplasmic reticulum stress signaling and neuronal cell death. *Int J Mol Sci*. 2022; 23 (23).
- Galehdar Z, Swan P, Fuerth B, Callaghan SM, Park DS, Cregan SP. Neuronal apoptosis induced by endoplasmic reticulum stress is regulated by ATF4-CHOP-mediated induction of the Bcl-2 homology 3-only member PUMA. *J Neurosci*. 2010; 30 (50): 16938–48.
- Deikin AV, Kovrazhkina EA, Ovchinnikov RK, Bronovitskii EV, Razinskaia OD, Smirnov AP, et al. A mice model of amyotrophic lateral sclerosis expressing mutant human FUS protein. *Zh Nevrol Psikhiatr Im S S Korsakova*. 2014; 114 (8): 62–9.
- Kukharsky MS, Quintiero A, Matsumoto T, Matsukawa K, An H, Hashimoto T, et al. Calcium-responsive transactivator (CREST) protein shares a set of structural and functional traits with other proteins associated with amyotrophic lateral sclerosis. *Mol Neurodegener*. 2015; 10: 20.
- Bai L, You Q, Feng X, Kovach A, Li H. Structure of the ER membrane complex, a transmembrane-domain insertase. *Nature*. 2020; 584 (7821): 475–8.
- Mello SS, Sinow C, Raj N, Mazur PK, Biegging-Rolett K, Broz DK, et al. Neat1 is a p53-inducible lincRNA essential for transformation suppression. *Genes Dev*. 2017; 31 (11): 1095–108.
- Zhong J, Jiang L, Huang Z, Zhang H, Cheng C, Liu H, et al. The long non-coding RNA Neat1 is an important mediator of the therapeutic effect of bexarotene on traumatic brain injury in mice. *Brain Behav Immun*. 2017; 65: 183–94.
- Zhang Y, Luo M, Cui X, O'Connell D, Yang Y. Long noncoding RNA NEAT1 promotes ferroptosis by modulating the miR-362-3p/MiOX axis as a ceRNA. *Cell Death Differ*. 2022; 29 (9): 1850–63.
- Dong LI, Zheng Y, Gao L, Luo X. lncRNA NEAT1 prompts autophagy and apoptosis in MPTP-induced Parkinson's disease by impairing miR-374c-5p. *Acta Biochim Biophys Sin (Shanghai)*. 2021; 53 (7): 870–82.
- Liu Y, Lu Z. Long non-coding RNA NEAT1 mediates the toxic of Parkinson's disease induced by MPTP/MPP+ via regulation of gene expression. *Clin Exp Pharmacol Physiol*. 2018; 45 (8): 841–8.
- Hirose T, Virnicchi G, Tanigawa A, Naganuma T, Li R, Kimura H, et al. NEAT1 long noncoding RNA regulates transcription via protein sequestration within subnuclear bodies. *Mol Biol Cell*. 2014; 25 (1): 169–83.
- Rutkowski DT, Arnold SM, Miller CN, Wu J, Li J, Gunnison KM, et al. Adaptation to ER stress is mediated by differential stabilities of pro-survival and pro-apoptotic mRNAs and proteins. *PLoS Biol*. 2006; 4 (11): e374.
- Hu H, Tian M, Ding C, Yu S. The C/EBP Homologous Protein (CHOP) Transcription factor functions in endoplasmic reticulum stress-induced apoptosis and microbial infection. *Front Immunol*.

- 2018; 9: 3083.
30. Chipuk JE, Moldoveanu T, Llambi F, Parsons MJ, Green DR. The BCL-2 family reunion. *Mol Cell*. 2010; 37 (3): 299–310.
31. Tian S, Wu Q, Zhou B, Choi MY, Ding B, Yang W, et al. Proteomic analysis identifies membrane proteins dependent on the ER membrane protein complex. *Cell Rep*. 2019; 28 (10): 2517–26 e5.

Литература

- Kopp F, Mendell JT. Functional Classification and Experimental Dissection of Long Noncoding RNAs. *Cell*. 2018; 172 (3): 393–407.
- Mercer TR, Dinger ME, Mattick JS. Long non-coding RNAs: insights into functions. *Nat Rev Genet*. 2009; 10 (3): 155–9.
- Zimmer-Bensch G. Emerging Roles of Long Non-Coding RNAs as Drivers of Brain Evolution. *Cells*. 2019; 8 (11).
- Wan P, Su W, Zhuo Y. The Role of Long Noncoding RNAs in Neurodegenerative Diseases. *Mol Neurobiol*. 2017; 54 (3): 2012–21.
- An H, Williams NG, Shelkovich TA. NEAT1 and paraspeckles in neurodegenerative diseases: A missing linc found? *Noncoding RNA Res*. 2018; 3 (4): 243–52.
- Tollervey JR, Curk T, Rogelj B, Briese M, Cereda M, Kayikci M, et al. Characterizing the RNA targets and position-dependent splicing regulation by TDP-43. *Nat Neurosci*. 2011; 14 (4): 452–8.
- Sunwoo JS, Lee S, Kim JH, Lim JA, Kim TJ, Byun JI, et al. Altered functional connectivity in idiopathic rapid eye movement sleep behavior disorder: a resting-state EEG study. *Sleep*. 2017; 40 (6).
- Cheng C, Spengler RM, Keiser MS, Monteys AM, Rieders JM, Ramachandran S, et al. The long non-coding RNA NEAT1 is elevated in polyglutamine repeat expansion diseases and protects from disease gene-dependent toxicities. *Hum Mol Genet*. 2018; 27 (24): 4303–14.
- An H, Tan JT, Shelkovich TA. Stress granules regulate stress-induced paraspeckle assembly. *J Cell Biol*. 2019; 218 (12): 4127–40.
- Kukharsky MS, Ninkina NN, An H, Telezhkin V, Wei W, Meritens CR, et al. Long non-coding RNA Neat1 regulates adaptive behavioural response to stress in mice. *Transl Psychiatry*. 2020; 10 (1): 171.
- Nishimoto Y, Nakagawa S, Hirose T, Okano HJ, Takao M, Shibata S, et al. The long non-coding RNA nuclear-enriched abundant transcript 1_2 induces paraspeckle formation in the motor neuron during the early phase of amyotrophic lateral sclerosis. *Mol Brain*. 2013; 6: 31.
- Shelkovich TA, Kukharsky MS, An H, Dimasi P, Alexeeva S, Shabir O, et al. Protective paraspeckle hyper-assembly downstream of TDP-43 loss of function in amyotrophic lateral sclerosis. *Mol Neurodegener*. 2018; 13 (1): 30.
- Matsukawa K, Kukharsky MS, Park SK, Park S, Watanabe N, Iwatsubo T, et al. Long non-coding RNA NEAT1_1 ameliorates TDP-43 toxicity in in vivo models of TDP-43 proteinopathy. *RNA Biol*. 2021; 18 (11): 1546–54.
- Nakagawa S, Naganuma T, Shioi G, Hirose T. Paraspeckles are subpopulation-specific nuclear bodies that are not essential in mice. *J Cell Biol*. 2011; 193 (1): 31–9.
- Wiseman RL, Mesgarzadeh JS, Hendershot LM. Reshaping endoplasmic reticulum quality control through the unfolded protein response. *Mol Cell*. 2022; 82 (8): 1477–91.
- Kukharsky MS, Everett MW, Lytkina OA, Raspopova MA, Kovrazhkina EA, Ovchinnikov RK, et al. Protein homeostasis dysregulation in pathogenesis of neurodegenerative diseases. *Mol Biol (Mosk)*. 2022; 56 (6): 1044–56.
- Merighi A, Lossi L. Endoplasmic reticulum stress signaling and neuronal cell death. *Int J Mol Sci*. 2022; 23 (23).
- Galehdar Z, Swan P, Fuerth B, Callaghan SM, Park DS, Cregan SP. Neuronal apoptosis induced by endoplasmic reticulum stress is regulated by ATF4-CHOP-mediated induction of the Bcl-2 homology 3-only member PUMA. *J Neurosci*. 2010; 30 (50): 16938–48.
- Deikin AV, Kovrazhkina EA, Ovchinnikov RK, Bronovitskii EV, Razinskaia OD, Smirnov AP, et al. A mice model of amyotrophic lateral sclerosis expressing mutant human FUS protein. *Zh Nevrol Psikhiatr Im S S Korsakova*. 2014; 114 (8): 62–9.
- Kukharsky MS, Quintiero A, Matsumoto T, Matsukawa K, An H, Hashimoto T, et al. Calcium-responsive transactivator (CREST) protein shares a set of structural and functional traits with other proteins associated with amyotrophic lateral sclerosis. *Mol Neurodegener*. 2015; 10: 20.
- Bai L, You Q, Feng X, Kovach A, Li H. Structure of the ER membrane complex, a transmembrane-domain insertase. *Nature*. 2020; 584 (7821): 475–8.
- Mello SS, Sinow C, Raj N, Mazur PK, Biegging-Rolett K, Broz DK, et al. Neat1 is a p53-inducible lincRNA essential for transformation suppression. *Genes Dev*. 2017; 31 (11): 1095–108.
- Zhong J, Jiang L, Huang Z, Zhang H, Cheng C, Liu H, et al. The long non-coding RNA Neat1 is an important mediator of the therapeutic effect of bexarotene on traumatic brain injury in mice. *Brain Behav Immun*. 2017; 65: 183–94.
- Zhang Y, Luo M, Cui X, O'Connell D, Yang Y. Long noncoding RNA NEAT1 promotes ferroptosis by modulating the miR-362-3p/MiOX axis as a ceRNA. *Cell Death Differ*. 2022; 29 (9): 1850–63.
- Dong LI, Zheng Y, Gao L, Luo X. lincRNA NEAT1 prompts autophagy and apoptosis in MPTP-induced Parkinson's disease by impairing miR-374c-5p. *Acta Biochim Biophys Sin (Shanghai)*. 2021; 53 (7): 870–82.
- Liu Y, Lu Z. Long non-coding RNA NEAT1 mediates the toxic of Parkinson's disease induced by MPTP/MPP+ via regulation of gene expression. *Clin Exp Pharmacol Physiol*. 2018; 45 (8): 841–8.
- Hirose T, Virnicchi G, Tanigawa A, Naganuma T, Li R, Kimura H, et al. NEAT1 long noncoding RNA regulates transcription via protein sequestration within subnuclear bodies. *Mol Biol Cell*. 2014; 25 (1): 169–83.
- Rutkowski DT, Arnold SM, Miller CN, Wu J, Li J, Gunnison KM, et al. Adaptation to ER stress is mediated by differential stabilities of pro-survival and pro-apoptotic mRNAs and proteins. *PLoS Biol*. 2006; 4 (11): e374.
- Hu H, Tian M, Ding C, Yu S. The C/EBP Homologous Protein (CHOP) Transcription factor functions in endoplasmic reticulum stress-induced apoptosis and microbial infection. *Front Immunol*. 2018; 9: 3083.
- Chipuk JE, Moldoveanu T, Llambi F, Parsons MJ, Green DR. The BCL-2 family reunion. *Mol Cell*. 2010; 37 (3): 299–310.
- Tian S, Wu Q, Zhou B, Choi MY, Ding B, Yang W, et al. Proteomic analysis identifies membrane proteins dependent on the ER membrane protein complex. *Cell Rep*. 2019; 28 (10): 2517–26 e5.

PREFRONTAL CORTEX TRANSCRANIAL THETA-BURST STIMULATION FREQUENCY-DEPENDENT EFFECTS ON COGNITIVE FUNCTIONS

Suponeva NA, Bakulin IS, Poydasheva AG , Sinitsyn DO, Zabirova AH, Lagoda DYU, Piradov MA

Research Center of Neurology, Moscow, Russia

Theta-burst stimulation (TBS) is widely used due to induction of the long-lasting effects with short protocol duration. To reduce the variability of the effect, approaches to personalize it, such as using theta-gamma coupling frequencies (TGC), are being investigated. The study was aimed to develop the personalized protocol of navigated intermittent theta-burst stimulation (iTBS-ind) based on TGC, and to compare this protocol with the standard one (iTBS-5/50) and sham stimulation (iTBS-sham). The study involved 16 healthy volunteers ($M = 7$; 29.6 years), who were randomized to receive one session of each protocol of the left dorsolateral prefrontal cortex iTBS. The effects were estimated using the n-back test with simultaneous presentation of verbal and spatial stimuli ($n = 2, 3$), Digit Span test, Corsi blocks task, Tower of London test; testing was performed immediately before, immediately after and 60 min after stimulation. No severe adverse events were reported. Significant effect was obtained when performing assessment after 60 min for iTBS-5/50 in the n-back test with spatial stimuli ($n = 3$) ($p_{\text{corr}} = 0.018$), for all protocols in the Tower of London test ($p_{\text{corr}} = 0.039$ for iTBS-5/50, $p_{\text{corr}} = 0.045$ for iTBS-ind, $p_{\text{corr}} = 0.003$ for iTBS-sham). The iTBS-5/50 effect was significantly higher compared to iTBS-sham in the spatial n-back test ($n = 3$) ($p_{\text{corr}} = 0.039$), but lower compared to iTBS-ind and iTBS-sham in the Corsi blocks task ($p_{\text{corr}} = 0.038$ and 0.048, respectively). Thus, we failed to confirm the personalized protocol efficacy and superiority to the standard protocol and sham stimulation. Considering the effect of standard protocol, its further investigation can be promising.

Keywords: transcranial magnetic stimulation, non-invasive neuromodulation, phase-amplitude coupling, theta-gamma coupling, left dorsolateral prefrontal cortex, cognitive functions, intermittent theta-burst stimulation

Funding: the study was supported by the Russian Science Foundation (RSF), grant № 22-25-00078, <https://www.rscf.ru/project/22-25-00078/>

Author contribution: Suponeva NA, Bakulin IS, Poydasheva AG, Piradov MA — study concept; Suponeva NA, Bakulin IS, Poydasheva AG, Sinitsyn DO, Piradov MA — study planning and design; Bakulin IS, Poydasheva AG, Zabirova AH, Lagoda DYU — research procedure and data acquisition; Bakulin IS, Poydasheva AG, Sinitsyn DO, Zabirova AH — data analysis; all authors — data interpretation; Suponeva NA, Bakulin IS, Poydasheva AG — manuscript draft writing; all authors — manuscript editing.

Compliance with ethical standards: the study was approved by the Ethics Committee of the Research Center of Neurology (protocol 3-7/22 dated 20 April 2022), it was conducted in accordance with the principles of the Declaration of Helsinki; the informed consent was submitted by all study participants.

 **Correspondence should be addressed:** Alexandra G. Poydasheva
Volokolamskoye shosse, 80, Moscow, 125310, Russia; poydasheva@neurology.ru

Received: 07.10.2023 **Accepted:** 13.11.2023 **Published online:** 07.12.2023

DOI: 10.24075/brsmu.2023.045

ЧАСТОТНО-ЗАВИСИМЫЙ ЭФФЕКТ ТРАНСКРАНИАЛЬНОЙ СТИМУЛЯЦИИ ТЕТА-ВСПЫШКАМИ ПРЕФРОНТАЛЬНОЙ КОРЫ НА КОГНИТИВНЫЕ ФУНКЦИИ

Н. А. Супонева, И. С. Бакулин, А. Г. Пойдашева , Д. О. Синицын, А. Х. Заброва, Д. Ю. Лагода, М. А. Пирадов

Научный центр неврологии, Москва, Россия

Стимуляция тета-вспышками (TBS) находит широкое применение благодаря индукции долговременных эффектов при короткой длительности протокола. Для уменьшения вариабельности эффекта исследуют подходы к ее персонализации, например, по частотам тета-гамма сопряжения (ТГС). Целью исследования было разработать протокол персонализированной по ТГС навигационной стимуляции интермиттирующими тета-вспышками (iTBS-ind) и сравнить его со стандартным (iTBS-5/50) и имитацией стимуляции (iTBS-sham). В исследование включены 16 здоровых добровольцев ($M = 7$; 29,6 лет), которым в случайном порядке проводили по одной сессии каждого протокола iTBS левой дорсолатеральной префронтальной коры. Эффект оценивали с помощью тестов n-back с одновременным предъявлением вербальных и пространственных стимулов ($n = 2, 3$), Digit span, Corsi blocks, Tower of London; тестирование проводили до, сразу и через 60 мин после стимуляции. Серьезных нежелательных явлений не зарегистрировали. Статистически значимый эффект получен при оценке через 60 мин для iTBS-5/50 на тест n-back с пространственными стимулами ($n = 3$) ($p_{\text{corr}} = 0,018$), для всех протоколов — на тест Tower of London ($p_{\text{corr}} = 0,039$ для iTBS-5/50, $p_{\text{corr}} = 0,045$ для iTBS-ind и $p_{\text{corr}} = 0,003$ для iTBS-sham). Эффект iTBS-5/50 был статистически значимо выше по сравнению с iTBS-sham в отношении пространственного теста n-back ($n = 3$) ($p_{\text{corr}} = 0,039$), но ниже по сравнению с iTBS-ind и iTBS-sham в отношении теста Corsi blocks ($p_{\text{corr}} = 0,038$ и 0,048 соответственно). Таким образом, не удалось подтвердить эффективность и преимущества персонализированного протокола по сравнению со стандартным и имитацией стимуляции. В связи с полученным эффектом стандартного протокола может быть перспективным дальнейшее его изучение.

Ключевые слова: транскраниальная магнитная стимуляция, стимуляция тета-вспышками, неинвазивная нейромодуляция, фазово-амплитудное сопряжение, тета-гамма сопряжение, левая дорсолатеральная префронтальная кора, когнитивные функции, intermittent theta-burst stimulation

Финансирование: исследование выполнено за счет гранта Российского научного фонда № 22-25-00078, <https://www.rscf.ru/project/22-25-00078/>

Вклад авторов: Н. А. Супонева, И. С. Бакулин, А. Г. Пойдашева, М. А. Пирадов — концептуализация исследования; Н. А. Супонева, И. С. Бакулин, А. Г. Пойдашева, Д. О. Синицын, М. А. Пирадов — планирование и дизайн исследования; И. С. Бакулин, А. Г. Пойдашева, А. Х. Заброва, Д. Ю. Лагода — проведение исследования и сбор данных; И. С. Бакулин, А. Г. Пойдашева, Д. О. Синицын, А. Х. Заброва — анализ данных; все авторы — интерпретация данных; Н. А. Супонева, И. С. Бакулин, А. Г. Пойдашева — подготовка черновика рукописи; все авторы — редактирование рукописи.

Соблюдение этических стандартов: исследование было одобрено этическим комитетом ФГБНУ «Научный центр неврологии» (протокол 3-7/22 от 20 апреля 2022 г.). Исследование проводили в соответствии с принципами Хельсинкской декларации; все участники подписали добровольное информированное согласие на участие в исследовании.

 **Для корреспонденции:** Александра Георгиевна Пойдашева
Волоколамское шоссе, д. 80, г. Москва, 125310, Россия; poydasheva@neurology.ru

Статья получена: 07.10.2023 **Статья принята к печати:** 13.11.2023 **Опубликована онлайн:** 07.12.2023

DOI: 10.24075/vrgmu.2023.045

Non-invasive neuromodulation, specifically transcranial magnetic stimulation (TMS), is used both in the study of cognitive function and as a potential method to enhance it in healthy individuals and patients [1–3].

The effect of repetitive TMS is thought to be due to its influence on neuroplasticity mechanisms [4, 5]. It is not confined to the stimulated area and extends over the functionally linked components of neural networks [1]. In recent years, an increasing attention was paid to investigation of patterned TMS protocols, including theta-burst stimulation (TBS), when “bursts” of three stimuli with a specified frequency (usually 30 or 50 Hz) are delivered at a frequency of 3 or 5 Hz. Bursts can be presented continuously for 20 or 40 s (continuous TBS, cTBS) or for 2 s with an interval of 8 s (intermittent TBS, iTBS) [6–7]. TBS is characterized by the sufficiently long neuromodulatory effect duration with short duration of stimulation, which makes the use of TBS in clinical practice promising [8].

The data on the TBS effect on cognitive functions in healthy volunteers are controversial [9]. One of the reasons can be high inter-individual variability in response to stimulation reducing the group effect. Furthermore, are poorly reproducible at the individual level: cognitive function improvement in healthy volunteers in response to the TBS session is observed in 70% of cases, however, it is reproduced only in 37.5% when reassessed on a different day [10].

The development of personalized protocols (particularly, based on stimulation frequency) represents one of the approaches to variability reduction. In addition to selection based on individual cortical rhythm frequencies [11, 12], selection based on the cortical oscillation phase-amplitude coupling (PAC) is a relatively new method.

The most studied variant of PAC is the theta-gamma coupling (TGC), which is important for memory processes. In TGC the amplitude of oscillations in the gamma range (over 30 Hz) is modulated by phase of oscillations in the theta range (4–8 Hz) [13–15]. TGC has been shown to correlate with working memory (WM) test scores and several other cognitive functions in healthy volunteers [16] and its decline has been observed in Alzheimer's disease, moderate cognitive impairment and mental disorders [13, 17].

The results of sporadic studies involving the use of the non-invasive neuromodulation protocols personalized based on the TGC frequency are available. A significantly more prominent effect of one session of personalized protocol on the n-back test results in healthy volunteers compared to standard iTBS (6/30 and 5/50 Hz) when performing assessment 45 min after stimulation was revealed, along with significant differences in the characteristics of the TMS-evoked EEG potentials between the standard and personalized protocols [18]. Considering these data, the study was aimed to assess the effects of the left dorsolateral prefrontal cortex (IDL PFC) personalized stimulation protocol based on TGC on the cognitive test results in healthy volunteers and to compare its efficacy with that of standard protocol and sham stimulation.

METHODS

Prior to inclusion in the study, participants completed a questionnaire to identify contraindications to TMS and a modified version of the Edinburgh Handedness Inventory (EHI) [19]. Medical history of each participant was taken and demographic data were acquired, routine electroencephalography (EEG) with standard functional tests was performed to exclude epileptiform activity (Neuron-Spectr 4/P, Neurosoft LLC; Russia). Inclusion criteria: informed consent; age 18–40 years; laterality index > 40

based on EHI. Non-inclusion criteria: contraindications to MRI/TMS; epileptiform activity on the routine EEG; history of neurological or mental disorders; the use of medications having an effect on the CNS; decompensated chronic somatic disorder. Exclusion criteria: severe adverse events (AEs) revealed during the TMS procedure (TMS-induced epileptic seizure, syncope, etc.); development of somatic, mental or neurological diseases; pregnancy; refusal to participate.

Determining individual theta-gamma coupling frequencies

To determine the TGC frequencies, the 64-channel EEG (10–10 electrode placement system) synchronized with the n-back test (Latin consonants were presented with $n = 3$, the details of the method are provided below) was recorded. The actiCHamp Plus 64 (BP-100-2511) system (Brain Products GmbH; Germany) was used for EEG recording; synchronization was performed using the Trigger Station (Brain Trends; Italy); paradigm was written in the E-Prime 3.0 software (Psychology Software Tools; USA). Three series of 24 stimuli were presented (6 matching stimuli per session were presented at 3000 ms intervals, the stimulus presentation time was 250 ms. There were breaks for rest between series, the duration of which was determined by volunteers (10–20 s). Training with $n = 1$ and 2 was conducted before the main test.

EEG preprocessing and analysis was performed in EEGLAB and MATLAB (The MathWorks, Inc.; USA). Preprocessing involved removal of channels with high noise levels; referencing to the average reference; 1–80 Hz band filtering with a 49–51 Hz band-stop filter; removal of intervals with artifactual signal; artifact removal by independent component analysis. The signals from the Fz and Pz electrodes were analyzed to calculate the phase and amplitude of the TGC, respectively [18]. The averaged signal of all recording electrodes was used as a reference. We analyzed intervals from 250 ms after the end of the stimulus display to the moment of the next stimulus display with a cutting of 750 ms on each side to reduce edge artifacts (69 intervals of 1000 ms each). Wavelet transform was applied with the cycle number of 6 and 4 for phase and amplitude to extract rhythms. The coupling strength was estimated using the mean vector length (MVL) as the most sensitive under the assumption of monophasic coupling. The index normalization procedure was used to eliminate unbalanced phase distribution and large amplitude fluctuations. The TGC comodulograms were plotted for each subject. The frequencies of maximum TGC were used to develop a personalized iTBS protocol.

Theta-burst stimulation protocols

TMS was performed with the MagPro X100 + MagOption stimulation device (Tonika Elektronik A/S; Denmark) in combination with the Localite TMS Navigator system (Localite GmbH; Germany) and the Axilum Robotics TMS-Cobot robotic positioning system (Axilum Robotics; France) using the liquid-cooled figure-of-eight coil. For navigated TMS, MRI was performed in the 3D-T1-MPR (3D T1 multiplanar reconstruction) mode using the MAGNETOM Verio and MAGNETOM Prisma scanners (Siemens Healthcare GmbH; Germany) (voxel size $1.0 \times 0.977 \times 0.977 \text{ mm}^3$, 176 sagittal slices). The target within IDLPFC was defined as a spot located 5 cm anterior to the “hot spot” of the first dorsal interosseous (FDI) muscle cortical representation; the localization was specified based on individual structural MRI data. Electromyography recording of motor evoked responses involved the use of the Ag/Cl electrodes (Neurosoft LLC; Russia) placed on the muscle

belly (active electrode) and the tendon (reference electrode). Intensity equal to 75% of individual resting motor threshold determined in accordance with the Rossini-Rothwell protocol for FDI prior to each session was used in the active stimulation protocols.

During the crossover study each subject underwent one stimulation session according to the protocols below with at least 72 hours between sessions. All sessions were conducted within the same time frame (8–14 or 14–17 hours). Protocols were pseudo-randomized by the Latin square method and included the following:

- iTBS-5/50 — standard iTBS protocol (bursts of 3 stimuli at 50 Hz, bursts were applied with a frequency of 5 Hz). One block consisted of 10 bursts, an interval between blocks was 8 s, the total number of stimuli per session was 600;
- iTBS-ind — personalized iTBS protocol (bursts of 3 stimuli, the stimulus frequency corresponded to the gamma rhythm frequency and the frequency of bursts corresponded to the frequency of theta rhythm at maximum TGC determining during the previous step). One block consisted of 10 bursts, an interval between blocks was 8 s, the total number of stimuli per session was as close to 600 as possible for this frequency ratio;
- iTBS-sham — sham stimulation involved the use of special figure-of-eight coil imitating the sounds of stimuli presented, but not inducing stimuli themselves, and local low-intensity electrical stimulation imitating the sensations of magnetic stimulation. The duration and frequency of the sound imitation of stimuli were similar to standard, and the electrical stimulation intensity was determined individually based on the severity of sensations in the area subjected to stimulation.

Cognitive tests

Neuropsychological testing was performed using PEBL v 2.0 (Psychology Experiment Building Language) [20]. Participants put on the noise-canceling headphones to minimize distractions. The following tests were used: n-back test involving simultaneous presentation of spatial and verbal stimuli; backwards Corsi blocks task; Forward Digit Span; Tower of London.

In the n-back test, the subjects were simultaneously presented with spatial (position of squares) and verbal (Latin consonants) stimuli [21]. The subject had to determine whether the current stimulus matched the one presented n steps before and to press the key when there was a match. The accuracy of performance was assessed using the d' sensitivity index [22]. It was calculated based on the number of correct keystrokes in response to a matching stimulus (hits) and the number of false keystrokes in response to a mismatching stimulus (false alarms). The number of hits was normalized to the total number of matching stimuli (6 for the version of the task used), and the number of false alarms was normalized to the total number of mismatching stimuli (16 and 17 for n-back test with $n = 2$ and $n = 3$, respectively). Z transformation was applied to each normalized value, and d' was calculated as a difference of Z -values for hits and false alarms. Considering the simultaneous presentation of verbal and spatial stimuli, the total d' value for two types of stimuli with each n was also determined. The results obtained with $n = 2$ and $n = 3$ were analyzed. Training involving separate presentation of verbal stimuli with $n = 1$ and 2, spatial stimuli with $n = 1$, and the combination of two types of stimuli with $n = 1$ was performed before each n-back test.

In the Corsi blocks task, one had to memorize the order, in which squares were presented, and reproduce it in reverse order. The maximum length of the correctly recalled sequence was estimated.

In the Digit Span test, the subject was presented a numerical sequence, which he/she had to reproduce in direct order, starting from the sequence of 5 digits, with the step of 1 digit, up to a maximum length of 10 digits. The maximum length of numerical sequence the subject could correctly recall or the total number of correctly recalled sequences (after the maximum length of 10 digits was achieved) was estimated.

In the Tower of London test, the subject was offered to reproduce the specified sequence of colored disks by moving the disks. The time of task performance was recorded.

The test scores were measured at three time points: T0 — before stimulation, T1 — immediately after the end of stimulation, T2 — 1 h after the end of stimulation. The effects of stimulation at T1 and T2 were estimated as the difference between the values at each of these points and the initial value at T0.

Statistical data processing

Statistical analysis was performed using the IBM SPSS Statistics software package (v.23) (IBM, SPSS Inc.; USA). Estimation of individual effects of each protocol at T1 and T2 compared to T0 as well as comparison of effects between different protocols was performed using the Friedman test. The Wilcoxon test with Bonferroni correction was used to identify significant differences for pairwise comparisons. The significance threshold was set as $p = 0.05$.

Assessment of the stimulation protocol safety and tolerability

All participants completed the standardized questionnaire for assessment of AEs during the TMS session immediately after stimulation and within 24 h after stimulation, before each subsequent stimulation session.

RESULTS

A total of 25 individuals were screened, among them four had contraindications to TMS (three individuals used drugs affecting the CNS, one had somatic disorder). Among the included volunteers five failed to complete the study (four for logistical reasons, one due to poor tolerability of TMS). The data of 16 volunteers were included in the final analysis (seven males, average age 29.6 years).

Individual theta–gamma coupling frequencies

The following TGC frequencies used for individual protocols were obtained based on the analysis of the EEG data with paradigm (Table 1). An example of individual comodulogram is provided in Fig.

Safety and tolerability

The data of 50 sessions were analyzed (16 iTBS-ind, 17 iTBS-5/50, 17 iTBS-sham). No severe AEs were reported. One volunteer refused to continue participating after the second session of stimulation (iTBS-5/50) due to the development of mild headache (3 points on the Numeric Pain Scale, NPS) and difficulty concentrating.

Mild AEs were reported in 29 sessions (78%) (Table 2). Mild to moderate pain in the area of stimulation was the most common AE reported during TMS (12 sessions, 24%; 2–5 points on NPS). more intense pain (7–8 points on NPS)

Table 1. Individual theta–gamma coupling frequencies

N	Theta–gamma coupling frequencies		Протокол стимуляции		
	Individual theta frequency, Hz	Individual gamma frequency, Hz	Frequency of bursts, Hz	Frequency of stimuli within the burst, Hz	Total number of stimuli
1	7,6	42	8	41.7	624
2	8	44	8	43.5	624
3	7	48	7	47.6	588
4	6	56	6	56	600
5	7	30	7	30	588
6	7	32	7	32.3	588
7	7	50	7	50	588
8	5	44	5	44	600
9	8	30	8	30	624
10	4	60	4	59.9	600
11	4	30	4	30	600
12	4	32	4	32	600
13	5	38	5	38	600
14	5	30	5	30	600
15	6	42	6	42	600
16	6	34	6	34	600

was reported during the iTBS-ind stimulation in one case and during the iTBS-sham in one case. Headache within 24 h after stimulation also had low intensity (2–3 points on NPS).

Cognitive effects

Analysis of effects of distinct protocols

When assessing the effects of distinct protocols using the Friedman test assessing differences at three time points), significant differences were revealed after the iTBS-5/50 protocol for the n-back tests with spatial stimuli ($n = 3$) ($p = 0.013$), Corsi blocks ($p = 0.044$) and Tower of London ($p = 0.015$), as well as after the iTBS-ind and iTBS-sham protocols for the Tower of London test ($p = 0.02$ and $p = 0.006$, respectively).

When performing pairwise comparison using the Wilcoxon test, significant differences were reported for the iTBS-5/50 protocol in the n-back test with spatial stimuli ($n = 3$) between

measurements at T2 and T0 ($p_{\text{corr}} = 0.018$, Bonferroni correction for multiple comparison) and in the Tower of London test between measurements at T2 and T1 ($p_{\text{corr}} = 0.039$); comparisons of other tests turned out to be non-significant. As for protocols iTBS-ind and iTBS-sham, significant differences were reported in the Tower of London test between measurements at T2 and T0 ($p_{\text{corr}} = 0.045$ and $p_{\text{corr}} = 0.003$, respectively) (Table 3).

Comparison of effects between protocols

When comparing protocols, significant differences were reported in the n-back test with spatial stimuli ($n = 3$) for differences between T1 and T2, as well as in the Corsi blocks task for differences between T0 and T2 and between T1 and T2 (Table 4). Pairwise comparison involving the use of the Wilcoxon test revealed significant differences in the n-back test with spatial stimuli ($n = 3$) between protocols iTBS-5/50 and iTBS-sham (the effects of the iTBS-5/50 was larger)

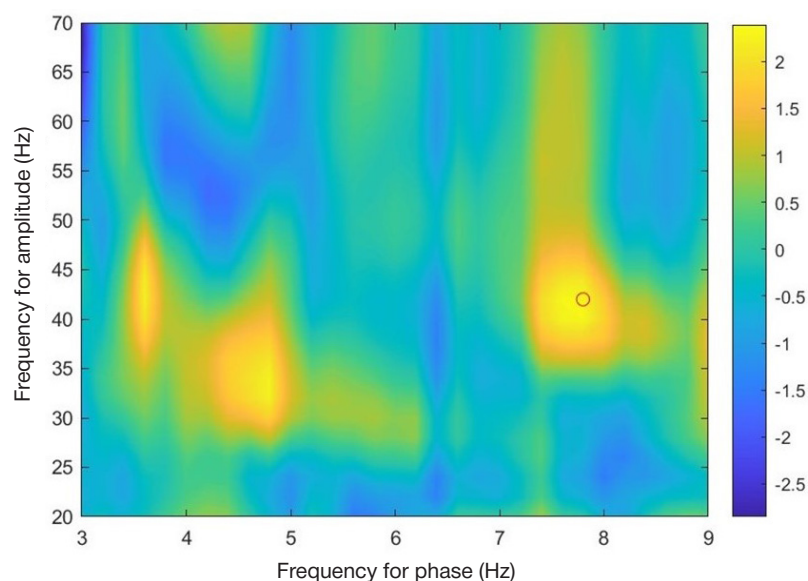


Fig. Individual comodulogram of healthy volunteer. The color scale indicates the values of mean vector length (MVL); maximum theta–gamma coupling is marked with the red circle (frequencies of 7,6; 40 Hz)

Table 2. Adverse events during stimulation and within 24 h after stimulation

Protocol	iTBS-5/50	iTBS-ind	iTBS-sham
Total number of sessions	17	16	17
AEs during stimulation			
Sessions with AEs	7	8	14
Cases of headache during stimulation	2	2	8
Non-painful unpleasant sensations	4	5	3
Drowsiness	2	1	2
Concentration difficulties	1	0	1
AEs within 24 h after stimulation			
Total number of sessions	4	1	1
Headache within 24 h after stimulation	3	1	1
Other unpleasant sensations within 24 h after stimulation	4	0	1

Note: iTBS-5/50 — standard theta-burst stimulation protocol, iTBS-ind — personalized theta-burst stimulation protocol, iTBS-sham — sham stimulation

($p_{corr} = 0.039$), in the Corsi blocks task between points T2 and T1 for protocols iTBS-5/50 and iTBS-ind, as well as iTBS-5/50 and iTBS-sham (the effects of the iTBS-5/50 protocol was smaller compared to other protocols; $p_{corr} = 0.038$ and 0.048 , respectively) (Table 5).

DISCUSSION

During the study we developed an IDLPFC iTBS personalized protocol based on individual TGC frequencies, gained experience of its application on healthy volunteers and showed a beneficial safety and tolerability profile. No significant differences from the standard protocol or sham stimulation were reported in the majority of tests. Significant effect was reported only in the Tower of London test for assessment of executive functioning. It was shown that standard protocol was effective for the spatial WM and divided attention test (n-back test with $n = 3$), and the change was significantly larger compared to sham stimulation. On the other hand, the simpler spatial WM test (Corsi blocks) revealed significantly worse execution

after this protocol showing significant differences from sham stimulation and personalized protocol.

In contrast to the earlier reported data, we failed to find benefits of the effects of personalized protocol compared to the standard protocol, there also were no differences from sham stimulation [18]. The observed decrease in task completion time in the Tower of London test may be due to learning, since the same statistically significant effect was observed during sham stimulation. However, no significant differences between protocols were revealed in this test. Perhaps, the lack of the personalized protocol effect results from the destructive TMS-induced activity interference with individual cortical rhythms. This assumption is in line with the results of studies focused on the use of transcranial alternating current stimulation (tACS), in which the effect was dependent on the theta cycle phase, during which the gamma frequency current was applied [23, 24]. When using TMS, control of the theta bursts' synchronization with endogenous theta rhythm is possible only with the use of the "closed-loop" systems with simultaneous EEG-TMS recording and synchronization of stimuli with the

Table 3. Effects of distinct protocols on the results of cognitive tests

Test		iTBS-5/50			iTBS-ind			iTBS-sham			
<i>n</i>	Stimulus type	T1-T0	T2-T0	T2-T1	T1-T0	T2-T0	T2-T1	T1-T0	T2-T0	T2-T1	
n-back	<i>n</i> = 2	L	-0.32 [-0.42; 0.42]	-0.04 [-0.75; 0.74]	-0.12 [-0.55; 0.35]	0.04 [-0.37; 0.45]	0.04 [-0.39; 0.44]	0.00 [-0.02; 0.71]	-0.07 [-0.76; 0.58]	0.19 [-0.23; 0.69]	0.10 [-0.32; 1.00]
		S	-0.10 [-0.35; 0.65]	0.05 [-0.08; 0.86]	0.27 [-0.33; 0.83]	0.00 [-0.29; 0.35]	0.00 [-0.29; 0.39]	0.07 [-0.42; 0.42]	-0.42 [-0.54; 0.49]	-0.26 [-1.09; 0.56]	0.05 [-1.12; 0.81]
		Total	0.02 [-0.60; 0.86]	0.67 [-0.70; 0.84]	0.57 [-0.68; 0.78]	0.22 [-0.56; 0.52]	0.26 [-0.56; 0.95]	0.24 [-0.36; 0.71]	-0.02 [-0.99; 0.39]	0.40 [-1.29; 0.97]	0.32 [-0.31; 1.17]
	<i>n</i> = 3	L	-0.13 [-0.61; 0.55]	-0.24 [-0.54; 0.13]	-0.23 [-0.68; 0.71]	0.03 [-0.50; 0.70]	0.19 [-0.26; 0.64]	-0.10 [-0.49; 0.58]	-0.11 [-0.77; 0.59]	-0.32 [-0.56; 0.70]	-0.06 [-0.88; 0.65]
		S	0.32 [-0.09; 0.89]	0.89 [0.00; 1.18]	0.40 [0.16; 0.74]	-0.05 [-0.61; 0.73]	0.16 [-0.70; 1.09]	0.12 [-0.35; 1.02]	0.06 [-0.35; 0.58]	-0.07 [-0.42; 0.05]	-0.16 [-0.39; 0.15]
		Total	0.29 [-0.60; 0.62]	0.62 [-0.58; 1.23]	0.50 [-0.93; 0.99]	-0.45 [-0.76; 0.50]	0.36 [-0.25; 1.41]	0.11 [-0.80; 1.24]	0.09 [-0.54; 0.49]	-0.05 [-0.96; 0.47]	-0.25 [-0.70; 0.74]
Digit span		0.00 [-1.00; 1.25]	1.00 [-0.25; 2.00]	1.00 [0.00; 1.00]	0.00 [-0.25; 1.00]	0.00 [-1.00; 1.00]	-0.50 [-1.00; 1.00]	-0.50 [-1.25; 1.00]	0.00 [-1.25; 0.25]	0.00 [-1.00; 0.25]	
Corsi blocks		0.00 [0.00; 1.00]	0.00 [-1.25; 0.00]	0.00 [-2.00; 0.00]	0.00 [-0.25; 1.25]	0.00 [0.00; 1.25]	0.00 [0.00; 0.25]	0.00 [0.00; 1.25]	0.00 [0.00 2.00]	0.00 [0.00; 0.00]	
Tower of London		-4.00 [-51.8; 17.25]	-23.50 [-43.8; -4.25]	-19.00 [-38.5; -3.25]	-26.00 [-48.3; 15.0]	-36.00 [-68.0; -4.25]	-19.00 [-35.3; 1.5]	-10.00 [-49.8; 9.25]	-32.00 [-54.5; -14.50]	-15.50 [-36.8; 3.5]	

Note: iTBS-5/50 — standard theta-burst stimulation protocol, iTBS-ind — personalized iTBS protocol, iTBS-sham — sham stimulation; T1-T0 — difference between values measured immediately after and before stimulation (hereinafter the data are presented as M [Q₁; Q₃]), T2-T0 — difference between values measured 60 min after the end of stimulation and before stimulation; L — verbal stimuli, S — spatial stimuli, Total — total d' value for verbal and spatial stimuli with the same n; Digit Span — test for assessment of the sequence of digits recall, Corsi blocks — test for assessment of the spatial sequence recall; Tower of London — Tower of London test; significant differences ($p < 0.05$, pairwise comparison using the Bonferroni adjusted Wilcoxon test) are marked in bold; positive difference values correspond to performance improvement in all tests, except Tower of London

Table 4. Comparison of effects between protocols

Test	Test		pT1-T0	pT2-T0	pT2-T1
	n	Stimulus type			
n-back	n = 2	L	0.57	0.779	0.56
		S	0.459	0.083	0.646
		Total	0.185	0.57	0.717
	n = 3	L	0.533	0.21	1
		S	0.276	0.236	0.028
		Total	0.57	0.21	0.829
Digit span		0.789	0.319	0.16	
Corsi blocks		0.872	0.04	0.006	
Tower of London		0.779	0.668	0.35	

Note: pT1-T0 — significance level for differences of values measured at T1 and T0, pT2-T0 and pT2-T1 — the same for T2 and T0, T2 and T1, respectively; L — verbal stimuli, S — spatial stimuli, Total — total χ^2 value for verbal and spatial stimuli with the same n; Digit Span — test for assessment of the sequence of digits recall, Corsi blocks — test for assessment of the spatial sequence recall; Tower of London — Tower of London test; significant differences are marked in bold ($p < 0.05$, comparison using the Friedman test)

peaks of individual theta rhythm [25], however, the protocol efficacy and feasibility need to be studied.

The reported spatial WM improvement in response to one session of standard iTBS protocol is compliant with the results of some other studies [26, 27]. The use of the n-back test variant with simultaneously presented verbal and spatial stimuli assessing both WM characteristics and divided attention is a peculiarity of our study. No significant differences were observed when evaluating the test with verbal stimuli and the total score, so it is unlikely that the observed effect is due to a change in task strategy. The standard protocol had an oppositely directed effect on the other spatial WM test — Corsi blocks, i.e. a decrease in the number of memorized stimuli, although it was non-significant. The possible explanation could be that the IDLPFC stimulation affected mainly the processes of information processing in the WM or divided attention important for the n-back test execution, while the process of information maintenance was more important for the Corsi blocks task. Such multidirectional effects of protocol on two important WM components, information maintenance and processing, agrees well with the concept of the zero-sum game, according to which improvement of one function in response to stimulation is accompanied by deterioration of the other one and eventually leads to a zero result [28].

The emergence of significant differences in testing only after the standard iTBS protocol can be explained by the fact that stimulation with a frequency of 5 and 50 Hz is most effective for induction of the long-term potentiation, as has been earlier shown in animal models [6]. An alternative explanation can be based on the assumption that the WM capacity is determined by the ratio of gamma/theta frequencies. In this case stimulation with a frequency lower than individual theta rhythm leads to the increase in the WM capacity, which has been confirmed by studies involving the use of tACS [29, 30]. A similar approach can be realized using iTBS protocols.

Table 5. Pairwise comparison of the effects of protocols

Test	Comparison	iTBS-5/50 vs iTBS-ind	iTBS-5/50 vs iTBS-sham	iTBS-ind vs iTBS-sham
n-back (S, n = 3)	pT2-T1	1	0.039	1
Corsi blocks	pT2-T0	0.186	0.105	1
	pT2-T1	0.033	0.048	1

Note: Identification of protocols: iTBS-5/50 — standard theta-burst stimulation protocol, iTBS-ind — personalized iTBS protocol, iTBS-sham — sham stimulation; pT2-T0 — significance level for differences of values measured at T2 and T0, pT2-T1 — significance level for differences of values measured at T2 and T1; S — spatial stimuli, Corsi blocks — test for assessment of the spatial sequence recall; significant differences are marked in bold ($p < 0.05$, Wilcoxon test adjusted for multiple comparisons)

All detected effects were noted when performing delayed measurements (an hour after the beginning of stimulation), while measurements performed immediately after stimulation revealed no significant differences for any of the protocols. The duration of the effect is consistent with the results obtained earlier, according to which the effect on cognitive functions is absent when measured immediately after stimulation, but is detected in repeated measurements in the delayed period (60 min in our study, 20 and 40 min — according to the literature) [26]. It is reasonable to estimate the stimulation effects not only immediately after the end of stimulation, but also throughout the intended effect duration.

Small sample size can be considered the study limitation, however, this power is sufficient to detect "large" effects. Furthermore, variability of individual TGC and the issues related to selection of algorithm for individual TGC calculation represent a significant limitation. The lack of significant effect on the results of some tests (such as n-back test with $n = 2$; Digit Span, Corsi blocks) can also be due to their low complexity and the "ceiling effect". One more limitation is the crossover design that can result in learning effect between sessions. However, the possible bias due to learning was minimized by the Latin square method. Furthermore, volunteers underwent several training tests before the beginning of stimulation sessions.

CONCLUSIONS

Thus, we have demonstrated safety and efficacy of the IDLPFC personalized theta-burst stimulation based on individual TGC frequencies, but the effect on cognitive test scores could not be confirmed. Standard iTBS protocol turned out to show a significant effect different from sham stimulation. In this regard, further investigation of this protocol, for example, in patients with cognitive impairment, can be promising. Considering the results obtained, it seems reasonable to test the alternative

hypotheses when conducting further research (for example, the hypothesis of individual stimulation with frequencies lower than the measured TGC frequencies or stimulation phase

synchronized with theta rhythm). Furthermore, it is necessary to further investigate optimal TGC calculation algorithms to improve measurement accuracy and reproducibility.

References

- Lefaucheur JP. Transcranial magnetic stimulation. *Handb Clin Neurol.* 2019; 160: 559–80. DOI: 10.1016/B978-0-444-64032-1.00037-0.
- Lefaucheur JP, Aleman A, Baeken C, Benninger DH, Brunelin J, Di Lazzaro V et al. Evidence-based guidelines on the therapeutic use of repetitive transcranial magnetic stimulation (rTMS): An update (2014–2018). *Clin Neurophysiol.* 2020; 131 (2): 474–528. DOI: 10.1016/j.clinph.2019.11.002.
- Begemann MJ, Brand BA, Čurčić-Blake B, Aleman A, Sommer IE. Efficacy of non-invasive brain stimulation on cognitive functioning in brain disorders: a meta-analysis. *Psychol Med.* 2020; 50 (15): 2465–86. DOI: 10.1017/S0033291720003670.
- Chervyakov AV, Chernyavsky AY, Sinitsyn DO, Piradov MA. Possible mechanisms underlying the therapeutic effects of transcranial magnetic stimulation. *Front Hum Neurosci.* 2015; 9: 303. DOI: 10.3389/fnhum.2015.00303.
- Tang A, Thickbroom G, Rodger J. Repetitive transcranial magnetic stimulation of the brain: mechanisms from animal and experimental models. *Neuroscientist.* 2017; 23 (1): 82–94. DOI: 10.1177/1073858415618897.
- Larson J, Munkácsy E. Theta-burst LTP. *Brain Res.* 2015; 1621: 38–50. DOI: 10.1016/j.brainres.2014.10.034.
- Rounis E, Huang YZ. Theta burst stimulation in humans: a need for better understanding effects of brain stimulation in health and disease. *Exp Brain Res.* 2020; 238 (7–8): 1707–14. DOI: 10.1007/s00221-020-05880-1.
- Wischniewski M, Schutter DJ. Efficacy and time course of theta burst stimulation in healthy humans. *Brain Stimul.* 2015; 8 (4): 685–92. DOI: 10.1016/j.brs.2015.03.004.
- Pabst A, Proksch S, Médé B, Comstock DC, Ross JM, Balasubramaniam R. A systematic review and meta-analysis of the efficacy of intermittent theta burst stimulation (iTBS) on cognitive enhancement. *Neurosci Biobehav Rev.* 2022; 135: 104587. DOI: 10.1016/j.neubiorev.2022.104587.
- Bakulin IS, Zabirowa AH, Poydasheva AG, Sinitsyn DO, Lagoda DY, Suponeva NA, et al. Effects of the metaplasticity-based theta-burst transcranial stimulation protocols on working memory performance. *Bulletin of RSMU.* 2023; 2: 33–41. DOI: 10.24075/vrgmu.2023.011. Russian.
- Philip NS, Leuchter AF, Cook IA, Massaro J, Goethe JW, Carpenter LL. Predictors of response to synchronized transcranial magnetic stimulation for major depressive disorder. *Depress Anxiety.* 2019; 36: 278–85. DOI: 10.1002/da.22862.
- Brownjohn PW, Reynolds JN, Matheson N, Fox J, Shemmell JB. The effects of individualized theta burst stimulation on the excitability of the human motor system. *Brain Stimul.* 2014; 7 (2): 260–8. DOI: 10.1016/j.brs.2013.12.007.
- Poydasheva AG, Bakulin IS, Sinitsyn DO, Zabirowa AH, Lagoda DY, Suponeva NA, et al. Literature review on theta-gamma phase-amplitude coupling: physiological basics, analysis methods, and perspectives of translation into clinical practice. *Annals of Clinical and Experimental Neurology.* 2022; 16 (4): 71–9. DOI: 10.54101/ACEN.2022.4.9. Russian.
- Lisman JE, Jensen O. The θ - γ neural code. *Neuron.* 2013; 77 (6): 1002–16. DOI: 10.1016/j.neuron.2013.03.007.
- Brooks H, Goodman MS, Bowie CR, Zomorodi R, Blumberger DM, Butters MA, et al. Theta-gamma coupling and ordering information: a stable brain-behavior relationship across cognitive tasks and clinical conditions. *Neuropsychopharmacology.* 2020; 45 (12): 2038–47. DOI: 10.1038/s41386-020-0759-z.
- Abubaker M, Al Qasem W, Kvašňák E. Working memory and cross-frequency coupling of neuronal oscillations. *Front Psychol.* 2021; 12: 756661. DOI: 10.3389/fpsyg.2021.756661.
- Goodman MS, Kumar S, Zomorodi R, Ghazala Z, Cheam ASM, Barr MS et al. Theta-gamma coupling and working memory in Alzheimer's dementia and mild cognitive impairment. *Front Aging Neurosci.* 2018; 10: 101. DOI: 10.3389/fnagi.2018.00101.
- Chung SW, Sullivan CM, Rogasch NC, Hoy KE, Bailey NW, Cash RFH, et al. The effects of individualised intermittent theta burst stimulation in the prefrontal cortex: a TMS-EEG study. *Hum Brain Mapp.* 2019; 40 (2): 608–27. DOI: 10.1002/hbm.24398.
- Oldfield RC. The assessment and analysis of handedness: the Edinburgh inventory. *Neuropsychologia.* 1971; 9 (1): 97–113.
- Mueller ST, Piper BJ. The Psychology Experiment Building Language (PEBL) and PEBL Test Battery. *J Neurosci Methods.* 2014; 222: 250–9. DOI: 10.1016/j.jneumeth.2013.10.024.
- Kirchner WK. Age differences in short-term retention of rapidly changing information. *J Exp Psychol.* 1958; 55 (4): 352–8. DOI: 10.1037/h0043688.
- Haatveit BC, Sundet K, Hugdahl K, Ueland T, Melle I, Andreassen OA. The validity of d prime as a working memory index: results from the "Bergen n-back task". *J Clin Exp Neuropsychol.* 2010; 32 (8): 871–80. DOI: 10.1080/13803391003596421.
- Turi Z, Mittner M, Lehr A, Bürger H, Antal A, Paulus W. θ - γ Cross-Frequency Transcranial Alternating Current Stimulation over the Trough Impairs Cognitive Control. *eNeuro.* 2020; 7 (5): ENEURO.0126-20.2020. DOI: 10.1523/ENEURO.0126-20.2020.
- Akkad H, Dupont-Hadwen J, Kane E, Evans C, Barrett L, Frese A, et al. Increasing human motor skill acquisition by driving theta-gamma coupling. *Elife.* 2021; 10: e67355. DOI: 10.7554/eLife.67355.
- Gordon PC, Belardinelli P, Stenroos M, Ziemann U, Zrenner C. Prefrontal theta phase-dependent rTMS-induced plasticity of cortical and behavioral responses in human cortex. *Brain Stimul.* 2022; 15 (2): 391–402. DOI: 10.1016/j.brs.2022.02.006.
- Hoy KE, Bailey N, Michael M, Fitzgibbon B, Rogasch NC, Saeki T, Fitzgerald PB. Enhancement of working memory and task-related oscillatory activity following intermittent Theta Burst Stimulation in healthy controls. *Cereb Cortex.* 2016; 26 (12): 4563–73. DOI: 10.1093/cercor/bhv193.
- Ngetich R, Jin D, Li W, Song B, Zhang J, Jin Z, Li L. Enhancing visuospatial working memory performance using intermittent Theta-Burst Stimulation over the right dorsolateral prefrontal cortex. *Front Hum Neurosci.* 2022; 16: 752519. DOI: 10.3389/fnhum.2022.752519.
- Brem AK, Fried PJ, Horvath JC, Robertson EM, Pascual-Leone A. Is neuroenhancement by noninvasive brain stimulation a net zero-sum proposition? *Neuroimage.* 2014; 85 Pt 3 (3): 1058–68. DOI: 10.1016/j.neuroimage.2013.07.038.
- Voskuhl J, Huster RJ, Herrmann CS. Increase in short-term memory capacity induced by down-regulating individual theta frequency via transcranial alternating current stimulation. *Front Hum Neurosci.* 2015; 9: 257. DOI: 10.3389/fnhum.2015.00257.
- Wolinski N, Cooper NR, Sauseng P, Romei V. The speed of parietal theta frequency drives visuospatial working memory capacity. *PLoS Biol.* 2018; 16 (3): e2005348. DOI: 10.1371/journal.pbio.2005348.

Литература

- Lefaucheur JP. Transcranial magnetic stimulation. *Handb Clin Neurol.* 2019; 160: 559–80. DOI: 10.1016/B978-0-444-64032-1.00037-0.
- Lefaucheur JP, Aleman A, Baeken C, Benninger DH, Brunelin J, Di Lazzaro V et al. Evidence-based guidelines on the therapeutic use of repetitive transcranial magnetic stimulation (rTMS): An update (2014–2018). *Clin Neurophysiol.* 2020; 131 (2): 474–528. DOI: 10.1016/j.clinph.2019.11.002.
- Begemann MJ, Brand BA, Ćurčić-Blake B, Aleman A, Sommer IE. Efficacy of non-invasive brain stimulation on cognitive functioning in brain disorders: a meta-analysis. *Psychol Med.* 2020; 50 (15): 2465–86. DOI: 10.1017/S0033291720003670.
- Chervyakov AV, Chernyavsky AY, Sinityn DO, Piradov MA. Possible mechanisms underlying the therapeutic effects of transcranial magnetic stimulation. *Front Hum Neurosci.* 2015; 9: 303. DOI: 10.3389/fnhum.2015.00303.
- Tang A, Thickbroom G, Rodger J. Repetitive transcranial magnetic stimulation of the brain: mechanisms from animal and experimental models. *Neuroscientist.* 2017; 23 (1): 82–94. DOI: 10.1177/1073858415618897.
- Larson J, Munkácsy E. Theta-burst LTP. *Brain Res.* 2015; 1621: 38–50. DOI: 10.1016/j.brainres.2014.10.034.
- Rounis E, Huang YZ. Theta burst stimulation in humans: a need for better understanding effects of brain stimulation in health and disease. *Exp Brain Res.* 2020; 238 (7–8): 1707–14. DOI: 10.1007/s00221-020-05880-1.
- Wischniewski M, Schutter DJ. Efficacy and time course of theta burst stimulation in healthy humans. *Brain Stimul.* 2015; 8 (4): 685–92. DOI: 10.1016/j.brs.2015.03.004.
- Pabst A, Proksch S, Médé B, Comstock DC, Ross JM, Balasubramaniam R. A systematic review and meta-analysis of the efficacy of intermittent theta burst stimulation (iTBS) on cognitive enhancement. *Neurosci Biobehav Rev.* 2022; 135: 104587. DOI: 10.1016/j.neubiorev.2022.104587.
- Бакулин И. С., Забирова А. Х., Пойдашева А. Г., Синицын Д. О., Лагода Д. Ю., Супонева Н. А. и др. Эффект основанных на метапластичности протоколов транскраниальной стимуляции тета-вспышками на показатели рабочей памяти. *Вестник РГМУ.* 2023; 2: 33–41. DOI: 10.24075/vrgmu.2023.011.
- Philip NS, Leuchter AF, Cook IA, Massaro J, Goethe JW, Carpenter LL. Predictors of response to synchronized transcranial magnetic stimulation for major depressive disorder. *Depress Anxiety.* 2019; 36: 278–85. DOI: 10.1002/da.22862.
- Brownjohn PW, Reynolds JN, Matheson N, Fox J, Shemmell JB. The effects of individualized theta burst stimulation on the excitability of the human motor system. *Brain Stimul.* 2014; 7 (2): 260–8. DOI: 10.1016/j.brs.2013.12.007.
- Пойдашева А. Г., Бакулин И. С., Синицын Д. О., Забирова А. Х., Лагода Д. Ю., Супонева Н. А. и др. Фазово-амплитудное тета-гамма сопряжение: физиологические основы, методы анализа и перспективы трансляции в клиническую практику. *Анналы клинической и экспериментальной неврологии.* 2022; 16 (4): 71–9. DOI: 10.54101/ACEN.2022.4.9.
- Lisman JE, Jensen O. The θ - γ neural code. *Neuron.* 2013; 77 (6): 1002–16. DOI: 10.1016/j.neuron.2013.03.007.
- Brooks H, Goodman MS, Bowie CR, Zomorodi R, Blumberg DM, Butters MA, et al. Theta-gamma coupling and ordering information: a stable brain-behavior relationship across cognitive tasks and clinical conditions. *Neuropsychopharmacology.* 2020; 45 (12): 2038–47. DOI: 10.1038/s41386-020-0759-z.
- Abubaker M, Al Qasem W, Kvašňák E. Working memory and cross-frequency coupling of neuronal oscillations. *Front Psychol.* 2021; 12: 756661. DOI: 10.3389/fpsyg.2021.756661.
- Goodman MS, Kumar S, Zomorodi R, Ghazala Z, Cheam ASM, Barr MS et al. Theta-gamma coupling and working memory in Alzheimer's dementia and mild cognitive impairment. *Front Aging Neurosci.* 2018; 10: 101. DOI: 10.3389/fnagi.2018.00101.
- Chung SW, Sullivan CM, Rogasch NC, Hoy KE, Bailey NW, Cash RFH, et al. The effects of individualised intermittent theta burst stimulation in the prefrontal cortex: a TMS-EEG study. *Hum Brain Mapp.* 2019; 40 (2): 608–27. DOI: 10.1002/hbm.24398.
- Oldfield RC. The assessment and analysis of handedness: the Edinburgh inventory. *Neuropsychologia.* 1971; 9 (1): 97–113.
- Mueller ST, Piper BJ. The Psychology Experiment Building Language (PEBL) and PEBL Test Battery. *J Neurosci Methods.* 2014; 222: 250–9. DOI: 10.1016/j.jneumeth.2013.10.024.
- Kirchner WK. Age differences in short-term retention of rapidly changing information. *J Exp Psychol.* 1958; 55 (4): 352–8. DOI: 10.1037/h0043688.
- Haatveit BC, Sundet K, Hugdahl K, Ueland T, Melle I, Andreassen OA. The validity of d prime as a working memory index: results from the "Bergen n-back task". *J Clin Exp Neuropsychol.* 2010; 32 (8): 871–80. DOI: 10.1080/13803391003596421.
- Turi Z, Mittner M, Lehr A, Bürger H, Antal A, Paulus W. θ - γ Cross-Frequency Transcranial Alternating Current Stimulation over the Trough Impairs Cognitive Control. *eNeuro.* 2020; 7 (5): ENEURO.0126-20.2020. DOI: 10.1523/ENEURO.0126-20.2020.
- Akkad H, Dupont-Hadwen J, Kane E, Evans C, Barrett L, Frese A, et al. Increasing human motor skill acquisition by driving theta-gamma coupling. *Elife.* 2021; 10: e67355. DOI: 10.7554/eLife.67355.
- Gordon PC, Belardinelli P, Sterroos M, Ziemann U, Zrenner C. Prefrontal theta phase-dependent rTMS-induced plasticity of cortical and behavioral responses in human cortex. *Brain Stimul.* 2022; 15 (2): 391–402. DOI: 10.1016/j.brs.2022.02.006.
- Hoy KE, Bailey N, Michael M, Fitzgibbon B, Rogasch NC, Saeki T, Fitzgerald PB. Enhancement of working memory and task-related oscillatory activity following intermittent Theta Burst Stimulation in healthy controls. *Cereb Cortex.* 2016; 26 (12): 4563–73. DOI: 10.1093/cercor/bhv193.
- Ngetich R, Jin D, Li W, Song B, Zhang J, Jin Z, Li L. Enhancing visuospatial working memory performance using intermittent Theta-Burst Stimulation over the right dorsolateral prefrontal cortex. *Front Hum Neurosci.* 2022; 16: 752519. DOI: 10.3389/fnhum.2022.752519.
- Brem AK, Fried PJ, Horvath JC, Robertson EM, Pascual-Leone A. Is neuroenhancement by noninvasive brain stimulation a net zero-sum proposition? *Neuroimage.* 2014; 85 Pt 3 (03): 1058–68. DOI: 10.1016/j.neuroimage.2013.07.038.
- Vosskuhl J, Huster RJ, Herrmann CS. Increase in short-term memory capacity induced by down-regulating individual theta frequency via transcranial alternating current stimulation. *Front Hum Neurosci.* 2015; 9: 257. DOI: 10.3389/fnhum.2015.00257.
- Wolinski N, Cooper NR, Sauseng P, Romei V. The speed of parietal theta frequency drives visuospatial working memory capacity. *PLoS Biol.* 2018; 16 (3): e2005348. DOI: 10.1371/journal.pbio.2005348.

PREDICTING THE OUTCOMES OF *IN VITRO* FERTILIZATION PROGRAMS USING A RANDOM FOREST MACHINE LEARNING MODEL

Vladimirsky GM¹, Zhuravleva MA¹, Dashieva AE²✉, Korneeva IE², Nazarenko TA²

¹ Higher School of Economics National Research University, Moscow, Russia

² Kulakov National Medical Scientific Centre for Obstetrics, Gynecology and Perinatal Medicine, Moscow, Russia

Currently, *in vitro* fertilization (IVF) with embryo transfer is the main method of treatment of all forms of infertility, but successful cases ending in pregnancy still account for only a third of all cycles performed. It is necessary to take into account many parameters and investigate the connections between them in order to properly evaluate the results of IVF. Over the past decades, a number of IVF prediction models have been developed with the aim at assessing the outcomes in individual cases, but, given the generally poor prognostic capacity, only a few of them have proven to be clinically significant. This study aimed to create nonlinear IVF outcomes prediction models and identify the most significant factors affecting the said outcomes. Using a database containing information on more than 700 indicators of 7004 women aged 18 to 45 years who participated in the IVF program in Russia from 2010 to 2020, we trained a random forest model that predicted pregnancy in the IVF cycle with ROC-AUC = 0.69. This paper describes 20 most successful predictors of the resulting model and interprets their contribution to the prognosis. Of these, body mass index (BMI) and the number of received and fertilized oocytes have been covered in the scientific literature previously as predictors of IVF outcomes, but other parameters, such as anamnestic data, previous participation in an IVF program (number of cases and their results), as well as serum concentration of AMH, rarely appear in foreign prognostic models.

Keywords: IVF, infertility, prognostic model, random forest

Author contribution: Vladimirsky GM — predictive models training, literature analysis, choice of research methods; Zhuravleva MA — preprocessing and analysis of data, literature analysis, manuscript authoring; Dashieva AE — processing of source material, analysis of results; Korneeva IE, Nazarenko TA — development of the survey for the database, manuscript editing.

✉ **Correspondence should be addressed:** Ayuna E. Dashieva, Akademiya Oparina, 4B, Moscow, 117198, Russia, dr.dashieva@mail.ru

Received: 24.11.2023 **Accepted:** 19.12.2023 **Published online:** 31.12.2023

DOI: 10.24075/brsmu.2023.057

ПРОГНОЗИРОВАНИЕ ИСХОДОВ ПРОГРАММ ЭКСТРАКОРПОРАЛЬНОГО ОПЛОДОТВОРЕНИЯ С ИСПОЛЬЗОВАНИЕМ МОДЕЛИ МАШИННОГО ОБУЧЕНИЯ «СЛУЧАЙНЫЙ ЛЕС»

Г. М. Владимирский¹, М. А. Журавлева¹, А. Э. Дашиева²✉, И. Е. Корнеева², Т. А. Назаренко²

¹ Национальный исследовательский университет «Высшая школа экономики», Москва, Россия

² Национальный медицинский исследовательский центр акушерства, гинекологии и перинатологии имени В. И. Кулакова, Москва, Россия

Программы экстракорпорального оплодотворения (ЭКО) с переносом эмбрионов в настоящее время являются основными методами лечения всех форм бесплодия, однако успешные случаи, заканчивающиеся наступлением беременности, по-прежнему составляют лишь треть из числа всех проведенных циклов. Для оценки результатов лечения бесплодия методом ЭКО необходимо учитывать множество показателей и изучать взаимосвязь между ними. За последние десятилетия был разработан ряд моделей прогнозирования ЭКО для оценки индивидуальных результатов лечения, но лишь немногие из них оказались клинически значимыми, из-за их плохой прогностической способности. Целью исследования было создать нелинейные модели прогнозирования исходов ЭКО и выявить наиболее значимые факторы, влияющие на результат лечения. На основе базы данных, содержащей информацию по более чем 700 показателям 7004 женщин в возрасте от 18 лет до 45 лет, прошедших лечение в программе ЭКО на территории Российской Федерации с 2010 по 2020 г., была обучена модель «Случайного леса», прогнозирующая беременность в цикле ЭКО с ROC-AUC = 0,69. Описаны 20 самых успешных предикторов полученной модели с интерпретацией их вклада в прогнозирование. Из них индекс массы тела (ИМТ), число полученных и оплодотворившихся ооцитов описаны в научной литературе как предикторы исхода программ ЭКО, в то время как другие признаки, например анамнестические данные, количество и исходы предыдущих программ ЭКО, а также сывороточная концентрация АМГ, редко фигурируют в зарубежных прогностических моделях.

Ключевые слова: ЭКО, бесплодие, прогностическая модель, «Случайный лес»

Вклад авторов: Г. М. Владимирский — обучение прогностических моделей, анализ литературы, выбор методов исследования; М. А. Журавлева — предобработка и анализ данных, анализ литературы, написание рукописи; А. Э. Дашиева — обработка исходного материала, анализ результатов; И. Е. Корнеева, Т. А. Назаренко — разработка анкеты для базы данных, редактирование рукописи.

✉ **Для корреспонденции:** Аюна Эрдэмовна Дашиева ул. Академика Опарина, д. 4Б, г. Москва, 117198, Россия, dr.dashieva@mail.ru

Статья получена: 24.11.2023 **Статья принята к печати:** 19.12.2023 **Опубликована онлайн:** 31.12.2023

DOI: 10.24075/vrgmu.2023.057

Infertility is a problem affecting tens of millions of families. The development of assisted reproductive technologies (ART) gives such couples the hope that they can be parents. According to the report by Russian Association of Human Reproduction, in 2020, 148660 ART cycles were performed in the Russian Federation (RF), and about 34250 children were born. However, despite the population's need for this treatment being satisfied, clinical pregnancy occurs only in 34.8% of all embryo transfers [1]. There are many factors influencing the outcome of IVF, and they complicate the assessment of effectiveness of the cycles.

Therefore, development of a decision-making tool based on the analysis of these factors could improve the quality of medical care and counseling for patients in an IVF program.

Scientific literature offers several machine learning models that predict IVF outcomes and help identify women's characteristics and parts of the the program's protocol that affect such prediction the most [2].

Linear models are the most common approach to predicting results of IVF. A 2020 review identified 35 such models, all of them based on either logistic regression or Cox regression [3].

Often, such studies do not assess the quality of the models, although there are preferred methods for this, like ROC-AUC and c-statistics. ROC (receiver operating characteristic) analysis and the resulting ROC curve underpin qualitative assessment of predictive models. ROC analysis implies building four-field tables and measuring the model's sensitivity and specificity. ROC curve is a graphical plot that allows evaluating quality of the model by two classes. The ordinate axis is frequency of true positive results (sensitivity), and the abscissa axis is frequency of false positive results (specificity). The values are from 0 to 1 (that is, from 0 to 100%). The resulting curve shows the dependence of correctly classified positive cases on the number of incorrectly classified negative cases. In an ideal classifier, the ROC curve graph passes through the upper-left corner, where the proportion of true positive cases is 1.0, or 100% (ideal sensitivity), and the proportion of false positive cases is 0. Another characteristic used in assessment of quality of the model is area under curve (AUC). The higher the AUC, the higher predictive power of the model. More often, AUC is intended for comparative analysis of several models. In literature, the values of ROC-AUC in IVF results prediction range from 0.58 to 0.73 [3–12].

Typically, linear IVF success predictive models include about seven attributes. The most common are the woman's age, causes of infertility, outcome of previous pregnancies and IVF program enrollments, number of oocytes obtained and embryos transferred [4, 5, 9–11]. Some researchers believe that a limited number of attributes, which are used in the vast majority of studies, makes the predictive power of models rather modest, and advocate identification of new factors affecting outcome of the procedure [13].

Despite being commonly used, logistic regression models have a number of disadvantages. For example, several studies have revealed the nonlinear character of relationship between the success of IVF and key attributes, such as woman's age, number of oocytes obtained, and treatment initiation year [10, 11]. In such cases, cubic spline function can enable data interpolation (for example, age) and make linear models non-linear, or the data can be transformed to be polynomial [8, 10, 11]. Still, such modifications of linear models are based on a simple (polynomial) relationship between the target variable and the attributes.

Besides, logistic regression models are interpreted, and they do not possess high predictive power. Therefore, many researchers have turned to non-linear, non-interpretable machine learning models relying on random forest, gradient boosting, and neural networks. Random forest and gradient boosting are often considered the most advanced methods applicable to binary classification problems involving tabular data, since they tend to be unequalled in accuracy and generalization power [2]. As a rule, ROC AUC for such models ranges from 0.68 to 0.86, which is higher than that for linear classifiers [14–16].

The main limitation of non-linear non-interpreted models is the complexity of estimation of significance of each attribute to the prediction model. However, methods developed in the recent years enable interpretation of attributes for any machine learning model, regardless of their complexity. For this study, we used the SHAP method, which is based on the Shapley value, a concept from cooperative game theory. This method calculates contribution of each attribute to the prediction relying on the approximated Shapley value (average contribution of an attribute to all coalitions thereof) [17], which allows accurate predictions of the IVF programs outcomes.

This study aimed to build nonlinear IVF outcome prediction models and identify the most significant factors affecting the said outcome.

METHODS

Clinical material

To build the model, we used data covering the characteristics of 7004 women and presenting the outcomes of their participation in the IVF programs. They were treated at 17 ART clinics in RF from 2011 to 2020. The inclusion criteria were age from 18 to 45 years, and infertility for any reason (N97). The exclusion criteria were contraindications for ART and pregnancy, as per the Order of the Ministry of Health of the Russian Federation #803n of July 31, 2020 "On the procedure of application of assisted reproductive technologies, respective contraindications and restrictions."

Figure 1 shows the distribution of clinics participating in the study by subjects of the RF. For the purpose of collection of the material, we developed questionnaires listing 770 attributes, which were filled by specialists at the said clinics. The resulting data were broken into several blocks: social characteristics of patients (124 questions), medical history (171 questions), which included data on the state of somatic health (58 questions), gynecological health (108 questions), history of infertility and treatment methods (73 questions), laboratory examination data (6 points), data on the patient's partner (210 questions), data on the protocol of ovarian stimulation (7 questions) and embryological stage (30 questions), support for the luteal phase, and outcome of participation in the IVF program.

Data processing and analysis

Preprocessing of the data for the model included selection of the minimum value among several analyses of serum hormone levels (anti-mullerian hormone, or AMH; follicle stimulating hormone, or FSH; lutenizing hormone, or LH; thyroid stimulating hormone, TSH; prolactin). After removal of sparse and duplicate data, there remained 408 attributes. Gaps were filled with averages. We used odds ratio (OR) for the statistical analysis [18]; the respective p value was calculated as per [19].

Selection of attributes and interpretation of their significance

In this study, we used random forest, a machine learning method that relies on an ensemble of decision trees for classification tasks. Each individual tree in such a forest gives a prediction of a class, and the class with the highest number of votes becomes the prediction. The purpose of this work was to forecast pregnancy after IVF.

After building the random forest, we applied the Gini coefficient to measure inequality of the attributes. This coefficient allows comparing distribution of an attribute in a sample with a different number of units [20]. The model used for attribute allocation had hyperparameters, which are manually adjusted before training and allow maximization of the ROC AUC value in a five-fold cross validation; subsequently the model was trained on a full dataset. Selecting the attributes in the optimal amount, we applied the recursive selection method with five-fold cross validation, which implies removal of the least significant attribute at each step. All of the above methods were used in the implementation of the scikit-learn library [21]. The SHAP method [17], designed for interpretation of significance of attributes in a non-linear model, enabled extended interpretation of the results.

Models used

Because of the large number of binary and categorical attributes, as well as nonlinear dependencies between the attributes and the



Fig. 1. Geographical scope of the study

target variable, we used the random forest model implemented in the scikit-learn library as the main classifier [21]. GridSearch method with five-fold cross validation [21] enabled selection of the model's parameters, and the classes of the model were assessed using ROC AUC, which is less sensitive to the imbalance of classes in the data. Ultimately, the best parameters for the random forest model were the maximum depth of 50, not less than 2 objects per sheet, and 2000 trees in total. In addition, we tested the Catboost classifier model [22], which was chosen for its built-in support of categorical attributes that distinguishes it from other implementations of the gradient boosting algorithm. The target variable for all trained models was pregnancy (or lack thereof).

RESULTS

Recursive selection of attributes has shown that ROC AUC reaches its maximum (0.69) when training of the random forest involves 220 of them. In cross validation, the maximum Catboost

ROC AUC value was 0.68, therefore, further on, we used the random forest model, which is more convenient for interpretation. Figure 2 presents dynamics of this model's ROC AUC metric when the attributes are gradually removed therefrom.

At the outset, gradual removal of the attributes translates into insignificant changes of the ROC AUC value, which drops abruptly only when the their number goes below 33. Therefore, we chose 33 as the optimal amount of attributes in the model, with the ROC AUC value therewith reaching 0.69.

Gini coefficient was applied to establish the significance of 20 attributes with the greatest impact on the prediction (Fig. 3).

The attributes most significant for the prediction were date of birth (age), the number of fertilized oocytes, and the total number thereof, which is consistent with the data reported by international studies [16].

Compared to other hormone indicators, serum AMH had the greatest weight in prediction, but in international studies,

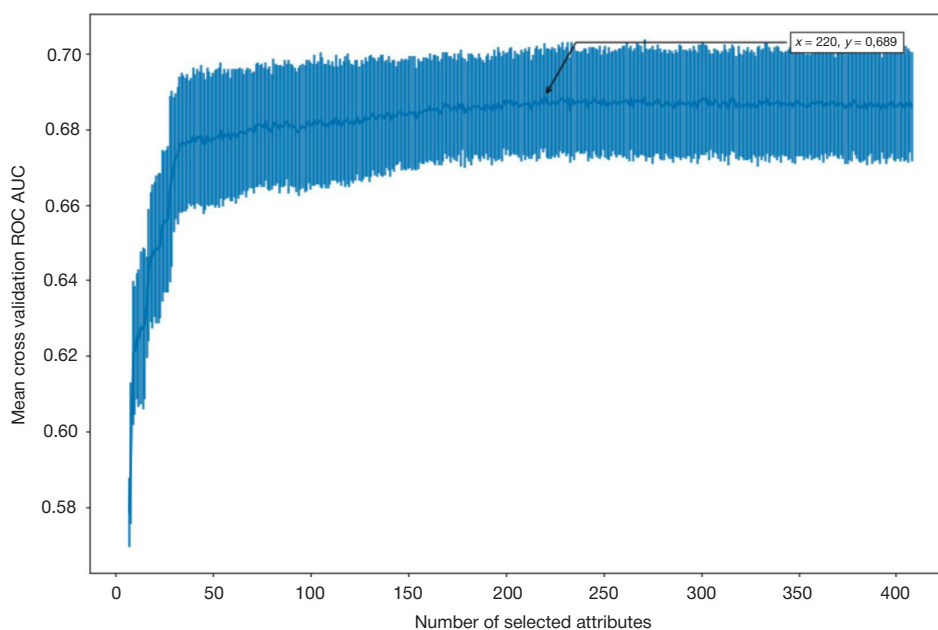


Fig. 2. Mean cross validation ROC AUC dynamics during elimination of attributes. The diagram shows the maximum ROC AUC and the standard deviation of the value in cross validation

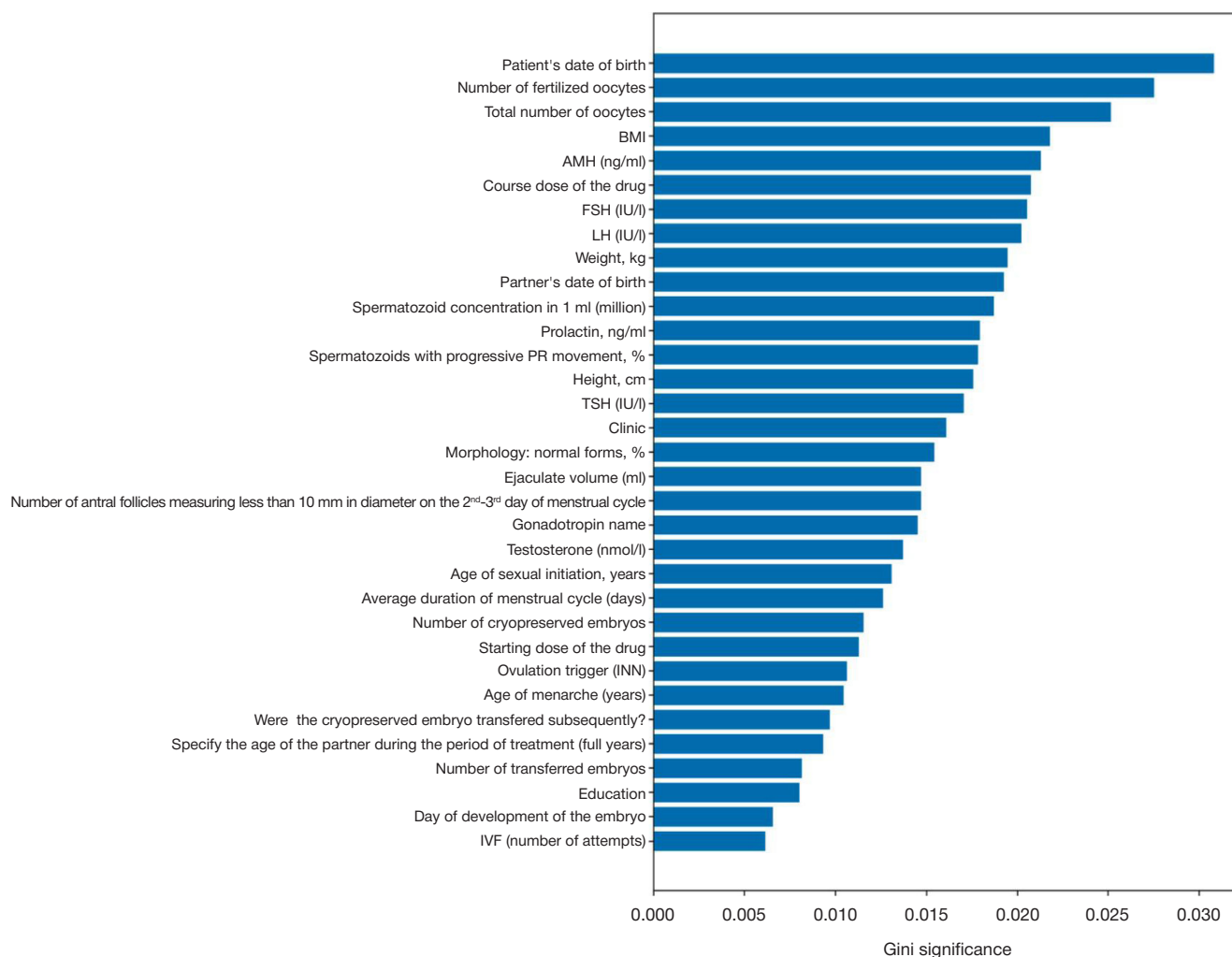


Fig. 3. Gini significance for 33 best attributes learned after training the random forest on 220 attributes

it is much less common than the levels of gonadotropins (FSH and LH) [8]. The clinic where the patient underwent IVF was also a significant factor.

The top 20 attributes were analyzed additionally using the SHAP method. As shown on Fig. 4, the chances of a successful outcome of IVF, as predicted by the model, grow along with the values of such attributes as the number of fertilized oocytes, date of birth of the patient, the level of AMH, use of progesterone in the luteal phase of the cycle.

We have built models predicting the outcome of IVF for individual infertility diagnoses. The resulting ROC AUC values did not exceed the value of the metric for the entire sample, which allows concluding that using models for certain types of infertility is impractical (Table).

Women with unsuccessful IVF in the past have a lower probability of a successful IVF than women joining the program for the first time or whose previous attempts were successful (OR = 0.7675; $p < 0.0001$). Therefore, it is natural that the variable reflecting the number of past attempts is one of the significant attributes selected via the random forest classifier, which performed best in the cross validation trial. Nevertheless, we consider the model described by us to be more relevant for the Russian population than the foreign models described in the literature.

DISCUSSION

Our data indicate that prognostic quality of the current random forest model (ROC AUC = 0.69) is comparable to that of the

similar models described in foreign studies. For example, a recent report presented a model with the best ROC AUC value of 0.68 [14].

Despite the said comparability of ROC AUC of our model and foreign models, in most cases, they are based on different criteria of selection of pairs, even with similar target variable. Some models described in the foreign literature disregard data on the past IVF attempts and consider the outcomes of the first program a woman participates in [14]. Our IVF model relies on the results of previous cycles: 40.9% of the women whose histories comprised the training dataset had unsuccessful IVF attempts previously. Thus, our model allows predicting IVF outcomes for a single cycle, which is an advantage, since some models by foreign researchers prognosticate cumulative success for several IVF cycles [10, 11].

All the above factors make comparison of the models by numerical indicators only partially objective. For example, it can be assumed that our model has a higher ROC AUC than the earlier described model [14], since it factors in data on the previous IVF attempts, which, for the 40.9% of women who enjoyed no success before (and whose data was part of the training dataset), translates into 92.95% chance of failure in the next IVF cycles.

Considering the effectiveness of the developed model from a clinical perspective, we should note the identified most important IVF outcome predictors peculiar to Russian infertile couples. The list of such attributes includes both those traditionally accounted for (woman's age, number of fertilized

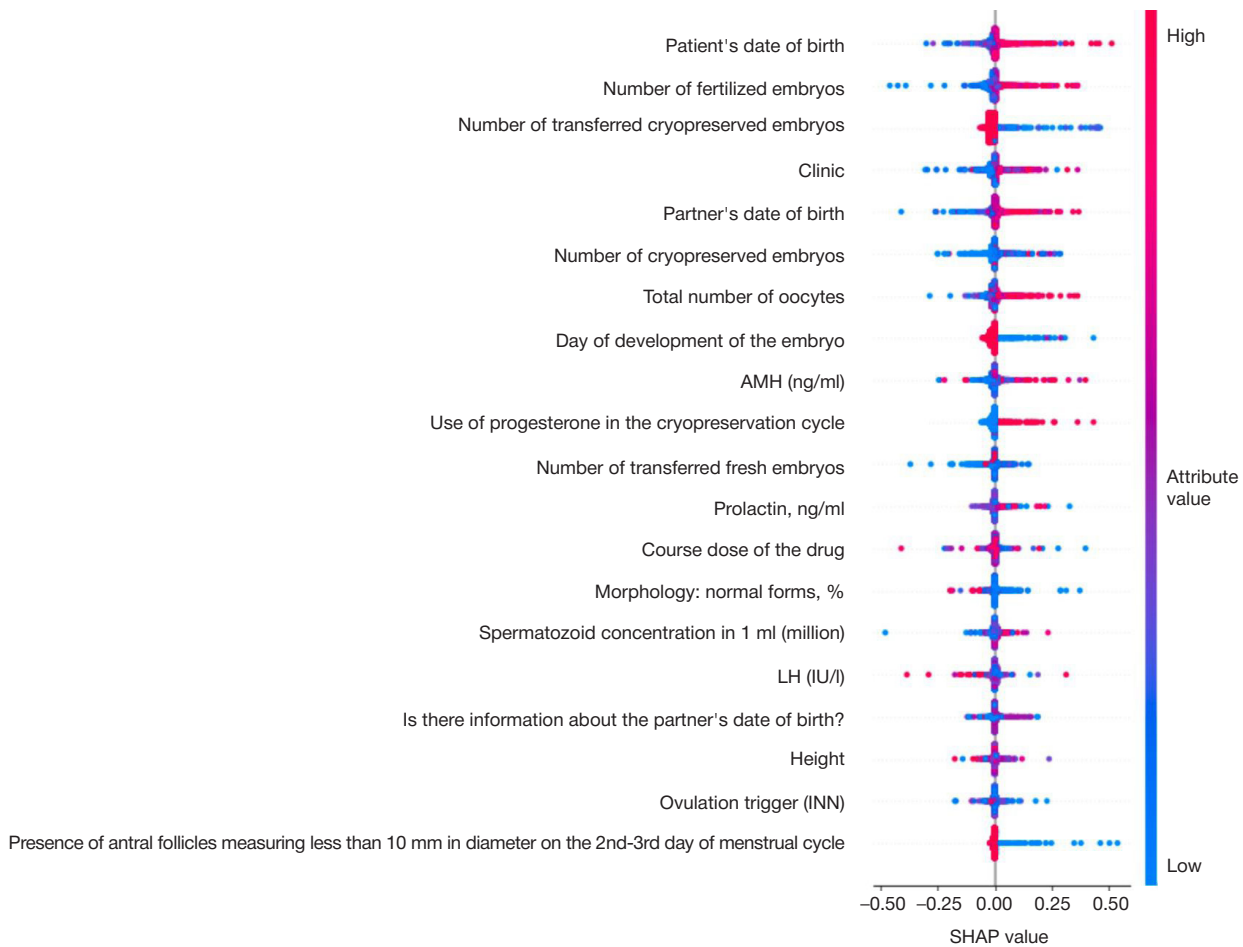


Fig. 4. Diagram of SHAP values for the 20 most significant attributes. A positive class means successful IVF, negative class — failure thereof

oocytes, total number of oocytes, BMI, AMH level) and the predictors typically unregarded. For example, progesterone drugs during the luteal phase were shown to be associated with successful outcomes. Although prescribing progesterone is a routine clinical tactic, until now there has been no mathematically proven justification for the need to support the luteal phase of the induced cycle. Besides, there is now an objective confirmation of the negative effect previous unsuccessful IVF attempts have on the planned one. This fact, apparently, necessitates a review of the treatment tactics when the patient's history cites several (four, in this study) IVF failures. Despite the fact that today IVF is a routine infertility treatment method, and it would seem that all clinics apply standard protocols and technology, our model revealed establishment-dependent differences based on the data provided by them, which may justify an analysis of their approaches. An interesting fact uncovered in this study is the lack of dependence of IVF outcome on the confirmed infertility diagnosis in situations when all other significant factors are similar. This is contradictory to the results of many studies that

seek a link between success/failure of IVF and infertility as a nosology.

CONCLUSIONS

Over the past decades, a number of IVF prediction models have been developed that aim at assessing the outcomes in individual cases, but, due to the insufficient prognostic capacity and statistical methods used, only a few of them have proven to be clinically significant. Machine learning, which enables interpretation of data and development of predictive models, finds increasingly wider application in clinical practice, especially for complex systems with multiple variables. In this study, we have built a model that predicts the outcome of IVF cycles with satisfactory forecasting efficiency, identified the important factors of IVF effectiveness, and uncovered interactions between them. We will continue to explore practical applications of the model seeking to assess the impact of variables on the efficacy of treatment.

Table. Results of five-fold cross validation of the random forest model, individual infertility diagnoses, in the context of selection of hyperparameters using the GridSearch method

Infertility diagnosis (ICD-10)	Number of patients	ROC-AUC
Female infertility associated with anovulation (N 97.0)	1279	0.69 ± 0.02
Female infertility of tubal origin (N 97.1)	3191	0.66 ± 0.02
Female infertility of uterine origin (N 97.2)	1248	0.66 ± 0.05
Female infertility associated with male factors (N 97.4)	3226	0.68 ± 0.01

References

- Korsak VS, Smirnova AA, Shurygina OV. Registr VRT Obshherossijskoj obshhestvennoj organizacii «Rossijskaja asociacija reprodukcii cheloveka». Otchet za 2020 god. Problemy reprodukcii. 2022; 28 (6): 12–27. DOI: 10.17116/repro20222806112. Russian.
- Hassan MR, Al-Insaf S, Hossain MI, Kamruzzaman J. A machine learning approach for prediction of pregnancy outcome following IVF treatment. *Neural Computing and Applications*. 2018; 32: 2283–97.
- Ratna MB, Bhattacharya S, Abdulrahim B, McLernon DJ. A systematic review of the quality of clinical prediction models in in vitro fertilisation. *Human Reproduction*. 2020; 35: 100–116.
- Lintsen A, Eijkemans M, Hunault C, Bouwmans C, Hakkaart L, Habbema J, et al. Predicting ongoing pregnancy chances after IVF and ICSI: A national prospective study. *Human Reproduction*. 2007; 22: 2455–62.
- van Weert JM, Repping S, van der Steeg JW, Steures P, van der Veen F, Mol BW. A prediction model for ongoing pregnancy after in vitro fertilization in couples with male subfertility. *J Reprod Med*. 2008; 53 (4): 250–6. PMID: 18472647.
- Jones CA, Christensen AL, Salihu H, Carpenter W, Petrozzino J, Abrams E, et al. Prediction of individual probabilities of livebirth and multiple birth events following in vitro fertilization (IVF): A new outcomes counselling tool for IVF providers and patients using HFEA metrics. *Journal of experimental clinical assisted reproduction*. 2011; 8: 3.
- Nelson SM, Lawlor DA. Predicting live birth, preterm delivery, and low birth weight in infants born from in vitro fertilisation: A prospective study of 144,018 treatment cycles. *PLoS Medicine*. 2011; 8: e1000386.
- van Loendersloot LL, van Wely M, Repping S, Bossuyt PMM, van der Veen F. Individualized decision-making in IVF: Calculating the chances of pregnancy. *Human Reproduction*. 2013; 28: 2972–80.
- Dhillon R, McLernon D, Smith P, Fishel S, Dowell K, Deeks J, et al. Predicting the chance of live birth for women undergoing IVF: A novel pretreatment counselling tool. *Human Reproduction*. 2015; 31: 84–92.
- McLernon DJ, Steyerberg EW, te Velde ER, Lee AJ, Bhattacharya S. Predicting the chances of a live birth after one or more complete cycles of in vitro fertilisation: Population based study of linked cycle data from 113 873 women. *BMJ*. 2016; p. i5735.
- McLernon DJ, Raja EA, Toner JP, Baker VL, Doody KJ, Seifer DB. Predicting personalized cumulative live birth following in vitro fertilization. *Fertility and Sterility*. 2022; 117 (2): 326–38.
- Vaegter KK, Lacic TG, Olovsson M, Berglund L, Brodin T, Holte J. Which factors are most predictive for live birth after in vitro fertilization and intracytoplasmic sperm injection (IVF/ICSI) treatments? Analysis of 100 prospectively recorded variables in 8,400 IVF/ICSI single-embryo transfers. *Fertility and Sterility*. 2017; 107 (3): 641–48.
- Ottosen LDM, Kesmodel U, Hindkjaer J, Ingerslev HJ. Pregnancy prediction models and eSET criteria for IVF patients—do we need more information? *Journal of assisted reproduction and genetics*. 2007; 24 (1): 29–36.
- Xu T, d. F. Veiga A, Hammer KC, Paschalidis ICh, Mahalingaiah Sh. Informative predictors of pregnancy after first IVF cycle using eIVF practice highway electronic health records. *Scientific Reports*. 2022; 12: 1–9.
- C N Barreto N, Castro GZ, Pereira RG, Pereira FAN, Reis FM, Junior WM, et al. Predicting in vitro fertilization success in the Brazilian public health system: a machine learning approach. *Med Biol Eng Comput*. 2022; 60 (7): 1851–61. DOI: 10.1007/s11517-022-02569-1. Epub 2022 May 4. PMID: 35508786.
- Barnett-Itzhaki Z, Elbaz M, Butterman R, Amar D, Amitay M, Racowsky C, et al. Machine learning vs. classic statistics for the prediction of IVF outcomes. *Journal of Assisted Reproduction and Genetics*. 2020; 37: 2405–12.
- Lundberg S, Lee S-I. A unified approach to interpreting model predictions. Available from: <https://arxiv.org/abs/1705.07874>, may 22 2017.
- Morris JA, Gardner MJ. Statistics in Medicine: Calculating confidence intervals for relative risks (odds ratios) and standardised ratios and rates. *BMJ*. 1988; 296: 1313–6.
- Sheskin DJ. Handbook of parametric and nonparametric statistical procedures. Chapman and Hall/CRC, 2003.
- Breiman L, Friedman JH, Olshen RA, Stone CJ. Classification and regression trees. Routledge, 2017.
- Cournapeau D, Brucher M, Perrot M, Duchesnay E. Scikit-learn: Machine learning in Python. *Journal of Machine Learning Research*. 2011; 12: 2825–30.
- Prokhorenkova L, Gusev G, Vorobev A, Dorogush AV, Gulina A. Catboost: Unbiased boosting with categorical features. 2017. Available from: <https://arxiv.org/abs/1706.09516>.

Литература

- Корсаков В. С., Смирнова А. А., Шурыгина О. В. Регистр ВРТ Общероссийской общественной организации «Российская ассоциация репродукции человека». Отчет за 2020 год. Проблемы репродукции. 2022; 28 (6): 12–27. DOI: 10.17116/repro20222806112.
- Hassan MR, Al-Insaf S, Hossain MI, Kamruzzaman J. A machine learning approach for prediction of pregnancy outcome following IVF treatment. *Neural Computing and Applications*. 2018; 32: 2283–97.
- Ratna MB, Bhattacharya S, Abdulrahim B, McLernon DJ. A systematic review of the quality of clinical prediction models in in vitro fertilisation. *Human Reproduction*. 2020; 35: 100–116.
- Lintsen A, Eijkemans M, Hunault C, Bouwmans C, Hakkaart L, Habbema J, et al. Predicting ongoing pregnancy chances after IVF and ICSI: A national prospective study. *Human Reproduction*. 2007; 22: 2455–62.
- van Weert JM, Repping S, van der Steeg JW, Steures P, van der Veen F, Mol BW. A prediction model for ongoing pregnancy after in vitro fertilization in couples with male subfertility. *J Reprod Med*. 2008; 53 (4): 250–6. PMID: 18472647.
- Jones CA, Christensen AL, Salihu H, Carpenter W, Petrozzino J, Abrams E, et al. Prediction of individual probabilities of livebirth and multiple birth events following in vitro fertilization (IVF): A new outcomes counselling tool for IVF providers and patients using HFEA metrics. *Journal of experimental clinical assisted reproduction*. 2011; 8: 3.
- Nelson SM, Lawlor DA. Predicting live birth, preterm delivery, and low birth weight in infants born from in vitro fertilisation: A prospective study of 144,018 treatment cycles. *PLoS Medicine*. 2011; 8: e1000386.
- van Loendersloot LL, van Wely M, Repping S, Bossuyt PMM, van der Veen F. Individualized decision-making in IVF: Calculating the chances of pregnancy. *Human Reproduction*. 2013; 28: 2972–80.
- Dhillon R, McLernon D, Smith P, Fishel S, Dowell K, Deeks J, et al. Predicting the chance of live birth for women undergoing IVF: A novel pretreatment counselling tool. *Human Reproduction*. 2015; 31: 84–92.
- McLernon DJ, Steyerberg EW, te Velde ER, Lee AJ, Bhattacharya S. Predicting the chances of a live birth after one or more complete cycles of in vitro fertilisation: Population based study of linked cycle data from 113 873 women. *BMJ*. 2016; p. i5735.
- McLernon DJ, Raja EA, Toner JP, Baker VL, Doody KJ, Seifer DB. Predicting personalized cumulative live birth following in vitro fertilization. *Fertility and Sterility*. 2022; 117 (2): 326–38.
- Vaegter KK, Lacic TG, Olovsson M, Berglund L, Brodin T, Holte J. Which factors are most predictive for live birth after in vitro fertilization and intracytoplasmic sperm injection (IVF/ICSI) treatments? Analysis of 100 prospectively recorded variables in 8,400 IVF/ICSI single-embryo transfers. *Fertility and Sterility*. 2017; 107 (3): 641–48.
- Ottosen LDM, Kesmodel U, Hindkjaer J, Ingerslev HJ. Pregnancy prediction models and eSET criteria for IVF patients—do we need more information? *Journal of assisted reproduction and genetics*.

- 2007; 24 (1): 29–36.
14. Xu T, d. F. Veiga A, Hammer KC, Paschalidis ICh, Mahalingaiah Sh. Informative predictors of pregnancy after first IVF cycle using eIVF practice highway electronic health records. *Scientific Reports*. 2022; 12: 1–9.
 15. C N Barreto N, Castro GZ, Pereira RG, Pereira FAN, Reis FM, Junior WM, et al. Predicting in vitro fertilization success in the Brazilian public health system: a machine learning approach. *Med Biol Eng Comput*. 2022; 60 (7): 1851–61. DOI: 10.1007/s11517-022-02569-1. Epub 2022 May 4. PMID: 35508786.
 16. Barnett-Itzhaki Z, Elbaz M, Buttermann R, Amar D, Amitay M, Racowsky C, et al. Machine learning vs. classic statistics for the prediction of IVF outcomes. *Journal of Assisted Reproduction and Genetics*. 2020; 37: 2405–12.
 17. Lundberg S, Lee S-I. A unified approach to interpreting model predictions. Available from: <https://arxiv.org/abs/1705.07874>, may 22 2017.
 18. Morris JA, Gardner MJ. *Statistics in Medicine: Calculating confidence intervals for relative risks (odds ratios) and standardised ratios and rates*. BMJ. 1988; 296: 1313–6.
 19. Sheskin DJ. *Handbook of parametric and nonparametric statistical procedures*. Chapman and Hall/CRC, 2003.
 20. Breiman L, Friedman JH, Olshen RA, Stone CJ. *Classification and regression trees*. Routledge, 2017.
 21. Cournapeau D, Brucher M, Perrot M, Duchesnay E. Scikit-learn: Machine learning in Python. *Journal of Machine Learning Research*. 2011; 12: 2825–30.
 22. Prokhorenkova L, Gusev G, Vorobev A, Dorogush AV, Gulin A. Catboost: Unbiased boosting with categorical features. 2017. Available from: <https://arxiv.org/abs/1706.09516>.

EXPLORATION OF THE FEMTOSECOND LASER PULSE THERMAL EFFECTS ON THE MOUSE EMBRYOS DURING THE ASSISTED HATCHING PROCEDURE

Kubekina MV^{1,2} ✉, Filatov MA^{1,2}, Silaeva YuYu^{1,2}, Sitnikov DS²

¹ Institute of Gene Biology of the Russian Academy of Sciences, Moscow, Russia

² Joint Institute for High Temperatures of the Russian Academy of Sciences, Moscow, Russia

Impaired hatching of the embryo from the *zona pellucida* (ZP), the specialized protective shell, immediately before implantation is one of the factors of infertility. Hatching impairment is often due to the ZP hardening or thickening. In such cases, the laser assisted hatching procedure is used to overcome infertility. During this procedure a hole is drilled in the ZP facilitating the embryo release. The question of the safe use of laser for assisted hatching remains open, since laser beam can heat the environment and cause thermal shock in embryos. The study was aimed to assess safety of the mouse embryo femtosecond laser exposure during the assisted hatching procedure using the embryo viability and HSP gene expression assessment methods. A new type of pulsed laser was used in the study for the ZP dissection — the femtosecond laser. The energy of such pulses was two orders of magnitude lower than the energy of laser dissectors currently used in the clinics. To assess the femtosecond laser exposure to the embryo, the house mouse (*Mus musculus*) embryos were stained with fluorescence dyes, and expression of the genes encoding heat shock proteins (*Hsp90aa1* and *Hspa5*) was assessed. The embryonic cells remained viable after the laser assisted hatching procedure involving the use of a femtosecond laser, while expression levels of the genes encoding heat shock proteins were slightly increased compared to the negative control group ($p = 0.408$).

Keywords: embryo, mouse, blastocyst, *zona pellucida*, laser assisted hatching, femtosecond laser pulses, heat shock proteins

Funding: the procedures involving manipulating embryos using a laser and assessment of expression of the genes responsible for synthesis of heat shock proteins were supported by RSF (project 23-19-00424) and conducted using the equipment of the UNU "Laser Terawatt Femtosecond Complex", which was a part of the Center for Collective Usage "Laser Femtosecond Complex" of the Joint Institute for High Temperatures RAS. The procedures to acquire embryos were supported by the UNU "Transgenbank" grant (№ 075-15-2021-668 of July 29, 2021).

Author contribution: Kubekina MV — immunofluorescence staining and assessment of the heat shock protein expression levels, manuscript writing; Filatov MA — handling embryos, statistical processing, manuscript writing; Silaeva YuYu — general management of the experiment; Sitnikov DS — laser microsurgery, data processing, manuscript writing; all authors — discussion and manuscript editing.

Compliance with ethical standards: the study was approved by the Ethics Committee of the Institute of Gene Biology RAS (protocol № 1 dated 25 September 2023) and conducted in strict compliance with the provisions of the Directive 2010/63/EU of the European Parliament and of the Council of 22 September 2010 on the protection of animals used for scientific purposes.

✉ **Correspondence should be addressed:** Marina V. Kubekina
Vavilova, 34/5, 119334, Moscow, Russia; marykumy@gmail.com

Received: 07.11.2023 **Accepted:** 07.12.2023 **Published online:** 26.12.2023

DOI: 10.24075/brsmu.2023.046

ИССЛЕДОВАНИЕ ТЕПЛООВОГО ВОЗДЕЙСТВИЯ ФЕМТОСЕКУНДНЫХ ЛАЗЕРНЫХ ИМПУЛЬСОВ НА ЭМБРИОНЫ МЫШИ В РАМКАХ ПРОЦЕДУРЫ ВСПОМОГАТЕЛЬНОГО ХЕТЧИНГА

М. В. Кубекина^{1,2} ✉, М. А. Филатов^{1,2}, Ю. Ю. Силаева^{1,2}, Д. С. Ситников²

¹ Институт биологии гена Российской академии наук, Москва, Россия

² Объединенный институт высоких температур Российской академии наук, Москва, Россия

Одной из причин бесплодия является нарушение хетчинга — процесса вылулления эмбриона из специальной защитной оболочки (ZP, *zona pellucida*), непосредственно перед имплантацией. Часто нарушение хетчинга обусловлено уплотнением или утолщением ZP. Для преодоления бесплодия в таких случаях прибегают к процедуре вспомогательного лазерного хетчинга, когда с помощью лазера в ZP делают отверстие, облегчая выход эмбриона из нее. Вопрос безопасности применения лазера для проведения процедуры вспомогательного хетчинга остается открытым, поскольку лазерное излучение способно нагревать окружающую среду и потенциально вызывать у эмбрионов термический шок. Целью настоящей работы было оценить безопасность фемтосекундного лазерного воздействия на эмбрионы мыши в рамках процедуры вспомогательного хетчинга, используя методы исследования жизнеспособности эмбрионов и уровней экспрессии генов HSP. Для диссекции ZP в работе использовали новый тип источника лазерных импульсов фемтосекундной длительности. Энергия указанных импульсов на два порядка ниже энергии миллисекундных лазерных диссекторов, применяемых в клиниках в настоящий момент. Для оценки фемтосекундного лазерного воздействия на эмбрион производили окрашивание эмбрионов доменной мыши (*Mus musculus*) флуоресцентными красителями, а также оценивали уровни экспрессии генов, кодирующих белки теплового шока: *Hsp90aa1* и *Hspa5*. После выполнения процедуры вспомогательного лазерного хетчинга с использованием фемтосекундного лазера клетки эмбрионов сохраняли жизнеспособность, а уровни экспрессии генов, кодирующих белки теплового шока, повышались незначительно по сравнению с группой отрицательного контроля ($p = 0,408$).

Ключевые слова: эмбрион, мышь, бластоциста, блестящая оболочка, *zona pellucida*, вспомогательный лазерный хетчинг, фемтосекундные лазерные импульсы, белки теплового шока

Финансирование: работы по проведению манипуляций с эмбрионами при помощи лазера и оценка уровней экспрессии генов, ответственных за синтез белков теплового шока, выполнены при финансовой поддержке РФФИ в рамках научного проекта 23-19-00424 на оборудовании УНУ «Лазерный тераваттный фемтосекундный комплекс», входящей в состав ЦКП «Лазерный фемтосекундный комплекс» ОИВТ РАН. Работы по получению эмбрионов были выполнены при финансовой поддержке гранта номер 075-15-2021-668 (от 29.07.2021) УНУ Трансгенбанк.

Вклад авторов: М. В. Кубекина — проведение иммунофлуоресцентного окрашивания и определение уровня экспрессии белков теплового шока, написание статьи; М. А. Филатов — работа с эмбрионами, статистические методы обработки, написание статьи; Ю. Ю. Силаева — общее руководство экспериментом; Д. С. Ситников — проведение лазерной микрохирургии, обработка результатов, написание статьи; все авторы — обсуждение и редактирование статьи.

Соблюдение этических стандартов: исследование одобрено этическим комитетом ИБГ РАН (протокол № 1 от 25 сентября 2023 г.) и проведено в строгом соответствии с положениями Директивы 2010/63/EU Европейского Парламента и Совета Европейского союза от 22 сентября 2010 г. по охране животных, используемых в научных целях.

✉ **Для корреспонденции:** Марина Владиславовна Кубекина
ул. Вавилова, д. 34/5, 119334, г. Москва, Россия; marykumy@gmail.com

Статья получена: 07.11.2023 **Статья принята к печати:** 07.12.2023 **Опубликована онлайн:** 26.12.2023

DOI: 10.24075/vrgmu.2023.046

The problem of infertility affects millions of people [1]. Its causes are extremely diverse; assisted reproductive technologies, such as *in vitro* fertilization (IVF) and *in vitro* (extracorporeal) embryonic culture are used for treatment. Mammalian preimplantation embryos (including human) are surrounded by the specialized protective shell: *zona pellucida* (ZP). It is composed of glycoproteins forming a porous structure [2, 3]. Due to the presence of very small pores (several dozen nanometers in diameter only), ZP provides access to the embryo for nutrients from the environment, but prevents the entry of viruses and bacteria, i.e. has a protective function. The embryo goes through several stages in its development: cleavage, formation of morula and blastocyst. When the blastocyst stage is reached, the embryo has to get off the ZP. The process of the embryo release from the ZP is called hatching. Hatching is normally followed by implantation, i.e. by the embryo attachment to the uterine wall. When hatching is impaired, the embryo cannot get off from the ZP and get implanted. Infertility due to impaired implantation is a very common phenomenon. The causes of hatching impairment are diverse: too thick or too hard ZP, insufficient levels of enzymes needed for local ZP breaching. In such cases the laser assisted hatching procedure, during which a hole is drilled in the ZP facilitating the embryo release, is used.

There are various assisted hatching methods: chemical, mechanical and laser. When using a chemical method, the ZP is treated with specific chemicals causing the ZP disruption, such as acidic Tyrode's solution [4], or enzymes, such as pronase [5]. However, such treatment can have a direct effect on the embryonic cells, which can result in the decrease of its capacity of further normal development. When using mechanical hatching, the hole in the ZP is made with a specialized microneedle [6, 7], however, embryonic cells are likely to be damaged during this procedure, which adversely affects embryogenesis. Laser assisted hatching (LAH) is most popular in many IVF clinics [8, 9]. During LAH, a cut-out in the ZP is made with millisecond laser dissectors. These allow one to make a 5–10 μm hole in the ZP, which is enough for both zona thinning and dissection to the full depth. The ZP disruption is due to heating the medium to a temperature of several hundred degrees [10]. The adverse effects of using millisecond (ms) dissectors include heating the environment surrounding the exposed area, which can result in embryonic cell damage. Thus, when using the Zylotk dissector (Hamilton Thorne; USA) with the pulse duration of 0.5 ms and power of 300 mW, heat spreads to the distance of about 16 μm from the laser beam center and leads to the temperature increase to 60 °C within the pulse duration [11]. That is why it is recommended to perform dissection of the embryo's ZP during the early stage of development, when the perivitelline space is large enough (more than 15 μm).

The use of femtosecond (fs) lasers allowing one to achieve high beam intensity with low laser pulse energy is considered to be promising. Femtosecond laser exposure results in medium heating of the area of beam focus, however, heat does not have time to spread sideways due to short pulse duration. Theoretical estimations have shown that the size of the heated area is comparable with the spot size of a focused laser beam [12], while maximum heating of aqueous medium with the laser pulse intensity of 1.8–5 TW/cm² at a wavelength of 514 nm matches the range of 5–30 °C [13]. In the earlier studies, irradiation at a specified wavelength with the intensity of ~2.5 TW/cm² was used for embryo microsurgery [14]. In this study, the intensity in laser beam focus was 3 TW/cm². To assess safety of using a femtosecond laser beam for assisted hatching of mouse

embryos, we conducted experiments focused on exploring embryo viability after the ZP laser microsurgery. Furthermore, the experiments focused on assessing the expression of genes encoding heat shock proteins (HSPs), the synthesis of which in the cells starts when the temperature increases, were conducted. HSPs are essential to maintain native spatial protein structure, which becomes especially important under heat stress. In eukaryotes, heat shock proteins of the families Hsp70 and Hsp90 are most strongly activated by heat stress; that is why members of these families were selected for the study [15].

Thus, the study was aimed to assess safety of the mouse embryo femtosecond laser exposure during the laser assisted hatching procedure. For this embryo viability and HSP gene expression in embryos were investigated.

METHODS

Experimental apparatus

Microsurgical manipulations on embryos were performed using the “Femtosecond Laser Scalpel” system (Joint Institute for High Temperatures RAS; Russia) [16]. The beam generated by the TETA femtosecond laser (Avesta; Troitsk, Russia) was used to produce a laser scalpel. Laser pulses emitted by the source had the following parameters: pulse duration τ — 280 fs, energy — 330 μJ , wavelength λ — 1028 nm, pulse repetition rate — 2.5 kHz. There was a KDP (potassium dihydrogen phosphate, KH_2PO_4) crystal installed on the beam path to convert infrared radiation into visible light; radiation leaving the crystal had a wavelength (λ) of 514 nm. Then it was fed through the right side port of the Olympus IX-71 inverted microscope and focused into a spot with a radius $r = 1.4 \mu\text{m}$ at the 1/e level with the 20xUPlanFL microlens (Olympus; Japan) having a 0.5 numerical aperture (NA). Attenuator installed next to the laser source (Fig. 1) was used to adjust pulse energy. A telescope was used to align the laser beam diameter with the objective lens aperture, as well as to avoid energy loss associated with

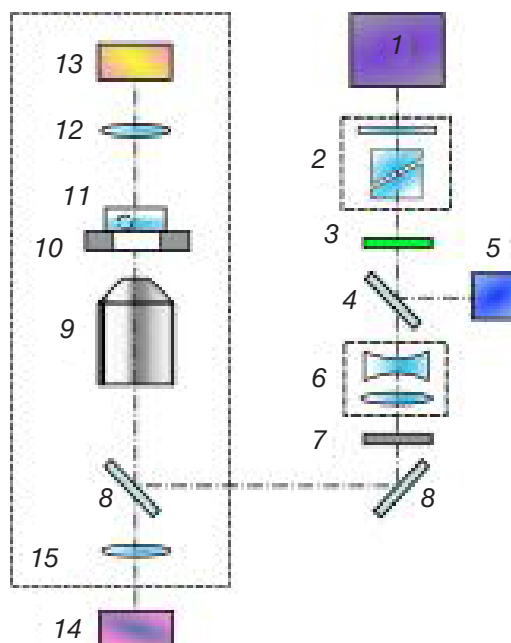


Fig. 1. Femtosecond laser scalpel scheme. 1 — fs laser, 2 — attenuator, 3 — KDP crystal, 4 — glass plate, 5 — photodiode, 6 — telescope, 7 — laser beam shutter, 8 — mirrors for the laser beam wavelength, 9 — microlens, 10 — motorized microscope stage, 11 — Petri dish with embryos, 12 — substage condenser, 13 — substage lamp, 14 — video camera, 15 — inverted microscope

the microlens frame beam limiting. The DET36A2 photodiode (Thorlabs Inc.; USA), to which part of the laser beam was branched using a thin glass plate (Fresnel reflection) was used to control the laser pulse energy. Photodiode output signal was digitized with the Tektronix TDS 5054 oscilloscope. The photodiode signal amplitude was calibrated using a power meter consisting of the S120VC photodiode detector and the PM100D console (Thorlabs Inc.; USA). The detector was temporarily installed on the SCAN IM 120×80 microscope stage (Märzhäuser Wetzlar; Germany) to record the power of laser beam leaving the microlens.

To perform microsurgery, embryos were placed in Petri dishes with the glass bottom. The thickness of the glass bottom was 170 µm (beam was focused through the dish bottom). The Petri dish was placed on the motorized microscope stage (Märzhäuser Wetzlar; Germany) to move the embryo relative to the stationary laser beam. Embryo imaging was performed with the DFK 72AUC02 camera (The Imaging Source; Germany), and the image was displayed on the personal computer screen. Software written in LabView (National Instruments, USA) was used for automatization of microsurgical procedure, which allowed the operator to control such parameters, as energy, pulse repetition rate and laser beam divergence, and set the laser beam trajectory drawing it directly on the image of the embryo. The ZP dissection was performed using a sequence of laser pulses with the speed of embryo movement relative to the beam of 0.01 mm/s.

Animal handling

The study involved CBA x C57Bl/6J F1 hybrid mice. Animals were kept at the 14 : 10 h light/dark cycle at a temperature within the range of 22–24 °C. They had *ad libitum* access to water and food (special extruded feed for mouse breeding). All the procedures involving animals were conducted in accordance with the guidelines of the Bioethics Commission, Institute of Gene Biology RAS.

Early embryo manipulation

A large number of zygotes were obtained using a widely used protocol for ovulation induction involving the use of the follicle-stimulating hormone and chorionic gonadotropin [17]. Hormonal ovulation induction was performed in accordance to the two-step protocol: PMSG was administered intraperitoneally at 13:00 of day 1 (Follimag; Mosagrogen, Russia), 5 IU per animal; hCG was administered intraperitoneally 48 h later (Chorulon, Merck Animal Health; USA), 10 IU per animal. After that these females were housed with males for mating. The fact of copulation was determined next morning based on the presence of the copulatory plug.

Obtaining embryos

The zygote stage embryos were collected (0.5 days of embryogenesis, E0.5) and cultured *in vitro*. Female mice were euthanized by cervical dislocation to obtain embryos. Collected oviducts were placed in the Ooclean medium (PanEco; Russia), where the adipose tissue was separated by the syringe needles and tweezers. Then oviducts were transferred to the 100 µL pure drop of the Ooclean medium, where the oviduct ampullae were dissected to obtain zygotes surrounded by the cumulus cells. Then about 0.03 g of hyaluronidase (Lydase; Microgen, Russia) were added to this drop to separate zygotes from the cumulus cells. The resulting zygotes were serially washed in

four droplets of Ooclean medium and transferred to the culture medium.

Embryo culture

The embryos were cultured to the morula stage (E2.5) in the four-well plates (Termo Scientific Nunc, USA) using the culture medium for gametes and embryos (Fujifilm Irvine Scientific; USA). During the morula and blastocyst stages (E3.5) the embryos were cultured in the 20 µL medium drops covered with mineral oil (Origio; Denmark), 2–3 embryos per drop.

Transportation of embryos

The embryos were obtained and cultured to the morula stage in the Institute of Gene Biology RAS, while embryo culture to the blastocyst stage and LAH were performed in the Joint Institute for High Temperatures RAS. The embryos were placed in the 0.5 mL eppendorf tube filled with the HEPES-containing medium (Ooclean; PanEco, Russia) for transportation. The eppendorf tube with embryos was placed in a thermos flask with water heated to 37 °C in order to ensure constant temperature during the embryo transportation. Embryos were transported within 90 min.

Groups of embryos

The embryos used in the study were divided into four groups: negative (1) and positive (2) controls, non-viable embryos (3), experimental group (4). There were four embryos in the group of non-viable embryos and 30 embryos per group in other groups.

1. The embryos cultured under standard conditions (5% CO₂/air 37 °C) in an incubator (Binder; Germany) were used as negative controls.

2. Blastocysts exposed to the temperature of 42 °C for 30 min were used as positive controls. Thermal exposure was also provided in a CO₂ incubator (5% CO₂/air 42 °C). During exposure, the embryos were in the same culture medium and in the same culture dishes (four-well plates) as intact embryos. Then blastocysts of this group were cultured under standard conditions for 2 h to produce response to thermal exposure.

3. To obtain non-viable embryos, the embryos were treated with a fixative solution (4% paraformaldehyde in phosphate buffered saline (PBS)) and permeabilized in the 0.003% PBS-Triton solution.

4. The experimental group included embryos exposed to laser beam during the LAH procedure. Microsurgery of the embryo's ZP was performed at the blastocyst stage (~E3.5). A day before the experiment, the morula stage embryos were distributed across well-prepared glass bottom Petri dishes (catalogue number 200350, SPL Lifesciences; Korea) (three embryos per droplet) and transferred to the incubator. Three ~20 µL droplets of culture medium were previously formed in each Petri dish and then covered with liquid paraffin oil for IVF 1 media (catalogue number E0350-160; PanEco, Russia). On the day of experiment, the Petri dish was taken out of the incubator and placed on the microscope stage. The embryos' total time out of the incubator did not exceed 10 min.

Experiment

To perform LAH, the operator applied the laser beam trajectory over the embryo image, thereby shaping the embryo's ZP incision (Fig. 2A, green polyline). The incision was U-shaped, as

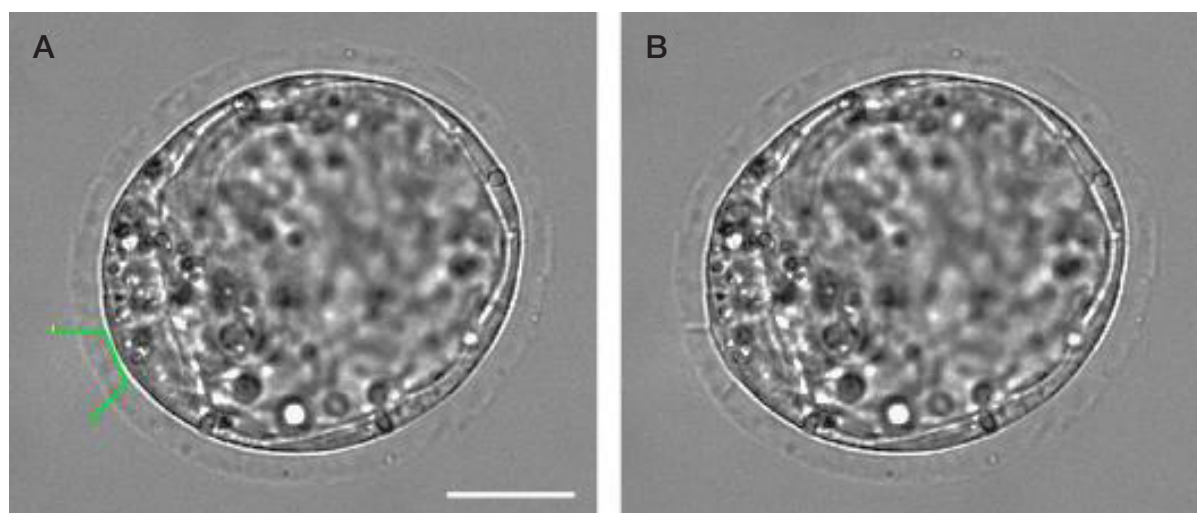


Fig. 2. Images of the embryos obtained before (A) and after (B) the zona pellucida microsurgery. The scale bar is 20 μm

in the earlier study [16]: laser beam cut the ZP to 80–90% of its thickness. The software performed microsurgery automatically, moving the embryo along the specified trajectory relative to the stationary beam and controlling the moment of the laser emission switch on/off. The laser pulse energy used in the experiment was 30 nJ. Microsurgery outcome is provided in Fig. 2B.

Fluorescence staining

The groups of embryos were stained simultaneously with three dyes:

- 1) Hoechst 33342 (Thermo Scientific; USA) — control stain, excitation/emission 350/461, working concentration 1 $\mu\text{g}/\text{mL}$;
- 2) Propidium Iodide (Thermo Scientific; USA) — non-viable cell stain, excitation/emission 493/636, working concentration 500 nmol;
- 3) Calcein-AM (Sigma Aldrich; USA) — living cell stain, excitation/emission 494/517, working concentration 1 μmol .

Fluorescent dyes were brought to the working concentration in the culture medium for gametes and embryos. This medium was used to culture the embryos for 30 min at 37 $^{\circ}\text{C}$ in the incubator. Then the embryos were washed in three droplets of fresh Ooclean medium (PanEco; Russia) to remove the dyes, and their viability was assessed using the Eclipse Ti-E fluorescence inverted microscope (Nikon; Japan).

Determining gene expression

RNA was extracted using the TRIzol reagent (Thermo Scientific; USA) in accordance with the manufacturer's protocol. To obtain complementary DNA (cDNA), reverse transcription was performed using the MMLV RT kit (Evrogen; Russia) according to the manufacturer's protocol. Gene expression was determined by real-time PCR in the CFX96 amplifier (Bio-Rad; USA) using the qPCRmix-HS SYBR ready-made mixture (Evrogen; Russia). The cDNA samples from blastocysts were amplified in three iterations using primers for the reference

Table. Primers used in the study (sequences are shown in the 5' to 3' direction)

Gene	Genbank No	Forward primer (5' \rightarrow 3')	Reverse primer (5' \rightarrow 3')	Product size
Hprt	NM_013556.2	CAGCGTCGTGATTAGCGATGA	GCCACAATGTGATGGCCTCC	174
Hsp90aa1	NM_010480.5	TGAGCAGTATGCCTGGGAGT	CGACCCATTGGTTCACCTGT	75
Hspa5	NM_001163434.1	GGAATGACCCTTCGGTGACG	GTCTTGGTTTGCCACCTCC	109

Hprt and *Hsp90aa1* and *Hspa5* heat shock protein genes. The nucleotide sequences of primers used in the study are provided in Table 1. The *Hsp90aa1* and *Hspa5* expression was calculated using the well-known ΔCt method [18].

RESULTS

Determining embryo viability by fluorescence staining

To determine the effects of laser microsurgery on the mouse embryo viability, all groups of embryos were subjected to fluorescence staining (Fig. 3).

After laser microsurgery the embryos were stained with the Calcein-AM dye, the same as positive and negative control groups; the Propidium Iodide dye was detected in embryos of non-viable group only. Such results make it possible to draw a conclusion that the experimental group embryos remain viable after laser microsurgery. Minor differences in the Calcein-AM and Hoechst 33342 staining intensity can be explained by bias in the settings of the microscope camera, which should be manually adjusted when assessing each group of embryos.

Determining expression of the *Hsp90aa1* and *Hspa5* heat shock genes

It is well-known that exposure of biological object to laser pulse is associated with local heating [19, 20]. The embryo culture at unphysiologically high temperatures (≥ 39 $^{\circ}\text{C}$) promotes the increase in the expression of genes encoding heat shock proteins [21]. Upregulation of these genes is part of the cellular response to thermal shock. To determine the laser microsurgery effects on the expression of genes *Hsp90aa1* (*Hsp90* family) and *Hspa5* (*Hsp70* family) encoding heat shock proteins in embryos, expression of these genes was assessed in the negative and positive control groups, as well as in the experimental group of embryos exposed to laser beam (Fig. 4).

Distribution of the data obtained was non-normal, therefore, a nonparametric test was used for analysis. The data were

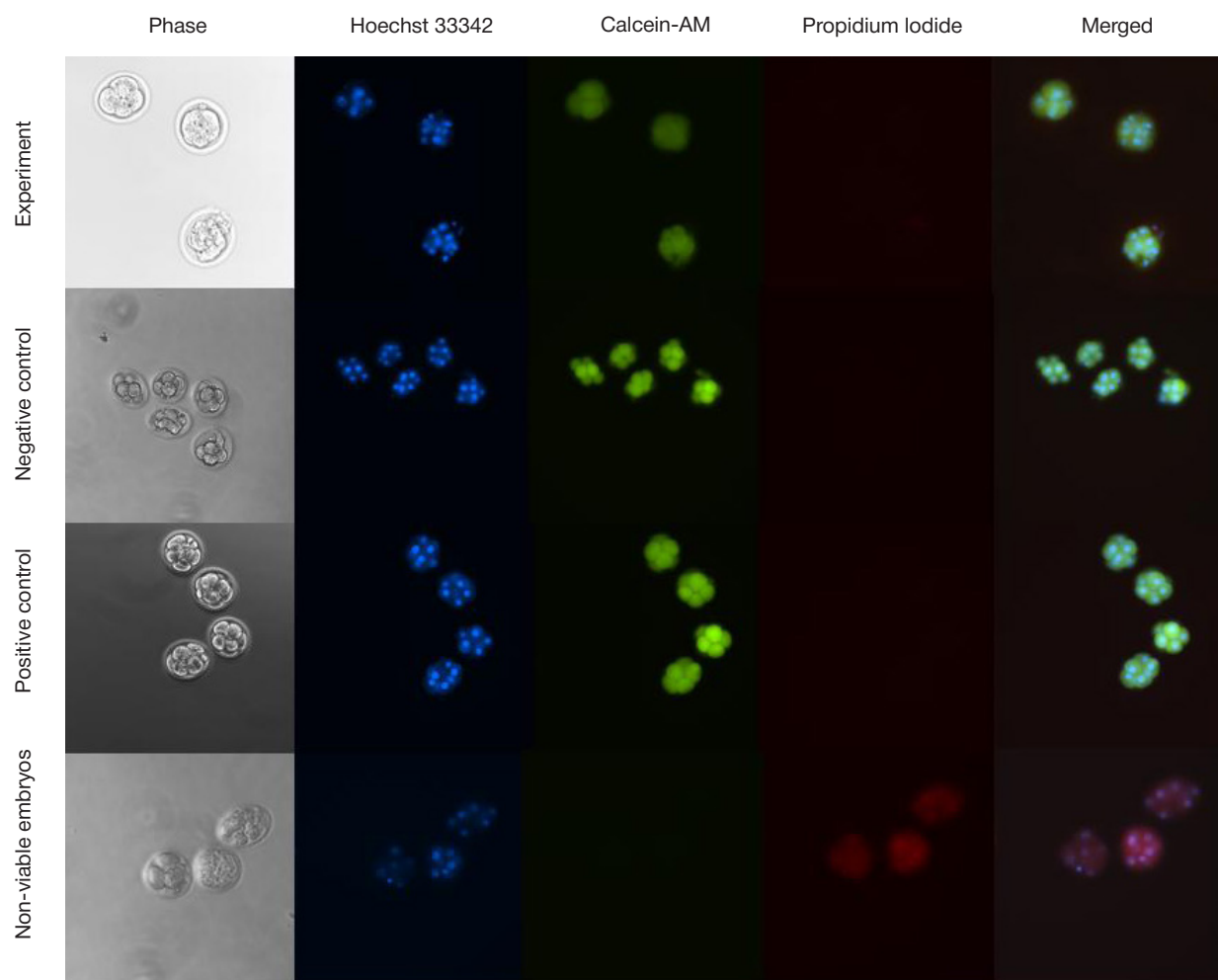


Fig. 3. Fluorescence staining of different groups of embryos. Viable embryos were stained with Calcein-AM, non-viable embryos with Propidium Iodide, nuclei of viable and non-viable embryos with Hoechst 33342

compared using the nonparametric Kruskal-Wallis test. The differences were considered significant at $p < 0.05$. Significant differences between the negative and positive control groups ($p = 0.033$) were reported for both studied genes. The differences between other groups were non-significant: $p = 0.408$ when comparing the experimental group with the positive control group, $p = 0.890$ when comparing the experimental group with the negative control group during assessment of the expression of both genes, *Hsp90aa1* and *Hspa5*.

Expression of genes *Hsp90aa1* and *Hspa5* in the negative and positive control groups shows significant differences, however, the differences in expression of both genes between the experimental and negative control group, as well as between the experimental and positive control group are non-significant. Consequently, it can be assumed that laser microsurgery can cause a slight increase in the HSP gene expression in mouse blastocysts.

DISCUSSION

Temperature is a key factor of embryogenesis, and its effects in the context of simulating physiological and biochemical environment of the genital tract have been assessed in a number of studies [22–24]. The earlier research confirms the impact of thermal stress on reproductive efficiency of both domestic animals and humans. The temperature increase affects oocyte maturation and embryogenesis, especially at early stages of

development, before the zygotic genome activation. This makes oocytes and embryos sensitive to thermal stress, which can disturb their development. Similar effects were reported as early as several decades ago [22–24].

There are data indicating that laser irradiation can exert adverse effects on the living objects, for example, effects related to thermal exposure [25, 26]. To date, the question of the embryos' millisecond laser exposure safety remains open. The research results show that this procedure has some risks and adverse effects [27]. In particular, the use of laser exposure for assisted hatching at the 6–8 cell stage resulted in significant reduction of the number of cells in the embryos. Similarly, at the two cell stage, elevation of DNA fragmentation at the blastocyst stage was detected. The authors expressed concern toward the fact that, despite the increased hatching rate, DNA damage could affect the implantation potential and further embryogenesis. Similar conclusions about the adverse effects of breaching the ZP integrity at the early stages of pre-implantation development were reported [28].

The study conducted as early as in 1999 showed that blastocyst usually responds to the millisecond laser pulses, which results in the blastocyst collapse [29]. Blastocyst recovery takes time, which makes it difficult to predict the terms of hatching and hampers trophoctoderm biopsy. In this regard, the use of femtosecond laser pulses can be more effective, since the ZP microsurgery, even that performed during late embryogenesis, does not result in the blastocyst collapse and delayed hatching. However, available data show that the use

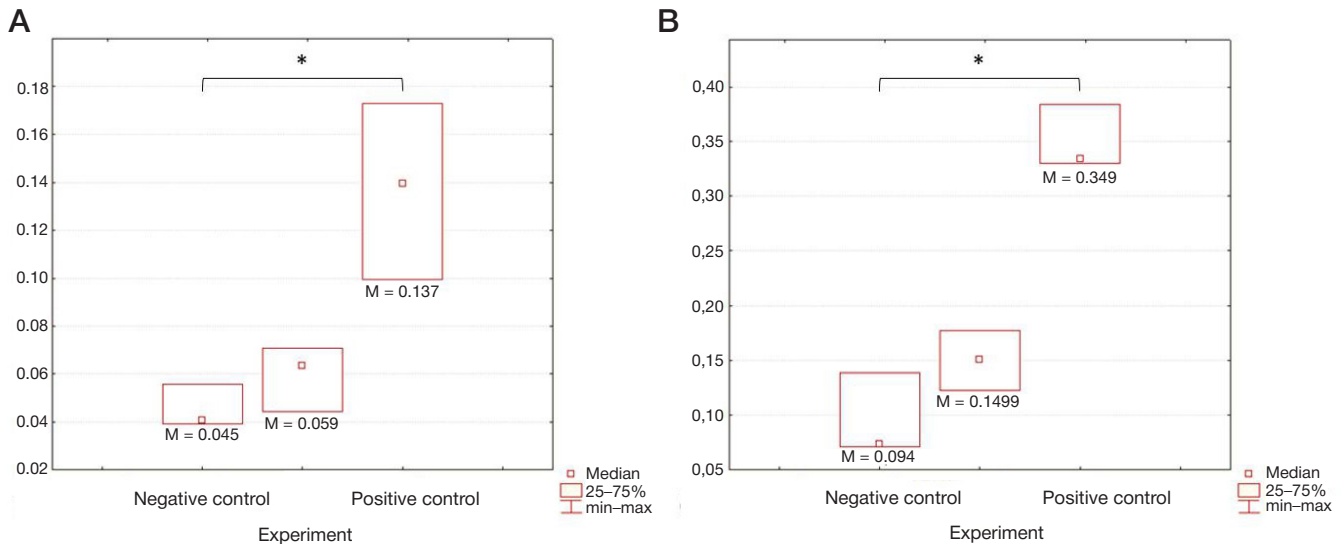


Fig. 4. Graphic representation of heat shock protein gene expression in the negative and positive control groups, as well as in the experimental group of embryos. Expression of genes *Hsp90aa1* (A) and *Hspa5* (B) encoding heat shock proteins

of femtosecond lasers can be also dangerous for biological objects. Their effects were shown to lead to the rabbit corneal stromal cells' death [30].

To assess thermal effects of laser pulses, modeling of the femtosecond pulse absorption vs. millisecond pulse absorption was performed (Fig. 5) [31]. Spatial distributions of temperatures for the ms ($\lambda = 1480$ nm, $\tau = 0.6$ ms, $P = 180$ mW) and fs ($\lambda = 514$ nm, $\tau = 280$ fs, intensity $I_0 = 2.5 \times 10^{12}$ W/cm²) pulses both at the time of reaching maximum temperature (solid curve) and at the stage of medium cooling (dotted curves) are provided. The exposure parameters are considered to be optimal for the ZP dissection [10, 31]. In case of femtosecond laser exposure, heat is concentrated primarily within the beam focus area ($r < 1.4$ μ m), which paves the way for safe embryo microsurgery within the framework of LAH. At the same time, a millisecond pulse is capable of heating a significantly larger area of the medium; one should be careful when performing the ZP dissection to minimize the risk of thermal damage to the embryonic cells adjacent to the ZP.

To assess safety of using femtosecond lasers for LAH, we conducted experiments involving staining of embryos with fluorescence dyes and determining the HSP gene expression. It was found that the embryos remained viable even after the

ZP microsurgery (staining of embryos with the Calcein-AM vital dye was observed).

To determine thermal shock experienced by the embryos due to laser beam exposure, we measured the expression of genes encoding two key heat shock proteins: *Hsp90aa1* and *Hspa5*. We found significant differences in expression of these genes between the positive and negative control groups, while expression of these genes in the experimental groups showed no significant differences from the control groups. The findings are consistent with theoretical estimates.

CONCLUSIONS

The findings of this pilot study suggest that the effects observed can result from local laser beam exposure, and the embryo generally remains viable. Thus, comprehensive assessment of the efficacy and safety of laser assisted hatching involving the use of the fs laser requires further research. It is necessary to perform experimental comparison of the femtosecond laser and millisecond lasers widely used in clinical practice in the context of their impact on the heat shock protein expression, as well as to assess the femtosecond laser effects on the mouse embryos *in vivo* by transferring the embryos to gestational surrogates.

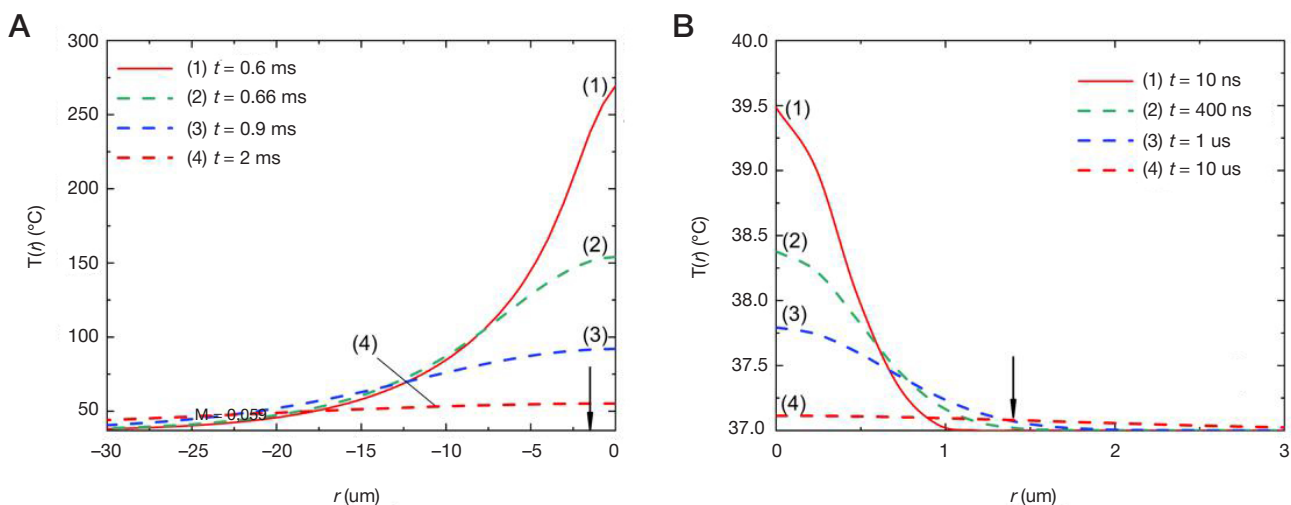


Fig. 5. Radial temperature profiles at different times for the millisecond (A) and femtosecond (B) pulse. Laser beam size at $1/e$ level is marked with arrows. Time (t) is counted down from the beginning of the pulse

References

- Inhorn MC, Patrizio P. Infertility around the globe: new thinking on gender, reproductive technologies and global movements in the 21st century. *Hum Reprod Update*. 2015; 21 (4): 411–26. DOI: 10.1093/humupd/dmv016. Epub 2015 Mar 22. PMID: 25801630.
- Krivosogova AS, Bruter AV, Makutina VA, Okulova YD, Ilchuk LA, Kubekina MV, et al. AAV infection of bovine embryos: Novel, simple and effective tool for genome editing. *Theriogenology*. 2022; 193: 77–86. DOI: 10.1016/j.theriogenology.2022.09.007.
- Báez F, Camargo AA, Gastal GDA. Ultrastructural Imaging Analysis of the Zona Pellucida Surface in Bovine Oocytes. *Microsc Microanal*. 2019; 25 (4): 1032–6. DOI: 10.1017/S1431927619000692. Epub 2019 May 28. PMID: 31134876.
- An L, Liu Y, Li M, Liu Z, Wang Z, Dai Y, et al. Site specificity of blastocyst hatching significantly influences pregnancy outcomes in mice. *FASEB J*. 2021; 35 (9): e21812. DOI: 10.1096/fj.202100653R. PMID: 34411354.
- Nishio E, Moriwaki T, Yoshii K, Udagawa Y. Chemical removal of zona pellucida versus laser assisted hatching after repeated failures of assisted reproductive technology. *Reprod Med Biol*. 2006; 5 (4): 263–7. DOI: 10.1111/j.1447-0578.2006.00151.x.
- Hammadeh ME, Fischer-Hammadeh C, Ali KR. Assisted hatching in assisted reproduction: a state of the art. *J Assist Reprod Genet*. 2011; 28 (2): 119–28. DOI: 10.1007/s10815-010-9495-3. Epub 2010 Nov 2. PMID: 21042844; PMCID: PMC3059528.
- Makrakis E, Angeli I, Agapitou K, Pappas K, Dafereras A, Pantos K. Laser versus mechanical assisted hatching: a prospective study of clinical outcomes. *Fertil Steril*. 2006; 86 (6): 1596–600. DOI: 10.1016/j.fertnstert.2006.05.031. Epub 2006 Oct 20. PMID: 17055494.
- Wang Y, Chen C, Liang J, Fan L, Liu D, Zhang X, et al. A comparison of the clinical effects of thinning and drilling on laser-assisted hatching. *Lasers Med Sci*. 2022; 37 (1): 1–9. DOI: 10.1007/s10103-020-03230-9.
- Xu W, Zhang L, Zhang L, Jin Z, Wu L, Li S, Shu J. Laser-assisted hatching in lower grade cleavage stage embryos improves blastocyst formation: results from a retrospective study. *J Ovarian Res*. 2021; 14 (1): 94. DOI: 10.1186/s13048-021-00844-7.
- Tadir Y, Douglas-Hamilton DH. Laser Effects in the Manipulation of Human Eggs and Embryos for In Vitro Fertilization. *Methods Cell Biol*. 2007; 82 (06): 409–31.
- Douglas-Hamilton DH, Conia J. Thermal effects in laser-assisted pre-embryo zona drilling. *J Biomed Opt*. 2001; 6 (2): 205.
- Vogel A, Noack J, Hüttman G, Paltauf G. Mechanisms of femtosecond laser nanosurgery of cells and tissues. *Appl Phys B*. 2005; 81 (8): 1015–47. DOI: 10.1007/s00340-005-2036-6.
- Liang X-X, Zhang Z, Vogel A. Multi-rate-equation modeling of the energy spectrum of laser-induced conduction band electrons in water. *Opt Express*. 2019; 27 (4): 4672. DOI: 10.1364/oe.27.004672.
- Ilina IV, Khramova YV, Ivanova AD, Filatov MA, Silaeva YY, Deykin AV, et al. Controlled hatching at the prescribed site using femtosecond laser for zona pellucida drilling at the early blastocyst stage. *J Assist Reprod Genet*. 2021; 38 (2): 517–29. DOI: 10.1007/s10815-020-01998-x.
- Hahn A, Bublak D, Schleiff E, Scharf KD. Crosstalk between Hsp90 and Hsp70 chaperones and heat stress transcription factors in tomato. *Plant Cell*. 2011; 23 (2): 741–55. DOI: 10.1105/tpc.110.076018.
- Sitnikov DS, Ilina IV, Filatov MA, Silaeva YY. Assessment of the zona pellucida microdissection on its thickness in mammalian embryos. *Bulletin of RSMU*. 2023; 1: 38–44. DOI: 10.24075/brsmu.2023.002.
- Filatov MA, Okulova JuD, Shafei RA, Korshunova DS, Silaeva JuJu. Kriokonservacija kak podhod k sohranjeniju unikal'nyh linij geneticheskij modifitsirovannyh zhivotnyh. *Biotehnologija*. 2022; 38 (6): 64–72. DOI: 10.56304/S0234275822060072. Russian.
- Kubekina MV, Kalinina AA, Korshunova DS, Bruter AV, Silaeva YY. Models of mitochondrial dysfunction with inducible expression of Polg pathogenic mutant variant. *Bulletin of RSMU*. 2022. № 2. P. 11–7. DOI: 10.24075/brsmu.2022.021.
- Sajjadi AY, Mitra K, Grace M. Expression of heat shock proteins 70 and 47 in tissues following short-pulse laser irradiation: assessment of thermal damage and healing. *Med Eng Phys*. 2013; 35 (10): 1406–14. DOI: 10.1016/j.medengphy.2013.03.011.
- Capon A, Mordon S. Can thermal lasers promote skin wound healing? *Am J Clin Dermatol*. 2003; 4 (1): 1–12. DOI: 10.2165/00128071-200304010-00001. PMID: 12477368.
- Choi I, Dasari A, Kim NH, Campbell KH. Effects of prolonged exposure of mouse embryos to elevated temperatures on embryonic developmental competence. *Reprod Biomed Online*. 2015; 31 (2): 171–9. DOI: 10.1016/j.rbmo.2015.04.017.
- Monty DE, Jr, Racowsky C. In vitro evaluation of early embryo viability and development in summer heat-stressed, superovulated dairy cows. *Theriogenology*. 1987; 28 (4): 451–65. DOI: 10.1016/0093-691x(87)90250-0. PMID: 16726328.
- Edwards JL, Ealy AD, Hansen PJ. Regulation of heat shock protein 70 synthesis by heat shock in the preimplantation murine embryo. *Theriogenology*. 1995; 44 (3): 329–37. DOI: 10.1016/0093-691x(95)00188-e. PMID: 16727733.
- Edwards JL, Hansen PJ. Differential responses of bovine oocytes and preimplantation embryos to heat shock. *Mol Reprod Dev*. 1997; 46 (2): 138–45. DOI: 10.1002/(SICI)1098-2795(199702)46:2<138::AID-MRD4>3.0.CO;2-R. PMID: 9021745.
- Douglas-Hamilton DH, Conia J. Thermal effects in laser-assisted pre-embryo zona drilling. *Journal of Biomedical Optics*. 2001; 6 (2): 205. DOI: 10.1117/1.1353796.
- Tucker M, Ball, G. Assisted hatching as a technique for use in human in vitro fertilization and embryo transfer is long overdue for careful and appropriate study. *The Journal of Clinical Embryology*. 2009; 12 (1): 9–14.
- Honguntikar SD, Uppangala S, Saliyan SR, Kalthur G, Kumar P, Adiga SK. Laser-assisted hatching of cleavage-stage embryos impairs developmental potential and increases DNA damage in blastocysts. *Lasers Med Sci*. 2015; 30 (1): 95–101. DOI: 10.1007/s10103-014-1625-1. Epub 2014 Jul 3. PMID: 24989334.
- Sanmee U, Piromlertamorn W, Vutyavanich T. The effect of the site of laser zona opening on the complete hatching of mouse blastocysts and their cell numbers. *Clin Exp Reprod Med*. 2016; 43 (3): 152–6. DOI: 10.5653/cerm.2016.43.3.152. Epub 2016 Sep 22. PMID: 27689037; PMCID: PMC5039307.
- Montag M, van der Ven H. Laser-assisted hatching in assisted reproduction. *Croat Med J*. 1999; 40 (3): 398–403. PMID: 10411968.
- de Medeiros FW, Kaur H, Agrawal V, Chaurasia SS, Hammel J, et al. Effect of femtosecond laser energy level on corneal stromal cell death and inflammation. *J Refract Surg*. 2009; 25 (10): 869–74. DOI: 10.3928/1081597X-20090917-08.
- Sitnikov DS, Ilina IV, Pronkin AA. Assessment of the thermal effect of femtosecond and millisecond laser pulses in microsurgery of mammalian embryos. *Quantum Electron*. 2022; 52 (5): 482–90. DOI: 10.1070/QEL18047.

Литература

- Inhorn MC, Patrizio P. Infertility around the globe: new thinking on gender, reproductive technologies and global movements in the 21st century. *Hum Reprod Update*. 2015; 21 (4): 411–26. DOI: 10.1093/humupd/dmv016. Epub 2015 Mar 22. PMID: 25801630.
- Krivosogova AS, Bruter AV, Makutina VA, Okulova YD, Ilchuk LA, Kubekina MV, et al. AAV infection of bovine embryos: Novel, simple and effective tool for genome editing. *Theriogenology*. 2022; 193: 77–86. DOI: 10.1016/j.theriogenology.2022.09.007.
- Báez F, Camargo AA, Gastal GDA. Ultrastructural Imaging Analysis of the Zona Pellucida Surface in Bovine Oocytes. *Microsc Microanal*. 2019; 25 (4): 1032–6. DOI: 10.1017/S1431927619000692. Epub 2019 May 28. PMID: 31134876.
- An L, Liu Y, Li M, Liu Z, Wang Z, Dai Y, et al. Site specificity of blastocyst hatching significantly influences pregnancy outcomes

- in mice. *FASEB J.* 2021; 35 (9): e21812. DOI: 10.1096/fj.202100653R. PMID: 34411354.
5. Nishio E, Moriwaki T, Yoshii K, Udagawa Y. Chemical removal of zona pellucida versus laser assisted hatching after repeated failures of assisted reproductive technology. *Reprod Med Biol.* 2006; 5 (4): 263–7. DOI: 10.1111/j.1447-0578.2006.00151.x.
 6. Hammadeh ME, Fischer-Hammadeh C, Ali KR. Assisted hatching in assisted reproduction: a state of the art. *J Assist Reprod Genet.* 2011; 28 (2): 119–28. DOI: 10.1007/s10815-010-9495-3. Epub 2010 Nov 2. PMID: 21042844; PMCID: PMC3059528.
 7. Makrakis E, Angeli I, Agapitou K, Pappas K, Dafereras A, Pantos K. Laser versus mechanical assisted hatching: a prospective study of clinical outcomes. *Fertil Steril.* 2006; 86 (6): 1596–600. DOI: 10.1016/j.fertnstert.2006.05.031. Epub 2006 Oct 20. PMID: 17055494.
 8. Wang Y, Chen C, Liang J, Fan L, Liu D, Zhang X, et al. A comparison of the clinical effects of thinning and drilling on laser-assisted hatching. *Lasers Med Sci.* 2022; 37 (1): 1–9. DOI: 10.1007/s10103-020-03230-9.
 9. Xu W, Zhang L, Zhang L, Jin Z, Wu L, Li S, Shu J. Laser-assisted hatching in lower grade cleavage stage embryos improves blastocyst formation: results from a retrospective study. *J Ovarian Res.* 2021; 14 (1): 94. DOI: 10.1186/s13048-021-00844-7.
 10. Tadir Y, Douglas-Hamilton DH. Laser Effects in the Manipulation of Human Eggs and Embryos for In Vitro Fertilization. *Methods Cell Biol.* 2007; 82 (06): 409–31.
 11. Douglas-Hamilton DH, Conia J. Thermal effects in laser-assisted pre-embryo zona drilling. *J Biomed Opt.* 2001; 6 (2): 205.
 12. Vogel A, Noack J, Hüttman G, Paltauf G. Mechanisms of femtosecond laser nanosurgery of cells and tissues. *Appl Phys B.* 2005; 81 (8): 1015–47. DOI: 10.1007/s00340-005-2036-6.
 13. Liang X-X, Zhang Z, Vogel A. Multi-rate-equation modeling of the energy spectrum of laser-induced conduction band electrons in water. *Opt Express.* 2019; 27 (4): 4672. DOI: 10.1364/oe.27.004672.
 14. Iliina IV, Khramova YV, Ivanova AD, Filatov MA, Silaeva YY, Deykin AV, et al. Controlled hatching at the prescribed site using femtosecond laser for zona pellucida drilling at the early blastocyst stage. *J Assist Reprod Genet.* 2021; 38 (2): 517–29. DOI: 10.1007/s10815-020-01998-x.
 15. Hahn A, Bublak D, Schleiff E, Scharf KD. Crosstalk between Hsp90 and Hsp70 chaperones and heat stress transcription factors in tomato. *Plant Cell.* 2011; 23 (2): 741–55. DOI: 10.1105/tpc.110.076018.
 16. Ситников Д. С., Ильина И. В., Филатов М. А., Силаева Ю. Ю. Исследование влияния микродиссекции блестящей оболочки эмбрионов млекопитающих на ее толщину. *Вестник РГМУ.* 2023; 1: 41–8. DOI: 10.24075/vrgmu.2023.002.
 17. Филатов М. А., Окулова Ю. Д., Шафеи Р. А., Коршунова Д. С., Силаева Ю. Ю. Криоконсервация как подход к сохранению уникальных линий генетически модифицированных животных. *Биотехнология.* 2022; 38 (6): 64–72. DOI: 10.56304/S0234275822060072.
 18. Кубекина, М. В., Калинина, А. А., Коршунова, Д. С., Брутер, А. В., Силаева, Ю. Ю. Модели митохондриальной дисфункции с индуцируемой экспрессией мутантного варианта гена Polg. *Вестник РГМУ.* 2022; 2: 12–19. DOI: 10.24075/vrgmu.2022.021.
 19. Sajjadi AY, Mitra K, Grace M. Expression of heat shock proteins 70 and 47 in tissues following short-pulse laser irradiation: assessment of thermal damage and healing. *Med Eng Phys.* 2013; 35 (10): 1406–14. DOI: 10.1016/j.medengphy.2013.03.011.
 20. Capon A, Mordon S. Can thermal lasers promote skin wound healing? *Am J Clin Dermatol.* 2003; 4 (1): 1–12. DOI: 10.2165/00128071-200304010-00001. PMID: 12477368.
 21. Choi I, Dasari A, Kim NH, Campbell KH. Effects of prolonged exposure of mouse embryos to elevated temperatures on embryonic developmental competence. *Reprod Biomed Online.* 2015; 31 (2): 171–9. DOI: 10.1016/j.rbmo.2015.04.017.
 22. Monty DE, Jr, Racowsky C. In vitro evaluation of early embryo viability and development in summer heat-stressed, superovulated dairy cows. *Theriogenology.* 1987; 28 (4): 451–65. DOI: 10.1016/0093-691x(87)90250-0. PMID: 16726328.
 23. Edwards JL, Ealy AD, Hansen PJ. Regulation of heat shock protein 70 synthesis by heat shock in the preimplantation murine embryo. *Theriogenology.* 1995; 44 (3): 329–37. DOI: 10.1016/0093-691x(95)00188-e. PMID: 16727733.
 24. Edwards JL, Hansen PJ. Differential responses of bovine oocytes and preimplantation embryos to heat shock. *Mol Reprod Dev.* 1997; 46 (2): 138–45. DOI: 10.1002/(SICI)1098-2795(199702)46:2<138::AID-MRD4>3.0.CO;2-R. PMID: 9021745.
 25. Douglas-Hamilton DH, Conia, J. Thermal effects in laser-assisted pre-embryo zona drilling. *Journal of Biomedical Optics.* 2001; 6 (2): 205. DOI: 10.1117/1.1353796.
 26. Tucker M, Ball, G. Assisted hatching as a technique for use in human in vitro fertilization and embryo transfer is long overdue for careful and appropriate study. *The Journal of Clinical Embryology.* 2009; 12 (1): 9–14.
 27. Honguntikar SD, Uppangala S, Salian SR, Kalthur G, Kumar P, Adiga SK. Laser-assisted hatching of cleavage-stage embryos impairs developmental potential and increases DNA damage in blastocysts. *Lasers Med Sci.* 2015; 30 (1): 95–101. DOI: 10.1007/s10103-014-1625-1. Epub 2014 Jul 3. PMID: 24989334.
 28. Sanmee U, Piromlertamorn W, Vutyavanich T. The effect of the site of laser zona opening on the complete hatching of mouse blastocysts and their cell numbers. *Clin Exp Reprod Med.* 2016; 43 (3): 152–6. DOI: 10.5653/cepm.2016.43.3.152. Epub 2016 Sep 22. PMID: 27689037; PMCID: PMC5039307.
 29. Montag M, van der Ven H. Laser-assisted hatching in assisted reproduction. *Croat Med J.* 1999; 40 (3): 398–403. PMID: 10411968.
 30. de Medeiros FW, Kaur H, Agrawal V, Chaurasia SS, Hammel J, et al. Effect of femtosecond laser energy level on corneal stromal cell death and inflammation. *J Refract Surg.* 2009; 25 (10): 869–74. DOI: 10.3928/1081597X-20090917-08.
 31. Sitnikov DS, Iliina IV, Pronkin AA. Assessment of the thermal effect of femtosecond and millisecond laser pulses in microsurgery of mammalian embryos. *Quantum Electron.* 2022; 52 (5): 482–90. DOI: 10.1070/QEL18047.

THE POSSIBILITY OF EVALUATION MRNA EXPRESSION PROFILING TO PREDICT PROGRESSION OF LOCAL STAGE COLORECTAL CANCER

Goncharov SV , Bozhenko VK, Zakharenko MV, Chaptikov AA, Kulinich TM, Solodkiy VA

Russian Scientific Center of Roentgenoradiology, Moscow, Russia

Progression assessment enables implementation of the colorectal cancer (CRC) tertiary prevention measures aimed at early detection and timely treatment of metastatic cancer. The study was aimed to develop a model of CRC progression using pathomorphological and molecular genetic characteristics of tumors. Relative expression of mRNAs of 63 genes from various functional groups was determined in the tumor specimens of 223 patients with stage $T_{1-4}N_{0-2}M_0$ CRC. The median follow-up period was 42 months. Binary logistic regression models were constructed, in which likelihood of progression within 36 months after the CRC diagnosis was a target variable. Explanatory variables were as follows: tumor grade, angiolymphatic invasion, ratio of the number of metastatic lymph nodes to the total number of lymph nodes in the surgical specimen, patient's age and tumor localization, as well as expression levels of genes *CCNB1*, *Ki67*, *GRB7*, *IGF1*, *IL2*, *IL6*, *IL8*, *GATA3*. Prediction accuracy of the model using clinical and morphological characteristics was 56.6%. Inclusion of *CCNB1*, *Ki67*, *GRB7*, *IGF1*, *IL2*, *IL6*, *IL8*, *GATA3* expression profiles in the model increased accuracy to 80.6%. Thus, prediction of CRC progression for treatment personalization requires additional parameters beyond information acquired within the framework of conventional morphological TNM classification. The use of molecular markers as predictors significantly increases the CRC progression prediction accuracy. Further research is needed for validation and quality improvement of prognostic models.

Keywords: colorectal cancer, predictive markers, prognostic models of colorectal cancer progression, CRC

Funding: the study was supported through the grant by RSF 22-15-00448.

Author contribution: Goncharov SV, Bozhenko VK, Solodkiy VA — study concept and design; Bozhenko VK, Goncharov SV, Kulinich TM, Zakharenko MV, Solodkiy VA — data acquisition and processing; Goncharov SV, Chaptikov AA, Bozhenko VK, Kulinich TM — manuscript writing; Goncharov SV, Chaptikov AA, Bozhenko VK, Kulinich TM, Zakharenko MV, Solodkiy VA — editing.

Compliance with ethical standards: the study was approved by the Ethics Committee of the Russian Scientific Center of Roentgenoradiology (protocol № 4 dated 26 April 2018) and conducted in accordance with the World Medical Association Declaration of Helsinki. All subjects submitted the informed consent to study participation.

 **Correspondence should be addressed:** Sergey V. Goncharov
Profsoyuznaya, 86, 117997, Moscow, Russia; 9015@mail.ru

Received: 13.09.2023 **Accepted:** 01.12.2023 **Published online:** 23.12.2023

DOI: 10.24075/brsmu.2023.050

ВОЗМОЖНОСТИ ИСПОЛЬЗОВАНИЯ ПРОФИЛИРОВАНИЯ ЭКСПРЕССИИ МРНК ДЛЯ ПРОГНОЗА ПРОГРЕССИРОВАНИЯ ЛОКАЛЬНЫХ СТАДИЙ КОЛОРЕКТАЛЬНОГО РАКА

С. В. Гончаров , В. К. Боженко, М. В. Захаренко, А. А. Чаптыков, Т. М. Кулинич, В. А. Солодкий

Российский научный центр рентгенодиагностики, Москва, Россия

Оценка прогрессирования позволяет реализовать меры третичной профилактики колоректального рака (КРР), направленные на раннее выявление и своевременное лечение метастатической болезни. Целью исследования было разработать модель прогрессирования КРР с использованием патоморфологических и молекулярно-генетических характеристик опухоли. У 223 пациентов с КРР в стадиях $T_{1-4}N_{0-2}M_0$ в образцах из опухоли были определены относительные уровни экспрессии мРНК 63 генов из разных функциональных групп. Медиана наблюдения 42 месяца. Сформированы логистические модели бинарного выбора, в которых целевой переменной служила вероятность прогрессирования в течение 36 месяцев от момента установки диагноза КРР. Объясняющими переменными были дифференцировка опухоли, ангиолимфатическая инвазия, соотношение числа метастатических лимфоузлов к их общему числу в операционном препарате, возраст пациента и локализация опухоли, а также показатели экспрессии генов *CCNB1*, *Ki67*, *GRB7*, *IGF1*, *IL2*, *IL6*, *IL8*, *GATA3*. Точность прогноза в модели с использованием клинико-морфологических показателей составила 56,6%. Включение в модель профиля экспрессии генов *CCNB1*, *Ki67*, *GRB7*, *IGF1*, *IL2*, *IL6*, *IL8*, *GATA3* повышает точность до 80,6%. Таким образом, прогнозирование прогрессирования КРР для персонализации лечения требует дополнительных показателей, выходящих за пределы информации, получаемой в рамках традиционной морфологической классификации TNM. Использование молекулярных маркеров в качестве предикторов значительно повышает точность прогнозирования прогрессирования КРР. Необходимы дальнейшие исследования для валидации и улучшения качества прогностических моделей.

Ключевые слова: колоректальный рак, предиктивные маркеры, прогностические модели прогрессирования КРР, КРР

Финансирование: работа поддержана грантом РФ 22-15-00448.

Вклад авторов: С. В. Гончаров, В. К. Боженко, В. А. Солодкий — концепция и дизайн исследования; В. К. Боженко, С. В. Гончаров, Т. М. Кулинич, М. В. Захаренко, В. А. Солодкий — сбор и обработка материала; С. В. Гончаров, А. А. Чаптыков, В. К. Боженко, Т. М. Кулинич — написание текста; С. В. Гончаров, А. А. Чаптыков, В. К. Боженко, Т. М. Кулинич, М. В. Захаренко, В. А. Солодкий — редактирование.

Соблюдение этических стандартов: исследование одобрено этическим комитетом ФГБУ «Российский научный центр рентгенодиагностики» МЗ РФ (протокол № 4 от 26 апреля 2018 г.), проведено в соответствии с Хельсинкской декларацией Всемирной медицинской ассоциации. Все участники подписали добровольное информированное согласие на участие в исследовании.

 **Для корреспонденции:** Сергей Владимирович Гончаров
ул. Профсоюзная, д. 86, 117997, г. Москва, Россия; 9015@mail.ru

Статья получена: 13.09.2023 **Статья принята к печати:** 01.12.2023 **Опубликована онлайн:** 23.12.2023

DOI: 10.24075/vrgmu.2023.050

Colorectal cancer (CRC) occupies one of the leading places in the structure of cancer incidence in Russia and all over the world. Furthermore, prevalence of colon cancer in the Russian Federation increased from 116.7 to 161.0 cases per 100,000 population over the last decade, while prevalence of rectal cancer increased from 90.4 to 121.1 cases [1].

Today, cancer stage according to the TNM system and grade are the main parameters determining the CRC prognosis. However, even the groups of patients with CRC clinically homogeneous based on stage and grade are characterized by high heterogeneity of the disease course and uncertain prognosis. Such diversity is due to the fact that several tumor variants with different molecular pathogenesis that form the tumor biological heterogeneity go under the guise of the same morphological type of cancer.

Clinical prediction tools that are traditionally based on the statistical regression models represent one of the methods to combine all the prognostic information allowing one to avoid further stratification of the intermediate TNM system based on binary logistic regression [2]. With appropriate development and testing, these tools will be able to integrate and personalize information about the prognosis of certain patient and provide refined assessment of progression risk for clinical use.

To date, several test systems for determination of the disease prognosis and therapy efficacy based on assessing expression of genes in the tumor tissue have been created. Such test systems, as OncotypeDX, ColoPrint, ColoPrint, ColoPrint, determine the likelihood of cancer progression based on the estimated expression of a number of genes in the tumor [3]. The efficiency of these commercially available systems is criticized in some papers. Thus, there is a report on the creation of a more effective system for prediction of CRC progression and I-II stage cancer response to treatment compared to OncotypeDX and ColoPrint [4]. The authors create a patient-specific treatment plan for early stage CRC, suggesting to include adjuvant chemotherapy in the treatment regimen, which is usually not done according to the current international and national guidelines.

There are also specific biological predictors for prediction of the possibility of CRC metastasis to the lymph nodes, such as heat shock protein 47 (HSP47) [5]. According to the authors, detection of this protein will also contribute to the treatment approach personalization in patients at high risk of metastasis to the lymph nodes.

Currently, various prognostic models based both on the use of advanced mathematical methods (neural network models, artificial intelligence models, construction of binary classification tree (BCT), peer reviews, etc.) and expansion of the set of explanatory variables (determination of point mutations, microsatellite instability, investigation of tumor microenvironment

and expression profiles) are constantly proposed. However, there is still a need for prognostic model improvement. These issues prompted us to assess the possibility of expression profiling of mRNAs from tumor specimens in order to evaluate the colorectal cancer prognosis.

METHODS

The mRNA expression profiles of 63 genes (Table 1) of potential contributors to various carcinogenesis pathways determined in 217 specimens of colorectal adenocarcinoma of different localization were included in the study. Adenocarcinoma specimens from the right half of the colon constituted 23% (50 specimens), while that from the left half of the colon constituted 39.6% (86 specimens). Rectal tumor specimens made up 37.4% (81 specimens). There were 97 males (44.7%), 120 females (45.3%). Specimens were collected during pathomorphological examination of surgical material. Inclusion criterion: morphologically verified colorectal adenocarcinoma, local stages T₁₋₃, N₀₋₂, M₀. No specific anticancer treatment was performed before surgery. During the study the long-term outcomes were monitored in all patients for at least 36 months. The median follow-up period was 42 months. Exclusion criterion: multiple primary colorectal cancer, history of other type of cancer or cancer of other type at the time of inclusion in the study.

We had earlier reported the method of RNA extraction and real-time PCR settings [6]. As a result, relative expression of mRNAs of the studied panel of genes belonging to different functional groups was determined in each specimen of adenocarcinoma having different embryonic-anatomical localization.

Statistical data processing was performed using the Jamovi open source statistical software package (The Jamovi project; Australia). The logistic regression models constructed were evaluated based on R² Durbin–Watson test for autocorrelation (DW). The model quality was considered acceptable at R² > 0.3 and DW > 1.5.

We set the task to construct a binary logistic regression model for prediction of 3-year disease-free survival in patients with CRC using the mRNA expression profiles obtained considering the data of pathomorphological report. For that we formed a set of explanatory variables conditionally divided into two categories. The first category included the data of the surgical specimen pathomorphological examination: T and N, grade, lymphovascular and angiolymphatic invasion, ratio of the total number of resected lymph nodes to the number of metastatic ones. The second category of explanatory variables included mRNA expression profiles of 63 genes in the tumor specimens. To test predictive ability of the model developed, initial sample of patients was randomized into two subsamples:

Table 1. Genes included in the analysis

Biological effects in the cell	Gene
Proliferation	<i>Ki-67, CCND1, CCNB1, PTEN, STK-15(AURKA), P16INK4A, P14ARF, HER2/neu(C-erbB2), TERT</i>
Apoptosis	<i>BCL2, BAX, BAG1, NDRG1, BIRC5</i>
Transcription	<i>C-MYC, MYBL2</i>
Cell–cell interactions	<i>MMP2, MMP7, MMP8, MMP9, MMP11, CTSL2, PAPP, TPA</i>
Cell differentiation	<i>ESR1, PGR, CYP19A1, GRB7, CD45, CD56, CD68, CD69</i>
Growth factors	<i>VEGFA121, VEGFA165, VEGFA189, SCUBE2, IGF1, IGF2, TGFβ</i>
Immune response regulation	<i>IL1β, IL2, IL6, IL7, IL8, IL10, IL12α, IL15, COX-2, TNFα, TLR2, TLR4, TLR7, IFNγ, GNLY, HLA-G1, HLA-G5, LIF, LIFR, LGALS1, GATA3, IL2Rα, GREM1</i>
Metabolism	<i>GSTM1</i>

Table 2. Logit model using conventional criteria to predict the risk of CRC progression

Variables	Coefficient	Standard error	z-Statistics	Probability
Grade (G)	-0.834489	0.368047	-2.267346	0.0234
Lymphovascular/angiolymphatic invasion	-2.444482	0.582805	-4.194337	0
Resected to metastatic lymph node ratio	-1.511334	0.583617	-2.589598	0.0096
Age	0.047712	0.017803	2.680001	0.0074
Tumor localization	0.724943	0.454279	1.595811	0.1105
constant	0.33256	1.114196	0.298475	0.7653
		McFadden R ²	0.292908	

Note: Grade (G) is "0" when grade is G1 or G2 and "1" when grade is G3; the variable is "0" when histological assessment reveals no signs of angiolymphatic and/or lymphovascular invasion and "1" when there is at least one such sign; the ratio of the number of metastatic lymph nodes to the total number of resected lymph nodes in the surgical specimen is 0–1; Age is the patient's age in whole years; Localization is tumor localization, which takes the value of "0" in cases of right-sided tumors (cecum, ascending colon, transverse colon) and "1" in cases of left-sided tumors (descending colon, sigmoid, rectum); 0.332 is a constant coefficient (constant) used in the model.

index (90% of observations) used to construct the model and control (10% of observations) used to assess the likelihood of prediction made using the model constructed. The percentages of the above subsamples suit the general practice adopted in modern scientific literature. Calculation was performed in the EViews v. 7.0 software package (IHS Global Inc.; USA). Assessment and comparison of the concurrent probit and logit models based on the McFadden's coefficient of determination and Akaike and Schwartz information criteria showed that logit specification was the most successful.

RESULTS

During the first phase, a logit model for prediction of CRC progression within 36 months after the diagnosis was constructed using conventional clinical and morphological criteria for CRC progression risk only as explanatory variables (Table 2).

R² was 0.29, and Durbin–Watson statistic was 1.51. These characteristics of binary logistic regression model suggest that the analysis of conventional morphological risk factors of progression, such as adenocarcinoma grade, tumor localization, total number of resected lymph nodes and number of metastatic ones predicts the CRC progression probability with the minimally satisfactory accuracy. Table 3 provides a classification matrix of this logit model.

Fig. 1 shows accuracy of the model developed with inclusion of conventional prognostic factors.

As we have pointed out before, the overall prediction accuracy of this model (56.62%) was not high, while prediction accuracy of 37% in patients with no progression was considered to be unsatisfactory. We used mRNA expression profiles of a panel of 63 genes from tumor specimens as supplementary explanatory variables during the next phase of the study.

The research resulted in construction of the second logit model, in which mRNA expression profiles from tumor specimens were added to morphological characteristics as explanatory variables. A total of 12 characteristics (variables) turned out to be significant in the mathematical model (Table 4).

R² coefficient was 0.4 in this model, while Durbin–Watson statistic was 1.64. A significant increase in the accuracy of the model constructed was achieved by including the expression levels of genes *CCNB1*, *Ki67*, *GRB7*, *IGF1*, *IL2*, *IL6*, *IL8*, *GATA3* from tumor specimens in the regression equation. Classification matrix is provided in Table 5.

The overall classification accuracy was 80.6% (Fig. 2). We would like to emphasize that prediction accuracy in patients with no progression increased from 37 to 70.5% relative to the first model.

This model was used to calculate a personalized prognosis for each patient in our sample. Fig. 3 presents graphic representation of personal risk distribution based on progression detection. The median risk indicator was 57.1% [38.2; 70.7] in the group with no progression detected and 79.2% [68.3; 96.4] in cases of progression detection. The differences in risk indicators turned out to be significant (Kruskal–Wallis test: $p < 0.05$).

The risk factors of colorectal cancer progression assessed by pathomorphologists during the routine examination enable construction of the prognostic model that is minimally satisfactory in terms of accuracy. The increase in the prognostic model accuracy can be achieved through analysis of information beyond the bounds of pathomorphological stage. Assessment of mRNA expression profiles of genes *CCNB1*, *Ki67*, *GRB7*, *IGF1*, *IL2*, *IL6*, *IL8*, *GATA3* in tumor specimens makes it possible to increase accuracy from 56.62 to 80.6%. The changes in expression of other genes of the panel also seem to be important, however, inclusion of those in the model does not result in higher accuracy due to multicollinearity, which can testify additionally that changes in the large intestinal mucosa associated with colorectal cancer are systemic.

We have noted that classical pathomorphological signs of high risk of CRC progression, such as lymphovascular and angiolymphatic invasion, grade, type of lymph node involvement, have negative regression coefficients, while *GATA3* tumor suppressor has a positive coefficient. This pattern seems to be consistent: increased activity of the *GATA3* cancer suppressor is typical for the less aggressive CRC course [7],

Table 3. Classification matrix of the logit model based on conventional clinical and morphological risk factors of CRC progression

	Actual data (number of patients)	Accurate prediction (number of patients)	Prediction accuracy (%)
No progression	139	123	88.4
Progression	78	29	37
Overall accuracy			56.62

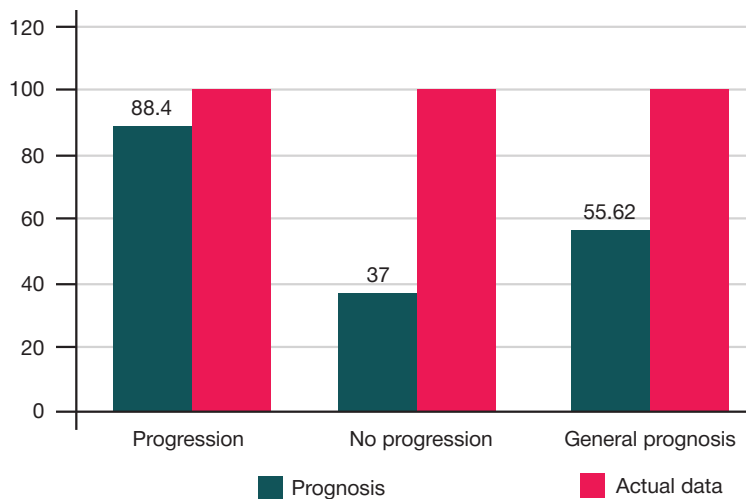


Fig. 1. Prediction accuracy when using conventional clinical and morphological risk factors of CRC progression

while the presence of metastatic lymph nodes in the specimen, low grade, and angiolymphatic invasion indicate high risk of progression.

DISCUSSION

The urgent task of improving the outcomes of local stage colorectal cancer tertiary prevention is inextricably linked with objective stratification of cancer prognosis aimed at treatment personalization and, which is especially important, assessing the effectiveness of the existing and prospective treatment regimens. Despite the fact that to date pathomorphological CRC stage is the basis for the disease progression prognosis, it is the study of information about pathological progression without any reference to CRC stage that can become the key to

overcoming the challenge of progression risk assessment. This information can be represented primarily by molecular genetic data obtained by analysis of tissues of the affected organ. We used 12 indicators obtained during pathomorphological examination and molecular genetic testing of the tumor to develop a prognostic logit model of progression. These include both generally accepted risk factors, such as tumor grade, angiolymphatic and perineural invasion, as well as nature of changes in the lymph nodes resected during surgery, and mRNA expression of eight genes: *CCNB1*, *Ki67*, *GRB7*, *IGF1*, *IL2*, *IL6*, *IL8*, *GATA3*.

The role of these genes in carcinogenesis was repeatedly discussed in the literature [8–12]. These genes belong to functional groups of regulators of cell cycle (*CCNB1*) and proliferation (*Ki-67* *GRB7*), growth factors (*IGF-1*) and cytokines

Table 4. Logit model using mRNA expression profiles

Variables	Coefficient	Standard error	z-Statistics	Probability
Lymphovascular/angiolymphatic invasion	-2.631111	0.657195	-4.003548	0.0001
Resected to metastatic lymph node ratio ("lymph nodes")	-2.101045	0.67982	-3.09059	0.002
Age	0.05032	0.019404	2.593334	0.0095
Grade (G)	-1.028091	0.415533	-2.474153	0.0134
<i>CCNB1</i>	0.535019	0.207419	2.579411	0.0099
<i>Ki67</i>	-0.511469	0.276974	-1.846634	0.0648
<i>GRB7</i>	-0.456156	0.185794	-2.455168	0.0141
<i>IGF1</i>	-0.196378	0.079666	-2.465027	0.0137
<i>IL2</i>	-0.245648	0.100843	-2.435952	0.0149
<i>IL6</i>	0.202048	0.092241	2.190427	0.0285
<i>IL8</i>	-0.234825	0.094272	-2.490925	0.0127
<i>GATA3</i>	0.333421	0.174847	1.906929	0.0565
Constant	11.04682	3.481664	3.172857	0.0015
		McFadden R ²		0.403

Note: Grade (G) is "0" when grade is G1 or G2 and "1" when grade is G3; the variable is "0" when histological assessment reveals no signs of angiolymphatic and/or lymphovascular invasion and "1" when there is at least one such sign; the ratio of the number of metastatic lymph nodes to the total number of resected lymph nodes in the surgical specimen is 0–1; Age is the patient's age in whole years; *CCNB1*, *Ki67*, *GRB7*, *IGF1*, *IL2*, *IL6*, *IL8*, *GATA3* are expression levels of appropriate genes in the tumor; 11.05 is a constant coefficient used in the model.

Table 5. Classification matrix of the logit model using mRNA expression profiles of eight genes

	Actual data (number of patients)	Accurate prediction (number of patients)	Prediction accuracy (%)
No progression	139	120	86.3
Progression	78	55	70.5
Overall accuracy			80.6

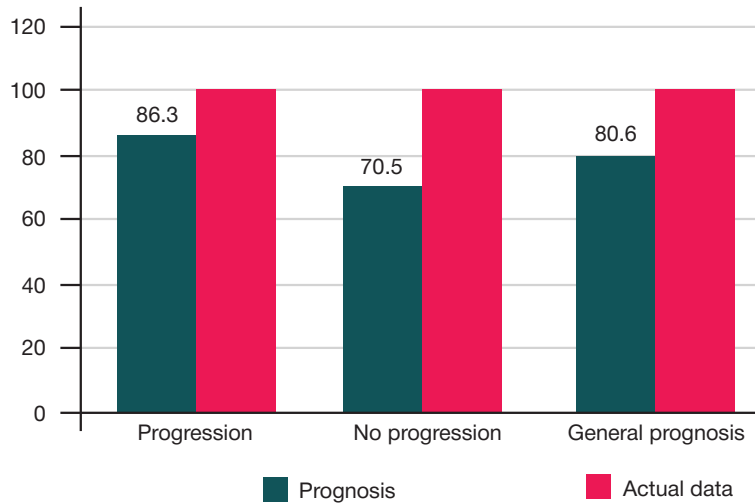


Fig. 2. Prediction accuracy of the logit model using mRNA expression profiles of eight genes

(IL2, IL6, IL8) involved in the colorectal cancer invasion and metastasis [12].

When comparing our findings with the earlier reported data, including the reports of large-scale studies, we noticed that it was difficult to clearly interpret the characteristics of tumor grade, angiolymphatic and lymphovascular invasion due to the lack of common classification system and assessment standards [13–15]. This enables considerable variation of these characteristics across different clinics [16, 17]. Thus, for example, it is believed that PNI detection rate is usually underestimated, and the detection rate values vary between 9 and 42% [18]. The role of the resected to metastatic lymph node ratio in the specimen in CRC was first explored in 2005 [19]. This indicator was defined as a negative independent prognostic factor in stage III disease associated with overall and disease-free survival of patients with CRC. The indicator has a stronger influence on the prognosis of rectal cancer, than that of colon cancer. Its prognostic value increases when assessing more than 12 lymph nodes. Critical values of this indicator vary between 0.125 and 0.3 in different studies. There is still no consensus about the minimum number of lymph nodes harvested for appropriate estimation of this parameter.

It should be noted that, thanks to the efforts of medical associations, the clinical genomic databases have become available in the recent years. The analysis of such datasets

allows one to better understand the CRC genomic landscape and assess treatment efficacy and safety in the subgroups of patients with different genomic profiles. It is noted in the literature that the differences between the databases on demographic, clinical characteristics, treatment regimens and overall survival should be considered when developing research and interpreting the results acquired from the clinical genomic databases [20].

Anyway, our findings confirm the trend: analysis of additional information, primarily molecular genetic data, beyond the bounds of pathomorphological stage in individuals with colorectal cancer significantly increases accuracy of predicting the likelihood of progression. Furthermore, the search for new predictors and, just as important, extensive validation of prognostic systems should be continued.

CONCLUSIONS

We have found that the risk factors of CRC progression identified during standard pathomorphological examination ensure prediction accuracy of 56.62% when using a binary prognostic logit model in our sample of patients. Moreover, classification errors occur primarily because of patients showing no progression throughout the 36-month follow-up period. Inclusion of mRNA expression levels of genes *CCNB1*, *Ki67*, *GRB7*, *IGF1*, *IL2*, *IL6*, *IL8*, *GATA3* from tumor

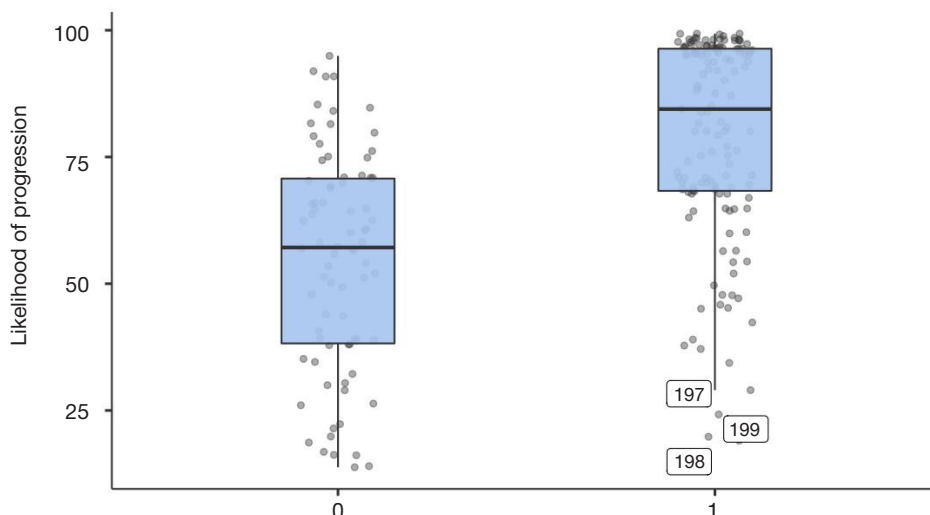


Fig. 3. Individual prognosis distribution in the model using clinical and morphological risk factors of progression

specimens in the model as explanatory variables increases prediction accuracy to 80.6%. This suggests that expansion of the search for outcome predictors beyond the bounds of

the TNM pathomorphological stage is a promising way to increase accuracy in order to implement effective CRC tertiary prevention measures.

References

- Kaprin AD, Starinskij VV, Shahzadova AO. Sostojanie onkologicheskoy pomoshhi naseleniju Rossii v 2021 godu. Rossijskij Centr informacionnyh tehnologij i jepidemiologicheskikh issledovanij v oblasti onkologii. Moskva, 2022. Russian.
- Steyerberg EW, Moons KGM, van der Windt DA, et al. Prognosis Research Strategy (PROGRESS) 3: prognostic model research. *PLoS medicine*. 2013; 10: e1001381.
- Brenner H, Chen C. The colorectal cancer epidemic: challenges and opportunities for primary, secondary and tertiary prevention. *Br J Cancer*. 2018; 119 (7): 785–92. DOI: 10.1038/s41416-018-0264-x. Epub 2018 Oct 4. PMID: 30287914; PMCID: PMC6189126.
- Lin XT, Wu QN, Qin S, Fan DJ, Lv MY, Chen X, et al. Identification of an Autophagy-Related Gene Signature for the Prediction of Prognosis in Early-Stage Colorectal Cancer. *Front Genet*. 2021; 12: 755789. DOI: 10.3389/fgene.2021.755789. PMID: 34899841; PMCID: PMC8657766.
- Mori K, Toiyama Y, Okugawa Y, Ichikawa T, Nagano Y, Oki S, et al. Preoperative heat shock protein 47 levels identify colorectal cancer patients with lymph node metastasis and poor prognosis. *Oncol Lett*. 2020; 20 (6): 333. DOI: 10.3892/ol.2020.12196. Epub 2020 Oct 7. PMID: 33123244; PMCID: PMC7583735.
- Bozhenko VK, Stanojevic US, Trotsenko ID, et al. Comparison of matrix proteinase mRNA expression in morphologically normal, neoplastic, and metastatic colon tissue and colon biopsies from healthy donors. *Biomed Khim*. 2018; 64 (1): 46–52. DOI: 10.18097/PBMC20186401046. Russian.
- French CL, Ye F, Revetta F, et al. Linking patient outcome to high throughput protein expression data identifies novel regulators of colorectal adenocarcinoma aggressiveness. *F1000Res*. 2015; 4: 99. DOI: 10.12688/f1000research.6388.1.
- Fang Y, Yu H, Liang X, Xu J, Cai X. Chk1-induced CCNB1 overexpression promotes cell proliferation and tumor growth in human colorectal cancer. *Cancer Biol Ther*. 2014; 15 (9): 1268–79. DOI: 10.4161/cbt.29691. Epub 2014 Jun 27. PMID: 24971465; PMCID: PMC4128869.
- Hu B, Song X, Ding W, Wang H, Cai H, Huang Z. Expression and Clinical Significance of Ki67 and SOX2 in Colorectal Cancer. *J Healthc Eng*. 2023; 2023: 3783631. DOI: 10.1155/2023/3783631. PMID: 37457497; PMCID: PMC10348847.
- Vermehren-Schmaedick A, Mhawech-Fauceglia P, Park BS, Pejovic T, Luoh SW. The prognostic significance of GRB7 protein expression and localization in human breast and ovarian cancers. *Oncotarget*. 2020; 11 (24): 2273–89. DOI: 10.18632/oncotarget.27593. PMID: 32595827; PMCID: PMC7299530.
- Kasprzak A. Insulin-Like Growth Factor 1 (IGF-1) Signaling in Glucose Metabolism in Colorectal Cancer. *Int J Mol Sci*. 2021; 22 (12): 6434. DOI: 10.3390/ijms22126434. PMID: 34208601; PMCID: PMC8234711.
- Li J, Huang L, Zhao H, Yan Y, Lu J. The Role of Interleukins in Colorectal Cancer. *Int J Biol Sci*. 2020; 16 (13): 2323–39. DOI: 10.7150/ijbs.46651. PMID: 32760201; PMCID: PMC7378639.
- Ueno H, Hase K, Hashiguchi Y, Shimazaki H, Tanaka M, Miyake O, et al. Site-specific tumor grading system in colorectal cancer: Multicenter pathologic review of the value of quantifying poorly differentiated clusters. *Am J Surg Pathol*. 2014; 38: 197–204. Available from: <https://doi.org/10.1097/pas.000000000000113/>
- Yuan H, Dong Q, Zheng BA, Hu X, Xu J-B, Tu S. Lymphovascular invasion is a high risk factor for stage I/II colorectal cancer: A systematic review and meta-analysis. *Oncotarget*. 2017; 8: 46565–79. Available from: <https://doi.org/10.18632/oncotarget.15425>.
- Al-Sukhni E, Attwood K, Gabriel EM, LeVea CM, Kanehira K, Nurkin SJ. Lymphovascular and perineural invasion are associated with poor prognostic features and outcomes in colorectal cancer: A retrospective cohort study. *Int J Surg*. 2017; 37: 42–49. Available from: <https://doi.org/10.1016/j.ijsu.2016.08.528>.
- Harris EI, Lewin DN, Wang HL, Lauwers GY, Srivastava A, Shyr Y, et al. Lymphovascular invasion in colorectal cancer: An interobserver variability study. *Am J Surg Pathol*. 2008; 32: 1816.
- Liebig C, Ayala G, Wilks JA, Berger DH, Albo D. Perineural invasion in cancer: A review of the literature. *Cancer: Inter-discip. Int J Am Cancer Soc*. 2009; 115: 3379–91.
- (CAP) CoAP. Protocol for the Examination of Specimens from Patients with Primary Carcinoma of the Colon and Rectum; 2020. Available online: <https://documents.cap.org/protocols/cp-gilower-colonrectum-resection-20-4100.pdf> (accessed on 15 August 2021).
- Berger AC, Sigurdson ER, LeVoyer T, Hanlon A, Mayer RJ, Macdonald JS, et al. Colon cancer survival is associated with decreasing ratio of metastatic to examined lymph nodes. *J Clin Oncol Off J Am Soc Clin Oncol*. 2005; 23: 8706–12. Available from: <https://doi.org/10.1200/jco.2005.02.8852>.
- Wang CY, Shao C, McDonald AC, Amonkar MM, Zhou W, Bortnichak EA, et al. Evaluation and Comparison of Real-World Databases for Conducting Research in Patients With Colorectal Cancer. *JCO Clin Cancer Inform*. 2023; 7: e2200184. DOI: 10.1200/CCI.22.00184. PMID: 37437227.

Литература

- Каприн А. Д., Старинский В. В., Шахзадова А.О. Состояние онкологической помощи населению России в 2021 году. Российский Центр информационных технологий и эпидемиологических исследований в области онкологии. Москва, 2022.
- Steyerberg EW, Moons KGM, van der Windt DA, et al. Prognosis Research Strategy (PROGRESS) 3: prognostic model research. *PLoS medicine*. 2013; 10: e1001381.
- Brenner H, Chen C. The colorectal cancer epidemic: challenges and opportunities for primary, secondary and tertiary prevention. *Br J Cancer*. 2018; 119 (7): 785–92. DOI: 10.1038/s41416-018-0264-x. Epub 2018 Oct 4. PMID: 30287914; PMCID: PMC6189126.
- Lin XT, Wu QN, Qin S, Fan DJ, Lv MY, Chen X, et al. Identification of an Autophagy-Related Gene Signature for the Prediction of Prognosis in Early-Stage Colorectal Cancer. *Front Genet*. 2021; 12: 755789. DOI: 10.3389/fgene.2021.755789. PMID: 34899841; PMCID: PMC8657766.
- Mori K, Toiyama Y, Okugawa Y, Ichikawa T, Nagano Y, Oki S, et al. Preoperative heat shock protein 47 levels identify colorectal cancer patients with lymph node metastasis and poor prognosis. *Oncol Lett*. 2020; 20 (6): 333. DOI: 10.3892/ol.2020.12196. Epub 2020 Oct 7. PMID: 33123244; PMCID: PMC7583735.
- Боженко В. К., Станоевич У. С., Троценко И. Д. и др. Сравнение экспрессии мРНК матричных металлопротеиназ в морфологически нормальной, неопластической и метастатической тканях толстого кишечника и в биоптатах здоровых доноров. *Биомедицинская химия*. 2018; 64 (1): 46–52. DOI: 10.18097/PBMC20186401046.
- French CL, Ye F, Revetta F, et al. Linking patient outcome to high

- throughput protein expression data identifies novel regulators of colorectal adenocarcinoma aggressiveness. *F1000Res*. 2015; 4: 99. DOI: 10.12688/f1000research.6388.1.
8. Fang Y, Yu H, Liang X, Xu J, Cai X. Chk1-induced CCNB1 overexpression promotes cell proliferation and tumor growth in human colorectal cancer. *Cancer Biol Ther*. 2014; 15 (9): 1268–79. DOI: 10.4161/cbt.29691. Epub 2014 Jun 27. PMID: 24971465; PMCID: PMC4128869.
 9. Hu B, Song X, Ding W, Wang H, Cai H, Huang Z. Expression and Clinical Significance of Ki67 and SOX2 in Colorectal Cancer. *J Healthc Eng*. 2023; 2023: 3783631. DOI: 10.1155/2023/3783631. PMID: 37457497; PMCID: PMC10348847.
 10. Vermehren-Schmaedick A, Mhawech-Fauceglia P, Park BS, Pejovic T, Luoh SW. The prognostic significance of GRB7 protein expression and localization in human breast and ovarian cancers. *Oncotarget*. 2020; 11 (24): 2273–89. DOI: 10.18632/oncotarget.27593. PMID: 32595827; PMCID: PMC7299530.
 11. Kasprzak A. Insulin-Like Growth Factor 1 (IGF-1) Signaling in Glucose Metabolism in Colorectal Cancer. *Int J Mol Sci*. 2021; 22 (12): 6434. DOI: 10.3390/ijms22126434. PMID: 34208601; PMCID: PMC8234711.
 12. Li J, Huang L, Zhao H, Yan Y, Lu J. The Role of Interleukins in Colorectal Cancer. *Int J Biol Sci*. 2020; 16 (13): 2323–39. DOI: 10.7150/ijbs.46651. PMID: 32760201; PMCID: PMC7378639.
 13. Ueno H, Hase K, Hashiguchi Y, Shimazaki H, Tanaka M, Miyake O, et al. Site-specific tumor grading system in colorectal cancer: Multicenter pathologic review of the value of quantifying poorly differentiated clusters. *Am J Surg Pathol*. 2014; 38: 197–204. Available from: <https://doi.org/10.1097/pas.000000000000113>
 14. Yuan H, Dong Q, Zheng BA, Hu X, Xu J-B, Tu S. Lymphovascular invasion is a high risk factor for stage I/II colorectal cancer: A systematic review and meta-analysis. *Oncotarget*. 2017; 8: 46565–79. Available from: <https://doi.org/10.18632/oncotarget.15425>.
 15. Al-Sukhni E, Attwood K, Gabriel EM, LeVea CM, Kanehira K, Nurkin SJ. Lymphovascular and perineural invasion are associated with poor prognostic features and outcomes in colorectal cancer: A retrospective cohort study. *Int J Surg*. 2017; 37: 42–49. Available from: <https://doi.org/10.1016/j.ijso.2016.08.528>.
 16. Harris EI, Lewin DN, Wang HL, Lauwers GY, Srivastava A, Shyr Y, et al. Lymphovascular invasion in colorectal cancer: An interobserver variability study. *Am J Surg Pathol*. 2008; 32: 1816.
 17. Liebig C, Ayala G, Wilks JA, Berger DH, Albo D. Perineural invasion in cancer: A review of the literature. *Cancer: Inter-discip. Int J Am Cancer Soc*. 2009; 115: 3379–91.
 18. (CAP) CoAP. Protocol for the Examination of Specimens from Patients with Primary Carcinoma of the Colon and Rectum; 2020. Available online: <https://documents.cap.org/protocols/cp-gilower-colonrectum-resection-20-4100.pdf> (accessed on 15 August 2021).
 19. Berger AC, Sigurdson ER, LeVoyer T, Hanlon A, Mayer RJ, Macdonald JS, et al. Colon cancer survival is associated with decreasing ratio of metastatic to examined lymph nodes. *J Clin Oncol Off J Am Soc Clin Oncol*. 2005; 23: 8706–12. Available from: <https://doi.org/10.1200/jco.2005.02.8852>.
 20. Wang CY, Shao C, McDonald AC, Amonkar MM, Zhou W, Bortnichak EA, et al. Evaluation and Comparison of Real-World Databases for Conducting Research in Patients With Colorectal Cancer. *JCO Clin Cancer Inform*. 2023; 7: e2200184. DOI: 10.1200/CCI.22.00184. PMID: 37437227.

METHODS FOR COMBINATION TREATMENT OF METASTATIC UVEAL MELANOMA

Kolomiets KV [✉], Ponomareva ES, Posypina YaR, Mihailov II, Mandzhiiev CB, Povetkina EV, Tuguz RR, Bulgakov SM, Repunova VI

Rostov State Medical University, Rostov-on-Don, Russia

Uveal melanoma (UM) is a rare primary malignant tumor originating from uveal melanocytes (choroid (90%), ciliary body (6%), iris (4%)) of the eye. According to the aggregate data, the tumor incidence is 5.2 cases per 1 million population. In Russia this value varies between 6.23–8 cases per 1 million adult population across the regions. UM most often spreads to the liver (89–93%). The clinical case of using transarterial chemoembolization (carboplatin) in combination with immunotherapy (nivolumab + ipilimumab) in patients with metastatic liver disease from UM is provided. The disease control within 12 months has been achieved, which, in turn, demonstrates the possibility and efficacy of multidisciplinary approach.

Keywords: uveal melanoma, transarterial chemoembolization, immunotherapy, carboplatin, metastatic liver disease

Author contribution: Kolomiets KV — manuscript writing, editing; Ponomareva ES, Posypina YaR — manuscript writing, literature review, data analysis; Mihailov II, Mandzhiiev CB — manuscript writing, literature review, data acquisition; Bulgakov SM, Repunova VI — manuscript writing, literature review, concept and design; Povetkina EV, Tuguz RR — manuscript writing, literature review, manuscript revision.

Compliance with ethical standards: the patient submitted the informed consent to publication of the anonymized personal medical data.

✉ **Correspondence should be addressed:** Karina V. Kolomiets
Krasnoarmeiskaya, 198, Novocherkassk, 346400, Russia; karina_kolomiets_99@mail.ru

Received: 22.10.2023 **Accepted:** 29.11.2023 **Published online:** 22.12.2023

DOI: 10.24075/brsmu.2023.051

КОМБИНИРОВАННЫЕ МЕТОДЫ ЛЕЧЕНИЯ МЕТАСТАТИЧЕСКОЙ УВЕАЛЬНОЙ МЕЛАНОМЫ

К. В. Коломиец [✉], Э. С. Пономарева, Я. Р. Посыпина, И. И. Михайлов, Ч. Б. Манджиев, Е. В. Поветкина, Р. Р. Тугуз, С. М. Булгаков, В. И. Репунова

Ростовский государственный медицинский университет Министерства здравоохранения Российской Федерации, Ростов-на-Дону, Россия

Уvealная меланомa (УМ) — редкая первичная злокачественная опухоль, формирующаяся из меланоцитов увеального тракта (хориоидеи (90%), цилиарного тела (6%), радужной оболочки (4%)) глазного яблока. По совокупным данным, уровень заболеваемости составляет 5,2 случая на 1 млн населения. В России этот показатель в разных регионах варьирует от 6,23 до 8 случаев на 1 млн взрослого населения. Наиболее часто (89–93%) УМ метастазирует в печень. Представлен клинический случай использования методики трансартериальной химиэмболизации (карбоплатин) в комбинации с иммунотерапией (ниволумаб + ипилимумаб) у пациента с метастатическим поражением печени увеальной меланомой. Был достигнут контроль заболевания на протяжении 12 месяцев, что, в свою очередь, демонстрирует возможность и эффективность мультидисциплинарного подхода.

Ключевые слова: увеальная меланомa, трансартериальная химиэмболизация, иммунотерапия, карбоплатин, метастатическое поражение печени

Вклад авторов: К. В. Коломиец — написание статьи, редактирование; Э. С. Пономарева, Я. Р. Посыпина — написание статьи, обзор литературы, анализ данных; И. И. Михайлов, Ч. Б. Манджиев — написание статьи, обзор литературы, сбор данных; С.М. Булгаков, В. И. Репунова — написание статьи, обзор литературы, концепция и дизайн; Е. В. Поветкина, Р. Р. Тугуз — написание статьи, обзор литературы, переработка статьи.

Соблюдение этических стандартов: пациент подписал добровольное информированное согласие на публикацию персональной медицинской информации в обезличенной форме.

✉ **Для корреспонденции:** Карина Викторовна Коломиец
ул. Красноармейская, д. 198, г. Новочеркасск, 346400, Россия; karina_kolomiets_99@mail.ru

Статья получена: 22.10.2023 **Статья принята к печати:** 29.11.2023 **Опубликована онлайн:** 22.12.2023

DOI: 10.24075/vrgmu.2023.051

Uveal melanoma (UM) is a rare primary malignant tumor originating from uveal melanocytes (choroid (90%), ciliary body (6%), iris (4%)) of the eye. According to the aggregate data, the incidence level is 5.2 cases per 1 million population. In Russia this value varies between 6.23–8 cases per 1 million adult population across the regions. The average age at diagnosis is 62 years, while the peak age range is 70–79 years [1, 2]. However, despite the achievements in treatment of primary tumor and radical nature of surgery, the majority of patients develop distant metastases. Metastatic disease is found in less than 2% of patients when performing initial diagnosis of the eye tumor. Liver is the main target organ for metastasis in 89–93% of cases. Such tropism of UM toward hepatocytes is explained by the fact that there are three types of receptors hyperexpressed in the primary tumor on the cell surface: IGF-1R (insulin-like growth factor receptor), cMET (HGFR — hepatocyte growth factor receptor) and CXCR4 (chemokine receptor). Their main

function is to control cell migration, cancer cell invasion and proliferation [3, 4]. The median overall survival (OS) without surgery in this group of patients reaches 2–3 months.

Immunotherapy, transarterial chemoembolization (TACE), immunoembolization, radioembolization, thermal ablation, and isolated chemoperfusion are the methods most commonly used for treatment of metastatic liver disease from UM.

The use of TACE to control growth of metastatic liver melanoma was first reported in 1986. In 1986, the use of cisplatin and polyvinyl alcohol particles during chemoembolization to control growth of UM metastases in the liver was started [5].

To date, a total of 19 studies focused on TACE efficacy in patients with metastatic liver disease from UM have been published, among them 13 retrospective studies, five prospective studies, and one randomized study. The median overall survival (OS) varies between 5.2 and 23 months. Cisplatin was the most commonly used drug. Other chemotherapy agents were

as follows: vinblastine, dacarbazine, vincristine, dactinomycin, carmustine, mitomycin C, doxorubicin, irinotecan, paclitaxel, carboplatin, and melphalan [1, 2].

Despite the achievements in treatment of metastatic melanoma of the skin, UM still shows poor sensitivity to drug therapy, including advanced immunotherapy with immune checkpoint inhibitors, target therapy and chemotherapy. Nevertheless, despite lower efficacy of combination immunotherapy for UM relative to melanoma of the skin, its positive role was noted in the recent years. According to the data provided by different authors, despite the 1-year survival rate within 30–50%, the combination of ipilimumab and nivolumab is considered to be the most effective among all other treatment options showing low efficacy.

A retrospective analysis of the treatment outcomes of eight patients with metastatic UM was conducted in 2019. The patients received combination therapy with ipilimumab and nivolumab along with TACE followed by nivolumab maintenance therapy. In 5 patients with stage M1a disease out of 8, life expectancy of 12–24 months was achieved. Life expectancy of three patients with stage M1b disease was 7–30 months. Partial response was achieved in two patients, stabilization of disease in four patients; disease progression was observed in two patients. The median OS (time from the date of initial immunotherapy administration to the date of death/last follow-up) of eight patients calculated using the Kaplan–Meier method was 14.2 months [6, 7].

Assessment of lactate dehydrogenase (LDH) levels showed that the complete response rate of patients with LDH levels above normal was very low: complete response was observed in only one patient out of 105. LDH levels were excluded from the list of the complete response prognostic factors to be considered, when PD-L1 and tumor burden were taken into account. The latter, as is known, represents an important factor when considering the likelihood of positive response and long-term survival associated with the use of such drug, as pembrolizumab (antibody that inhibits PD-L1) [8].

The case study was aimed to demonstrate the possibility and efficacy of multidisciplinary approach: using TACE (carboplatin) in combination with immunotherapy in patient with metastatic liver disease from UM.

Clinical case

Patient P., 62 years old, contacted the clinic in February 2023. Ophthalmic examination performed in February 2019 revealed a left eye ciliochoroidal melanoma sized 13 x 14 mm on ultrasound. Given the neoplasm size and the lack of media transparency, eye removal surgery was recommended. Enucleation of the left eye was performed on July 7, 2020 at the City Emergency Hospital (Volgodonsk).

Findings of the surgical specimen histopathological examination, August 27, 2020: UM composed of nevus-like and spindle cells. Scleral tumor invasion in certain areas. Tumor containing large amounts of melanin. High mitotic count, vascular invasion.

Then the patient underwent scheduled follow-up examinations every 3 months, with which together with the two-fold increase in the interval between the last instrumental examinations (6 months) 17 month later a mass in the right lobe of the liver (S6–S7) up to 8 cm in diameter, which had not been seen before, was found after enucleation of the left eye. Two weeks later abdominal computed tomography (abdominal CT) revealed one more mass up to 1.5 cm in diameter in S8 of the liver. This suggests that it is reasonable to perform appropriate diagnostic imaging in all patients:

- Abdominal MRI (magnetic resonance imaging), August 21, 2020: MR features of diffuse changes in the pancreas;

- Laboratory tests, November 23, 2020 within the age norm, except for LDH level elevation to 458 U/L (reference range: 135–225 U/L).

November 18, 2020 — spiral CT (spiral computed tomography) of the abdomen and retroperitoneal space that revealed diffuse changes in the liver tissue and the pancreas, simple cyst on the right kidney;

- Laboratory tests, November 29, 2021 within the age norm, LDH 223.0 U/L, ESR (erythrocyte sedimentation rate) 48 mm.

Abdominal spiral CT, November 19, 2021: left adrenal mass sized 1.7 x 1.4 cm could be seen, probably due to adenoma.

abdominal MRI, November 18, 2021 — summary: diffuse changes in the pancreas, cyst on the right kidney, left adrenal adenoma;

- Laboratory tests, May 13, 2022 within the age norm, LDH 277.0 U/L, ESR 42 mm.

- Abdominal MRI, May 19, 2022: MR features of diffuse changes in the liver and pancreatic tissue. Left adrenal mass lesion (adenoma, incidentaloma).

Abdominal CT, November 25, 2022, summary: masses in the right lobe of the liver (not previously seen).

Contrast-enhanced abdominal CT, December 13, 2022: CT features of metastasis masses in the liver right lobe (S7–S6 — low density heterogeneous mass without clear margins sized 78 x 47 x 75 mm showing contrast uptake heterogeneity; S8 — low density lesion 14 mm in diameter (not previously seen) showing low contrast uptake).

Histological examination protocol of December 19, 2022, summary: liver fragment showing the presence of a solid tumor with necrotic foci consisting of atypical epithelioid cells with hyperchromatic nuclei and eosinophilic cytoplasm without clear margins; some cells contained the pigment melanin. Liver trephine biopsy showed metastatic melanoma.

The following diagnosis was established: secondary liver cancer; stage III A T3bN0M0 left eye uveal melanoma, postoperative condition (July 2020), progression (November 2022), (HEP), clinical group 2.

Status localis on ophthalmic examination: left-sided anophthalmos, recurrent herpes simplex keratitis (epithelial corneal dystrophy), immature mixed senile cataract, pigmented choroidal nevus in the right eye.

During the scheduled chemotherapist consultation (December 29, 2022) it was recommended to prescribe the following immunotherapy (IT) regimen in case of satisfactory blood cell counts and no somatic contraindications considering the disease dynamics: nivolumab 3 mg/kg on day 1 + ipilimumab 1 mg/kg on day 1; 21 day cycle.

The patient contacted the clinic of the Rostov State Medical University after one course of IT, in February 2023. Given liver involvement, medical history and instrumental assessment data, as well as tumor expansion, it was decided to perform transarterial chemoembolization (TACE) on the case conference.

Surgical intervention specifications, February 24, 2023: the right radial artery puncture using the common site was performed in the supine patient in aseptic environment of the cath lab after the appropriate surgical site conditioning (18G angiographic needle). The Seldinger technique of catheter placement was used (5F introducer, 11 cm). A 5F HH1 catheter (125 cm) was sequentially introduced into the right brachial artery, axillary artery, brachiocephalic trunk, aortic arch, thoracic aorta through the O35" hydrophilic sheath (180 cm). Sheath was removed, and aortography was performed: the celiac

trunk arised at the level of the L1 vertebral body. Selective catheterization of the celiac trunk orifice was performed: cranial approach, non-dilated and tortuous splenic artery, no hypertrophy of gastric branches (anastomoses). The common hepatic artery arised from the celiac trunk in a normal way, division into the left and right hepatic arteries, gastroduodenal artery were normal. The catheter sheath was replaced. The right hepatic artery supplying the tumor foci was selectively catheterized using the H1 catheter (125 cm) with the 0.014" Asahi Chikai microsheat (ASAHI INTECC CO., LTD; Japan) (165 cm). TACE of the arteries supplying the foci was performed (lipiodol 20 mL + carboplatin 450 mg). Artery embolization was performed using the Cutanplast hemostatic sponge (Mascia Brunelli; Italy). The follow-up angiography revealed a prominent contrast uptake reduction along the right hepatic artery segmental branches supplying the tumor foci. No signs of nontarget embolization were revealed. Catheter was inserted into the aorta; the follow-up angiography showed that the right and left hepatic, gastroduodenal, superior mesenteric arteries were not compromised. The instruments were sequentially removed. Introducer was removed, compression hemostasis was provided (8 min, stable, aseptic pressure dressing).

To prevent thromboembolic complications, supportive drug therapy was prescribed after surgery that included anticoagulants and nonsteroidal anti-inflammatory drugs as analgesics, since post-embolization syndrome (PES) with the duration between two days and three weeks was observed in many patients (90–100%) after TACE. It is believed that PES is mediated by inflammatory cytokines released due to liver necrosis caused by embolization or chemotherapy drugs. The major PES manifestations are as follows: fever, pain in the right hypochondriac/epigastric region, nausea, vomiting, liver failure worsening and, as a result, transaminase level increase. However, fortunately, PES can be successfully relieved by symptomatic drug therapy.

The patient was discharged on day 8 after surgery; at the time of discharge he considered his condition to be satisfactory despite the size of metastatic foci; a low-grade fever was reported within three days after TACE, along with moderate pain in the right hypochondriac and epigastric regions.

Then the patient underwent IT courses (3 courses) at the place of residence, and the follow-up examination revealed improvement.

The contrast-enhanced abdominal CT performed on April 24, 2023, revealed CT features of metastasis masses in the liver right lobe (S7–S6 — low density heterogeneous mass without clear margins sized 54 × 43 × 61 mm showing contrast uptake heterogeneity; S8 – low density lesion 9 mm in diameter showing low contrast uptake). Comparison with the abdominal CT scan of November 25, 2022 revealed improvement. The TACE efficacy was assessed one month later based on CT/MRI with intravenous contrast using the RECIST 1.1 (2009) (Response evaluation criteria in solid tumours) criteria, according to which partial response (regression) was achieved: > 30% sum of the largest sizes (long axes) of lesions.

On May 14, 2023 (3 months later), the patient was admitted again for the second TACE procedure, because of the previously achieved partial response to combination therapy. He underwent four IT courses. Given liver involvement, expansion and improvement, TACE was performed: lipiodol 20 mL + carboplatin 450 mg. Artery embolization was performed using the Cutanplast hemostatic sponge. Supportive drug therapy was prescribed after surgery. The patient was discharged on day 7 after surgery; at the time of discharge he considered his condition to be satisfactory and reported no fever or subcostal pain.

According to the National Cancer Institute Common Terminology Criteria for Adverse Events (NCI-CTCAE), in which the adverse event severity varies between 0 (normal range) and 4 and 5 (disability and death, respectively), grade 1 fever was observed. Furthermore, after TACE, moderate pain in the right hypochondriac and epigastric regions (grade 1) was reported during the early postoperative period.

To date, the follow-up period is 12 month with no signs of disease progression. The patient's condition is satisfactory. He leads an active life and undergoes the courses of systemic IT since June 2023 until now (November 2023) according to the maintenance phase regimen: nivolumab 3 mg/kg by intravenous infusion once every 14 days.

Clinical case discussion

TACE for UM liver metastases using carboplatin and lipiodol, viscous ethiodized oil that is selectively delivered through a catheter to induce ischemic tumor necrosis by blocking arterial inflow into the tumor (while healthy liver parenchyma is preserved due to dual blood supply from the portal vein and hepatic artery), in combination with the gradual release of chemotherapy agent in the area of metastasis and its selective cytostatic effect with minimal systemic side effects. It is obvious that more than 70% patients with malignant hepatic tumors require palliative chemotherapy. However, systemic chemotherapy efficacy in inoperable cancer does not exceed 20–30% with survival of 3–4 months even in case of using several drugs. Apparently, when the chemotherapy drugs are administered intravenously, the therapeutic concentration is achieved only for a short while and does not have a necessary effect on the tumor cells, while prominent impairment of the liver detoxication function limits the use of high anticancer drug doses. Immunotherapy significantly improved the prognosis of patients with melanoma of the skin, but no such clinical effect is observed in patients with metastatic UM. However, the efficacy of combination immunotherapy is higher than that of other drug treatment options (anti-PD-1 monotherapy, chemotherapy, etc.) used for UM. Partial hepatectomy can be considered in patients with good liver function only, to avoid potential decompensation of liver function. Systemic chemotherapy is also of limited use in patients with unresectable liver metastases. That is why alternative treatment methods, such as radiofrequency ablation and microwave ablation, are recommended for such patients. When neither surgery, nor local ablation techniques succeed, TACE is an option for local tumor control. This treatment gave promising results in patients with inoperable liver metastases. Due to the combination of direct chemotherapeutic use and a vascular occlusion technique, cytostatic substances are in contact with the target malignant cells over a longer time.

One of the TACE shortcomings is represented by formation of hypoxic microenvironment that enhances neoangiogenesis and can thereby contribute to early progression. It is well known that angiogenesis is a key factor of tumor growth and metastasis in many cancer types, including metastatic liver cancer [9].

CONCLUSION

The features of the UM clinical course compared to the skin form of the disease include longer time to progression and predominance of liver metastasis; molecular genetic features are also different (the major molecular abnormalities typical for melanoma of the skin (BRAF, NRAS mutations) are not involved in induction of the disease processes associated with UM).

Based on the available data, the combined use of ipilimumab and nivolumab represents one of the main treatment regimens for this group of patients. The new combination treatment methods involving TACE and immunotherapy (nivolumab + ipilimumab in the reported case study) used to treat metastatic liver disease from UM made it possible to control the disease course throughout 12 months. The patient demonstrated improvement in the form of reduced metastatic foci size, which was nevertheless encouraging, since minimal median OS of this category of patients associated with TACE and no surgical treatment was exceeded by 2 and 4 times, respectively. However, further research is needed to determine optimal therapy in order to achieve maximum efficacy and minimize side effects.

Prospective randomized studies will help determine safety and efficacy of the combination locoregional and systemic therapy for metastatic UM. TACE is an alternative treatment method for patients with unresectable liver metastases allowing for selective delivery of high chemotherapy agent doses to the tumor bed and embolize the target vessels with minimum systemic bioavailability, which minimizes systemic side effects, thereby preserving the surrounding liver tissue. The lack of effective treatment methods for metastatic liver disease from UM forces us to seek for new approaches to treatment of this disorder. In this regard, today, it is necessary to optimize treatment based on the available methods, such as systemic (chemotherapy/immunotherapy) and local (TACE and other) methods.

References

- Carle X, Gastaud L, Salleron J, Tardy MP, Caujolle JP, Thyss A, et al. Optimizing the treatment of liver metastases from uveal melanomas with transarterial chemoembolization using melphalan and calibrated microspheres. *Bull Cancer*. 2020; 107 (12): 1274–83. DOI: 10.1016/j.bulcan.2020.09.010.
- Tao YX, Li HW, Luo JT, Li Y, Wei WB. Regional chemotherapy for uveal melanoma liver metastases. *Int J Ophthalmol*. 2023; 16 (2): 293–300. DOI: 10.18240/ijo.2023.02.18.
- Aronow ME, Topham AK, Singh AD. Uveal Melanoma: 5-Year Update on Incidence, Treatment, and Survival (SEER 1973-2013). *Ocul Oncol Pathol*. 2018; 4 (3): 145–51. DOI: 10.1159/000480640.
- Gonsalves CF, Adamo RD, Eschelmann DJ. Locoregional therapies for the treatment of uveal melanoma hepatic metastases. *Semin Intervent Radiol*. 2020; 37 (5): 508–17. DOI: 10.1055/s-0040-1720948.
- Sajan A, Fordyce S, Sideris A, Liou C, Toor Z, Filtes J, et al. Minimally invasive treatment options for hepatic uveal melanoma metastases. *Diagnostics (Basel)*. 2023; 13 (11): 1836. DOI: 10.3390/diagnostics13111836.
- Karivedu V, Eldessouki I, Taftaf A, Zhu Z, Makramalla A, Karim NA. Nivolumab and Ipilimumab in the treatment of metastatic uveal melanoma: a single-center experience. *Case Rep Oncol Med*. 2019; 2019: 3560640. DOI: 10.1155/2019/3560640.
- Nazarova VV, Orlova KV, Utyashev IA, Yarovoy AA, Yarovaya VA, Markina IG, et al. Combined Immunotherapy for Metastatic Uveal Melanoma. Single Centre Experience. *Effective Pharmacotherapy*. 2023; 19 (16): 64–71. Russian.
- Weber JS. Immunotherapy complete response data suggest metastatic melanoma cures. 2018 Aug 09. Available from: <https://www.medscape.com/viewarticle/900259?form=fpf>.
- Van Cutsem E, Paccard C, Chiron M, Taberero J. Impact of Prior Bevacizumab Treatment on VEGF-A and PlGF Levels and Outcome Following Second-Line Aflibercept Treatment: Biomarker Post Hoc Analysis of the VELOUR Trial. *Clin Cancer Res*. 2020; 26 (3): 717–25. DOI: 10.1158/1078-0432.CCR-19-1985.

Литература

- Carle X, Gastaud L, Salleron J, Tardy MP, Caujolle JP, Thyss A, et al. Optimizing the treatment of liver metastases from uveal melanomas with transarterial chemoembolization using melphalan and calibrated microspheres. *Bull Cancer*. 2020; 107 (12): 1274–83. DOI: 10.1016/j.bulcan.2020.09.010.
- Tao YX, Li HW, Luo JT, Li Y, Wei WB. Regional chemotherapy for uveal melanoma liver metastases. *Int J Ophthalmol*. 2023; 16 (2): 293–300. DOI: 10.18240/ijo.2023.02.18.
- Aronow ME, Topham AK, Singh AD. Uveal Melanoma: 5-Year Update on Incidence, Treatment, and Survival (SEER 1973-2013). *Ocul Oncol Pathol*. 2018; 4 (3): 145–51. DOI: 10.1159/000480640.
- Gonsalves CF, Adamo RD, Eschelmann DJ. Locoregional therapies for the treatment of uveal melanoma hepatic metastases. *Semin Intervent Radiol*. 2020; 37 (5): 508–17. DOI: 10.1055/s-0040-1720948.
- Sajan A, Fordyce S, Sideris A, Liou C, Toor Z, Filtes J, et al. Minimally invasive treatment options for hepatic uveal melanoma metastases. *Diagnostics (Basel)*. 2023; 13 (11): 1836. DOI: 10.3390/diagnostics13111836.
- Karivedu V, Eldessouki I, Taftaf A, Zhu Z, Makramalla A, Karim NA. Nivolumab and Ipilimumab in the treatment of metastatic uveal melanoma: a single-center experience. *Case Rep Oncol Med*. 2019; 2019: 3560640. DOI: 10.1155/2019/3560640.
- Назарова В. В., Орлова К. В., Утяшев И. А., Яровой А. А., Яровая В. А., Маркина И. Г. и др. Комбинированная иммунотерапия при метастатической увеальной меланоме. Опыт одного центра. Эффективная фармакотерапия. 2023; 19 (16): 64–71.
- Weber JS. Immunotherapy complete response data suggest metastatic melanoma cures. 2018 Aug 09. Available from: <https://www.medscape.com/viewarticle/900259?form=fpf>.
- Van Cutsem E, Paccard C, Chiron M, Taberero J. Impact of Prior Bevacizumab Treatment on VEGF-A and PlGF Levels and Outcome Following Second-Line Aflibercept Treatment: Biomarker Post Hoc Analysis of the VELOUR Trial. *Clin Cancer Res*. 2020; 26 (3): 717–25. DOI: 10.1158/1078-0432.CCR-19-1985.

EFFICACY OF THE JAWBONE DEFECT ELIMINATION

Poryadin GV, Eremin DA, Khelminskaya NM , Kravets VI, Zhitareva IV, Posadskaya AV, Krasnov NM, Shen PA, Gureshidze MA

Pirogov Russian National Research Medical University, Moscow, Russia

The regenerative medicine methods are being actively developed both in Russia and abroad due to relevance of this direction, especially in the field of the jaw osteoplasty. Autologous, allogeneic and xenoplastic materials, as well as the calcium phosphate ceramics synthetic preparations are conventionally used to normalize and stimulate osteogenesis, however, the treatment outcomes are not always unequivocal. The study was aimed to substantiate the use of the biocomplex consisting of plasma rich in growth factors (PRGF) and xenoplastic material to improve the jawbone osteogenesis efficacy. The study involved 136 patients (105 females and 31 males aged 21–67) divided into four groups based on the method of bone defect restoration. In group 1, no osteoplastic material was used; in group 2, osteoplasty involved the use of the PRGF fibrin gel; in group 3, the Osteobiol Gen-Os material was used; in group 4, osteoplasty involved using the combination of the Osteobiol Gen-Os material and plasma rich in growth factors (PRGF). Computed tomography and digital densitometry were performed before surgery and 3, 6, 12 months after it to assess the dynamics of osteogenesis. A year later restoration of the lost bone tissue volume was reported in 100% of patients in group 4, 70.27% of patients in group 3, 43.47% of patients in group 2, 37.5% of patients in group 1; Fisher's exact test revealed significant differences in the osteoplasty outcomes in groups 3 and 4 ($p = 0.00002$). There were significant differences in bone density between patients of groups 1 and 2 twelve months after surgery ($p = 0.044$), between patient of groups 3 and 4 three ($p = 0.004$), six ($p = 0.0001$) and 12 ($p = 0.0001$) months after surgery. The findings show that the method proposed is effective.

Keywords: jaw defect, osteoplasty, plasma rich in growth factors, xenograft, osteostimulation, osteoconduction

Author contribution: Kravets VI, Posadskaya AV, Krasnov NM — study concept and design; Shen PA, Gureshidze MA, Krasnov NM — patient follow-up and data processing; Zhitareva IV — statistical processing; Krasnov NM — manuscript draft writing; Poryadin GV, Eremin DA, Khelminskaya NM — editing.

Compliance with ethical standards: the study was approved by the Ethics Committee of the Pirogov Russian National Research Medical University (protocol № 131 of 27 January 2014), the patients submitted the informed consent to study participation.

✉ **Correspondence should be addressed:** Natalia M. Khelminskaya
Ostovitianov, 1, Moscow, 117997, Russia; Khelminskaya@mail.ru

Received: 02.10.2023 **Accepted:** 17.10.2023 **Published online:** 21.11.2023

DOI: 10.24075/brsmu.2023.044

ЭФФЕКТИВНОСТЬ УСТРАНЕНИЯ КОСТНЫХ ДЕФЕКТОВ ЧЕЛЮСТЕЙ

Г. В. Порядин, Д. А. Еремин, Н. М. Хелминская , В. И. Кравец, И. В. Житарева, А. В. Посадская, Н. М. Краснов, П. А. Шень, М. А. Гурешидзе

Российский национальный исследовательский медицинский университет имени Н. И. Пирогова, Москва, Россия

Методы регенеративной медицины в России и за рубежом активно развиваются в связи с актуальностью этого направления, особенно в вопросах костной пластики челюстей. Для нормализации и стимуляции остеогенеза традиционно применяют ауто-, алло- и ксенопластические материалы, а также синтетические препараты на основе кальций-фосфатной керамики, но результаты лечения не всегда однозначны. Целью исследования было обобщить применение биокомплекса плазмы крови, богатой факторами роста PRGF, и ксенопластического материала для повышения эффективности остеогенеза костных дефектов челюстей. В исследовании участвовало 136 пациентов (105 женщин и 31 мужчина, в возрасте 21–67 лет), в зависимости от метода замещения костного дефекта разделенных на четыре группы. В 1-й группе остеопластические материалы не применяли, во 2-й пластику проводили фибриновым гелем PRGF, в 3-й — материалом Osteobiol Gen-Os, в 4-й — материалом Osteobiol Gen-Os совместно с препаратом плазмы, богатой факторами роста PRGF. Для динамической оценки процесса остеогенеза проводили компьютерную томографию с цифровой денситометрией до операции и через 3, 6, 12 месяцев после нее. Через год восстановление объема костной ткани в 4-й группе зафиксировано у 100% пациентов, в 3-й — у 70,27%, во 2-й — у 43,47%, а в 1-й у — 37,5%, точный критерий Фишера выявил статистически значимые различия результатов костной пластики в 3-й и 4-й группах ($p = 0,00002$). Статистически значимо различаются показатели плотности костной ткани у пациентов 1-й и 2-й групп через 12 месяцев после операции ($p = 0,044$), у 3-й и 4-й групп — через 3 ($p = 0,004$), 6 ($p = 0,0001$) и 12 ($p = 0,0001$). Полученные результаты говорят об эффективности применения предложенной нами методики.

Ключевые слова: дефект челюсти, костная пластика, плазма, богатая факторами роста, ксенографт, остестимуляция, остеокондукция

Вклад авторов: В. И. Кравец, А. В. Посадская, Н. М. Краснов — концепция и дизайн исследования; П. А. Шень, М. А. Гурешидзе, Н. М. Краснов — курация пациентов и обработка данных; И. В. Житарева — статистическая обработка; Н. М. Краснов — подготовка черновика рукописи; Г. В. Порядин, Д. А. Еремин, Н. М. Хелминская — редактирование.

Соблюдение этических стандартов: исследование одобрено этическим кабинетом РНИМУ имени Н. И. Пирогова (протокол №131 от 27 января 2014 г.), от пациентов было получено добровольное информированное согласие на участие в исследовании.

✉ **Для корреспонденции:** Наталья Михайловна Хелминская
ул. Островитянова, д. 1, г. Москва, 117997, Россия; Khelminskaya@mail.ru

Статья получена: 02.10.2023 **Статья принята к печати:** 17.10.2023 **Опубликована онлайн:** 21.11.2023

DOI: 10.24075/vrgmu.2023.044

The features of reparative regeneration of the jawbone defects result primarily from the high degree of the oral cavity microbial contamination. One milliliter of oral fluid contains billions of microorganisms that form associations consisting of various bacterial species (streptococci, neisserias, vibrios, spirilla and spirochetes), the majority of which are obligate or facultative

anaerobes that maintain viability over a long time and actively replicate [1].

Chemical composition of the saliva has a significant impact on the jawbone tissue spontaneous regeneration, since the increased activity of proteolytic enzymes and fibrinolytic activators promotes the blood clot dissolution and washing

out of the defect cavity, thereby complicating the course of postoperative period and disrupting the organotypic bone graft formation [2].

Some clinical and experimental studies have shown that extraction of maxillary and mandibular teeth is followed by bone resorption in the tooth extraction sockets. Furthermore, bone deterioration is more prominent on the buccal side than on the lingual and palatal sides [3, 4]. Two thirds of the alveolar bone tissue is lost three months after tooth extraction [5]. Six months after surgery, the average clinical width and height loss in the tooth socket is 63% and 22% of the baseline, respectively [4], that is why many clinicians point to the need to preserve the alveolar process (part) after tooth extraction using various osteoplastic materials [6, 7].

Bacterial contamination of the bone defect adversely affects regeneration by distorting bone repair, therefore, there is no full bone cavity replenishment. A similar pattern is observed in the projection of bone defects caused by benign neoplasms of the jaw, the invasion of which results in bone tissue resorption and causes compression of the trigeminal nerve branches with typical neurological symptoms [8].

To date, numerous studies have been published reporting good outcomes of spontaneous jawbone defect regeneration after enucleation of cysts, including in cases of large defects [9–11]. Comparative assessment of the use of xenografts, allografts and synthetic material to preserve the volume of the alveolar process (part) of the jaw for the 25-year period was performed. Computer analysis of the data obtained revealed no clinically significant differences between application of osteoplastic materials and barrier membranes of different origin used for preservation of the alveolar process (part) of the jaw. Furthermore, postoperative complications significantly slowed bone tissue repair and thwarted formation of the full-fledged organotypic graft [12]. This suggests the need for further study of the methods for bone tissue regeneration stimulation using various materials and their combinations, as well as for identification of standard indications for the use of osteoplasty techniques.

The study was aimed to substantiate the use of the biocomplex consisting of plasma rich in growth factors and osteoplastic material to improve the effectiveness of osteogenesis in the limited jawbone defects.

METHODS

The clinical x-ray study was performed at the Pirogov City Clinical Hospital № 1, department of maxillofacial surgery and dentistry of the Pirogov Russian National Research Medical University of the Ministry of Health of the Russian Federation, in 2014–2022.

To assess the dynamics of the jawbone tissue regeneration, we performed the clinical x-ray study and surgical treatment of 136 patients aged 21–67, among them 105 (77.2%) females and 31 (22.8%) males. The patient inclusion criteria were as follows: the established diagnosis of chronic periodontitis, periapical abscess with a fistula, root cyst, follicular cyst, incisive canal cyst. Exclusion criteria: decompensation of concomitant disorder, malignant neoplasms of any stage or remission for less than five years, circulatory system diseases, hepatitis B and C, diabetes mellitus, thrombocytopenia, moderate to severe generalized periodontitis. Pregnancy and the history of concomitant disorder with complications during the study period were also considered to be the exclusion criteria. In 15 cases (11.03%), resorption of mandibular canal and incisive canal walls with the development of trigeminal neuropathy was

reported. The bone cavities were divided into three subgroups based on their size: small cavities (volume up to 1 cm³) were diagnosed in 52 cases (39%), medium cavities (volume up to 2 cm³) were observed in 53 patients (38.2%), large cavities (volume exceeding 2 cm³) were reported in 31 cases (22.8%).

Clinical groups were formed based on the jaw osteoplasty method. Group 1 consisting of 24 individuals (17.65%) showed spontaneous bone tissue regeneration due to filling the cavity with a blood clot; in group 2 consisting of 23 patients (16.91%), the bone defect was filled with plasma rich in growth factors (PRGF) in the form of gel. Group 3 included 37 patients (27.20%), among them seven patients showed resorption of the alveolar canals and compression of the trigeminal nerve branches. In this group osteoplasty was performed using the Osteobiol Gen-Os xenogeneic material (TecnoSS; Italy). Group 4 consisted of 53 patients, among them eight patients had neurological symptoms associated with compression of the inferior alveolar and nasopalatine nerves in the mandibular and incisive canals, respectively. The jaw defects in this group were repaired using a complex consisting of the Osteobiol Gen-Os material and plasma rich in growth factors (PRGF). The complex was obtained by polymerization of the xenogeneic material granules in the liquid phase. In group 4, the PRGF fibrin membrane was used to ensure decompression of the neurovascular bundle and separation of the augmentation area from the canal cavity. The PRGF Sistema IV centrifuge (BTI Biotechnology Institute; Spain) was used to obtain the plasma preparation rich in growth factors (PRGF). Preoperative dental examination and treatment were conducted in accordance with the general guidelines "Periapical Tissue Diseases" [13].

During the postoperative period, clinical assessment of patients was performed on days 1, 3, 5, and 7. All patients were recommended to rinse the oral cavity with an antiseptic solution, to apply antiseptic gel to the surgical wound area, to use the methods to ensure local hypothermia in the operated areas within 3 days after surgery for 10–15 min every hour. The broad-spectrum antibiotics and medium therapeutic doses of non-steroidal anti-inflammatory drugs were prescribed. Suture removal was performed on day 10–14 after surgery.

To study the jaw structure and determine the studied materials' capability of full-fledged bone tissue volume restoration, the data of cone beam computed tomography scans obtained using the Galileos (Sirona; Germany) or KaVo 3D eXam (KaVo; Korea) dental computed tomography system before treatment and 3, 6, 12 months after surgery were used. The Galileos Viewer and Vidar Dicom Viewer 3.1 software tools were used to determine the defect shape, size, and localization, as well as the contact with adjacent anatomical structures; the jawbone volume and density were measured in the Hounsfield units (HU).

Mathematical and statistical processing of the data obtained was performed using the IBM SPSS Statistics 21.0 software package, the following modules were used: descriptive statistics, t-test for independent samples (Student's t-test), nonparametric Mann–Whitney *U* test for two independent samples. The medstatistic.ru online resource (calculator) was also used. The following programs were applied: analysis of contingency tables using the χ^2 test, two-sided Fisher's exact test.

RESULTS

The analysis of the jawbone tissue regeneration dynamics performed a year after surgery suggested that the best osteoplasty outcomes were observed in group 4, where the lost volume of bone tissue was restored in all 52 cases (100%),

while in group 3 a full-fledged filling of bone cavity with the graft was reported only in 26 cases (70.27%) ($p = 0.00002$, < 0.05). In groups 1 and 2, complete restoration was reported for small defects only, in 9 cases (37.5%) among patients of group 1 and 10 cases (43.47%) among patients of group 2, while no restoration of volume was reported for medium to large cavities; no significant advantage of one of the groups was also found ($p = 0.905$, > 0.05 ; $p = 0.77$, > 0.05). However, the slightly higher x-ray intensity values were reported for clinical group 2 on month 3, 6 and 12 after surgery.

Patients of groups 1 and 2 demonstrated significant differences in the digital densitometry data 12 months after surgery ($p = 0.044$, < 0.05), which suggested that the use of the PRGF preparation in the form of gel significantly improved the bone tissue regeneration qualitative characteristics. In patients of clinical group 4, the average jawbone density values obtained three months after surgery were 721.73 ± 24.41 HU, while in group 3 these were significantly lower: 445.11 ± 7.92 HU ($p = 0.004$, < 0.005). After 6 months the difference between the average bone tissue x-ray intensity values became smaller; the values of group 3 were within in range of 600.54 ± 11.68 HU, while that of group 4 were in the range of 843.58 ± 19.7 HU. However, significant differences persisted ($p = 0.0001$, < 0.05). The average bone density value of patients of control clinical group 3 did not change significantly over a year after surgery, it was 608.95 ± 18.71 HU. In group 4, this indicator slightly increased (898.64 ± 20.18 HU), but it was still significantly different ($p = 0.0001$, < 0.05).

DISCUSSION

Auto-osteoplasty is considered to be a gold standard of osteoplasty in surgical practice, however, allogeneic bone,

xenografts and synthetic materials are extensively used to restore medium to large bone defects, when a large amount of bone is needed [14–18]. Good outcomes of the jawbone defect osteoplasty were achieved when using plasma preparations rich in autologous and allogeneic platelets and growth factors [19–22]. The results of the randomized controlled trial involving comparative analysis of bone tissue repair following the use of xenogeneic and allogeneic osteoplastic materials, as well as plasma rich in growth factors, showed that plasma preparation was significantly superior to other studied materials [23]. Many authors note that it is necessary to combine materials of different origin in order to enhance the augmentation material regeneration potential [24–28].

CONCLUSIONS

Comparative analysis of the dynamic changes in the volume and density of bone tissue in the projection of limited defects in all clinical groups demonstrated that the use of biocomplex of the Osteobiol Gen-Os bone material and plasma rich in growth factors (PRGF) was superior to that of the conventional method used in control group 1, as well as to the separate use of Osteobiol Gen-Os and plasma rich in growth factors (PRGF) in the form of gel. Simplicity and accessibility of the method to generate the plasma preparation rich in growth factors (PRGF), along with the relatively low cost, absolute level of biological safety and no toxic effects on the organism, make this technique one of the methods to address the issues of regenerative medicine. The study results obtained based on the informative clinical x-ray data have shown that the proposed method of using the Osteobiol Gen-Os osteoplastic material in combination with plasma rich in growth factors (PRGF) is promising for everyday use in clinical practice.

References

- Zelenova EG, Zaslavskaya MI, Salina EV, Rassanov SP. Mikroflora polosti rta: norma i patologiya: Uchebnoe posobie. Nizhniy Novgorod: Izdatel'stvo NGMA, 2004; 158 s. Russian.
- Samoylova MV, Kosyreva TF, Anurova AE, Abramovich RA, Mironov AYu, Zhilenkova OG, et al. Oral cavity microbiocenosis assessment on the basis of bacterial endotoxin and plasmalogens in a saliva by method gas-liquid chromatography-mass spectrometry. *Clinical Laboratory Diagnostics*. 2019; 64 (3): 186–92. DOI: 10.18821/0869-2084-2019-64-3-186-192. Russian.
- Cardaropoli G, Araújo M, Hayacibara R, Sukekava F, Lindhe J. Healing of extraction sockets and surgically produced —augmented and non-augmented — defects in the alveolar ridge. An experimental study in the dog. *J Clin Periodontol*. 2005 May; 32 (5): 435–40. DOI: 10.1111/j.1600-051X.2005.00692.x. PMID: 15842256.
- Van der Weijden F, Dell'Acqua F, Slot DE. Alveolar bone dimensional changes of post-extraction sockets in humans: a systematic review. *J Clin Periodontol*. 2009 Dec; 36 (12): 1048–58. DOI: 10.1111/j.1600-051X.2009.01482.x. PMID: 19929956.
- Araújo MG, Lindhe J. Dimensional ridge alterations following tooth extraction. An experimental study in the dog. *J Clin Periodontol*. 2005 Feb; 32 (2): 212–8. DOI: 10.1111/j.1600-051X.2005.00642.x. PMID: 15691354.
- Canullo L, Del Fabbro M, Khijmatgar S, et al. Dimensional and histomorphometric evaluation of biomaterials used for alveolar ridge preservation: a systematic review and network meta-analysis. *Clin Oral Invest*. 2022; 26: 141–58. DOI: 10.1007/s00784-021-04248-1.
- Stumbras A, Januzis G, Kubilius R, Gervickas A, Juodzbalsys G. Randomized clinical trial of bone healing after alveolar ridge preservation using xenografts and allografts vs. plasma rich in growth factors. *Journal of Oral Implantology*. 2020; 46 (5). DOI: 10.1563/aaid-joi-D-19-00179.
- Ku JK, Han M, Yongvikul A, Huh JK, Kim JY. Volumetric analysis of spontaneous bone healing after jaw cyst enucleation. *Sci Rep*. 2022 Sep 2; 12 (1): 14953. DOI: 10.1038/s41598-022-16921-w. PMID: 36056044. PMCID: PMC9440199.
- Chiapasco M, Rossi A, Motta JJ, Crescentini M. Spontaneous bone regeneration after enucleation of large mandibular cysts: A radiographic computed analysis of 27 consecutive cases. *J Oral Maxillofac Surg*. 2000; 58: 942–8. DOI: 10.1053/joms.2000.8732.
- latrou I, Theologie-Lygidakis N, Leventis M. Intraosseous cystic lesions of the jaws in children: a retrospective analysis of 47 consecutive cases. *Oral Surgery, Oral Medicine, Oral Pathology, Oral Radiology, and Endodontology*. 2009; 107 (4): 485–92.
- Ihan Hren N, Miljavec M. Spontaneous bone healing of the large bone defects in the mandible. *Int. J. Oral Maxillofac. Surg*. 2008; 37 (12): 1111–6. DOI: 10.1016/j.ijom.2008.07.008.
- Atieh MA, Alsabeeha NH, Payne AG, Ali S, Faggion CMJ, Esposito M. Interventions for replacing missing teeth: alveolar ridge preservation techniques for dental implant site development. *Cochrane Database Syst Rev*. 2021; 4: CD010176. DOI: 10.1002/14651858.
- Bolezni periapikal'nykh tkaney. Obshchie klinicheskie rekomendatsii. Postanovlenie №18 Soveta Assotsiatsii obshchestvennykh ob"edineniy «Stomatologicheskaya Assotsiatsiya Rossii» ot 02.08.2018; 128 s. Russian.
- Drobyshev AYu, Redko NA, Sviridov EG, Deev RV. Features of bone regeneration of the jaws alveolar ridge using hydroxyapatite-based material. *Traumatology and Orthopedics of Russia*. 2021;

- 27 (1): 9–18. DOI: 10.21823/2311-2905-2021-27-1-9-18. Russian.
15. Moiseeva NS, Kharitonov DYU, Kharitonov ID, Stepanov IV, Podoprigora AV. Clinical and laboratory evaluation of morphological parameters in osteoplastic materials used in alveolar bone augmentation. *Journal of new medical technologies*. 2021; 15(4): 18–23. DOI: 10.24412/2075-4094-2021-4-1-3. Russian.
 16. Stogov MV, Dyuryagina OV, Silanteva TA, Kireeva EA, Shipitsyna IV, Stepanov MA. Preclinical evaluation of the efficacy and safety of a new osteoplastic material of xenogenic origin containing vancomycin or meropenem. *Orthopaedic Genius*. 2022; 28 (4): 565–73. DOI: 10.18019/1028-4427-2022-28-4-565-573. Russian.
 17. Han JJ, Moon JE, Lee E-H, Yang HJ, Hwang SJ. Clinical and Radiographic Outcomes of Dental Implant after Maxillary Sinus Floor Augmentation with RhBMP-2/Hydroxyapatite Compared to Deproteinized Bovine Bone. *PLOS ONE*. 2022; 17: e0273399. DOI: 10.1371/journal.pone.0273399.
 18. Ho SKC, Peel SAF, Hu ZM, Sándor GKB, Clokie CML. Augmentation of the Maxillary Sinus: Comparison of Biomaterials Containing Bone Morphogenetic Protein and Autogenous Bone in a Rabbit Model. *J Can Dent Assoc*. 2010; 76: 108.
 19. Blazhenko AN, Rodin IA, Ponkina ON, Mukhanov ML, Samoilova AS, Verevkin AA, et al. Aim To evaluate the effect of A-PRP therapy on reparative bone regeneration in acute limb bone fractures. *Innovative Medicine of Kuban*. 2019; 3 (15): 32–8. Russian.
 20. Burykin KI, Parshikov MV, Yarygin NV, Svetlov DV, Govorov MV, Chemyanov IG, et al. Opportunities and prospects for the use of plasma enriched in platelets in the treatment of fractures and bone defects. *Polytrauma*. 2020; 3: 108–19. Russian.
 21. Samoday VG, Starikov AO, Kalashnikov PI. Lyophilized allogenic growth factors in traumatology and orthopedics as a promising direction of regenerative medicine. *Polytrauma*. 2019; 4: 15–28. Russian.
 22. Fayn AM, Vaza AYU, Gnetetskiy SF, Skuratovskaya KI, Bondarev VB, Bogolyubskiy YuA, et al. Available methods to enhance regenerative potential of plastic materials for bone defects replacement in orthopedics. Part 1. Autologous platelet rich plasma. *The Russian Journal of Transplantation*. 2022; 14 (1): 79–97. DOI: 10.23873/2074-0506-2022-14-1-79-97. Russian.
 23. Skwarcz S, Bryzek I, Gregosiewicz A, Warda E, Gaweda K, Tarczynska M, et al. Autologous activated platelet-rich plasma (PRP) in bone tissue healing - does it work? Assessment of PRP effect on bone defect healing in animal models. *Polish Journal of Veterinary Sciences*. 2019; 22 (1): 109–15. DOI: 10.24425/pjvs.2019.127077.
 24. Vasilyev AV, Kuznetsova VS, Galitsyna EV, Bukharova TB, Osidak EO, Fatkhudinova NL, et al. Biocompatibility and osteoinductive properties of collagen and fibronectin hydrogel impregnated with rhBMP-2. *Stomatology*. 2019; 98 (6–2): 5–11. DOI: 10.17116/stomat2019980625. Russian.
 25. Konev VA, Labutin DV, Bozhkova SA. Experimental justification for clinical application of bone growth stimulators in traumatology and orthopaedics (a review). *Siberian Medical Review*. 2021; 4: 5–17. DOI: 10.20333/25000136-2021-4-5-17. Russian.
 26. Kuznetsova VS, Vasilyev AV, Bukharova TB, Nedorubova IA, Goldshtein DV, Kulakov AA. Advantages and disadvantages of bone graft materials activated by BMP-2 and constructs carrying its gene. *Stomatology*. 2023; 102 (4): 76–80. DOI: 10.17116/stomat202310204176. Russian.
 27. Petrov IYu, Larionov EV, Ippolitov YuA, But LV, Petrov AI. Morphohistochemical studies of osteoplastic material based on hyaluronic acid, hondroitinsulfate and under-mineralized bone collagen for bone defects recovery in experiment. *Journal of new medical technologies*. 2018; 3: 41–6. DOI: 10.24411/2075-4094-2018-16038. Russian.
 28. Skwarcz S, Bryzek I, Gregosiewicz A, Warda E, Gaweda K, Tarczynska M, et al. The effect of activated platelet-rich plasma (PRP) on tricalcium hydroxyapatite phosphate healing in experimental, partial defects of long bone shafts in animal models. *Polish Journal of Veterinary Sciences*. 2019; 22 (2): 243–50. DOI: 10.24425/pjvs.2019.127092.

Литература

1. Зеленова Е. Г., Заславская М. И., Салина Е. В., Рассанов С. П. Микрофлора полости рта: норма и патология: Учебное пособие. Нижний Новгород: Издательство НГМА, 2004; 158 с.
2. Самойлова М. В., Косырева Т. Ф., Анурова А. Е., Абрамович Р. А., Миронов А. Ю., Жиленкова О. Г. и др. Оценка микробиотоза полости рта на основе гх-мс-определения плазмалогена и бактериального эндотоксина в ротовой жидкости. *Клиническая лабораторная диагностика*. 2019; 64 (3): 186–92. DOI: 10.18821/0869-2084-2019-64-3-186-192.
3. Cardaropoli G, Araújo M, Hayacibara R, Sukekava F, Lindhe J. Healing of extraction sockets and surgically produced —augmented and non-augmented — defects in the alveolar ridge. An experimental study in the dog. *J Clin Periodontol*. 2005 May; 32 (5): 435–40. DOI: 10.1111/j.1600-051X.2005.00692.x. PMID: 15842256.
4. Van der Weijden F, Dell'Acqua F, Slot DE. Alveolar bone dimensional changes of post-extraction sockets in humans: a systematic review. *J Clin Periodontol*. 2009 Dec; 36 (12): 1048–58. DOI: 10.1111/j.1600-051X.2009.01482.x. PMID: 19929956.
5. Araújo MG, Lindhe J. Dimensional ridge alterations following tooth extraction. An experimental study in the dog. *J Clin Periodontol*. 2005 Feb; 32 (2): 212–8. DOI: 10.1111/j.1600-051X.2005.00642.x. PMID: 15691354.
6. Canullo L, Del Fabbro M, Khijmatgar S, et al. Dimensional and histomorphometric evaluation of biomaterials used for alveolar ridge preservation: a systematic review and network meta-analysis. *Clin Oral Invest*. 2022; 26: 141–58. DOI: 10.1007/s00784-021-04248-1.
7. Stumbras A, Januzis G, Kubilius R, Gervickas A, Juodzbalsys G. Randomized clinical trial of bone healing after alveolar ridge preservation using xenografts and allografts vs. plasma rich in growth factors. *Journal of Oral Implantology*. 2020; 46 (5). DOI: 10.1563/aaid-joi-D-19-00179.
8. Ku JK, Han M, Yongvikul A, Huh JK, Kim JY. Volumetric analysis of spontaneous bone healing after jaw cyst enucleation. *Sci Rep*. 2022 Sep 2; 12 (1): 14953. DOI: 10.1038/s41598-022-16921-w. PMID: 36056044. PMCID: PMC9440199.
9. Chiapasco M, Rossi A, Motta JJ, Crescentini M. Spontaneous bone regeneration after enucleation of large mandibular cysts: A radiographic computed analysis of 27 consecutive cases. *J Oral Maxillofac Surg*. 2000; 58: 942–8. DOI: 10.1053/joms.2000.8732.
10. Iatrou I, Theologie-Lygidakis N, Leventis M. Intraosseous cystic lesions of the jaws in children: a retrospective analysis of 47 consecutive cases. *Oral Surgery, Oral Medicine, Oral Pathology, Oral Radiology, and Endodontology*. 2009; 107 (4): 485–92.
11. Ihan Hren N, Miljavec M. Spontaneous bone healing of the large bone defects in the mandible. *Int. J. Oral Maxillofac. Surg*. 2008; 37 (12): 1111–6. DOI: 10.1016/j.ijom.2008.07.008.
12. Atieh MA, Alsabeeha NH, Payne AG, Ali S, Faggion CMJ, Esposito M. Interventions for replacing missing teeth: alveolar ridge preservation techniques for dental implant site development. *Cochrane Database Syst Rev*. 2021; 4: CD010176. DOI: 10.1002/14651858.
13. Болезни периапикальных тканей. Общие клинические рекомендации. Постановление №18 Совета Ассоциации общественных объединений «Стоматологическая Ассоциация России» от 02.08.2018; 128 с.
14. Дробышев А. Ю., Редько Н. А., Свиридов Е. Г., Деев Р. В. Особенности регенерации костной ткани альвеолярного гребня челюстей при применении материала на основе гидроксиапатита. *Травматология и ортопедия России*. 2021; 27 (1): 9–18. DOI: 10.21823/2311-2905-2021-27-1-9-18.
15. Моисеева Н. С., Харитонов Д. Ю., Харитонов И. Д., Степанов И. В., Подопригора А. В. Клинико-лабораторная оценка морфологических параметров остеопластических материалов, применяемых при костной аугментации

- альвеолярного отростка. Вестник новых медицинских технологий. 2021; 15(4): 18–23. DOI: 10.24412/2075-4094-2021-4-1-3.
16. Стогов М. В., Дюрягина О. В., Силантьева Т. А., Киреева Е. А., Шипицына И. В., Степанов М. А. Доклиническая оценка эффективности и безопасности нового костнопластического материала ксеногенного происхождения, содержащего в своем объеме ванкомицин и меропенем. Гений ортопедии. 2022; 28 (4): 565–73. DOI: 10.18019/1028-4427-2022-28-4-565-573.
 17. Han JJ, Moon JE, Lee E-H, Yang HJ, Hwang SJ. Clinical and Radiographic Outcomes of Dental Implant after Maxillary Sinus Floor Augmentation with RhBMP-2/Hydroxyapatite Compared to Deproteinized Bovine Bone. PLOS ONE. 2022; 17: e0273399. DOI: 10.1371/journal.pone.0273399.
 18. Ho SKC, Peel SAF, Hu ZM, Sándor GKB, Clokie CML. Augmentation of the Maxillary Sinus: Comparison of Bioimplants Containing Bone Morphogenetic Protein and Autogenous Bone in a Rabbit Model. J Can Dent Assoc. 2010; 76: 108.
 19. Блаженко А. Н., Родин И. А., Понкина О. Н., Муханов М. Л., Самойлова А. С., Веревкин А. А. и др. Влияние А-PRP-терапии на репаративную регенерацию костной ткани при свежих переломах костей конечностей. Инновационная медицина Кубани. 2019; 3 (15): 32–8.
 20. Бурькин К. И., Паршиков М. В., Ярыгин Н. В., Светлов Д. В., Говоров М. В., Чемянов И. Г. и др. Возможности и перспективы использования обогащенной тромбоцитами плазмы в лечении переломов и дефектов костей. Политравма. 2020; 3: 108–19.
 21. Самодай В. Г. Стариков А. О. Калашников П. И. Лиофилизированные аллогенные факторы роста в травматологии и ортопедии как перспективное направление регенеративной медицины. Политравма. 2019; 4: 15–28.
 22. Файн А. М., Ваза А. Ю., Гнетецкий С. Ф., Скуратовская К. И., Бондарев В. Б., Боголюбский Ю. А. и др. Доступные способы повышения регенераторного потенциала пластического материала в неотложной травматологии. Часть 1. Использование аутологичной богатой тромбоцитами плазмы крови. Трансплантология. 2022; 14 (1): 79–97. DOI: 10.23873/2074-0506-2022-14-1-79-97.
 23. Skwarcz S, Bryzek I, Gregosiewicz A, Warda E, Gaweda K, Tarczyska M, et al. Autologous activated platelet-rich plasma (PRP) in bone tissue healing - does it work? Assessment of PRP effect on bone defect healing in animal models. Polish Journal of Veterinary Sciences. 2019; 22 (1): 109–15. DOI: 10.24425/pjvs.2019.127077.
 24. Васильев А. В., Кузнецова В. С., Галицына Е. В., Бухарова Т. Б., Осидак Е. О., Фатхудинова Н. Л., и др. Биосовместимость и остеогенные свойства коллаген-фибронектинового гидрогеля, импрегнированного BMP-2. Стоматология. 2019; 98 (6–2): 5–11. DOI: 10.17116/stomat2019980625.
 25. Конев В. А., Лабутин Д. В., Божкова С. А. Экспериментальное обоснование клинического применения стимуляторов остеогенеза в травматологии и ортопедии (обзор литературы). Сибирское медицинское обозрение. 2021; 4: 5–17. DOI: 10.20333/25000136-2021-4-5-17.
 26. Кузнецова В. С., Васильев А. В., Бухарова Т. Б., Недорубова И. А., Гольдштейн Д. В., Кулаков А. А. Преимущества и недостатки костно-пластических материалов, активированных BMP-2 и несущими его ген конструкциями. Стоматология. 2023; 102 (4): 76–80. DOI: 10.17116/stomat202310204176.
 27. Петров И. Ю., Ларионов Е. В., Ипполитов Ю. А., Бут Л. В., Петров А. И. Морфогистохимические исследования остеопластического материала на основе гиалуроновой кислоты, хондроитинсульфата и недеминерализованного костного коллагена для восстановления костных дефектов в эксперименте. Вестник новых медицинских технологий. 2018; 3: 41–6. DOI: 10.24411/2075-4094-2018-16038.
 28. Skwarcz S, Bryzek I, Gregosiewicz A, Warda E, Gaweda K, Tarczyska M, et al. The effect of activated platelet-rich plasma (PRP) on tricalcium hydroxyapatite phosphate healing in experimental, partial defects of long bone shafts in animal models. Polish Journal of Veterinary Sciences. 2019; 22 (2): 243–50. DOI: 10.24425/pjvs.2019.127092.

PREOPERATIVE PLANNING OF HIP ARTHROPLASTY

Minasov BSh, Yakupov RR, Bilyalov AR, Minasov TB, Valeev MM, Mavlyutov TR, Nigamedzanov IE, Akbashev VN ✉, Karimov KK

Bashkir State Medical University, Ufa, Russia

Preoperative planning of hip arthroplasty provides surgeons with a unique opportunity of thorough investigation of the patient's anatomy, allows them to determine optimal implant size and position, as well as to prevent potential complication. Advances in digital technology enable expansion of opportunities of preoperative planning due to using three-dimensional modeling. The study was aimed to compare precision of the three-step preoperative planning of hip arthroplasty and the standard method. Methods: The study involved 224 patients with various forms of degenerative and dystrophic diseases of the hip joint, who were divided into the index and control groups based on the planning method. In the index group, preoperative planning of arthroplasty was conducted in three steps: assessment of bone density in the zones of fixation based on CT; virtual design involving the use of automated programs; 3D model construction based on the computer model. X-ray images and endoprosthesis templates were used in the comparison group. The results showed that there were no significant differences between planning methods in patients with osteoarthritis and avascular necrosis of the femoral head ($p > 0.05$), in contrast to the group with traumatic hip joint pathology showing significant differences ($p_e = 0.002$). Conclusions: the three-step algorithm for preoperative planning of hip arthroplasty showed higher efficacy in patients with various nosological forms of degenerative and dystrophic diseases of the hip joint compared to the standard method.

Keywords: hip replacement, arthroplasty, preoperative planning, volumetric modeling, 3D printing

Funding: the study was supported by grant of the Government of the Republic of Bashkortostan for state support of scientific research guided by the leading scientists within the framework of the Eurasian Research and Educational Center programs; it was also supported by the Strategic Academic Leadership Program of the Bashkir State Medical University (PRIORITY-2030).

Author contribution: Minasov BSh, Yakupov RR, Bilyalov AR — developing the study design, data analysis; Minasov TB, Valeev MM, Mavlyutov TR — intraoperative control of determining the size of the endoprosthesis components, data acquisition, data analysis; Nigamedzanov IE, Akbashev VN, Karimov KK — statistical analysis, data estimation, literature review, computer, volumetric modeling, 3D printing of pelvic bones, acetabular and femoral components of the endoprosthesis.

Compliance with ethical standards: the study was approved by the Ethics Committee of the Bashkir State Medical University (protocol № 11 dated 15 November 2023)

✉ **Correspondence should be addressed:** Vladislav N. Akbashev
Lenina, 3, 45008, Ufa, Russia; Vlad-akb@mail.ru

Received: 12.11.2023 **Accepted:** 19.12.2023 **Published online:** 31.12.2023

DOI: 10.24075/brsmu.2023.052

ПРЕДОПЕРАЦИОННОЕ ПЛАНИРОВАНИЕ АРТРОПЛАСТИКИ ТАЗОБЕДРЕННОГО СУСТАВА

Б. Ш. Минасов, Р. Р. Якупов, А. Р. Билялов, Т. Б. Минасов, М. М. Валеев, Т. Р. Мавлютов, И. Э. Нигамедзянов, В. Н. Акбашев ✉, К. К. Каримов

Башкирский государственный медицинский университет, Уфа, Россия

Предоперационное планирование артропластики ТБС предоставляет хирургам уникальную возможность тщательного изучения анатомии пациента, позволяет определить оптимальный размер, позиционирование импланта, а также предупредить потенциальные осложнения. Развитие цифровых технологий позволяет повысить возможности предоперационного планирования за счет использования трехмерного моделирования. Цель: провести сравнение точности трехэтапного предоперационного планирования артропластики ТБС по сравнению со стандартным методом. В исследование было включено 224 пациента с различными формами дегенеративно-дистрофических заболеваний ТБС, которые были разделены на основную и контрольную группу в зависимости от метода планирования. В группе исследования предоперационное планирование артропластики проводилось в три этапа: оценка плотности костной ткани в области опорных зон на основании КТ-томографии; виртуальное проектирование с использованием автоматизированных программ; изготовление 3D-модели на основе компьютерного моделирования. В группе сравнения использовали рентгенограммы и шаблоны эндопротеза. Результаты показали, что статистически значимой разницы между методами планирования не было у пациентов, страдающих остеоартрозом и аваскулярным некрозом головки бедра ($p > 0,05$), в отличие от группы с посттравматической патологией ТБС, у которой отмечалась статистически значимая разница ($p_k = 0,002$). Выводы: алгоритм трехэтапной методики предоперационного планирования артропластики ТБС показал более высокую эффективность для пациентов с различной нозологической формой дегенеративно-дистрофических заболеваний ТБС по сравнению со стандартным методом.

Ключевые слова: эндопротезирование тазобедренного сустава, артропластика, предоперационное планирование, объемное моделирование, 3D-печать

Финансирование: работа выполнена при поддержке гранта Правительства Республики Башкортостан для государственной поддержки научных исследований, проводимых под руководством ведущих ученых, в рамках программы Евразийского НОЦ; и при поддержке Программы стратегического академического лидерства Башкирского государственного медицинского университета (ПРИОРИТЕТ-2030).

Вклад авторов: Б. Ш. Минасов, Р. Р. Якупов, А. Р. Билялов — разработка дизайна исследования, анализ результатов; Т. Б. Минасов, М. М. Валеев, Т. Р. Мавлютов — интраоперационный контроль определения размеров компонентов эндопротеза, сбор данных, анализ результатов; И. Э. Нигамедзянов, В. Н. Акбашев, К. К. Каримов — статистический анализ, оценка результатов, обзор литературы, компьютерное, объемное моделирование, 3D-печать костей таза, вертлужного и бедренного компонентов эндопротеза.

Соблюдение этических стандартов: исследование одобрено этическим комитетом БГМУ (протокол № 11 от 15 ноября 2023 г.).

✉ **Для корреспонденции:** Владислав Николаевич Акбашев
ул. Ленина, д. 3., 45008, г. Уфа, Россия; Vlad-akb@mail.ru

Статья получена: 12.11.2023 **Статья принята к печати:** 19.12.2023 **Опубликована онлайн:** 31.12.2023

DOI: 10.24075/vrgmu.2023.052

In recent decades, the share of high-tech medical care in traumatology and orthopedics dramatically increased, including endoprosthetic replacement of major joints in the lower limbs: hip and/or knee joint [1]. Total hip replacement (THR) is a standard surgical procedure used for treatment of severe disorders [2]. The main purpose of hip replacement is pain relief and functional lower limb restoration allowing the patient to return to active role and improve his/her quality of life. When performing total hip replacement (THR), the endoprosthesis acetabular component and stem should have appropriate component size and position, which is essential for achieving good functional outcome and longevity of the prosthesis. However, incorrect positioning or sizing of the endoprosthesis components increases the risk of intraoperative and postoperative complications, such as limb lengthening or shortening, intraoperative fractures, aseptic loosening, dislocation of the endoprosthesis head, etc. [3]. All these contribute to postoperative pain in the operated joint, instability and premature failure of the endoprosthesis components, thereby bringing dissatisfaction to the patient and reducing his/her quality of life [4]. Joint replacement of any type requires preoperative planning and intraoperative control. Preoperative planning is of utmost importance for optimization of the THR outcome. It helps the surgeon to visualize the final implant position after thorough assessment of clinical and radiography data [5]. In case of primary arthroplasty, preoperative planning can be performed using standard x-ray images, 2D templates or appropriate software. When performing primary arthroplasty in patients having a history of injury, osteotomy, surgical procedures, preoperative planning is hampered by non-compliance with the radioanatomical criteria.

Superimposition of the endoprosthesis templates onto the standard x-ray image of the hip joint for accurate sizing and positioning of the acetabular and femoral endoprosthesis components represents a conventional method of preoperative planning of THR.

Three-dimensional planning makes it possible to more clearly define the patient's unique anatomical features and reference points and ensures optimal visualization for preoperative implant sizing. The 3D planning methods allow one to more accurately determine the size of the endoprosthesis acetabular component and stem (96–100%) compared to 2D templates (16–43%). The results confirm superiority of 3D methods over 2D templates in terms of implant sizing accuracy. The computed tomography data used in 3D planning represent an appealing alternative to navigation for restoration of the limb length and axis [6–9].

The lack of unified approaches to planning of surgical treatment prevents achieving identical treatment outcomes in similar clinical situations. It is necessary to create certain preoperative planning algorithm for selection of treatment tactics in patients with various joint disorders.

The study was aimed to compare the effectiveness of the three-step preoperative planning of hip arthroplasty based on the nosological form of degenerative and dystrophic disease of the hip joint and that of the standard method.

METHODS

Comparative analysis of outcome estimates for various methods of preoperative planning of THR was conducted. A total of 224 patients were enrolled. Inclusion criteria: grade III–IV (Kellgren & Lawrence classification) primary (idiopathic) osteoarthritis of the hip associated with grade III or more joint function impairment; grade II–III aseptic necrosis of the femoral head with severe pain; post-traumatic condition (condition after osteosynthesis for proximal femur or acetabulum fractures) with complications in the form of post-traumatic osteoarthritis or nonunion, and individuals in need of hip arthroplasty. The diagnosis was established based on the clinical and anamnestic data, as well as using instrumental assessment methods (radiography, computed tomography and magnetic resonance imaging). Exclusion criteria: infectious inflammatory disease of the

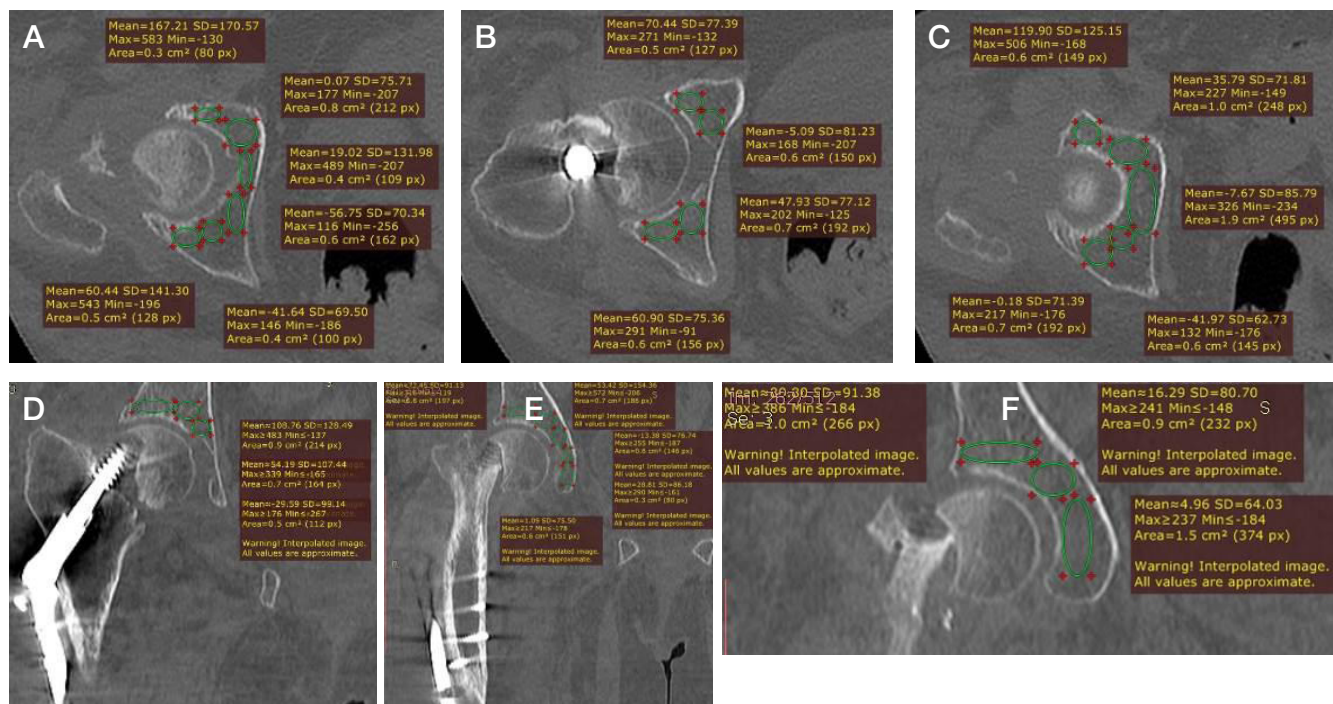


Fig. 1. Determination of bone density in the zones of fixation located in the acetabular area based on the horizontal (A, B, C) and frontal (D, E, F) CT scans of the 73-year-old patient: at the level of inferior acetabulum (A); at the level of the acetabulum middle part (B); at the level of superior acetabulum (C) (Average total bone density according to the Hounsfield scale — 30.65 HU.); at the level of posterior acetabulum (D); at the level of the acetabulum middle part (E); at the level of anterior acetabulum (F). (Average total bone density according to the Hounsfield scale — 30.09 HU.)

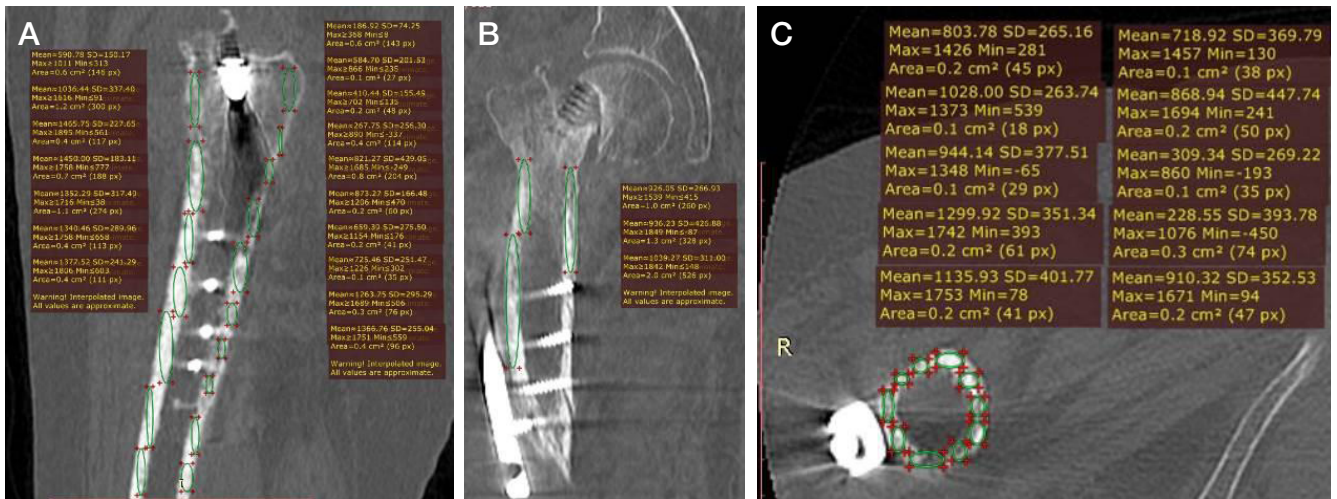


Fig. 2. Determination of bone density in the zones of fixation located in the acetabular area based on the sagittal, horizontal and frontal CT scans of the 73-year-old patient. **A.** Bone density estimation based on the sagittal scan. **B.** Bone density estimation based on the frontal scan. **C.** Bone density estimation based on the horizontal scan. (Average total bone density according to the Hounsfield scale — 869.13 HU.)

affected segment; concomitant somatic disorders representing absolute contraindications to surgery; no informed consent submitted by the patient, age under 18 years. All patients were divided into two groups: index group (116 people) and comparison group (108 people). The index group was divided into three subgroups: 34 patients with osteoarthritis (average age 60.8 ± 7.2 years), 30 patients with avascular necrosis of the femoral head (average age 43.9 ± 7.9 years), 52 patients with post-traumatic hip joint disorders (patients of this group underwent osteosynthesis for fractures of the femoral neck, trochanter region of the femur, acetabulum of the pelvis, etc.) (60.2 ± 11.1 years). The comparison group was also divided into three subgroups: 33 patients with osteoarthritis (average age 61.3 ± 6.8 years), 29 patients with avascular necrosis of the femoral head (42.6 ± 8.4 years), 46 patients with post-traumatic hip joint disorders (59.3 ± 12.7 years). The average age of all surveyed patients was 57 ± 6.2 years, 119 people (53.12%) were females, 105 people (46.87%) were males.

In the index group ($n = 116$), preoperative planning of hip arthroplasty was performed in three phases.

In the first phase, bone density in the acetabular and femoral areas was determined in three planes based on the hip joint computed tomography (CT) data using the Hounsfield scale. Bone density was assessed around the perimeter of the zones of fixation considering the planned implant location and installation site. Determination of the zone with optimal

bone density and the regions with reduced bone density, osteosclerosis, cysts and various defects was an important criterion of the endoprosthesis installation and positioning. When performing preoperative planning in patients having a history of osteosynthesis, it was difficult to determine bone density in the zones of fixation due to the presence of “metal artifacts” (Fig. 1 and 2).

In the second phase, the TraumaCad v. 2.4 software (Brainlab; USA) was used to determine the optimal size and position of the endoprosthesis components. For that x-ray image of the pelvis with the hip joint was uploaded to the program, over which the digital template of the endoprosthesis femoral and acetabular components was superimposed. However, when performing preoperative planning of endoprosthetic replacement using software, complete proximal femur visualization was hampered by the presence of surgical hardware (Fig. 3).

In the third phase, the Geomagic Studioc (Raindrop Geomagic Inc.; USA) and 3D Slicer (Copyright 2023, Slicer Community; USA) software was used for virtual installation of the endoprosthesis components following construction of a volumetric model of the baseline condition (Fig. 4). This phase enabled estimation of the segment anatomy distortion, more accurate adjustment of the endoprosthesis positioning, provision of starting biomechanics, and determination of the hip arthroplasty tactics. In cases of severe hip joint deformities,

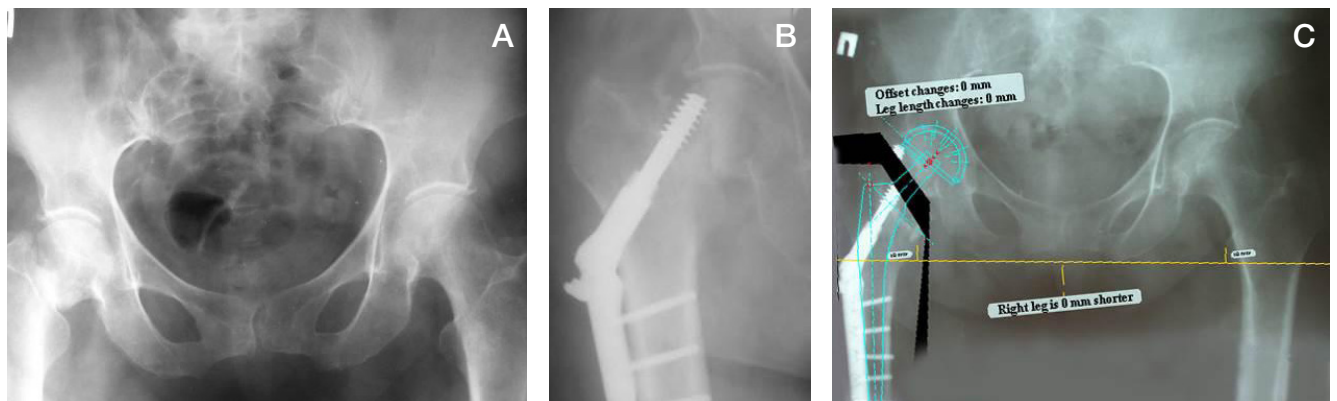


Fig. 3. Survey frontal x-ray image of the pelvis and the right hip joint of the 73-year-old patient. Diagnosis: condition after osteosynthesis involving the use of the DHS system. False joint of the right femoral neck. **A.** X-ray image acquired at admission to surgery — osteosynthesis of the right femur involving the use of the DHS system. **B.** X-ray image acquired after osteosynthesis involving the use of the DHS system. **C.** Sizing and positioning of the endoprosthesis components using the TraumaCad v. 2.4 software. (Planned size of the acetabular component — 50, femoral component — 4)

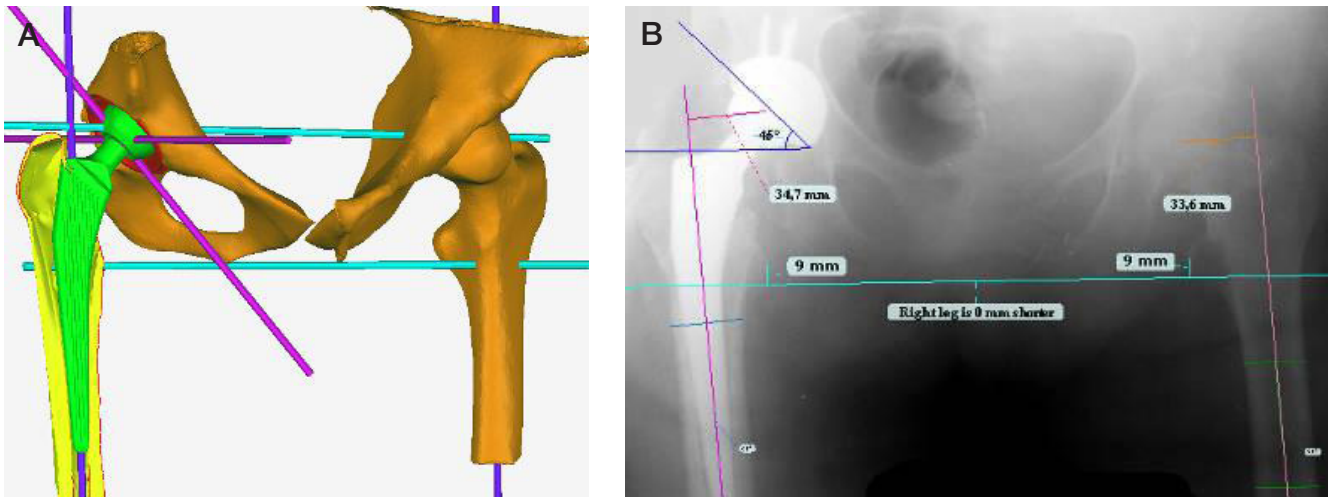


Fig. 4. Female patient, 73 years. Comparison of the endoprosthesis component dimensions during preoperative planning based on volumetric modeling performed before and after hip arthroplasty. **A.** Volumetric model of the right hip joint with virtual installation of the endoprosthesis components (planned size of the acetabular component — 52, femoral component — 6). **B.** Survey x-ray image of the pelvis and right hip joint after installation of endoprosthesis, the dimensions of acetabular and femoral components corresponded to the planned dimensions

computer modeling was combined with 3D printing of the affected segment before and after hip arthroplasty (Fig. 5).

In the control group ($n = 108$), preoperative planning was performed by standard methods: posteroanterior x-ray images of the pelvis with the hip joint were used, over which the templates of the endoprosthesis components (draft) were superimposed to determine the implant size.

Preoperative planning was followed by surgical treatment, THR, in both studied groups.

RESULTS

The results were assessed based on the match of the endoprosthesis component dimensions determined before and during surgery (intraoperatively). The index group patients with osteoarthritis and avascular necrosis of the femoral head showed higher implant sizing accuracy, however, it was

comparable with that of the control group ($p > 0.05$). The subgroup with post-traumatic disorders showed significant differences in the accuracy of the intended endoprosthesis component size determination between the index and the control groups ($p_c = 0.002$). The main results and the implant sizing accuracy depending on the disease entity and the preoperative planning method are provided in Table 1 and Fig. 6.

DISCUSSION

Comparability of the results of the index and control group patients with osteoarthritis and aseptic necrosis could result from minor anatomy distortion in the segment of the pelvis and the lower limb, while in patients with post-traumatic disorders the planned endoprosthesis component dimensions in controls did not match actual size in more than a half of cases, which suggested low effectiveness of standard planning method

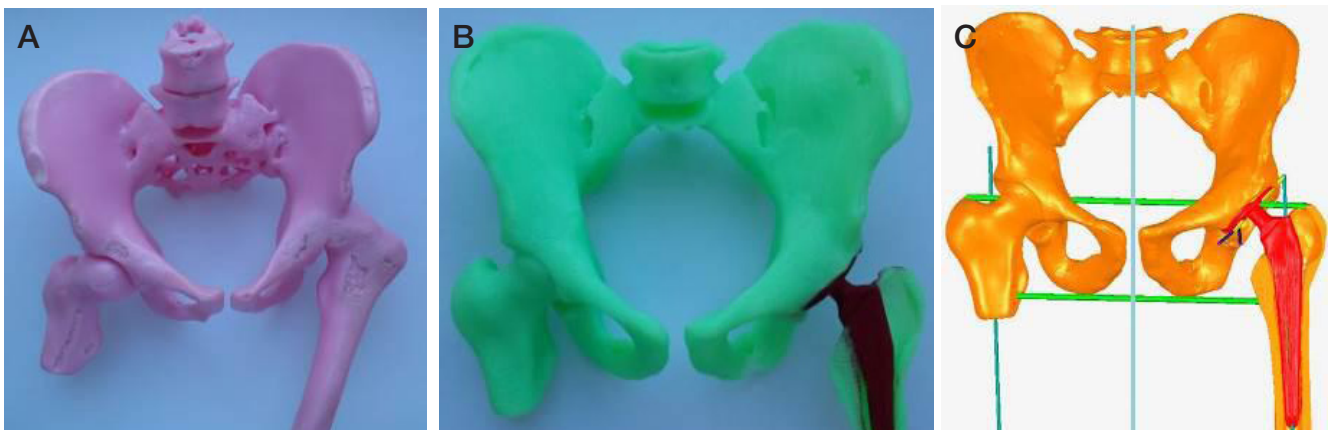


Fig. 5. Patient, 45 years. Preoperative planning based on volumetric prototyping. **A.** Printed 3D model of the hip joint before arthroplasty. **B.** Printed 3D model of the hip joint after arthroplasty. **C.** Preoperative planning of the right hip arthroplasty based on volumetric modeling

Table 1. Endoprosthesis component sizing accuracy depending on the nosological form of degenerative and dystrophic disease of the hip joint (%)

	Osteoarthritis (subgroup I)		Avascular necrosis of the femoral head (subgroup II)		Post-traumatic disorder (subgroup III)	
	Control group	Index group	Control group	Index group	Control group	Index group
Number of people	$n = 33$	$n = 34$	$n = 29$	$n = 30$	$n = 46$	$n = 52$
Endoprosthesis component sizing accuracy (%)	81.82	85.29 ($p_c = 0.7$)	82.76	86.67 ($p_c = 0.68$)	47.83	78.85 ($p_x = 0.002$)

Note: p_c — significance of differences from controls.

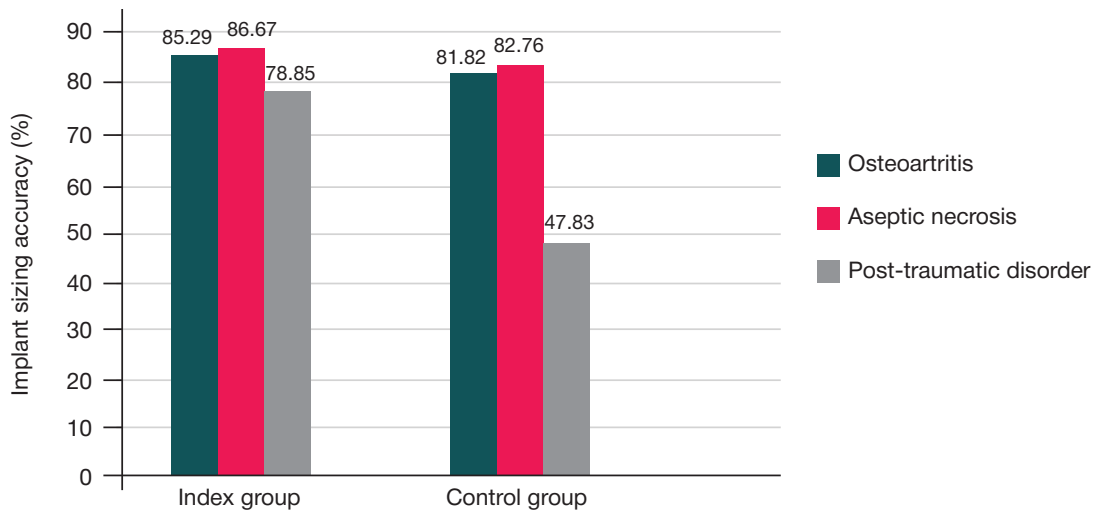


Fig. 6. Implant sizing accuracy when using different preoperative planning methods

in this group of patients due to more prominent segment anatomy distortion resulting from fractures, osteosynthesis or reconstructive surgery, as well as to the hip joint anatomy distortion, impaired joint congruence, secondary pelvic and spinal deformities, lower limb shortening by more than 3 cm [10–12].

The analysis resulted in creation of the algorithm for selection of preoperative planning method based on the forms of degenerative and dystrophic diseases of the hip joint and severity of the hip joint anatomy distortion (Table 2).

CONCLUSIONS

The proposed approach to selection of preoperative planning technique makes it possible to accurately determine the

endoprosthesis component dimensions and contributes to correct orientation and positioning of the endoprosthesis components during hip arthroplasty. The proposed algorithm of the three-step method showed higher effectiveness of preoperative planning and personalized design for patients with various nosological forms of degenerative and dystrophic diseases of the hip joint compared to the standard method, it also enabled accurate endoprosthesis component sizing. Preoperative planning of hip arthroplasty by the proposed method allows one to assess the disease characteristics at the local and systemic levels. The most challenging situations are observed in patients with post-traumatic disorders of the hip joint. This is due to the fact that patients of this group usually show severe bone disruption in the femoral and acetabular zones of fixation.

Table 2. Selection of preoperative planning technique based on the form of degenerative and dystrophic disease of the hip joint

Groups of patients	Preoperative planning phases
Patients with avascular necrosis of the femoral head, primary osteoarthritis and no prominent anatomy distortion	Determination of bone density in the acetabulum and zones of fixation based on CT in accordance with the Hounsfield scale Using the automated software to determine the endoprosthesis component dimensions based on 2D design
Patients with avascular necrosis of the femoral head, primary osteoarthritis and prominent anatomy distortion (secondary deformities of the spine and pelvis, rigidity, lower limb shortening by more than 3 cm)	Determination of bone density in the acetabulum and zones of fixation based on CT in accordance with the Hounsfield scale Using the automated software to determine the endoprosthesis component dimensions based on 2D design
Patients with post-traumatic disorders of the hip joint having a history of various types of proximal femur surgery (osteosynthesis) or acetabular fractures	Preoperative planning involving construction of volumetric 3D models

References

- Khoziainova SS, et al. Physical therapy in the rehabilitation of patients after endoprosthetic replacement of major joints in the lower extremities: a scientometric analysis of evidence-based studies. *Vopr kurortol fizioter lech fiz kul't.* 2019; 96 (6): 22. DOI: 10.17116/kurort20199606122. Russian.
- Thirion T, Georis P, Gillet P. Preoperative planning interest of a total hip prosthesis. *Rev Med Liege.* 2019; 74 (11): 593–597.
- Huo Jet et al. Value of 3D preoperative planning for primary total hip arthroplasty based on artificial intelligence technology. *J Orthop Surg Res.* 2021; 16 (1): 156. DOI: 10.1186/s13018-021-02294-9.
- Knafo Y, Houfani F, Zaharia B, Egrise F, Clerc-Urmès I, Mainard D. Value of 3D preoperative planning for primary total hip arthroplasty based on biplanar weightbearing radiographs. *BioMed Research International.* 2019; 2019: 1–7. DOI: 10.1155/2019/1932191.
- Moralidou M, Di Laura A, Henckel J, Hothi H, Hart AJ. Three-dimensional pre-operative planning of primary hip arthroplasty: a systematic literature review. *EFORT Open Reviews.* 2020; 5 (12): 845–55. DOI: 10.1302/2058-5241.5.200046.
- Alagha MA, Logishetty K, O'Hanlon C, Liddle AD, Cobb J. Three-dimensional preoperative planning software for hip resurfacing arthroplasty. *Bioengineering (Basel).* 2023; 10 (8): 939. DOI: 10.3390/bioengineering10080939.
- Schiffner E, et al. Is computerised 3D templating more accurate than 2D templating to predict size of components in primary total hip arthroplasty. *HIP International.* 2019; 29 (3): 270–275. DOI: 10.1177/1120700018776311.
- Ding X, et al. Value of preoperative three-dimensional planning software (AI-HIP) in primary total hip arthroplasty: a retrospective study. *J Int Med Res.* 2021; 49 (11). DOI: 10.1177/03000605211058874.
- Inoue D, et al. Value of computed tomography-based three-dimensional

- surgical preoperative planning software in total hip arthroplasty with developmental dysplasia of the hip. *Journal of Orthopaedic Science*. 2015; 20 (2): 340–46. DOI: 10.1007/s00776-014-0683-3.
10. Zheng Cao, Wei Yang, Minzhi Yang, Xiangpeng Kong, Yi Wang, Renwen Guo, et al. Application of preoperative digital-template planning in total hip arthroplasty via direct anterior approach. *Zhongguo Xiu Fu Chong Jian Wai Ke Za Zhi*. 2019; 33 (11): 1374–1378. DOI: 10.7507/1002-1892.201903108. In Chinese.
 11. Takegami Y, Komatsu D, Seki T, Ishiguro N, Hasegawa Y. Total hip arthroplasty after failed curved intertrochanteric varus osteotomy for avascular necrosis of the femoral head. *Nagoya J Med Sci*. 2016; 78 (1): 89–97. Available from: <https://www.ncbi.nlm.nih.gov/pmc/articles/PMC4767517/>.
 12. Gautam D, Gupta S, Malhotra R. Total hip arthroplasty in acetabular fractures. *J Clin Orthop Trauma*. 2020; 11 (6): 1090–8. DOI: 10.1016/j.jcot.2020.10.037.

Литература

1. Khoziainova SS, et al. Physical therapy in the rehabilitation of patients after endoprosthetic replacement of major joints in the lower extremities: a scientometric analysis of evidence-based studies. *Vopr kurortol fizioter lech fiz kul't*. 2019; 96 (6): 22. DOI: 10.17116/kurort20199606122. Russian.
2. Thirion T, Georis P, Gillet P. Preoperative planning interest of a total hip prosthesis. *Rev Med Liege*. 2019; 74 (11): 593–597.
3. Huo Jet et al. Value of 3D preoperative planning for primary total hip arthroplasty based on artificial intelligence technology. *J Orthop Surg Res*. 2021; 16 (1): 156. DOI: 10.1186/s13018-021-02294-9.
4. Knafo Y, Houfani F, Zaharia B, Egrise F, Clerc-Urmès I, Mainard D. Value of 3D preoperative planning for primary total hip arthroplasty based on biplanar weightbearing radiographs. *BioMed Research International*. 2019; 2019: 1–7. DOI: 10.1155/2019/1932191.
5. Moraliidou M, Di Laura A, Henckel J, Hothi H, Hart AJ. Three-dimensional pre-operative planning of primary hip arthroplasty: a systematic literature review. *EFORT Open Reviews*. 2020; 5 (12): 845–55. DOI: 10.1302/2058-5241.5.200046.
6. Alagha MA, Logishetty K, O'Hanlon C, Liddle AD, Cobb J. Three-dimensional preoperative planning software for hip resurfacing arthroplasty. *Bioengineering (Basel)*. 2023; 10 (8): 939. DOI: 10.3390/bioengineering10080939.
7. Schiffner E, et al. Is computerised 3D templating more accurate than 2D templating to predict size of components in primary total hip arthroplasty. *HIP International*. 2019; 29 (3): 270–275. DOI: 10.1177/1120700018776311.
8. Ding X, et al. Value of preoperative three-dimensional planning software (AI-HIP) in primary total hip arthroplasty: a retrospective study. *J Int Med Res*. 2021; 49 (11). DOI: 10.1177/03000605211058874.
9. Inoue D, et al. Value of computed tomography-based three-dimensional surgical preoperative planning software in total hip arthroplasty with developmental dysplasia of the hip. *Journal of Orthopaedic Science*. 2015; 20 (2): 340–46. DOI: 10.1007/s00776-014-0683-3.
10. Zheng Cao, Wei Yang, Minzhi Yang, Xiangpeng Kong, Yi Wang, Renwen Guo, et al. Application of preoperative digital-template planning in total hip arthroplasty via direct anterior approach. *Zhongguo Xiu Fu Chong Jian Wai Ke Za Zhi*. 2019; 33 (11): 1374–1378. DOI: 10.7507/1002-1892.201903108. In Chinese.
11. Takegami Y, Komatsu D, Seki T, Ishiguro N, Hasegawa Y. Total hip arthroplasty after failed curved intertrochanteric varus osteotomy for avascular necrosis of the femoral head. *Nagoya J Med Sci*. 2016; 78 (1): 89–97. Available from: <https://www.ncbi.nlm.nih.gov/pmc/articles/PMC4767517/>.
12. Gautam D, Gupta S, Malhotra R. Total hip arthroplasty in acetabular fractures. *J Clin Orthop Trauma*. 2020; 11 (6): 1090–8. DOI: 10.1016/j.jcot.2020.10.037.

FOVEAL MICROSURGICAL RECONSTRUCTION TECHNIQUE FOR MACULAR HOLE

Takhchidi KP ✉

Pirogov Russian National Research Medical University, Moscow, Russia

Macular rupture is among major vitreoretinal disorders resulting in significant visual function decline. In recent years, the use of platelet-rich autoplasm in the macular rupture surgery is considered to be promising. However, despite high rate of macular rupture closure (78–96%), the development of new technology for foveal microarchitectonics restoration and visual function improvement currently remains a pressing issue. The study was aimed to develop a new foveal reconstruction technique for macular rupture involving the use of autologous conditioned plasma. The reported study involved 9 patients (10 eyes) with idiopathic macular hole, who underwent standard three-port 27G vitrectomy involving the use of autologous conditioned plasma in accordance with the technique developed. The proposed technique makes it possible to achieve good clinical and functional surgical treatment outcome and ensures optimal and more manageable reconstruction of foveal microarchitectonics.

Keywords: macular rupture, optical coherence tomography, autologous conditioned plasma, vitrectomy, microperimetry

Compliance with ethical standards: the study was approved by the Ethics Committee of the Pirogov Russian National Research Medical University (protocol № 224 dated 19 December 2022). All patients submitted the informed consent to surgical treatment and personal data processing.

✉ **Correspondence should be addressed:** Khristo P. Takhchidi
Volokolamskoe shosse, 30, korp. 2, Moscow, 123182, Russia; hpt1301@gmail.com

Received: 04.12.2023 **Accepted:** 18.12.2023 **Published online:** 31.12.2023

DOI: 10.24075/brsmu.2023.055

ТЕХНОЛОГИЯ МИКРОХИРУРГИЧЕСКОЙ РЕКОНСТРУКЦИИ ФОВЕА ПРИ МАКУЛЯРНЫХ РАЗРЫВАХ

Х. П. Тахчиди ✉

Российский национальный исследовательский медицинский университет имени Н. И. Пирогова, Москва, Россия

Одной из ведущих витреоретинальных патологий, приводящих к значительному ухудшению зрительных функций, является макулярный разрыв. В последние годы в хирургии макулярных разрывов перспективно использование аутоплазмы крови с повышенным содержанием тромбоцитов. Но, несмотря на высокий процент закрытия макулярных разрывов (78–96%), на сегодняшний день актуальным вопросом остается разработка новых технологий, направленных на восстановление микроархитектоники фовеолярной области и повышения зрительных функций. Целью исследования было разработать новую технологию реконструкции фовеолярной области при макулярных разрывах с использованием аутологичной кондиционированной плазмы. В представленную работу вошли 9 пациентов (10 глаз) с идиопатическим сквозным макулярным разрывом, которым была выполнена стандартная трехпортовая 27G-витрэктомия с применением аутологичной кондиционированной плазмы по разработанной технологии. В результате хирургического лечения предлагаемая технология позволяет получить высокие клинико-функциональные результаты, а также обеспечивает оптимальную и более управляемую реконструкцию микроархитектонику фовеа.

Ключевые слова: макулярный разрыв, оптическая когерентная томография, аутологичная кондиционированная плазма, витрэктомия, компьютерная микропериметрия

Соблюдение этических стандартов: исследование одобрено этическим комитетом РНИМУ имени Н. И. Пирогова (протокол № 224 от 19 декабря 2022 г.). Все пациенты подписали добровольное информированное согласие на хирургическое лечение и обработку персональных данных.

✉ **Для корреспонденции:** Христо Периклович Тахчиди
Волоколамское шоссе, д. 30, корп. 2, г. Москва, 123182, Россия; hpt1301@gmail.com

Статья получена: 04.12.2023 **Статья принята к печати:** 18.12.2023 **Опубликована онлайн:** 31.12.2023

DOI: 10.24075/vrgmu.2023.055

Idiopathic macular hole is a foveal defect affecting all neuroretinal layers and characterized by decreased visual acuity, central scotoma and metamorphopsia [1–4]. According to the literature data, the macular hole incidence is about 3–5 cases per 1000 population aged over 55, it is more prevalent among women aged 60–70. The disorder is unilateral in 80% of cases [5].

In 2013, the researchers of the International Vitreomacular Traction Study Group (IVTSG) proposed an optical coherence tomography (OCT)-based anatomic classification system for assessment of the central retina condition in individuals with macular holes. According to the classification, macular holes are classified as small ($\leq 250 \mu\text{m}$), medium ($250\text{--}400 \mu\text{m}$), and large ($>400 \mu\text{m}$) based on minimal diameter [6, 7].

The internal limiting membrane (ILM) peeling with subsequent gas-air mixture tamponade had been considered the gold standard treatment for full-thickness macular hole [8]. To further improve the efficacy, modified surgical approaches to treatment of macular holes were proposed: mechanical

approximation of the hole edges, ILM peeling followed by the hole sealing with inverted ILM flap, amniotic membrane plug, anterior lens capsule transplantation, ILM preservation [9–12].

In recent years, the use of platelet-rich autoplasm is one of the promising directions of the macular hole surgery. Two methods to obtain plasma are currently being actively used in treatment of retinal disorders: PRP (platelet-rich plasma with the platelet content 3–4 times higher compared to baseline blood levels) and ACP (autologous conditioned plasma almost deprived of white blood cells and having an increased platelet concentration that is 2–3 times higher compared to baseline blood levels). The local use of autologous factors in macular surgery makes it possible to achieve good anatomic and functional outcomes and minimize retinal tissue injury during surgery [6, 13–15]. However, despite high rate of macular hole closure (78–96%) [16, 17], the quest for restoration of foveal microarchitectonics and, therefore, for improvement of visual functions, currently remains a pressing issue.

The study was aimed to develop a new technique for foveal reconstruction in individuals with macular holes based on the use of autologous conditioned plasma.

METHODS

The study involved 9 patients (10 eyes) aged 62–76 (average age 66.1 ± 7.41 years), who underwent surgery due to idiopathic full-thickness macular hole at the Ophthalmology Research Center, Pirogov Russian National Research Medical University.

All patients underwent comprehensive eye examination involving the use of standard (visometry to determine uncorrected visual acuity (UCVA) and best-corrected visual acuity (BCVA), pneumatonometry, biomicrophthalmoscopy with a MaxField indirect lens (Ocular Inc.; USA) and specific assessment methods, such as spectral-domain optical coherence tomography (SD-OCT) performed with the Spectralis HRA+OCT system (Spectralis HRA+OCT, Heidelberg Engineering, Module, OCT-2 85,000 Hz, Inc.; Germany), microperimetry (MAIA, CenterVue; Italy).

Inclusion criteria: idiopathic full-thickness macular hole. Exclusion criteria: concomitant eye disorder (age-related macular degeneration, glaucoma, partial optic atrophy, vascular disorders, diabetic retinopathy, intraocular mass, retinal detachment, corneal scars or opacities), traumatic macular hole, macular hole duration exceeding 6 months.

The macular hole duration before surgery was between 3 weeks and 5 months. The follow-up period was 3–16 months. The study results were processed using standard descriptive statistical tools of the Microsoft Office Excel. The data were provided as $M \pm \sigma$, where M was the mean, σ was the standard deviation.

Assessment showed that UCVA was 0.18 ± 0.13 and BCVA was 0.3 ± 0.17 . OCT revealed macular holes with intraretinal cysts in all cases. The maximum macular hole diameter was $759.2 \pm 174.7 \mu\text{m}$, the minimum diameter was $343.4 \pm 96.6 \mu\text{m}$, the average central retinal thickness (CRT) was $416 \pm 65.3 \mu\text{m}$. According to the IVTSG classification, the patients were divided into groups as follows: group with $\leq 250 \mu\text{m}$ — 0 eyes; group with $251\text{--}400 \mu\text{m}$ — 7 eyes; group with $\geq 401 \mu\text{m}$ — 3 eyes. Microperimetry showed that the average retinal sensitivity (RS) in the studied group was 22.7 ± 1.52 dB.

All the patients underwent treatment involving the use of the developed technique: in the first phase phacoemulsification and intraocular lens implantation was performed in patients with lens opacities. Then three-port 27G vitrectomy with isolation and removal of the posterior hyaloid membrane was performed. After that the ILM was stained and removed. After the ILM removal, at least 1/3 of the vitreous cavity volume was substituted with the perfluorocarbon liquid (PFCL) that filled the posterior pole of the eye and hermetically “sealed” the macular hole. As a result, the hermetically sealed intraocular fluid pressurized by the irrigation fluid and the pressure head of PFCL stayed in the macular hole intrawound area. Then the fluid was passively evacuated from the macular hole area with an extrusion needle, the irrigation fluid pressure was 15 mm Hg. The vertical needle bevel was brought close to the hole area, not touching the retina. Owing to the differences in viscosity between PFCL and intraocular fluid, intraocular fluid, that was a priority when performing evacuation from the hole area, turned out to be more motile in terms of competitive aspiration (Fig. 1). As the wound fluid was evacuated, the negative pressure (“mild micro-vacuum”) occurred in the hole area, which ensured even and atraumatic approximation of the ragged macular hole

walls around the perimeter of the wound. To ensure visual control of the process of bringing together the hole walls, we lifted the needle tip above the hole area. When the hole walls fail to fuse completely, the manipulation involving the wound fluid aspiration can be repeated many times to achieve the necessary outcome (fusion). In case of unintended aspiration (“adhesion”) of the inner retinal surface of the macular hole edges, it is necessary to stop passive aspiration by closing the extrusion needle hole with the finger and slowly lifting the needle tip over the retina perpendicularly to the surface. As a result of this action, the retinal surface uniformly pressurized by PFCL gravity easily peels off the needle bevel without damaging the retinal tissue. This procedure is associated with no risk.

When exposed to negative pressure in the hole area, the aggregate foveal tissue of the fused macular hole walls was held in this position due to the PFCL gravity for at least 10 min (hole retention time) (Fig. 2). During this time we intraoperatively prepared ACP using the Arthrex ACP double-syringe system. A total of 15 mL of the patient’s venous blood were collected in the Arthrex ACP syringe. After blood collection, the syringe was installed in the ROTOFIX 32A centrifuge (Hettich; Germany) for further centrifugation for 5 min at 1700 rpm. A total of 0.2–0.4 mL of ACP was taken up in the micro-syringe for application to the macular hole area. After the required time of the macular hole retention in the closed state (at least 10 min) was over, PFCL was substituted with the irrigation fluid. At this point the fused macular hole walls temporarily stayed closed due to weakening of the centrifugal force of the stretched retinal tissue elasticity. This time was enough to apply the prepared autoplasm forming a hermetic plaque sealing the hole area on the surface of the macular area of the retina. The autoplasm layers were applied to the macular area until a faint translucent plaque emerged (Fig. 3A). After that the irrigation fluid was substituted with air.

RESULTS

After a month of postoperative follow up (eight patients, 10 eyes) UCVA increased to 0.45 ± 0.21 , BCVA was 0.54 ± 0.13 . Microperimetry showed that the average RS was 24.86 ± 1.53 dB. According to the OCT data, the average CRT decreased from $416 \pm 65.3 \mu\text{m}$ to $299.3 \pm 49.2 \mu\text{m}$.

On the follow-up examination three months later UCVA increased to 0.53 ± 0.22 and BCVA increased to 0.66 ± 0.12 . The average RS was 25.27 ± 3.3 dB. The average CRT decreased to $290.3 \pm 46.3 \mu\text{m}$.

After six months of follow up (seven patients, eight eyes) UCVA was 0.53 ± 0.3 , BCVA was 0.73 ± 0.15 . The average CRT was $274.6 \pm 37.6 \mu\text{m}$. The average RS was 25.7 ± 2.11 dB.

In a year (five patients, six eyes), UCVA was 0.42 ± 0.33 , BCVA was 0.75 ± 0.21 . According to the OCT data, the average CRT was $285.2 \pm 31.8 \mu\text{m}$. The average RS was 25.4 ± 2.32 dB.

The longest follow-up period (up to 16 months) was reported for one patient (one eye) with preoperative UCVA of 0.05 and BCVA of 0.1. CRT was $450 \mu\text{m}$. The average RS was 22.7 dB. On the follow-up examination 16 months after surgery UCVA and BCVA increased to 0.1 and 0.8, respectively. CRT decreased to $336 \mu\text{m}$. The average RS was 27.8 dB.

As a result of surgical treatment, OCT showed complete macular hole closure and foveal structure restoration in all cases. According to the OCT findings, regression of the intraretinal cysts diagnosed before surgical intervention was observed in the early postoperative period (after 6 h and 3 days) (Fig. 4, 5).

No postoperative complications were reported in any case; there were no relapses throughout the postoperative follow-up period.

DISCUSSION

Part of the foveal tissue dies when the macular hole is formed. The remaining highly functional foveal tissue of the retina provides a morphofunctional basis for visual function restoration. However, after the macular rupture, the surviving part of the foveal tissue is shifted from its microanatomical/microhistological site. Therefore, microarchitectonics of the remaining foveal tissue part is impaired and, consequently, visual functions are reduced. The situation of macular tissue disorganization is aggravated by edema and microcysts, the traumatic inflammation and degeneration sequelae. Furthermore, the presence of the circular tissue defect in the fovea creates the priority for centrifugal forces related to the surviving retinal tissue elasticity, which more and more actively stretch the remaining foveal tissue and shift it towards the macular area periphery as time passes.

Some authors have reported the methods of mechanical approximation of the macular hole edges by smoothing the retina surrounding the hole with the vitreous spatula from the periphery to the center [18] or by using the retinal “massage” with the silicone cannula [19] for repositioning of the macular hole edges. However, these manipulations dramatically increase the risk of reactive retinal edema, retinal pigment epithelial dislocation and spontaneous retinal detachment along the hole edge, which, in turn, can result in the foveal tissue loss and reduced functional potential of the retina after the anatomical fusion [20–22].

The proposed technique of fluid removal from the macular hole area by passive aspiration involving hermetic sealing of the area with the PFCL ensures manageable and maximally atraumatic fluid evacuation from the hole and the surrounding macular tissues of the retina. The fluid removed by this method creates the steadily increasing negative pressure, micro-vacuum that generates centripetal forces primarily pulling up and fusing the most functionally valuable parietal edge foveal tissue remains, in the intrawound space of the macular hole. At the same time, the fused macular hole walls are fixed in the foveal area by the PFCL gravity.

Thus, the “micro-vacuum” steadily increasing around the perimeter of the circular macular hole results in simultaneous minimally traumatic retraction, smoothing and fusion of the opposite macular hole walls behind the torn parts of the surviving foveal tissue. Along with this process, exposure to the PFCL gravity results in the fact that the fused remains of the macular hole wall tissue are fixed and retained in the foveal area. This micro-manipulation brings the surviving foveal tissue to the baseline microanatomical/microhistological position.

The time of the hole wall retention in the closed state by the PFCL gravity proposed by the technique (at least 10 min) makes it possible to significantly weaken the centrifugal forces associated with elasticity in the stretched retinal tissue. This important feature enables temporary retention of the fused macular hole walls in the closed state after the PFCL removal. Thus, there is enough time to cover the wound surface with ACP to achieve the hermetic plaque formation. The following takes place when applying ACP to the sealed wound along with the process of finalizing the plaque formation in the macular hole intrawound space.

Under the forming ACP plaque, after the holding force effect termination (fixing force, PFCL gravity), the remaining centrifugal forces of the retinal tissue elasticity are activated, which begin to stretch the closed walls of the macular hole from the center to the periphery. As a result, partial micro-separation of the macular wound walls occurs under the hermetic plaque. When

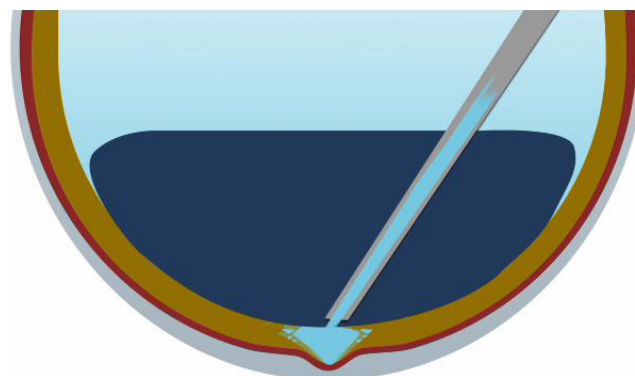


Fig. 1. Phases of the technique: vitreous cavity volume substitution with the perfluorocarbon liquid with subsequent aspiration of intraocular fluid from the hole area

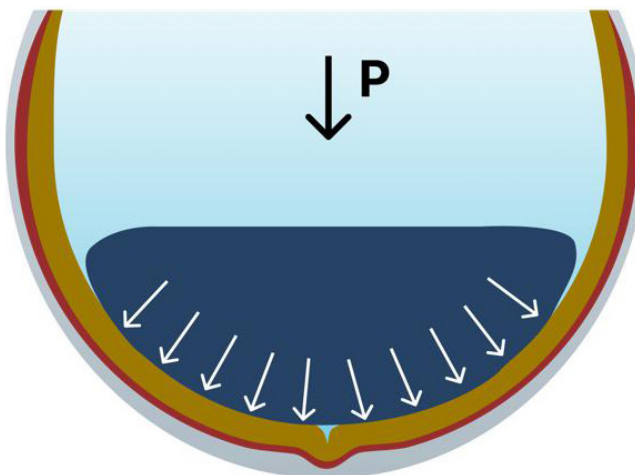
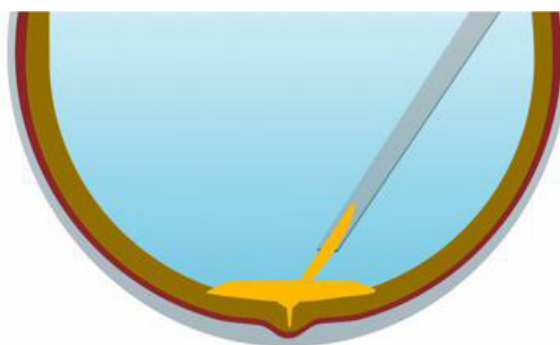


Fig. 2. Phases of the technique: under exposure to negative pressure in the hole area, the aggregate foveal tissue of the macular hole fused walls is held in this position due to the perfluorocarbon liquid gravity

A



B

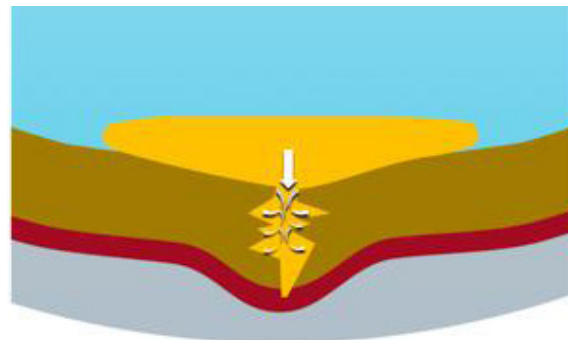


Fig. 3. Phases of the technique: application of the ACP prepared to the surface of the macular area of the retina with subsequent emergence of the hermetic plaque sealing the hole area (A) and filling the entire intrawound space (B)

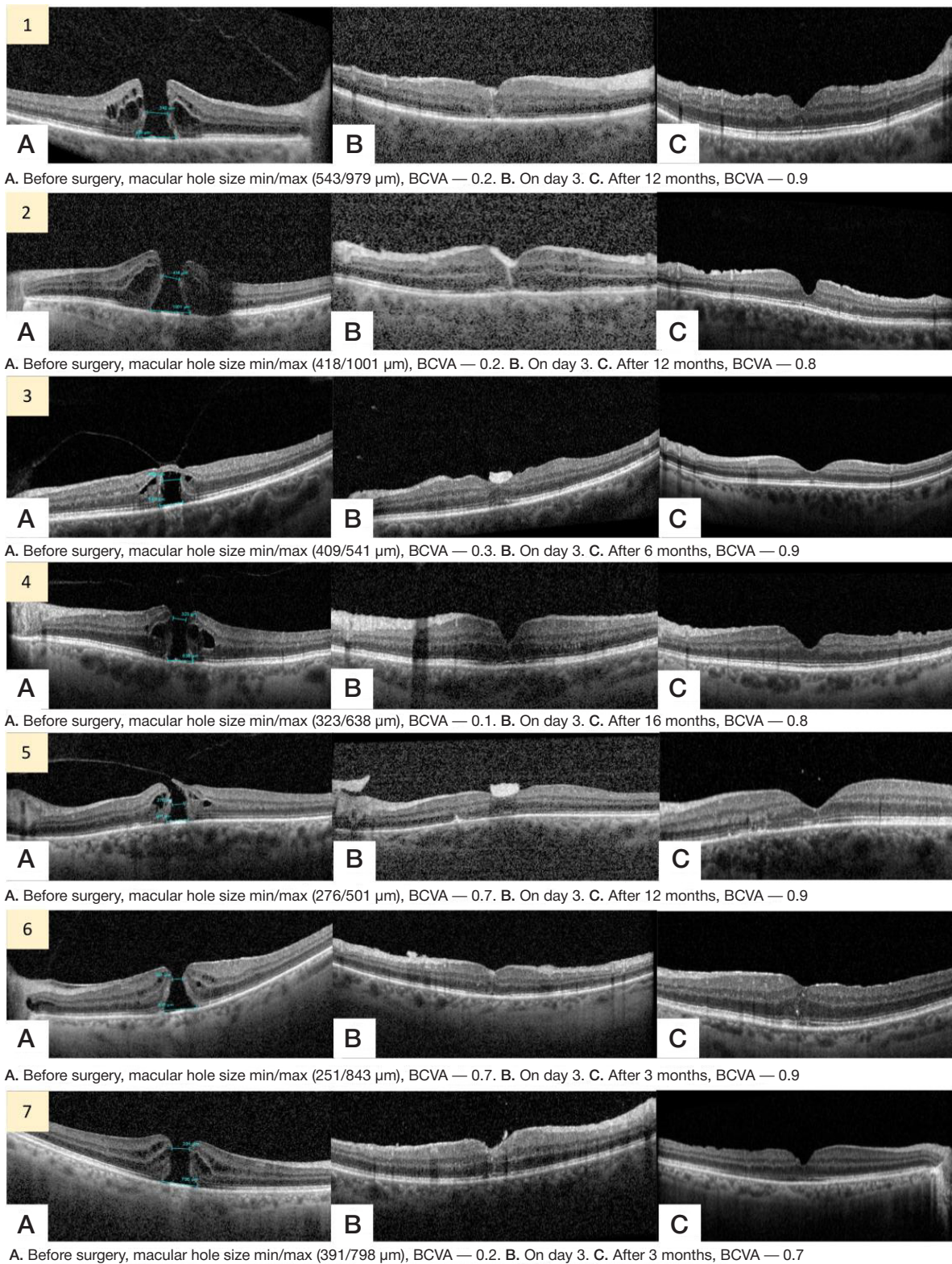


Fig. 4. OCT on the retina. Phases of macular hole closure after vitrectomy involving the use of ACP. **A.** Defect of all neuroretinal layers (macular hole). **B.** Follow up in the early postoperative period (on day 3). **C.** Follow up in the late postoperative period

micro-separation of the macular wound walls occurs, negative pressure is created in the resulting wound micro-lumen that increases with increasing micro-lumen size and forms a micro-vacuum effect ensuring suction of the liquid fractions of the entirely noncoagulated ACP. This process changes over time and continues at the level of microscopic alterations.

ACP soaked up into the micro-lumen (Fig. 3B) ensures the best and fullest microscopic coverage of the glued uneven

surfaces of the torn macular tissue. Furthermore, autoplasm leaks into irregularities, micro-cracks and micro-cavities. Thus, the maximum ACP (“biological glue”) coverage of the fused (glued) macular hole wound surfaces is achieved.

An adhesive biological insert (clot) of coagulated ACP (Fig. 5), where we managed to obtain OCT images with air tamponade 6 h after surgery, clearly demonstrate that ACP fills the entire intrawound

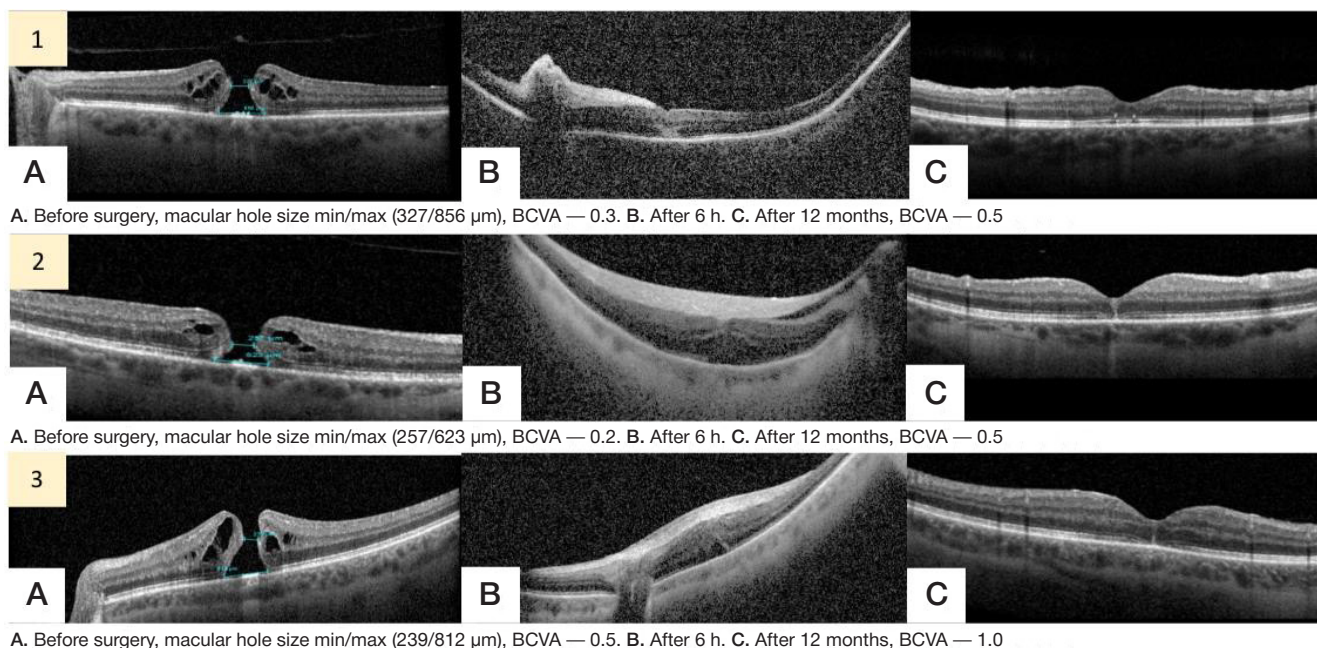


Fig. 5. Phases of macular hole closure after vitrectomy involving the use of ACP. **A.** Defect of all neuroretinal layers (macular hole). **B.** Follow up in the early postoperative period (after 6 h). **C.** Follow up in the late postoperative period

space, leaking into the wound wall irregularities. The ACP insert having a branched configuration duplicates the macular hole wall uneven curvature. This confirms the mechanism of micro-vacuum ACP suction from the plaque covering the macular hole. Moreover, already at this stage, the lack of parietal retinal cysts and cavities attracts attention, which demonstrates effective evacuation of both wound fluid and tissue fluid of patiental macular hole areas, including retinal cysts and hole wall cavities, from the macular hole.

On day three, all these signs become more prominent, which confirms the described foveal reconstruction mechanisms (Fig. 4). In the majority of cases, the insert transforms into a macular tear junction (adhesion line), which is associated with the macular profile formation and morphological organization of the macular/foveolar area tissue structure. The macular/foveolar area architectonics is restored. The images make it possible to see the processes of retinal segmentation and restoration of the most important retinal structures: foveal profile, ellipsoid zone, external limiting membrane, outer plexiform layer, inner plexiform layer.

In the long-term period, the architectonics restoration is completed and a soft scar is formed in the fovea at the site of the tear, around which the macular/foveolar retinal area framework structures fuse. The surviving neuronal cell structures of the fovea tend to occupy their normal microanatomical/microhistological positions, thereby ensuring restoration of preserved visual potential of the retina. Thus, the process of foveal architectonics micro-reconstruction is completed.

References

1. Aksenova SV, Hozina EA, Vasileva OA, Kumakshveva TN, Zotov RA. Makuljarnyj razryv: sovremennye aspekty jetiologii, diagnostiki i lechenija. *Sovremennye problemy nauki i obrazovanija*. 2023; 2. Russian.
2. Sen S, Udaya P, Maheshwari JJ, Ramasamy K, Kannan NB, Dharmalingam K. Profiling of idiopathic macular hole vitreous proteome identifies the role of extracellular matrix remodelling, epithelial-mesenchymal transformation and unfolded protein-response pathways. *Indian J Ophthalmol*. 2023; 71 (5): 2027–40.
3. Nicolosi C, Vicini G, Bacherini D, Giattini D, Lombardi N, Esposito C, Rizzo S, Giansanti F. Non-Invasive Retinal Imaging Modalities for the Identification of Prognostic Factors in Vitreoretinal Surgery for Full-Thickness Macular Holes. *Diagnostics*. 2023; 13 (4): 589.
4. Shukla D, Kalliath J, Srinivasan K, Neelakantan N, Rajendran A, Naresh KB, et al. Management of rhegmatogenous retinal detachment with coexisting macular hole: a comparison of vitrectomy with and without internal limiting membrane peeling. *Retina*. 2013; 33 (3): 571–78.

Along with the adhesive potential, the insert contains an equally significant range of natural biological substances ensuring the regeneration and reparation potential. In fact, the proposed technique is very close to micro-mechanisms underlying the natural tissue restoration process that ensures continuous physiological self-repair of the tissue microdamage occurring throughout the human body's active life.

CONCLUSIONS

1. The use of mild micro-vacuum for atraumatic fusion of the remaining foveal tissue of the retina, as well as for the maximum coverage of uneven surfaces of the torn macular tissue with the adhesive compound, ensures optimal foveal microarchitectonics reconstruction.
2. Understanding of the micro-processes associated with the proposed technology of the macular hole wall fusion (adhesion) results in the possibility of improving the technique and achieving the better and more full-fledged restoration of visual functions.
3. Bringing the techniques closer to the natural processes of the living tissue self-repair enables the optimal use of body's resources for restoration of damaged foveal microstructures and vital functions.
4. The more nuanced understanding of micro-processes associated with manipulations in the living tissue microworld opens up new opportunities for the development of clinical medicine dealing with microworld of the living human.

5. Duker JS, Kaiser PK, Binder S, et al. The Internation Vitreomacular Traction Study Group classification of vitreomacular adhesion, traction, and macular hole. *Ophthalmology*. 2013; 120 (12): 2611–19.
6. Bronskii DI, Zaika VA, Yakimov AP. Ocenka izmenenija jellipsoidnoj zony setchatki do i posle hirurgicheskogo lechenija skvoznyh makuljarnyh razryvov. *Oftal'mohirurgija*. 2023; 3: 72–77. Russian.
7. Lachance A, You E, Garneau J, Bourgault S, Caissie M, Tourville E, Dirani A. Revision surgery for idiopathic macular hole after failed primary vitrectomy. *J Ophthalmol*. 2021; p. 1–7.
8. Shkvorchenko DO, Krupina EA, Fomin AV. OKT-angiografija v ocenke rezul'tatov hirurgicheskogo lechenija makuljarnyh razryvov. *Oftal'mologija*. 2019;16 (3): 310–6. Russian.
9. Bronskii DI, Zhukova SI, Zaika VA, Shhuko AG. Ocenka stepeni vosstanovlenija struktury setchatki i horioretinal'nogo krovotoka posle hirurgicheskogo lechenija makuljarnyh razryvov bol'shogo diametra. *Acta biomedica scienti ca*. 2021; 6 (6–1): 159–67. Russian.
10. Stappeler T, Montesel A, Konstantinidis L, Wolfensberger TJ, Eandi CM. Inverted internal limiting membrane flap technique for macular hole coexistent with rhegmatogenous retinal detachment. *Retina*. 2022; 42 (8): 1491–7.
11. Zhao PP, Wang S, Liu N, Shu ZM, Zhao JS. A review of surgical outcomes and advances for macular holes. *J Ophthalmol*. 2018; p.1–10.
12. Abouhoussein MA, Elbaha SM, Aboushousha M. Human amniotic membrane plug for macular holes coexisting with rhegmatogenous retinal detachment. *Clin Ophthalmol*. 2020; (14): 2411–6.
13. Krupina EA. Hirurgicheskoe lechenie idiopaticeskogo makuljarnogo razryva s primeneniem bogatoj trombocitami plazmy krovi [dissertacija]. M., 2019. Russian.
14. Popov EM, Kulikov AN, Churashov SV, Gavriljuk IO, Egorova EN, Abbasova AI. Sravnenie pokazatelej poluchaemoj raznymi sposobami autoplazmy, ispol'zuemoj dlja lechenija pacientov s makuljarnym razryvom. *Oftal'mologicheskie vedomosti*. 2021; 14 (4): 27–34. Russian.
15. Arsjutov DG. Ispol'zovanie autologichnoj kondicionirovannoj plazmy, obogashhennoj trombocitami, v hirurgii regmatogennoj otslojki setchatki s central'nym i perifericheskimi razryvami. *Acta biomedica scientifica*. 2019; 4 (4): 61–65. Russian.
16. Bajborodov YaV, Zhogolev KS. Autologichnaja kondicionirovannaja plazma — inducirovannaja fibrinnaja plenka v hirurgicheskom lechenii makuljarnyh razryvov. *Sovremennye tehnologii v oftal'mologii*. 2020; (4): 283. Russian.
17. Meuer SM, Myers CE, Klein BE, Swift MK, Huang Y, Gangaputra S, Pak JW, Danis RP, Klein R. The epidemiology of vitreoretinal interface abnormalities as detected by spectral-domain optical coherence tomography: the beaver dam eye study. *Ophthalmology*. 2015; 122 (4): 787–95.
18. Bikbov MM, Altynbaev UR. Sposob hirurgicheskogo lechenija makuljarnogo razryva. Patent RF #2407493. 27.12.2010. Russian.
19. Bikbov MM, Altynbaev UR, Gilmanshin TR, Chernov MS. Vybora sposoba intraoperacionnogo zakrytija idiopaticeskogo makuljarnogo razryva bol'shogo diametra. *Oftal'mohirurgija*. 2010; 1: 25–28. Russian.
20. Balashevich LI, Bajborodov YaV. Hirurgicheskoe lechenie makuljarnyh razryvov, vyzvannyh lazernym povrezhdeniem foveoly (klinicheskij sluchaj). *Sovremennye tehnologii lechenija vitreoretinal'noj patologii 2013: materialy nauch.-prakt. konf. M., 2013; 27 c. Russian.*
21. Fajzrahmanov RR, Shishkin MM, Pavlovskij OA, Larina EA. Operativnoe lechenie makuljarnogo razryva. Ufa: Bashk. jencikl., 2020; 144 c. Russian.
22. Zaharov VD, Kislicina NM, Kolesnik SV, Novikov SV, Kolesnik AI, Veselkova MP. Sovremennye podhody k hirurgicheskomu lecheniju skvoznyh idiopaticeskikh makuljarnyh razryvov bol'shogo diametra (obzor literatury). 2018; 3 (4): 64–70. Russian.

Литература

1. Аксенова С. В., Хозина Е. А., Васильева О. А., Кумакшева Т. Н., Зотов Р. А. Макулярный разрыв: современные аспекты этиологии, диагностики и лечения. *Современные проблемы науки и образования*. 2023; 2.
2. Sen S, Udaya P, Maheshwari JJ, Ramasamy K, Kannan NB, Dharmalingam K. Profiling of idiopathic macular hole vitreous proteome identifies the role of extracellular matrix remodelling, epithelial-mesenchymal transformation and unfolded protein-response pathways. *Indian J Ophthalmol*. 2023; 71 (5): 2027–40.
3. Nicolosi C, Vicini G, Bacherini D, Giattini D, Lombardi N, Esposito C, Rizzo S, Giansanti F. Non-Invasive Retinal Imaging Modalities for the Identification of Prognostic Factors in Vitreoretinal Surgery for Full-Thickness Macular Holes. *Diagnostics*. 2023; 13 (4): 589.
4. Shukla D, Kalliath J, Srinivasan K, Neelakantan N, Rajendran A, Naresh KB, et al. Management of rhegmatogenous retinal detachment with coexisting macular hole: a comparison of vitrectomy with and without internal limiting membrane peeling. *Retina*. 2013; 33 (3): 571–78.
5. Duker JS, Kaiser PK, Binder S, et al. The Internation Vitreomacular Traction Study Group classification of vitreomacular adhesion, traction, and macular hole. *Ophthalmology*. 2013; 120 (12): 2611–19.
6. Бронский Д. И., Зайка В. А., Якимов А. П. Оценка изменения эллипсоидной зоны сетчатки до и после хирургического лечения сквозных макулярных разрывов. *Офтальмохирургия*. 2023; 3: 72–77.
7. Lachance A, You E, Garneau J, Bourgault S, Caissie M, Tourville E, Dirani A. Revision surgery for idiopathic macular hole after failed primary vitrectomy. *J Ophthalmol*. 2021; p. 1–7.
8. Шкворченко Д. О., Крупина Е. А., Фомин А. В. ОКТ-ангиография в оценке результатов хирургического лечения макулярных разрывов. *Офтальмология*. 2019;16 (3): 310–6.
9. Бронский Д. И., Жукова С. И., Зайка В. А., Щуко А. Г. Оценка степени восстановления структуры сетчатки и хориоретинального кровотока после хирургического лечения макулярных разрывов большого диаметра. *Acta biomedica scientifica*. 2021; 6 (6–1): 159–67.
10. Stappeler T, Montesel A, Konstantinidis L, Wolfensberger TJ, Eandi CM. Inverted internal limiting membrane flap technique for macular hole coexistent with rhegmatogenous retinal detachment. *Retina*. 2022; 42 (8): 1491–7.
11. Zhao PP, Wang S, Liu N, Shu ZM, Zhao JS. A review of surgical outcomes and advances for macular holes. *J Ophthalmol*. 2018; p.1–10
12. Abouhoussein MA, Elbaha SM, Aboushousha M. Human amniotic membrane plug for macular holes coexisting with rhegmatogenous retinal detachment. *Clin Ophthalmol*. 2020; (14): 2411–6.
13. Крупина Е. А. Хирургическое лечение идиопатического макулярного разрыва с применением богатой тромбоцитами плазмы крови [диссертация]. М., 2019.
14. Попов Е. М., Куликов А. Н., Чурашов С. В., Гаврилук И. О., Егорова Е. Н., Аббасова А. И. Сравнение показателей получаемой разными способами аутоплазмы, используемой для лечения пациентов с макулярным разрывом. *Офтальмологические ведомости*. 2021; 14 (4): 27–34.
15. Арсютов Д. Г. Использование аутологичной кондиционированной плазмы, обогащенной тромбоцитами, в хирургии регматогенной отслойки сетчатки с центральным и периферическими разрывами. *Acta biomedica scientifica*. 2019; 4 (4): 61–65.
16. Байбородов Я. В., Жоголев К. С. Аутологичная кондиционированная плазма — индуцированная фибринная пленка в хирургическом лечении макулярных разрывов. *Современные технологии в офтальмологии*. 2020; (4): 283.
17. Meuer SM, Myers CE, Klein BE, Swift MK, Huang Y, Gangaputra S, Pak JW, Danis RP, Klein R. The epidemiology of vitreoretinal interface abnormalities as detected by spectral-domain optical coherence tomography: the beaver dam eye study. *Ophthalmology*. 2015; 122 (4): 787–95.
18. Бикбов М. М., Алтынбаев У. Р. Способ хирургического лечения

- макулярного разрыва. Патент РФ №2407493. 27.12.2010
19. Бикбов М. М., Алтынбаев У. Р., Гильманшин Т. Р., Чернов М. С. Выбор способа интраоперационного закрытия идиопатического макулярного разрыва большого диаметра. Офтальмохирургия. 2010; 1: 25–28.
 20. Балашевич Л. И., Байбородов Я. В. Хирургическое лечение макулярных разрывов, вызванных лазерным повреждением фовеолы (клинический случай). Современные технологии лечения витреоретинальной патологии — 2013: материалы науч.-практ. конф. М., 2013; 27 с.
 21. Файзрахманов Р. Р., Шишкин М. М., Павловский О. А., Ларина Е. А. Оперативное лечение макулярного разрыва. Уфа: Башк. энцикл., 2020; 144 с.
 22. Захаров В. Д., Кислицина Н. М., Колесник С. В., Новиков С. В., Колесник А. И., Веселкова М. П. Современные подходы к хирургическому лечению сквозных идиопатических макулярных разрывов большого диаметра (обзор литературы). 2018; 3 (4): 64–70.